

QUANTUM ORDER, ENTANGLEMENT AND
LOCALIZATION IN MANY-BODY SYSTEMS

VEDIKA KHEMANI

A DISSERTATION
PRESENTED TO THE FACULTY
OF PRINCETON UNIVERSITY
IN CANDIDACY FOR THE DEGREE
OF DOCTOR OF PHILOSOPHY

RECOMMENDED FOR ACCEPTANCE
BY THE DEPARTMENT OF
PHYSICS
ADVISER: S. L. SONDHI

SEPTEMBER 2016

© Copyright by Vedika Khemani, 2016.

All rights reserved.

Abstract

The interplay of disorder and interactions can have remarkable effects on the physics of quantum systems. A striking example is provided by the long conjectured—and recently confirmed—phenomenon of many-body localization. Many-body localized (MBL) phases violate foundational assumptions about ergodicity and thermalization in interacting systems, and represent a new frontier for non-equilibrium quantum statistical mechanics.

We start with a study of the dynamical response of MBL phases to time-dependent perturbations. We find that that an asymptotically slow, local perturbation induces a highly non-local response, a surprising result for a localized insulator. A complementary calculation in the linear-response regime elucidates the structure of many-body resonances contributing to the dynamics of this phase

We then turn to a study of quantum order in MBL systems. It was shown that localization can allow novel high-temperature phases and phase transitions that are disallowed in equilibrium. We extend this idea of “localization protected order” to the case of symmetry-protected topological phases and to the elucidation of phase structure in periodically driven Floquet systems. We show that Floquet systems can display nontrivial phases, some of which show a novel form of correlated spatiotemporal order and are *absolutely stable* to all generic perturbations.

The next part of the thesis addresses the role of quantum entanglement, broadly speaking. Remarkably, it was shown that even highly-excited MBL eigenstates have low area-law entanglement. We exploit this feature to develop tensor-network based algorithms for efficiently computing and representing highly-excited MBL eigenstates. We then switch gears from disordered, localized systems and examine the entanglement Hamiltonian and its low energy spectrum from a statistical mechanical lens, particularly focusing on issues of universality and thermalization.

We close with two miscellaneous results on topologically ordered phases. The first studies the nonequilibrium “Kibble-Zurek” dynamics resulting from driving a system through a phase transition from a topologically ordered phase to a trivial one at a finite rate. The second shows that the four-state Potts model on the pyrochlore lattice exhibits a “Coulomb Phase” characterized by three emergent gauge fields.

Acknowledgements

As I reflect back on the last decade of my life which has culminated in this thesis, I am struck by the support I have received from so many different, often unexpected, quarters.

I am deeply grateful to my advisor, Shivaji Sondhi, for his insightful mentorship and for the extraordinary time and care he has invested in my education. From the very beginning, Shivaji has been a constant source of encouragement. He has patiently shared his road map of condensed matter physics (and politics, history, and life, more generally!) and has helped me craft my own worldview in the process. Physics with Shivaji was always inspiring and fun. He has the remarkable ability to simultaneously ask the “big questions” which can synthesize seemingly unremarkable calculations into a beautiful edifice, while also teasing apart the smallest subtleties of an idea. Shivaji’s curiosity and keen insight have constantly pushed me to examine and expand the boundaries of my understanding, and his dry humor and sharp wit made for many enjoyable hours at the blackboard. Of course, the transition from student to collaborator wasn’t always easy. However, Shivaji’s patience, his thoughtful criticism, and his astute advice on everything from setting research priorities to finding problems best suited to my skills to navigating the human aspects of collaborative (and sometimes competitive) research have been invaluable in mitigating the growing pains. I will be forever grateful for his counsel and mentorship.

I especially thank David Huse for working closely with me over the last year. David’s insight and clarity of thought is truly remarkable, and I have left every conversation with a deeper understanding of the problem at hand. It has been amazing to witness the care and precision with which David chooses his words, and how the right choice can immediately illuminate and sharpen a half-formed thought. David has the uncanny ability to rapidly distinguish between superfluous distractions and key results, whether it be in numerical data or conceptual ideas, and it has been an

invaluable learning experience working with him. I am also extremely grateful to him for his patience through the various interruptions of our projects, and his willingness to read the many pages that follow.

I am lucky to come after a long line of overachievers, and I am extremely grateful for the friendship and counsel of my elder academic siblings Fiona Burnell, Chris Lauermann, Sid Parameswaran and Anushya Chandran. Sid worked with me on my first project, showed me the ropes of the physics department, introduced me to Nomad Pizza, and even taught me the basics of the tight-binding model when I was a clueless first year with no knowledge of condensed matter physics! Over the years, we have had numerous valuable discussions on physics and life in academia. My understanding of many aspects of physics wouldn't be half as solid without the many discussions (both direct and indirect) with Chris, and his care and attention to detail is truly aspirational. I am extremely grateful for all the advice on life, physics, talks, applications, and for the many fun dinners and outings. Finally, I would like to thank Anushya, my closest friend in physics, for her unwavering support and friendship over the years. Physics would have been far less fun and far more lonely without our many intense discussions on life, the universe (well mostly physics), and everything (we have certainly irritated many office mates with our never ending skypes!). A good third of this thesis and well over half my time in graduate school reflects work with Anushya, and our uncountable physics discussions and revision sessions have built my understanding of more topics than one.

I have had the immense good fortune of collaborating closely with an extraordinary group of physicists during my graduate years. Roderich Moessner worked with me on both frustrated magnetism and Floquet theory, and generously allowed me to accompany Shivaji during his sabbatical year in Dresden. My time in Dresden was among the most intense and focused periods of research in my graduate career, and I benefited tremendously from conversations with the numerous residents and visitors

of MPI. Frank Pollmann taught me almost everything I know about tensor-network methods, and learning the ins and outs of his code libraries has been invaluable in developing my own numerical skills. I'm trying hard to emulate Frank's remarkable ability to write hundreds of lines of code overnight! I worked with Rahul Nandkishore on the dynamical response of MBL systems and the paper we wrote together will always be a favorite. I benefited greatly from Rahul's presence across the 4th floor and am extremely grateful for our numerous conversations on MBL and academia. Achilleas Lazarides introduced me to the intricacies of the Floquet problem, and I learned a lot from our collaboration. Curt von Keyserlingk and I worked together on Floquet phases, and I was fortunate to witness Curt's impressive mathematical physics skills and his ability to represent just about anything with a compact symbol. Our many discussions contributed greatly to my understanding, and I am grateful for Curt's patience in walking me through his various proofs. While I cannot possibly thank all the scientists whose insights I have benefited from, I would especially like to acknowledge many valuable discussions with John Chalker, Vadim Oganesyan, Sarang Gopalakrishnan, Andrei Bernevig, Ignacio Cirac and Fiona Burnell.

The physics department at Jadwin has been a very stimulating environment thanks to the present and past members of the condensed matter group, including Hyungwon Kim, Mike Kolodrubetz, Aris Alexandradinata, Arijeet Pal, Bryan Clark, Joe Maciejko, Titus Neupert, Akshay Kumar, Scott Geraedts, Jennifer Cano, Barry Bradlyn, Liangsheng Zhang and Bo Zhao. I would also like to thank my thesis committee members, Silviu Pufu and Ali Yazdani. I am especially grateful to Ali for supervising my experimental project and giving me a first hand feel for experimental condensed matter physics, and to Eduardo da Silva Neto and Andras Gyenis for putting up with me in the lab. I thank Herman Verlinde for being a part of my pre-thesis committee and for taking an interest in my work over the years. I'd like to also acknowledge the administrators who have made my graduate years as bu-

reaucratically painless as possible: Toni Sarchi, Jessica Heslin, Kate Brosowsky and Charlene Borsack. Vinod Gupta and Sumit Saluja went out of their way to remove computational hurdles, and always came through in a pinch when I needed extra cluster resources.

This thesis would not have been possible without the early encouragement of my undergraduate professors, especially Vatche Sahakian, John Townsend, Patti Sparks and Rachel Levy. Their support and willingness to discuss physics and mathematics with me for hours fostered my interest and convinced me to pursue a career in research.

I thank all the wonderful friends I made at Princeton. Exploring the many restaurants around Princeton with Chaney Lin, Akshay Kumar, Aris Alexandradinata, Tim Lou, Liangsheng Zhang, Bo Zhao and Hyungwon Kim was always fun. I especially thank Akshay for making Dresden less socially isolated than it would have otherwise been. Board game nights with Emily and Jason Shields were always competitive and enjoyable. My “New-York friends”, Jason and Mengjia Christiansen, Ben Taborsky, Alex Korn and Rebecca Burns provided a welcome break from the academic bubble.

Above all, I am grateful to my family, especially my parents Rashmi and Navneet, for their unwavering love, support and encouragement. No words can acknowledge their sacrifices over the years to get me to this point. Phone calls from my younger brothers Vedant and Devansh injected a dose of humor into the gloomiest of days. Calls from my grandmother, Rajkumari, and my uncle and aunt, Vineet and Vinty, were always loving and shrunk the vast distance between me and India. My uncle, Rajesh, was my earliest champion and introduced me to the beauty of physics and mathematics at a young age. I thank Valerie, Jake and Lori for being my family in the U.S. and for their steady encouragement. Last, but certainly not the least, I thank my husband David Coats for being my rock, my partner in adventure, and for always reminding me that the best is yet to come.

Publications and Presentations associated with this Dissertation

Chapter 2 is based on [172]; Chapter 3 on [121]; Chapter 4 on [64], and Chapter 5 on [169]. Chapters 6 and 7 are based on the preprints [315] (to appear in Physical Review B) and [249] (to appear in Physical Review B) respectively. Chapter 8 is based on [173]; Chapter 9 on [65]; Chapter 10 on [167]; Chapter 11 on [60] and Chapter 12 on [171]. Most of these chapters have been slightly modified from the published articles. Nevertheless, the copyright to the original articles rests with the relevant journals.

The following public presentations were based on materials from this dissertation:

1 *Absolute Stability and Spatiotemporal Long Range Order in Floquet Systems*

- (a) Seminar at University of Colorado, Boulder, June 2016

2 *Dynamical Response of Many-Body Localized Systems*

- (a) Invited Talk at APS March Meeting, March 2016
- (b) Seminar at Harvard University, December 2016
- (c) Seminar at the University of Illinois, Urbana Champagne, December 2016
- (d) Seminar at the Joint Quantum Institute, Maryland, November 2015
- (e) Invited Talk at *Aspects and Applications of Many-Body Localization*, Kavli Institute of Theoretical Physics, November 2015
- (f) Seminar at UC Berkeley, November 2015
- (g) Seminar at Microsoft Station Q, November 2015
- (h) Seminar at Stanford University, November 2015
- (i) Seminar at California Institute of Technology, October 2015
- (j) Invited Talk at *Aspects of non-equilibrium dynamics in quantum computation*, City University of New York, April 2015.

3 *Many Body Localization and Symmetry Protected Topological Order*

- (a) Seminar at Rice University, May 2014
- (b) Invited Talk at *Emergent Phenomena in the Dynamics of Quantum Matter*,
City University of New York, April 2014
- (c) Talk at APS March Meeting, March 2014

4 *Kibble-Zurek Scaling and String Net Coarsening in Topologically Ordered Systems*

- (a) Invited talk at APS March Meeting, March 2014
- (b) Talk at APS March Meeting, March 2013

To my family, who believed from the beginning,
and saw me to the end.

Contents

| | |
|--|----------|
| Abstract | iii |
| Acknowledgements | v |
| Publications and Presentations associated with this Dissertation | ix |
| List of Tables | xix |
| List of Figures | xx |
| | |
| I Introductory Material | 1 |
| | |
| 1 Ergodicity and Localization | 2 |
| 1.1 Anderson Localization | 2 |
| 1.2 Many-Body Localization (MBL) | 5 |
| 1.2.1 Basko, Aleiner, Altshuler (BAA) | 6 |
| 1.2.2 MBL in a Spin Model | 9 |
| 1.3 Quantum Ergodicity/Thermalization | 13 |
| 1.3.1 The Eigenstate Thermalization Hypothesis (ETH) | 16 |
| 1.4 Local Integrals of Motion | 18 |
| 1.5 Quantum Entanglement in Localized Systems | 21 |
| 1.6 Eigenstate Order and Eigenstate Phase Transitions | 24 |
| 1.7 Experimental Probes | 27 |
| 1.8 Floquet Systems | 29 |
| 1.8.1 Floquet Formalism | 29 |

| | | |
|--|---|-----------|
| 1.8.2 | Ergodicity and Localization in the Floquet Setting | 35 |
| 1.9 | Open Problems | 37 |
| 1.10 | This Thesis | 40 |
| II Dynamical Response of Many-Body Localized Systems | | 42 |
| 2 Non-local Adiabatic Response of a Localized System to Local Manipulations | | 43 |
| 2.1 | Introduction | 44 |
| 2.2 | The Anderson Insulator | 46 |
| 2.2.1 | Orthogonality Catastrophe | 51 |
| 2.2.2 | Failure of linear response | 53 |
| 2.3 | Contrast with Clean Insulators and with Metals | 55 |
| 2.4 | Generalization to MBL | 56 |
| 2.5 | Discussion and Ramifications | 58 |
| 2.5.1 | Quantum computation with quantum Hall systems | 60 |
| 2.5.2 | Other proposals for quantum computation | 62 |
| 3 Low-Frequency Linear-Response Conductivity in Many-Body Localized Systems | | 65 |
| 3.1 | Introduction | 65 |
| 3.2 | Assumptions | 67 |
| 3.3 | MBL-Mott regime | 69 |
| 3.3.1 | Many-body “Mott” conductivity | 69 |
| 3.3.2 | Rare-region Mott resonances | 73 |
| 3.4 | MBL-Griffiths regime | 74 |
| 3.5 | Transition between MBL-Mott and MBL-Griffiths regimes | 78 |
| 3.6 | Numerical simulations | 79 |

| | | |
|--|--|------------|
| 3.7 | Experimental aspects | 80 |
| 3.8 | Discussion | 82 |
| 3.A | Structure of a thermal inclusion | 83 |
| 3.B | Details of conductivity numerics | 85 |
| III Eigenstate Order in Many-Body Localized Systems | | 91 |
| 4 | Many-body Localization and Symmetry Protected Topological Order | 92 |
| 4.1 | Introduction | 92 |
| 4.2 | Haldane phase | 94 |
| 4.2.1 | Review of low energy physics | 94 |
| 4.2.2 | Ergodicity and localization in highly excited states | 95 |
| 4.3 | Topological Ising paramagnet in $d=2$ | 103 |
| 4.3.1 | Review of low energy physics | 103 |
| 4.3.2 | Ergodicity and localization in highly excited states | 105 |
| 4.4 | Concluding remarks | 110 |
| 4.A | Entanglement spectrum of dihedral symmetric MPS without translational symmetry | 111 |
| 5 | Phase Structure Of Driven Quantum Systems | 116 |
| 5.1 | Introduction | 116 |
| 5.2 | Floquet Paramagnet and Spin Glass | 118 |
| 5.3 | Paramagnet-Spin Glass Phase transition | 122 |
| 5.4 | π Spin Glass and 0π Paramagnet | 122 |
| 5.5 | Summary and open questions: | 126 |
| 6 | Absolute Stability and Spatiotemporal Long-Range Order in Floquet Systems | 128 |

| | | |
|-------|---|-----|
| 6.1 | Introduction | 128 |
| 6.2 | The π Spin glass: Absolute stability and emergent symmetries | 132 |
| 6.2.1 | Properties of the π SG phase | 132 |
| 6.2.2 | Absolute stability and emergent symmetries | 134 |
| 6.2.3 | Long range order and numerics | 137 |
| 6.3 | The π Spin Glass: Spatiotemporal Long Range Order | 141 |
| 6.3.1 | Eigenstate correlations and response | 141 |
| 6.3.2 | Quenches from general initial states | 144 |
| 6.3.3 | Comments | 146 |
| 6.4 | Generalizations | 147 |
| 6.4.1 | \mathbb{Z}_n and non-abelian models: | 148 |
| 6.4.2 | Stability of SPTs and boundary time crystallinity | 148 |
| 6.5 | Concluding remarks | 152 |
| 6.A | $\tau_{r,\lambda}^z$ either commutes or anti-commutes with $U_{f\lambda}$ | 154 |
| 6.B | Symmetries and the \mathcal{V}_λ unitaries | 155 |

IV Tensor-Network Approach to Many-Body Localization 158

| | | |
|----------|--|------------|
| 7 | Efficient Variational Diagonalization of Many-Body Localized Hamiltonians | 159 |
| 7.1 | Introduction | 159 |
| 7.2 | MPS and MPO notation | 162 |
| 7.3 | Method | 163 |
| 7.4 | Results | 166 |
| 7.4.1 | Energy Spectrum | 166 |
| 7.4.2 | Spectral Functions | 167 |
| 7.4.3 | Comments on accuracy | 168 |

| | | |
|-----------|---|------------|
| 7.5 | Summary and discussion | 169 |
| 7.A | Efficient evaluation of the cost functional | 171 |
| 8 | Obtaining Highly-Excited Eigenstates of MBL Hamiltonians by the Density Matrix Renormalization Group | 173 |
| 8.1 | Introduction | 173 |
| 8.2 | DMRG-X Method | 175 |
| 8.3 | Comparison with ED for small systems | 177 |
| 8.4 | Larger systems | 179 |
| 8.5 | Energy targeting | 183 |
| 8.6 | Summary and Outlook | 183 |
| 8.A | Details of the DMRG-X Method | 184 |
| V | Statistical Mechanics with the Entanglement Hamilto- nian | 188 |
| 9 | How Universal is the Entanglement Spectrum? | 189 |
| 9.1 | Introduction | 189 |
| 9.2 | Systems with symmetry breaking | 191 |
| 9.3 | Chern Insulator/QH Hall fluid | 196 |
| 9.4 | Conclusions | 199 |
| 10 | Eigenstate Thermalization and Representative States on Subsys- tems | 201 |
| 10.1 | Introduction | 201 |
| 10.2 | Free fermions | 204 |
| 10.2.1 | $T = 0$ | 205 |
| 10.2.2 | $T > 0$ | 208 |
| 10.3 | Generic eigenstates | 210 |

| | |
|---|------------|
| 10.4 Random states | 215 |
| 10.5 Concluding Remarks | 217 |
| VI Miscellaneous Results on Topological Phases | 219 |
| 11 Kibble-Zurek Scaling and String-Net Coarsening in Topologically Ordered Systems | 220 |
| 11.1 Introduction | 220 |
| 11.2 Review of the phase diagram of the \mathbb{Z}_2 Gauge Theory | 224 |
| 11.2.1 The perturbed toric code | 225 |
| 11.2.2 Pure matter theory ($\Gamma = 0$) | 227 |
| 11.2.3 Pure Gauge Theory ($J = 0$) | 228 |
| 11.2.4 The full phase diagram | 230 |
| 11.3 Kibble Zurek I - Ramp across the Higgs transition | 230 |
| 11.3.1 Scaling theory: Review | 231 |
| 11.3.2 Coarsening | 233 |
| 11.4 Kibble Zurek II - Ramp across the confinement transition | 236 |
| 11.5 Kibble Zurek III - Ramp across a generic transition in the \mathbb{Z}_2 theory . | 240 |
| 11.6 Extension to generalized Levin-Wen models | 242 |
| 11.6.1 Levin-Wen Hamiltonians with Ising transitions | 242 |
| 11.6.2 Away from the pure \mathbb{Z}_2 limit | 249 |
| 11.7 Concluding Remarks | 250 |
| 11.A Scattering times in coarsening | 251 |
| 11.B Mapping of general $SU(2)_k$ models to the \mathbb{Z}_2 gauge theory | 252 |
| 11.B.1 Equal weighting of loops in the ground states at the solvable points | 254 |
| 11.B.2 Away from the solvable points | 257 |

| | |
|--|------------|
| 12 A Bionic Coulomb Phase on the Pyrochlore Lattice | 261 |
| 12.1 Introduction | 261 |
| 12.2 The Model | 264 |
| 12.3 Flux Fields and Correlations | 267 |
| 12.3.1 Flux Fields | 267 |
| 12.3.2 Coarse-grained Free Energy and Correlations | 269 |
| 12.3.3 Monte Carlo Simulations | 272 |
| 12.4 Charges, defects and Dirac Strings | 274 |
| 12.5 Worm length distributions | 279 |
| 12.6 Concluding Remarks | 281 |
| 12.A Spin-Spin Correlation Functions | 281 |
| 12.B Symmetries and Stability of the Free Energy | 284 |
| Bibliography | 291 |

List of Tables

| | | |
|------|--|-----|
| 1.1 | Properties of the many-body-localized phase, contrasted with those of the thermal and the single-particle-localized phases | 24 |
| 12.1 | Catalog of defects and charges in the bionic Coulomb phase | 290 |

List of Figures

| | | |
|-----|--|----|
| 1.1 | Phase diagram of the disordered Heisenberg chain | 11 |
| 1.2 | Quantum Statistical Mechanics | 14 |
| 1.3 | A cold-atoms experiment showing signatures of MBL | 28 |
| 1.4 | An illustration of the Floquet replica formalism | 34 |
| 2.1 | Schematic illustration of non-local charge response | 45 |
| 2.2 | Adiabatic charge response, zone of disturbance, and the statistical orthogonality catastrophe in an Anderson insulator | 47 |
| 2.3 | Level crossings in the Anderson insulator | 48 |
| 2.4 | Comparison of exact and linear-response density difference for an Anderson insulator and a non-interacting metal | 54 |
| 2.5 | Schematic of a proposal for topological quantum computation using a quantum Hall platform | 60 |
| 3.1 | A.C. conductivity exponent across the many-body localization transition | 68 |
| 3.2 | Contribution of thermal inclusions to the conductivity in many-body localized phases | 76 |
| 3.3 | Power-law dependence of the a.c. conductivity on frequency | 79 |
| 3.4 | Effects of boundary conditions and finite-sizes on the low-frequency a.c. conductivity | 86 |
| 3.5 | Effect of interactions on the conductivity exponent | 88 |

| | | |
|-----|---|-----|
| 3.6 | Distribution of dipole moments showing the resonances contributing to the a.c. conductivity | 89 |
| 4.1 | Typical eigenstates of the BKLT model in the single-triplon manifold | 99 |
| 4.2 | Entanglement spectra of excited eigenstates in the BKLT model | 101 |
| 4.3 | Illustration of trivial and topological Ising paramagnets in 2D | 104 |
| 5.1 | Level statistics and spin-glass order parameter for a disordered Ising model | 120 |
| 5.2 | Phase diagram showing the $0, \pi$ spin-glass phases and the trivial, 0π paramagnetic phases in a driven Ising chain, and the stability of the π phase to weak interactions | 123 |
| 5.3 | Spectral functions and time-dependent correlators in the π SG phase | 125 |
| 6.1 | Schematic depictions of the manifold of absolutely stable Floquet unitaries and the associated spatiotemporal order | 130 |
| 6.2 | Spectral pairing in the absolutely stable π SG phase | 138 |
| 6.3 | Correlation functions showing long-range order in the absolutely stable π SG phase | 139 |
| 6.4 | Fourier transform of time-dependent expectation values of generic initial states in the π SG phase | 146 |
| 6.5 | Phase diagram of the driven Ising chain showing the $0, \pi$ spin-glass phases and the trivial, 0π paramagnetic phases. Only the π SG phase is absolutely stable to generic perturbations | 149 |
| 7.1 | Representation of the variational ansatz for the diagonalizing unitary in MPO notation | 161 |
| 7.2 | Comparison of the exact energy levels with those obtained variationally using the VUMPO method | 163 |

| | | |
|------|---|-----|
| 7.3 | Variance of the energy levels obtained using the variational VUMPO method | 167 |
| 7.4 | Comparison of exact spectral functions with those obtained variationally using the VUMPO method | 168 |
| 7.5 | Diagrammatic representation of the tensor contractions required to evaluate the cost function for the VUMPO method | 172 |
| 8.1 | Comparison of the exact energy levels with those obtained variationally using the DMRG-X method | 177 |
| 8.2 | Variance of the energy levels obtained using the variational DMRG-X method and an energy-based variational method | 179 |
| 8.3 | Violation of the ETH in states obtained via the variational DMRG-X method | 182 |
| 8.4 | Diagrammatic representation of the DMRG-X algorithm in MPS/MPO notation | 184 |
| 9.1 | Phase diagram of the entanglement Hamiltonian in an Ising model showing the location of both the actual and spurious transitions . . . | 192 |
| 9.2 | Schematic depiction of the Rokhsar-Kivelson Ising model on the square lattice, and a three layer Chern model with inter-layer magnetic flux | 194 |
| 9.3 | Entanglement spectrum of the ground state of a three-layer Chern insulator model showing spurious reconstructions | 197 |
| 10.1 | Expectation values of local observables plotted in representative states which are eigenstates of the Entanglement Hamiltonian | 207 |
| 10.2 | Level statistics of the entanglement Hamiltonian computed from a generic Rokhsar-Kivelson state | 213 |

| | |
|--|-----|
| 11.1 Schematic of the toric code model showing electric and magnetic string operators | 227 |
| 11.2 $T = 0$ phase diagram of the \mathbb{Z}_2 theory in $d = 2$ dimensions | 229 |
| 11.3 Summary of the duality between the pure \mathbb{Z}_2 gauge theory and the transverse field Ising model in $d = 2$ | 237 |
| 11.4 Illustration of scaling functions showing adiabatic behavior in the deconfined phase at early scaled times and coarsening behavior in the confined phase at late scaled times | 239 |
| 12.1 Geometry of the pyrochlore lattice | 268 |
| 12.2 Spin space representation of Ising, Potts and Heisenberg spins | 271 |
| 12.3 Monte Carlo data showing dipolar correlations in the Coulomb phase | 273 |
| 12.4 Monte Carlo data showing dipolar correlations in the Coulomb phase | 274 |
| 12.5 Charges of the twelve types of bions in the Coulomb phase | 276 |
| 12.6 Depiction of the Dirac string connecting bions | 277 |
| 12.7 Probability distribution of worm-lengths in the Coulomb phase | 280 |

Part I

Introductory Material

Chapter 1

Ergodicity and Localization

1.1 Anderson Localization

In 1958, P. W. Anderson published his seminal paper with the ambitious aim to “lay the foundation for a quantum mechanical theory of transport” [15]. At the time, experiments by Fletcher and Feher at Bell Laboratories had observed anomalously long relaxation times for electron spins in Si semiconductors doped with impurities [104, 103, 105]. In the course of understanding these experiments, Anderson discovered that the eigenfunctions of non-interacting electrons in a disordered landscape are exponentially localized for strong enough disorder—a phenomenon now termed Anderson Localization [15]. Such exponentially localized electrons cannot conduct heat or electricity, which has dramatic consequences for the transport properties of disordered materials. Anderson’s paper thus went to the heart of two fundamental streams of research in condensed matter physics: (i) the study of transport and conductance in solids and (ii) the role of disorder and impurities which are ubiquitously present.

Anderson’s results explained Feher’s experimental observations, but broke with the prevailing orthodoxy at the time which was rooted in band theory and a picture

of extended Bloch electrons diffusively scattering off impurities. Although his work went on to win the Nobel Prize two decades later and now has over 5500 citations, it was initially only appreciated by a few notables including Sir Neville Mott, Elihu Abrahams and David Thouless. As Anderson said in his Nobel acceptance speech in 1979, “*Very few believed [localization] at the time and even fewer saw its importance; among those who failed to fully understand it at first was certainly its author. It has yet to receive adequate mathematical treatment, and one has to resort to the indignity of numerical simulations to settle even the simplest questions about it.*”

We now discuss Anderson’s calculation more concretely. Anderson simplified Feher’s experimental setup by neglecting electron-electron interactions and used a conceptually tractable non-interacting tight-binding model of electrons hopping on a lattice with disordered onsite potentials

$$H = \sum_i E_i c_i^\dagger c_i + \sum_{i \neq j} V_{i,j} c_i^\dagger c_j + h.c., \quad (1.1)$$

where c_i^\dagger is the creation operator for an electron on site i , the onsite potentials E_i are independent and identical random variables drawn from a distribution of width W , and the hopping terms $V_{i,j}$ are translationally invariant and short-ranged. For concreteness, we can specialize to the case with only nearest-neighbor hopping with $V_{i,i+1} = V$. This problem can be analyzed in the “locator limit” where $V \ll W$ and the hopping is treated perturbatively. In this limit, the unperturbed eigenstates live on individual sites $|i\rangle = c_i^\dagger |0\rangle$ and the hopping is highly detuned from the typical nearest-neighbor potential difference $|E_i - E_{i+1}| \sim W \gg V$. Intuitively, this weak off-resonant hopping is ineffectual at hybridizing nearby sites, and two sites a distance r apart typically only “mix” at r th order in perturbation theory with a strength $\sim V (\frac{V}{W})^r \sim V e^{-r/\xi}$. This leads to exponentially localized eigenstates, $|\psi(r)|^2 \sim e^{-r/\xi}$.

The actual calculation is, of course, more nuanced and requires a careful probabilistic treatment of the disorder. The heuristic perturbative picture above can break down in individual samples at some high order n in perturbation theory due to “resonances” wherein two sites a distance n apart could, by chance, have almost degenerate on-site potentials, $|E_i - E_{i+n}| \lesssim V e^{-r/\xi}$, leading to a vanishing energy denominator and a large tunneling. One needs to carefully estimate the probability of such resonances and show that they are exponentially rare for localization to be stable. Anderson’s calculation sums the perturbative series to all orders and renormalizes the bare on-site energies to account for resonances before arriving at the conclusion of localization.

Anderson’s model marked the beginning of a long and sustained investigation into the quantum mechanical properties of localization-delocalization transitions¹, a topic which continues to be intensely studied to this date. It was eventually shown that in one and two dimensions, *all* electronic wavefunctions at all energies are exponentially localized even for arbitrarily weak disorder, thereby implying a vanishing conductivity $\sigma(T) = 0$ at all temperatures T . In three and higher dimensions, Mott introduced the idea of a sharp *mobility edge* in energy which separates localized and extended states [221]. Thus, for $d \geq 3$, the conductivity is only zero at $T = 0$ and obeys $\sigma(T) \sim e^{-E_c/T}$ at finite temperatures where E_c is the distance from the Fermi level (located inside the localized band) to the mobility edge. A universal scaling theory of the localization transition was eventually developed [5] by the “gang of four”—Abrahams, Anderson, Licciardello and Ramakrishnan—building on earlier work by Edwards and Thouless who identified the Thouless energy, E_T , as the inverse diffusion time across a system with open boundaries [97]. The Thouless conductance, defined

¹There are a subset of more general metal-insulator transitions which can include, for example, the transition from a Mott insulator to a metal.

as the ratio of E_T to the mean electronic level spacing δ ,

$$g = \frac{E_T}{\delta} = \frac{G}{e^2/h}$$

was identified as the universal variable in the scaling theory of the transition (G is a dimensionless conductance).

For completeness, we note that the properties of localization transitions is a vast and extensively studied topic (for a review, see [102] and references therein). The phenomenological “gang-of-four” scaling theory of localization was buttressed by the discovery of an effective field-theoretic description of Anderson localization in terms of a non-linear σ model [322]. The RG treatment of the σ model gave the same flow equations as the scaling theory, and an ϵ expansion in $2 + \epsilon$ dimensions was used to compute the critical exponents. More generally, universal aspects of Anderson transitions (which include quantum Hall transitions) have been extensively analyzed, emphasizing the role of dimensionality and symmetry classes. A complete set of all symmetry classes of disordered systems was found—characterized by time-reversal, spin-rotation, chiral or particle-hole symmetries—and a classification of disordered systems based on these symmetry classes was established by Altland and Zirnbauer [11]. Finally, it has now been realized that, in many cases, the symmetry class does not uniquely determine the universality class of the transition; a notable example of this is the quantum Hall transition which is described by a σ model with an additional topological term [257].

1.2 Many-Body Localization (MBL)

We now turn to the many-body Anderson problem with interactions. As mentioned earlier, the original experiment which motivated Anderson’s calculations comprised a system of *interacting* spins in a doped semiconductor. The fate of Anderson localiza-

tion in the presence of weak, short-ranged many-body interactions was a long-standing problem for decades. Notable progress on this question was first made by the work of Fleishman and Anderson in 1980 [111], which was followed by many other attempts at a definitive solution [13, 123]. Nevertheless, the issue remained largely unresolved till the work of Basko, Aleiner and Altshuler in 2006 [27].

Consider a non-interacting system (say in $d < 3$) in which all single-particle eigenstates are localized. If we only consider elastic scattering processes between localized states, it is clear that the conductivity will always be strictly zero. On the other hand, it was shown early on by Mott [220] that the presence of a heat bath allows electrons to hop between localized states by exchanging phonons with the bath which leads to a *variable-range hopping conductivity*

$$\sigma(T) = \sigma_0 e^{-(T_0/T)^{1/d+1}} \quad (1.2)$$

which is finite for arbitrarily low T , even though all single-particle (SP) states are localized. The existence of MBL turns on whether electron-electron interactions in an *isolated* many-body system (not coupled to any external bath) can play the role of an “internal bath” and lead to a finite conductivity through a similar hopping mechanism.

1.2.1 Basko, Aleiner, Altshuler (BAA)

The first compelling evidence in favor of MBL was presented in BAA’s work [27] where they undertook a rigorous perturbative treatment of the many-body interactions to all orders in perturbation theory and showed that the localization persists upto a finite energy density which is extensive in the system size L . In other words, they predicted a *many-body* mobility-edge separating the extended and localized eigenstates of the interacting problem, and a finite T_c such that the system has strictly zero conduc-

tivity $\sigma(T) = 0$ for $T < T_c$. (Henceforth we will refer to energy densities as far as possible since the notion of temperature is ill-defined for an isolated many-body insulator). There is a metal-insulator transition separating the insulating (localized) and conducting phases.

Note that the presence of a delocalized thermal bath with a *continuous* energy spectrum will always give a conductivity of the form (1.2) since a phonon of the requisite frequency can always be found to match the energy difference between any pair of localized states. On the other hand, BAA showed that local electron-electron interactions can only couple SP states localized within a small localization volume which effectively leads to a *discrete* electronic spectrum. We now briefly review some salient features of BAA's arguments which have important similarities with Anderson's original treatment.

The electron-electron interaction is assumed to be short-ranged and is treated as a perturbation to an Anderson insulator in which all SP states are localized. In the basis of localized SP states, the Hamiltonian takes the form

$$H = \sum_{\alpha} \xi_{\alpha} c_{\alpha}^{\dagger} c_{\alpha} + \sum_{\alpha\beta\gamma\delta} V_{\alpha\beta\gamma\delta} c_{\alpha}^{\dagger} c_{\beta}^{\dagger} c_{\gamma} c_{\delta}, \quad (1.3)$$

where c_{α}^{\dagger} creates a localized SP state with energy ξ_{α} , localization center \vec{r}_{α} , and localization length ζ_{loc} . The unperturbed eigenstates are localized in Fock space and labeled by the occupation numbers $n_{\alpha} = 0, 1$ of SP orbitals $|n\rangle = |n_{\alpha_1} n_{\alpha_2} \cdots n_{\alpha_N}\rangle$ and $N = L^d$.

We define [27] the *local spectral gap* δ_{ζ} as the typical energy spacing between SP states whose spatial separation does not exceed ζ_{loc}

$$\delta_{\zeta} = \frac{1}{\nu \zeta_{\text{loc}}^d} \sim O(1) \quad (1.4)$$

where ν is the SP density of states per unit volume. Since V is a short-range operator, the matrix elements $V_{\alpha\beta\gamma\delta}$ are constrained in both energy and space and decrease exponentially with scale ζ_{loc} as the spatial separation between SP states is increased. For simplicity, the matrix elements are chosen to be finite $V_{\alpha\beta\gamma\delta} \sim \lambda\delta_\zeta$ only when

$$|\vec{r}_\alpha - \vec{r}_\beta| \lesssim \zeta_{\text{loc}}, \quad |\vec{r}_\alpha - \vec{r}_\gamma| \lesssim \zeta_{\text{loc}}, \quad |\vec{r}_\beta - \vec{r}_\gamma| \lesssim \zeta_{\text{loc}}, \quad \text{etc.},$$

$$|\xi_\alpha - \xi_\delta|, |\xi_\beta - \xi_\gamma| \lesssim \delta_\zeta \quad \text{or} \quad |\xi_\alpha - \xi_\gamma|, |\xi_\beta - \xi_\delta| \lesssim \delta_\zeta.$$

(We note that the case of longer-ranged interactions has been considered in Refs. [111, 333] which derive bounds on how long-ranged the interaction can be for localization to still be stable.) A single application of the interaction leads to the decay of an electronic excitation in state α into three excitations: a hole in state β and two electrons in γ, δ . Further applications produce five-particle, seven-particle excitations etc. If the matrix element for the decay at each step is comparable to the energy mismatch, the exact many-body eigenstates become delocalized in Fock space. The inelastic quasiparticle relaxation rate Γ quantifies the rate of transition between different localized states and is, heuristically, proportional to the conductivity.

Anderson [15] considered a tight-binding model on d dimensional lattice with nearest neighbor coupling V and typical nearest-neighbor energy mismatch $\sim W$. The full many-body problem across all particle number sectors looks like the Anderson problem on an N -dimensional hypercubic lattice where each “site” is a basis state in Fock space and $V_{\alpha\beta\gamma\delta}$ generates “hops” in Fock space. For a fixed particle number sector, the shape of the graph depends on the filling and the local structure looks tree-like. If make the following identifications [27]:

1. $V \rightarrow \lambda\delta_\zeta$ – typical value of the coupling matrix element
2. $W \rightarrow \delta_\zeta$ – typical energy mismatch for transitions, $|\xi_\alpha + \xi_\beta - \xi_\gamma - \xi_\delta| \sim \delta_\zeta$

3. coordination number $2d \rightarrow T/\delta_\zeta$ which represents the number of electrons within a localization volume available for collision with α ,

and use Anderson’s estimate [15] for the localization-delocalization transition (which is a good approximation in high dimensions $d > 2$ and is exact on the Cayley tree [4]),

$$\frac{Vd}{W} \ln \frac{W}{V} \rightarrow \frac{\lambda T}{\delta_\zeta} \ln \frac{1}{\lambda} \sim 1$$

we would predict a finite temperature localization-delocalization transition for the many-body problem.

Once again, the actual calculation is much more nuanced. Anderson’s estimate of the transition depends on the details of the lattice and the analogy between real and Fock space is not exact. Further, one now needs to estimate the probability of *many-body resonances* in Fock space which could destabilize localization. BAA’s formidable calculation used the self-consistent Born approximation to obtain the imaginary part of the single-particle self-energy $\text{Im} \Sigma$ —equal to the relaxation rate Γ —and found a strictly zero conductivity below a finite transition temperature T_c , even in the many-body setting.

1.2.2 MBL in a Spin Model

Basko, Aleiner and Altshuler’s calculation [27] was a perturbative *tour de force* which put the theory of many-body localization on a solid theoretical footing. Nevertheless, the combination of disorder and interactions makes MBL an extremely challenging problem with few theoretical tools at its disposal. It is fair to say that progress on this topic would have been slow and scant had the community not resorted to the “indignity of numerical simulations” [227, 234, 152, 182, 208] to better understand this problem. In fact, even simulations are restricted to small systems of ~ 20 sites

in one dimension due to the exponential growth of the many-body Hilbert space². Even so, guided by these small-size numerics, an intense period of focused effort over the last five years has led to great strides in our understanding and has uncovered several remarkable properties of the MBL phase which we will discuss in the following sections and chapters.

A now canonical model for studying MBL was introduced by Pal and Huse [234] in an exact diagonalization study of a Heisenberg spin-1/2 chain with random z-directed fields

$$H = \sum_{i=1}^{L-1} J(S_i^x S_{i+1}^x + S_i^y S_{i+1}^y + S_i^z S_{i+1}^z) + h_i S_i^z \quad (1.5)$$

where $S_i^\alpha = \sigma_i^\alpha$ for $\alpha = x, y, z$ and the σ_i^α are Pauli spin 1/2 degrees of freedom on site i . The fields h_i are drawn randomly and independently from a distribution that is uniform in $[-W, W]$ and $J = 1$. Under a Jordan-Wigner transformation, this model maps to the fermionic Anderson model (1.1) with an additional nearest-neighbor density-density interaction of strength $J_z = 1$. This model conserves energy and total S^z (particle number in fermion language).

When $J = 0$, the many-body eigenstates of (1.5) are simply product states of σ_i^z of the form $|n\rangle = |\uparrow\downarrow\downarrow\cdots\uparrow\rangle$. The full set of 2^L basis states which are the simultaneous eigenstates of all the $\{\sigma_i^z\}$ form the corners of an L -dimensional hypercube, with nearest neighbors on the hypercube differing by one spin flip. As discussed in the previous sections, perturbing with $J \ll W$ is ineffectual at hybridizing the basis states and the system looks many-body localized on the hypercube. It is striking to note that for large enough disorder W , the system is many-body localized even at *infinite* temperature [227, 234] by which we mean that every many-body eigenstate of (1.5) at every energy is localized. This model has a delocalization transition at $W_c \simeq 3.5$ [234, 208] although there is some evidence that the actual transition might

²See Chapters 7 and 8 for alternate numerical techniques based on tensor networks which are in incipient stages of development but are promising in their potential to probe much larger system sizes.

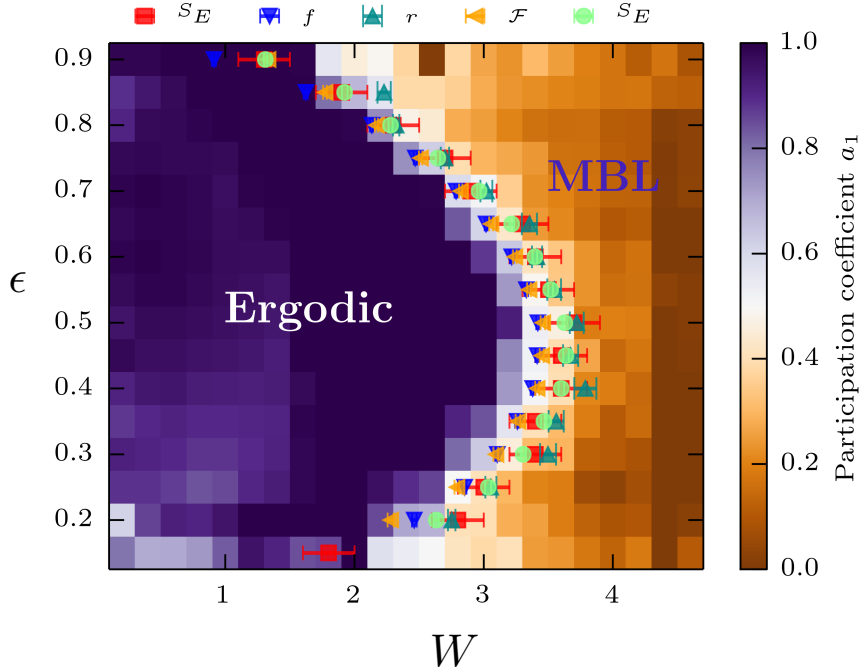


Figure 1.1: Phase diagram of the disordered Heisenberg chain (1.5) as a function of energy density ϵ and disorder strength W showing the many-body localized and extended (ergodic) phases separated by the many-body mobility edge. Figure from [208].

be at a larger disorder strength [90]. The delocalization transition is a quantum mechanical phase transition (even though it occurs at finite temperatures) across which the nature of the system's eigenstates changes in a singular fashion. This is a *dynamical* phase transition and not a thermodynamic one in that there are no singularities in equilibrium thermodynamic observables as the transition is crossed. Fig. 1.1, taken from Ref. [208], shows the phase diagram of the disordered Heisenberg chain (1.5) as a function of energy density ϵ and disorder strength W showing the many-body localized and delocalized phases and the many-body mobility edge. For $W \gtrsim 3.5$, all MB eigenstates are localized.

While the eigenstates of the model (1.5) are localized on the hypercube of basis states for large W , it is important to note that, in the spin language, localization refers to locality in *real space* which may or may not imply localization on the hypercube [223]. Each spin on each site has a local Hilbert space and, in general, localized

eigenstates look like product states of spins pointing in different directions on the Bloch sphere at each site. Such a state can look quite extended on the hypercube depending on the choice of local bases. As an example, a product state which is a simultaneous eigenstate of all $\{\sigma_i^x\}$ operators is local in real space but looks completely extended on the hypercube defined by the $\{\sigma_i^z\}$ basis states.

There are many diagnostics which can be used to distinguish the MBL and delocalized phases and to detect the transition between them [234, 182, 208] (such as the ones used to obtain the phase boundary in Fig 1.1). A particularly useful numerical diagnostic probes the transition through the properties of the spectral statistics of adjacent energy levels of the many-body Hamiltonian [227]. In the MBL phase, the eigenstates are localized and states that are close in energy look very different spatially. To see why this is, consider the model (1.5) with $J = 0$: $H = \sum_i h_i S_i^z$. The average many-body level spacing is exponentially small in L —because while the many-body bandwidth is extensive and scales as L , the many-body Hilbert space for this spin 1/2 system has dimension 2^L . A particular eigenstate $|n\rangle = |\uparrow\downarrow\downarrow\cdots\uparrow\rangle$ has eigenenergy $E_n = \sum_i s_i h_i$ where s_i is the σ_i^z quantum number on site i . Flipping a single spin (or a few) gives a new eigenstate which is close to $|n\rangle$ on the hypercube, but one with an $O(1)$ energy separation $\sim W$ which is much larger than the MB level spacing. To get an exponentially small energy separation, one typically has to flip extensively many $\sim O(L)$ spins. More generally, nearby energy levels in the localized phase look very different spatially; as a result, they do not interact or show level repulsion and the energy spacings follow a Poisson distribution. On the other hand, in the delocalized phase, the level statistics are those of random matrix theory, specifically the Gaussian Orthogonal Ensemble (GOE). The mean value of the level spacing crosses over from the Poisson limit to the GOE limit as the transition is crossed by varying W , and the crossover becomes sharper as the system size is increased.

1.3 Quantum Ergodicity/Thermalization

In Section 1.2 we, following BAA, predicated the existence of MBL on whether electron-electron interactions in an *isolated* many-body system could act as an “internal bath” for the system. In fact, this question gets to the heart of quantum statistical mechanics (QSM) —a topic which, while developed nearly a century ago, is still surprisingly incomplete in its formulation. In this section, we consider some basic notions about quantum thermalization and discuss how “ergodicity” and “localization” emerge as two distinct classes of many-body systems that are distinguished by their late-time dynamical properties³.

The theory of classical statistical mechanics (CSM) allows us to tractably treat systems with macroscopically many particles, $\mathcal{N} \sim 10^{23}$. A microstate of the system labels the properties (like position, momentum etc.) of every particle in the system. A fundamental assumption of CSM is that all microstates are equally likely, and that a system prepared in an initial state dynamically explores all its microstates—the classic textbook example being a collection of atoms prepared in one corner of a room which eventually explores both the entire room spatially and the full Maxwell-Boltzmann distribution of velocities. As a result of this exploration, the system reaches an equilibrium state at late times in which it forgets most details about its initial condition and can be characterized by a few macroscopic variables like temperature, pressure etc. This allows us to replace detailed equations tracking the time evolution of many individual particles with much simpler statistical averages over possible macroscopic states. Since classical dynamics is deterministic, the averaging can be thought of as either a time-average or as an average over ensembles of initial states. Quantum dynamics, on the other hand, is inherently probabilistic so averaging is natural. Additionally, we note that almost all microstates correspond to the same

³For an excellent recent review of this topic, see [223]. Parts of this section are based on the discussion in this review.

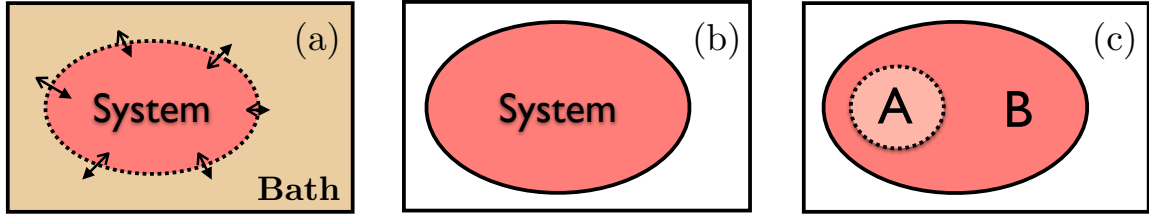


Figure 1.2: (a) Textbook formulations of statistical mechanics assume that a system reaches equilibrium as a result of exchanging energy and particles with a bath. (b) Isolated quantum systems are not coupled to any bath and unitary evolve under their own dynamics. (c) The system quantum thermalizes if the bulk of the system (B) is able to act as a reservoir for a small subsystem (A).

macrostate (the probability of finding atoms equally divided between the two halves of a room is exponentially more likely than the alternatives). An alternate, but related, view of classical thermalization posits that atypical starting configurations quickly evolve to typical states with typical macroscopic observables. This view gets around the experimentally inaccessible, exponentially large in \mathcal{N} time needed to explore phase-space that the first approach implicitly demands.

Most textbook formulations of classical and quantum statistical mechanics imagine a system coupled to an external bath. The system eventually equilibrates at late times as a result of exchanging energy, particles etc. with the bath (Fig. 1.2a). However, there is no bath when considering isolated quantum systems which are not coupled to any external reservoirs (Fig. 1.2b). Indeed, the phenomenon of MBL is formulated in exactly such an isolated setting. Additionally, the concept of thermal equilibration implies that the system at late times can be characterized by a few parameters like temperature, pressure etc. and has little memory of its initial state. However, the late time state of an isolated quantum system is obtained by unitarily evolving the initial state with the system's own Hamiltonian, and unitary evolution preserves all quantum information for all times. What, then, does thermalization mean for an isolated quantum system?

The key insight is that while unitary evolution preserves quantum information, this information can be scrambled among thermodynamically many variables. However, a physical measurement on the system can only involve a few *local* degrees of freedom and memory of local properties can be “hidden” in highly non-local inaccessible observables. We say that an isolated system thermalizes if it is able to act as its own reservoir from the perspective of local observables. More concretely, let us consider a small subregion A in the system which contains a vanishing fraction of the total number of degrees of freedom in the system in the thermodynamic limit. The region B labels the rest of the system not in A (Fig. 1.2c). In an ergodic, thermalizing system B is able to act as a bath for A . To be precise, say we prepare the state in some initial density matrix $\rho(0)$ which could be a pure state. The state at time t is obtained via

$$\rho(t) = e^{-iHt}\rho(0)e^{iHt}; \quad i\frac{d\rho}{dt} = [H, \rho]; \quad \text{Tr}\rho = 1,$$

and the reduced density matrix for the subsystem A is obtained by tracing out the degrees of freedom in B ,

$$\rho_A(t) = \text{Tr}_B\{\rho(t)\}.$$

The equilibrium Gibbs ensemble for this system is defined by

$$\rho^{\text{eq}}(T) = \frac{1}{Z}e^{-H/k_B T}, \quad \rho_A^{\text{eq}}(T) = \text{Tr}_B\{\rho^{\text{eq}}(T)\}$$

where the temperature T is fixed by the energy density of the initial state. The system thermalizes if $\rho_A(t)$ approaches $\rho_A^{\text{eq}}(T)$ as the limits $t \rightarrow \infty$ and $L \rightarrow \infty$ are taken together. That is, in the long-time and large system limit, local measurements on the system agree with thermodynamic ensemble averages with an appropriately defined temperature.

1.3.1 The Eigenstate Thermalization Hypothesis (ETH)

Having discussed what it means for a system to thermalize, we can discuss how the system approaches equilibrium in time. Examining this question leads one to the remarkable conclusion of the eigenstate thermalization hypothesis wherein individual many-body eigenstates of a thermalizing system look thermal [89, 291, 267]. Thus, observables computed in the extreme limit of the microcanonical ensemble defined by just a single eigenstate are indistinguishable from their canonical average. Let us briefly describe some of the steps in this result.

Denote the eigenstates of the thermalizing quantum system by $|E_\alpha\rangle$ with eigenenergy E_α . The system is prepared in an initial pure state $|\psi_0\rangle = \sum_\alpha c_\alpha |E_\alpha\rangle$ with a well-defined average energy $\bar{E} = \sum_\alpha |c_\alpha|^2 E_\alpha$ and a small quantum uncertainty $\Delta = \sqrt{\langle\psi_0|H^2|\psi_0\rangle - \bar{E}^2} \ll \bar{E}$. The expectation value of a local observable A at time t is given by

$$A(t) \equiv \langle\psi(t)|A|\psi(t)\rangle = \sum_\alpha |c_\alpha|^2 A_{\alpha\alpha} + \sum_{\alpha\neq\beta} c_\alpha^* c_\beta e^{-i(E_\beta - E_\alpha)t/\hbar} A_{\alpha\beta} \quad (1.6)$$

where $A_{\alpha\beta} = \langle E_\alpha|A|E_\beta\rangle$. We can define the time-average of $A(t)$ as

$$\bar{A} \equiv \lim_{\tau \rightarrow \infty} \frac{1}{\tau} \int_0^\tau dt \langle\psi(t)|A|\psi(t)\rangle = \sum_\alpha |c_\alpha|^2 A_{\alpha\alpha}. \quad (1.7)$$

The off-diagonal terms in (1.6) dephase on taking the time average in a thermodynamically large system⁴ such that \bar{A} is determined solely by the diagonal contribution.

On the other hand, in a thermalizing system, the time-averaged observable should

⁴While we consider the time-average of $A(t)$ for simplicity of illustration, similar results can be obtained for the long-time limit of $A(t)$ as long as the off-diagonal matrix elements $A_{\alpha\beta}$ decay strongly enough to allow us to neglect temporal fluctuations.

agree with the microcanonical average

$$\bar{A} = A_{\text{mc}} = \frac{1}{\mathcal{N}} \sum_{\beta=1}^{\mathcal{N}} A_{\beta\beta} \quad (1.8)$$

where the sum is over all states in the microcanonical window defined by $\bar{E} - \Delta < E_{\beta} < \bar{E} + \Delta$. Equating (1.7) and (1.8) gives

$$\bar{A} = \frac{1}{\mathcal{N}} \sum_{\beta=1}^{\mathcal{N}} A_{\beta\beta} = \sum_{\alpha} |c_{\alpha}|^2 A_{\alpha\alpha}. \quad (1.9)$$

Note that the RHS of (1.9) explicitly depends on the initial state through the coefficients c_{α} while the microcanonical average on the LHS makes no reference to the initial state. It is hard to see how (1.9) holds in general for all generic initial states with a fixed energy unless one posits that the matrix elements $A_{\alpha\alpha}$ are effectively constant over the relevant energy window with sufficiently small fluctuations. In that case, $A_{\alpha\alpha} \sim A(\bar{E})$ can be pulled out of the sum from both expressions in (1.9) giving the desired equality. Thus, stated differently, ETH says that the expectation value of A in a single energy eigenstate is equal to the value predicted by a microcanonical ensemble constructed at that energy scale.

Note that the ETH is a hypothesis and need not hold for all classes of quantum systems. We have already discussed in Section 1.2.2 that MBL eigenstates that are nearby in energy have very different spatial properties. Thus, local observables measured in MBL eigenstates do not vary smoothly with energy and ETH does not hold for localized systems. Connecting back to the discussion in Section 1.3, we can say that closed MBL systems do *not* act as their own baths and do not quantum thermalize. Thus, some memory of local initial conditions is preserved in local observables for arbitrarily long times. This in turn implies a vanishing DC conductivity for conserved charge/energy densities in consonance with BAA's results.

1.4 Local Integrals of Motion

Localized systems are not the only examples of many-body systems that fail to thermalize. Translationally invariant integrable systems have been studied for decades and have infinitely many conserved quantities which can be written as sums of local or quasi-local operators. These conserved quantities highly constrain the dynamics of integrable systems and prevent thermalization in the sense described in the previous section (although these systems can be described by what is known as a generalized Gibbs ensemble [268, 54, 58]). A crucial difference between localization and integrability is that the latter only exists in highly fine-tuned models and is not robust to small changes in the Hamiltonian. On the other hand, MBL exists for generically interacting Hamiltonians with strong enough disorder and is highly robust to perturbations⁵. Nevertheless, a key similarity between the two phenomena is that, in both cases, the lack of thermalization can be explained by the existence of extensively many local conserved quantities.

It was argued in [283, 148] that in fully MBL (fMBL) systems in which all eigenstates are localized, one can define an extensive set of Pauli operators τ_i^z termed l-bits (l = local) which all commute with each other and with the Hamiltonian H . For specificity, we consider a system of length L in one dimension. The operator expansion of τ^z in the 4^L dimensional basis of the physical σ_i^α spins which we call p-bits (p = physical) takes the general form

$$\tau_i^z = \sum_j K_{ij}^\alpha \sigma_j^\alpha + K_{ijk}^{\alpha\beta} \sigma_j^\alpha \sigma_k^\beta + \dots, \quad (1.10)$$

where $\alpha = 1, x, y, z$. The locality of τ_i^z means that the coefficients $K_{ij_1 j_2 \dots j_m}^{\alpha_1 \alpha_2 \dots \alpha_m}$ in the expansion (1.10) decay exponentially with the maximum separation between any two

⁵This robustness of many-body localization is an example of a phenomenon coined *absolute stability* as we discuss in Chapter 6.

spins in the cluster $\{i, j_i, j_2, \dots, j_m\}$, although there is no additional decay with m in one dimension [168]. These l-bits are often referred to as *emergent* integrals of motion.

The Hamiltonian written in terms of l-bits is itself local and diagonal in the τ_i^z s:

$$H = \sum_i h_i \tau_i^z + \sum_{ij} J_{ij} \tau_i^z \tau_j^z + \sum_{m=3}^{\infty} \sum_{\{i\}} J_{i_1 i_2 \dots i_m} \tau_{i_1}^z \tau_{i_2}^z \dots \tau_{i_m}^z \quad (1.11)$$

and the co-efficients $J_{i_1 i_2 \dots i_m}$ again decay with distance in a manner analogous to the decay of the K coefficients. The MB eigenstates are product states of all the τ_i^z . Note that in a non-interacting system, the τ_i^z are simply the number operators for the localized single-particle eigenorbitals written in spin-language, and all interaction terms J_{ij} are zero.

It is intuitively appealing to think of the τ_i^z s as weakly dressed versions of the σ_i^z operators; certainly $\tau_i^z = \sigma_i^z$ in the extreme localized limit of $J = 0$ in (1.5). By now, there are a few different proposals for constructing l-bits [66, 271, 238, 260] and a mathematical proof of their existence for strongly localized systems in $d = 1$ was provided in [153]. Nevertheless, the best technique for constructing the most local l-bits remains a challenging open question. To gain some intuition for why this is such a hard problem, note that the τ_i^α operators are constructed via a unitary rotation of the p-bits σ_i^α

$$\tau_i^\alpha = U \sigma_i^\alpha U^\dagger \quad (1.12)$$

where U is a unitary which diagonalizes the Hamiltonian and relates basis states, which are product states of $\{\sigma_i^z\}$, to the MB eigenstates which are product states of $\{\tau_i^z\}$. By construction, τ_i^z commutes with H . However, note that the diagonalizing unitary is not unique since there is a massive set — of size $(2^L)!$ — of possible pairings between eigenstates and basis states [238] which corresponds to different permutations of the columns of U . These permutations lead to very different locality properties

for the τ^z operators and a brute-force search through all possible permutations is super-exponentially hard in L . Of course, from (1.12), it is clear that making U as “diagonal” as possible gives the most local l-bit. In strongly disordered cases where each MB eigenstate can be identified as a weakly dressed version of a single basis state, the matching problem is easy. However, away from the strongly localized limit, MB eigenstates can have nearly equal weight on few to several basis states—we term these many-body resonances—and finding the best U is highly non-trivial. The transition from the localized to the delocalized phase is driven by the proliferation of such many-body resonances [320, 254, 121] which make the “best” l-bits both more delocalized and harder to uniquely define. We also note that recent work [69] posits that MBL systems might be characterized by only *approximately* conserved l*-bits—in such systems, eigenstates can look thermalizing while dynamical properties still predict localization.

Nevertheless, the l-bit formalism provides a very useful phenomenological description of the properties of the MBL phase and transparently highlights the dephasing dynamics in this phase. Note that the equation of motion for each τ_i^α operator simply predicts a precession for the l-bit about its z axis at a rate set by the effective field experienced at site i (which depends on its interactions with the other l-bits and the state of the other l-bits). The dephasing dynamics leads to a logarithmic in time growth of quantum entanglement in MBL systems as we will explain in the next section. For now, we simply note that (i) the dephasing dynamics are extremely slow due to the exponentially weak interactions between τ_i^z spins and (ii) there is no dissipation since there are no spin-flip terms in (1.11). Strikingly, it was shown in Refs. [24, 282] that even the effects of dephasing can be reversed by using spin-echo procedures.

The infinitely persistent memory of local initial conditions in MBL phases combined with only slow, reversible dephasing dynamics has raised the tantalizing possi-

bility of using localized systems as novel platforms for a new generation of quantum memories and computing devices. We expound on some of these ideas and their limitations in Chapter 2.

1.5 Quantum Entanglement in Localized Systems

An important development in modern condensed matter physics has been the porting of ideas from quantum information theory to condensed matter, especially the notion of entanglement. Quantum entanglement allows distant parts of the system to be much more correlated than is classically allowed, and is the key ingredient in the operation of a quantum computer. For specificity, consider a pure state of a system $|\psi\rangle$ defined on a Hilbert space \mathcal{H} in one dimension. Consider a bipartition of the Hilbert space into two subregions $\mathcal{H} = \mathcal{H}_L \otimes \mathcal{H}_R$, where \mathcal{H}_L (\mathcal{H}_R) is the Hilbert space of all states living on the left (right) half of some bond. The state $|\psi\rangle$ can be decomposed as

$$|\psi\rangle = \sum_{i=1}^{N_L} \sum_{j=1}^{N_R} c_{ij} |i\rangle_L \otimes |j\rangle_R \quad (1.13)$$

where $|i\rangle_{L/R}$ are basis states for the left and right halves and N_L, N_R denote the size of the Hilbert spaces $\mathcal{H}_L, \mathcal{H}_R$. By performing a singular value decomposition on the matrix of coefficients c_{ij} , the state $|\psi\rangle$ can be written in its Schmidt form

$$|\psi\rangle = \sum_{\alpha=1}^{N_{\min}} \Lambda_{\alpha} |\alpha\rangle_L \otimes |\alpha\rangle_R \quad (1.14)$$

where the states $|\alpha\rangle_{L/R}$ form an orthonormal basis for $\mathcal{H}_{L/R}$, $N_{\min} = \min(N_L, N_R)$, and the Schmidt values $\Lambda_{\alpha} \geq 0$. For a normalized state, $\sum_{\alpha} \Lambda_{\alpha}^2 = 1$. A state with no entanglement between the left and right halves can be written as a product state in the Schmidt basis and only one Schmidt value is non-zero. In an entangled state, more than one Schmidt value contributes. The relation between entanglement and

the Schmidt decomposition can be made more precise by considering the reduced density matrix on the left half of the system

$$\rho_L = \text{Tr}_R |\psi\rangle\langle\psi| = \sum_{\alpha} \Lambda_{\alpha}^2 |\alpha\rangle_L \langle\alpha|_L.$$

The *entanglement entropy* is the von Neumann entropy of the reduced density matrix

$$S = - \sum_{\alpha=1}^{N_{\min}} \Lambda_{\alpha}^2 \log \Lambda_{\alpha}^2. \quad (1.15)$$

The entanglement entropy varies from 0 for a product state with a single $\Lambda_{\alpha} = 1$ to $\log N_{\min}$ for a maximally entangled state in which all Schmidt values are equal. If we consider an equal bipartition of the a system of length L with spin 1/2 degrees of freedom at each site, $N_{\min} = 2^{L/2}$ in which case the maximal entanglement entropy $S = L \log(2)/2$ scales extensively with the volume of the subregion.

We discussed in Section 1.3.1 that in thermalizing systems which obey the ETH, local observables computed in individual eigenstates agree with thermodynamic ensemble averages. This means that the entanglement entropy of any subregion A with length $L_A \ll L$ must agree with the thermodynamic entropy of A which scales extensively with the L_A . This is the famous “volume-law” scaling for generic, highly excited eigenstates of thermalizing systems. Quantum information is “maximally scrambled” in such states and representing them requires exponentially many expansion coefficients of the wave function in terms of local basis states.

On the other hand, it has been rigorously proven that ground states of gapped, local Hamiltonians instead follow an “area law” [135], i.e., the entanglement entropy is proportional to the length of the boundary of the subregion instead of its volume. In a one-dimensional system, this implies that $S(L)$ scales as a constant independent of L . This can be intuitively understood from the fact that a gapped ground state only fluctuates within some correlation length ξ and thus only degrees of freedom near the

bipartition cut are entangled. Since only $O(1)$ Schmidt values contribute substantially to the entanglement, it is clear that specifying ground states in the full exponentially large Hilbert space is unnecessary and inefficient. Instead, it has been shown that states obeying the area law can be efficiently specified using matrix-product state (MPS) / tensor network representations of many-body states [124, 281, 115].

Strikingly, it was noted early on [234] that even highly excited eigenstates of MBL systems have only local entanglement and show only an area law. The l-bit formalism provides an intuitive explanation for the area law since only the l-bits localized near the entanglement cut give a sizeable contribution to the entropy. By now, several numerical studies have examined the behavior of the entanglement entropy in detail and demonstrated the area law as well as deviations due to rare regions and states [29, 208, 182]. This area law is a sharp signature of the violation of ETH in MBL systems, and is the basis for Chapters 7 and 8 which exploit the area law to find more efficient tensor-network based representations and algorithms for MBL eigenstates.

Finally, we note that while Anderson and many-body localized systems both show area-law entanglement in their many-body eigenstates, the two can be distinguished by considering the dynamics of entanglement growth starting from an initial product state. In thermalizing systems, entanglement spreads ballistically [175] with an energy-density dependent speed akin to the Lieb-Robinson velocity. This can be understood by realizing that two distant regions A and B get entangled only as entanglement locally spreads sequentially through the subsystems between them. On the other hand, in single-particle localized systems, the l-bits are localized and they do not interact so there is no growth of entanglement at long times.

Interestingly, it was found [25, 284] that entanglement grows *logarithmically* in time in MBL systems. This is again most easily understood in the l-bits formalism. Since the l-bit Hamiltonian (1.11) is purely diagonal in τ^z , two l-bits a distance r apart can only get entangled through their direct interaction (the τ_i^z quantum

| Thermal phase | Single-particle localized | Many-body localized |
|---|--|--|
| Memory of initial conditions ‘hidden’ in global operators at long times | Some memory of local initial conditions preserved in local observables at long times | Some memory of local initial conditions preserved in local observables at long times |
| ETH true | ETH false | ETH false |
| May have non-zero DC conductivity | Zero DC conductivity | Zero DC conductivity |
| Continuous local spectrum | Discrete local spectrum | Discrete local spectrum |
| Eigenstates with volume-law entanglement | Eigenstates with area-law entanglement | Eigenstates with area-law entanglement |
| Power-law spreading of entanglement | No spreading of entanglement | Logarithmic spreading of entanglement |
| Dephasing and dissipation | No dephasing, no dissipation | Dephasing, no dissipation |

Table 1.1: A list of some properties of the many-body-localized phase, contrasted with properties of the thermal and the single-particle-localized phases. Taken from Ref. [223].

numbers of all l-bits between them are constants of motion). The effective interaction between two l-bits is a sum of many terms which depends on the state of all other l-bits [148]. Nevertheless, this interaction decays exponentially with r in the MBL phase, $J \sim e^{-r/\xi}$. Thus, two initially unentangled l-bits get entangled after a time t such that $Jt \sim 1$ implying that for any fixed time t , all l-bits within a radius $\sim \xi \ln(Jt)$ get entangled. Table 1.1, taken from Ref. [223] summarizes several properties of the MBL phase and contrasts them with those of Anderson localized and thermalizing phases.

1.6 Eigenstate Order and Eigenstate Phase Transitions

Thus far, we have characterized the MBL phase solely by its inability to thermalize. We have described how individual eigenstates of MBL/ thermalizing systems obey area/volume law scaling for the entanglement entropy respectively. The transi-

tion between the MBL and ergodic phases is an *eigenstate phase transition* in which the entanglement properties of the eigenstates and eigenvalues changes in a singular manner to restore statistical mechanics on the ETH side of the transition. We emphasize that this is a dynamical phase transition which shows no singularities in usual thermodynamic observables which average over several eigenstates.

Of course, in a conventional setting, phases are described according to whether they spontaneously break or preserve global symmetries and by whether or not they display some form of topological order. This raises the question of whether MBL eigenstates can also exhibit forms of symmetry breaking or topological order. Remarkably, it was shown in Refs. [149, 239] that highly excited MBL eigenstates can indeed come in various flavors classified by the usual notions of phase ordering. Further, the nature of ordering can change as some parameter is varied within the localized phase thereby leading to eigenstate phase transitions between different classes of localized states.

What is especially remarkable is that these MBL eigenstates can display patterns of order which might even be disallowed in equilibrium due to general constraints of statistical mechanics. For example, the well known Landau-Peierls-Mermin-Wagner theorems prohibit symmetry breaking order in one dimension at any finite temperature. The basic idea is that entropic considerations always beat energetic ones at finite temperatures in 1d, and the fluctuations destroy ordering. However, in the presence of disorder, these fluctuations can get pinned by localization in a manner which might allow individual eigenstates to display nontrivial correlations, even at finite energy densities. Likewise, in equilibrium, topological order (TO) is only defined in the presence of a bulk gap; without a gap, thermal fluctuations destroy TO. Again, the presence of disorder can localize the fluctuations and allow TO to persist without a bulk gap and at finite energy densities. Appropriately, these ideas were termed “localization protected quantum order” (LPQO) [149].

We now briefly illustrate the basic idea in a simple Ising model with disorder

$$H = \sum_{i=1}^L h_i \sigma_i^x + \sum_{i=1}^{L-1} J_i \sigma_i^z \sigma_{i+1}^z + \lambda \sigma_i^x \sigma_{i+1}^x \quad (1.16)$$

where the couplings J_i and h_i are random and positive with means \bar{J}, \bar{h} , and the interaction λ is small compared to both J and h .

First, consider the clean system with translationally invariant couplings and $J \gg h$. There are two nearly degenerate ferromagnetically ordered low-lying “cat” states $|\pm\rangle \simeq \frac{1}{\sqrt{2}}(|\uparrow\uparrow\uparrow + \dots \uparrow\rangle \pm |\downarrow\downarrow\downarrow + \dots \downarrow\rangle)$ which are global superposition states that are respectively even and odd under the Ising symmetry $P = \prod_i \sigma_i^x$. The arrows denote the σ_i^z eigenvalues, and the ground state is exactly two fold degenerate in the thermodynamic limit. At any finite temperature, there is a finite density of domain walls which are delocalized throughout the system. Thus, any two-point connected correlation of the form $\langle \sigma_i^z \sigma_j^z \rangle_c$ decays exponentially with $|i - j|$ consistent with the Landau-Peierls theorem.

Now consider the situation with disorder in the couplings J, h . First, if the interaction λ is set to zero, the model (1.16) maps to a non-interacting fermion problem in which the excitations are Anderson localized. When $\bar{J} \gg \bar{h}$, the excitations of the model are domain walls which get pinned by the disorder. Thus, excited eigenstates of the problem now look like frozen configurations of spins pointed randomly up or down in a superposition state with their Ising reversed partner $|\pm\rangle_{\text{excited}} \simeq \frac{1}{\sqrt{2}}(|\uparrow\downarrow\uparrow + \dots \uparrow\rangle \pm |\downarrow\uparrow\downarrow + \dots \downarrow\rangle)$. Correlation functions measured in such highly-excited states do not decay exponentially with distance, but are $O(1)$ with a randomly fluctuating sign which depends on the number of frozen domain walls crossed between sites i and j — this form of order is called spin-glass order and the phase is termed an MBL spin glass (SG). All these statements carry through in the presence of weak interactions λ since they remain now becomes many-body local-

ized. In the opposite limit, $\bar{h} \gg \bar{J}$, the eigenstates look like frozen spins pointing randomly left or right in the σ^x direction on every site and the system is an MBL paramagnet. The transition between the SG and PM phases [182, 239] is an eigenstate phase transition characterized by an infinite randomness fixed point, at least in the noninteracting setting [110, 239]. The fate of the critical point in the presence of interactions is a delicate question. It was suggested that the critical point would remain localized [149] and exhibit the same scaling as the non-interacting fixed point [239], although there is also a possibility of a delocalized (or partially delocalized) critical point/phase between the SG and PM MBL phases.

1.7 Experimental Probes

Until recently, the phenomenon of many-body localization was only realizable in the ideal universe of a theorist's imagination. As we have discussed, MBL only exists for *isolated* quantum systems which are decoupled from all reservoirs and baths. However, any realistic materials system contains both electron-electron and electron-phonon interactions and these couplings cannot be controlled by the experimenter. As a result, experimental investigations of MBL in conventional solid-state systems [232, 230] are extremely challenging. In fact, even for Anderson insulators, direct experimental observation of the localization of electronic wavefunctions proved elusive, although indirect signatures in transport and other measurements were found (such as the original experiments which motivated Anderson's work), and a scanning-tunnelling microscopy study strikingly observed signatures of multifractality and critical correlations near the metal-insulator transition [266].

However, recent advances in atomic, molecular and optical systems have resulted in the realization of isolated, synthetic many-body systems with highly tunable interactions and disorder. These have already proved extremely promising as platforms

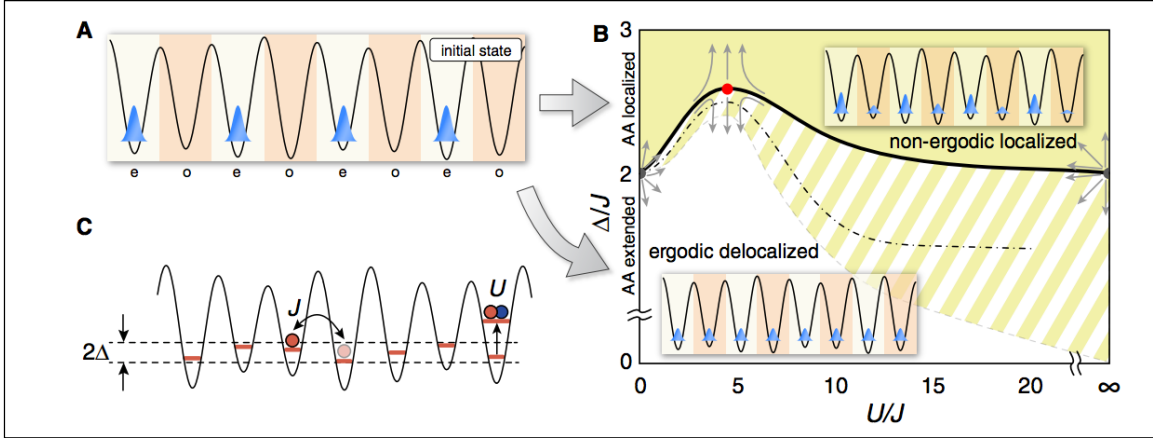


Figure 1.3: A cold-atoms experiment showing signatures of MBL, taken from Ref. [279]. A) An initial charge-density wave (CDW) state is prepared in a quasiperiodic optical lattice. B) Schematic phase diagram as a function of the interaction strength U and disorder Δ . Signatures of the initial CDW persist to late times in the MBL phase, while the charge imbalance quickly decays to zero in the ergodic phase.

for exploring questions about MBL and quantum statistical mechanics in isolated systems. State of the art experiments in ultracold atomic systems [279, 191, 42, 75] have demonstrated that a fingerprint of the initial state persists in MBL systems for arbitrarily late times. These systems are isolated to a good approximation⁶ and the strength of the interactions can be tuned via a Feshbach resonance. The onsite disorder can be realized either using an optical speckle pattern, or by superimposing lasers with incommensurate frequencies which realizes a quasiperiodic potential which is also known to show many-body localization [157]. These systems also offer remarkable single-site resolution for imaging and manipulating individual degrees of freedom which allows one to study local deviations from thermal equilibrium. A very recent cold-atoms experiment [75] remarkably demonstrated signatures of localization in an interacting two-dimensional system which goes well beyond the sizes and dimensions accessible to theory and numerics! Signatures of MBL have also been observed in trapped ion systems [289].

⁶While there is heating in these systems [75], its effects are believed to set in at much longer time-scales than those probed by the experiment.

Figure 1.3, taken from Ref. [279] depicts a particular experimental setup in Bloch’s group which demonstrated convincing signatures of localization. A quasiperiodic optical lattice was prepared by superimposing two lasers with incommensurate frequencies and the system was prepared in an initial charge density wave and then allowed to relax. It was shown that, at late times, the density imbalance between the even and odd sublattices persisted in the MBL phase while it vanished for a different set of parameters corresponding to the ergodic phase—thus demonstrating that memory of local initial conditions persists in the MBL phase and quantum statistical mechanics does not hold.

1.8 Floquet Systems

Thus far, our discussion has been restricted to static time-independent Hamiltonians. We have examined ideas of quantum thermalization, equilibration and quantum order in this setting and shown that interacting many-body systems fall into two categories: ergodic and many-body localized. We now add an additional ingredient to our analysis and examine these ideas in a driven, time-dependent setting. We will consider Floquet systems whose Hamiltonians depend on time periodically with period T , $H(t) = H(t + T)$. Such systems ubiquitously arise, for example, whenever a quantum system is driven by external time-varying fields.

1.8.1 Floquet Formalism

In periodically driven systems, energy is no longer conserved, being replaced instead with *quasi*-energies defined modulo $2\pi/T$. According to the Floquet-Bloch theorem⁷,

⁷The proof of the Floquet-Bloch theorem proceeds exactly analogously to the proof of Bloch’s theorem for spatially periodic lattices.

the time dependent Schrödinger equation

$$i\frac{d|\psi(t)\rangle}{dt} = H(t)|\psi(t)\rangle \quad (1.17)$$

has special solutions

$$|\psi_\alpha(t)\rangle = e^{-i\epsilon_\alpha t}|\phi_\alpha(t)\rangle \quad (1.18)$$

defined by periodic states $|\phi_\alpha(t)\rangle = |\phi_\alpha(t+T)\rangle$ and quasi-energies ϵ_α defined modulo $\omega = 2\pi/T$. These replace the eigenstates of the time independent problem; in them observables have periodic expectation values, and they form a complete basis. Similar to the crystal momentum of a system with discrete translational symmetry, the quasienergy can be thought of as a periodic variable defined on a quasienergy Brillouin zone $-\pi/T < \epsilon \leq \pi/T$. The central object determining the long-time behavior of driven systems is the Floquet unitary $U(T)$ which is the time evolution operator over a full period

$$U(T) = \mathcal{T} \int_0^T dt e^{-itH(t)}. \quad (1.19)$$

Under the action of $U(T)$, the Floquet states (1.18) are mapped onto themselves upto a phase

$$|\psi_\alpha(T)\rangle = U(T)|\psi_\alpha(0)\rangle = e^{-i\epsilon_\alpha T}|\psi_\alpha(0)\rangle.$$

Thus, the $|\phi_\alpha(0)\rangle$ are eigenstates of $U(T)$ with eigenvalues $e^{-i\epsilon_\alpha T}$. We will henceforth denote $|\phi_\alpha(0)\rangle$ as $|\alpha\rangle$ for brevity. The ‘‘Floquet Hamiltonian’’ H_F is defined via $U(T)$ as

$$U(T) = e^{-iH_F T}. \quad (1.20)$$

The states $|\alpha\rangle$ are also eigenstates of H_F with eigenvalues ϵ_α ; however, since ϵ_α is not uniquely defined, neither is H_F .

If we probe the system stroboscopically, *i.e.* at multiples of the period T , it appears from (1.20) that the Floquet problem has been mapped to standard unitary evolution

with a time-independent Hamiltonian H_F . However, this apparent simplicity is misleading since, in general, it is nearly impossible to obtain the Floquet Hamiltonian in closed form for an interacting many-body system and one has to resort to various approximation schemes (briefly described below). Moreover, it turns out that in most cases it is impossible to find a “physical” H_F which can be written as a sum of local terms; H_F is either ill-defined (such that any expansion scheme to compute it does not converge as $L \rightarrow \infty$), or it generically looks highly non-local and unphysical. It was shown that in “Floquet many-body localized” systems [199, 252, 2], a local H_F can be defined (upto boundary terms) and the system can have non-trivial late-time states. On the other hand, in “Floquet-ergodic” systems [198, 78, 251], no local H_F can be found and system continuously absorbs energy from the drive and heats up a trivial late-time state characterized by a Gibbs ensemble at infinite temperature. We will discuss both classes of systems in Section 1.8.2.

We now turn to some theoretical techniques commonly employed in the study of Floquet systems.

Magnus Expansion

The Magnus expansion [210, 37, 45] is a series expansion for the Floquet Hamiltonian, $H_F = \sum_{n=0}^{\infty} H_F^{(n)}$, which is similar in spirit to the Baker-Campbell-Hausdorff formula. It is applicable in the high-frequency limit since the terms at n th order in the series are proportional to ω^{-n} . The first two terms in the series are

$$\begin{aligned} H_F^{(0)} &= \frac{1}{T} \int_0^T dt H(t) \\ H_F^{(1)} &= \frac{-i}{2!T} \int_0^T dt_1 \int_0^{t_1} dt_2 [H(t_1), H(t_2)], \end{aligned} \tag{1.21}$$

where we note that the leading zeroth-order term is simply the time-averaged Hamiltonian. There are very few exact results on the convergence of the Magnus expansion,

and there no rigorous proofs in the many-body setting, although Ref [2] attempts to construct a proof of Floquet localization in the MBL setting. It is certainly the case that a convergent expansion implies a local Floquet Hamiltonian and thus dynamical energy localization in which the system does not continuously absorb energy from the drive in the infinite time limit. On the other hand, a divergent expansion indicates that there is no local Floquet Hamiltonian and the system heats up indefinitely. It is known that a sufficient (but not necessary) condition which guarantees convergence is $\omega > W(T)$ where $W(T)$ is the maximum bandwidth of $H(t)$ during the period. While this result is exact, it is not particularly useful for many-body systems in which the bandwidth scales extensively with system size. Nevertheless, such expansions can be very useful for gaining intuition about the dynamics for short times and/or finite system sizes. Finally, it is certainly the case that the Magnus expansion *can* be convergent even in the thermodynamic limit— for example, this happens if the time-dependent Hamiltonian can be mapped to a static one by going to some rotating frame. We turn to this topic next.

Rotating Frame

There are cases, for example if the driving amplitude scales with frequency, where one needs to re-sum an infinite sub-series in the Magnus expansion to obtain H_F even in the infinite-frequency limit [45]. In such cases, among others, the convergence of the Magnus expansion can often be significantly improved by unitarily transforming to a rotating frame. If the unitary $U_R(t)$, maps a state $|\psi(t)\rangle$ in the original frame (whose time evolution is governed by $H(t)$) into a state $|\psi_R(t)\rangle = U_R(t)|\psi(t)\rangle$, then the time-evolution of $|\psi_R(t)\rangle$ is governed by

$$H_R(t) = U_R(t)H(t)U_R^\dagger(t) - iU_R(t)\partial_t U_R^\dagger(t).$$

The zeroth order piece in the Magnus expansion is now the time-average of $H_R(t)$, and the expansion could have much better convergence properties for cleverly chosen unitaries $U_R(t)$ which can be found in special cases.

Replica Formalism

We end this section by describing the replica formalism [285, 276] which analyses the Floquet problem in the frequency domain instead of the time domain. This formalism is especially transparent in the non-interacting setting and provides a useful intuitive picture for the Floquet states (1.18). Since $H(t)$ and $|\phi_\alpha(t)\rangle$ are periodic functions in time, we can decompose them into their Fourier series:

$$H(t) = \sum_n e^{in\omega t} \tilde{H}(n) \quad (1.22)$$

$$|\phi_\alpha(t)\rangle = \sum_n e^{in\omega t} |\tilde{\phi}_\alpha(n)\rangle. \quad (1.23)$$

Plugging these into the time-dependent Schrodinger equation (1.17) and using (1.18), we get the equivalent eigenvalue problem

$$\sum_p \tilde{H}(m-p) |\tilde{\phi}_\alpha(p)\rangle + m\omega |\tilde{\phi}_\alpha(m)\rangle = \alpha |\tilde{\phi}_\alpha(m)\rangle \quad (1.24)$$

Thus, the original time-dependent problem has been mapped onto a time-independent problem in one higher—and infinitely extended—dimension indexed by the Fourier index m . This may not look like much progress, but this structure transparently illustrates the how an undriven eigenstates of the original problem will mix as a result of introducing a drive. To see this, consider the single particle Anderson problem with a drive

$$H(t) = \sum_{i=1}^{L-1} v_i c_i^\dagger c_i + t \cos(\omega t) (c_i^\dagger c_{i+1} + c_{i+1}^\dagger c_i) \quad (1.25)$$

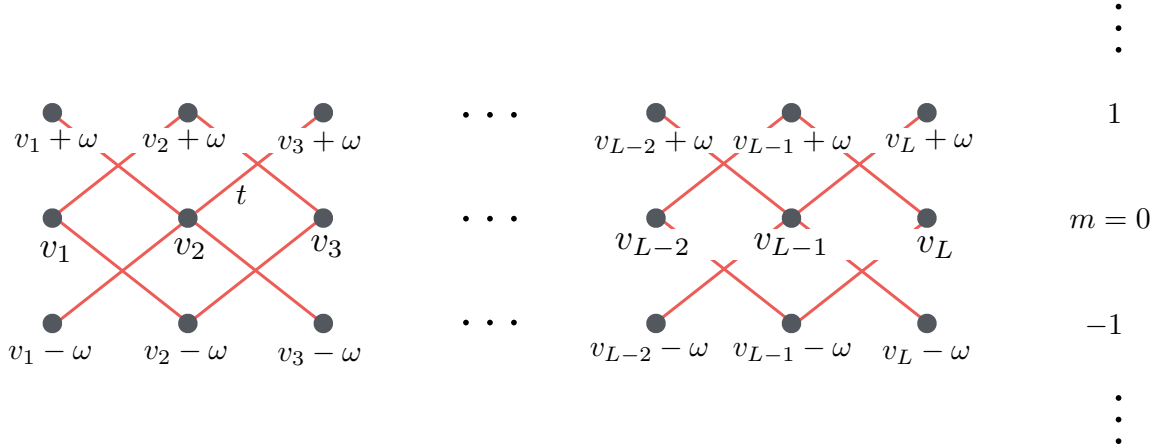


Figure 1.4: Schematic representation of the monochromatic single-particle drive (1.25) in replica space. The replica index runs from $-\infty$ to ∞ , the onsite energies on site i in layer m are given by $v_i + m\omega$ and the hopping with strength t (red lines) is between nearest neighbor sites in adjacent layers .

The eigenstates of the undriven system with $t = 0$ are simply localized on individual sites. For this monochromatically driven system, only $\tilde{H}(0)$ and $\tilde{H}(\pm 1)$ are non-zero; $\tilde{H}(0)$ contains the time-independent piece in H and $\tilde{H}(\pm 1)$ couples nearest spatial neighbors with strength t in adjacent replicas. Fig. 1.4 shows a schematic depiction of the eigenvalue problem in replica space.

A few points worth noting. First, as a result of the drive, the hopping can now resonantly couple pairs of sites whose on-site energies differ by multiples of ω (whereas in the undriven setting, we required nearly equal energy differences for resonant coupling). This introduces extra channels for delocalization. Second, for this single-particle problem, the onsite energies in layer m have an extra confining potential $m\omega$. This leads to localization in replica space via a mechanism analogous to the well-known Wannier-Stark localization in real space. This means that we can effectively truncate the replica index at some finite M without much error, making an actual solution tractable.

This main take-home message from the replica picture—which also holds in the many-body setting—is that the drive allows eigenstates of the undriven problem dif-

fering mod ω to be coupled, and the Floquet eigenstates could look extremely delocalized in the original eigenbasis as a result of this coupling. Let us reiterate this in a slightly different language. Instead of working in the “repeated-zone” scheme in energy space as the replica picture does, we could work in a single Brillouin zone of width ω . Say $H(t) = H_0 + \lambda V(t)$ and we treat the drive perturbatively. Then, to arrive at the Floquet eigenstates we (i) fold the spectrum of H_0 into a width ω i.e. all eigenvalues of H_0 are only considered mod ω . As a result of this folding, previously separated energy levels now overlap and there are level crossings. (ii) We then consider the effect of the potential V in resolving these level crossings. If V has matrix elements between the states at a crossing, they mix. The Floquet eigenstates look localized or delocalized in the basis of H_0 depending on how much folding there is (*i.e.* the size of ω) and the efficacy of the the potential in resolving the induced level crossings.

1.8.2 Ergodicity and Localization in the Floquet Setting

We end by addressing the question of thermalization in the driven Floquet setting for many-body quantum systems. The general belief is that a driven, ergodic many body system continuously absorbs energy from the drive and the late-time state looks like a trivial state at infinite temperature [198, 78, 251, 252]. This is consistent with standard linear response reasoning wherein any nonzero frequency exhibits dissipation. Unfortunately, there are no rigorous results proving that this “heat death” is the only allowable outcome, but this picture has been suggested by a few different numerical works [198, 78, 251, 252]. In terms of the band-folding view described in the previous section, the idea is that the undriven eigenstates of generic systems obey ETH, exhibit level repulsion, and lie in an extensive bandwidth which scales with system size. If these states are folded in a narrow $O(1)$ bandwidth set by ω , the drive immediately mixes a finite fraction of all unperturbed states leading to delocal-

ization of the Floquet states in the eigenbasis of the undriven problem. Given this strong mixing across the entire many-body spectrum of H_0 , we expect observables computed in the Floquet eigenstates to effectively average essentially uniformly over the eigenstates of H_0 , whence the expectation that the infinite temperature ensemble is appropriate.

We note that similar arguments as the ones presented in Section 1.3.1 can be used to show that stroboscopically probed observables at late times in the Floquet setting are derived from the diagonal ensemble of the Floquet eigenstates $|\alpha\rangle$. Since all static and dynamic correlations are trivial in the infinite-temperature ensemble, the Floquet eigenstates exhibit a maximally trivial form of ergodicity and look maximally random in Hilbert space. Finally, while the drive eventually heats the system, there can be regimes where this heating is slow, leading to long-lived prethermal states [193, 3, 53, 46, 47].

This discussion shows that to get any nontrivial dynamics in the Floquet setting requires a mechanism for energy localization wherein the absorption from the driving field saturates, and the long-time state of the system is sensitive to initial conditions. In a striking development, a set of recent works has shown that a disordered many-body localized system can remain Floquet-localized in the presence of weak enough driving [198, 78, 251]. The basic intuition is that the heating in translationally invariant systems stems from spatially extended modes which interact with and transfer energy between each other. This can be different when disorder spatially localizes the modes, with individual modes exhibiting something like Rabi oscillations while interacting only weakly with distant modes.

To see more concretely why Floquet localization might be possible in an MBL system, recall that MBL eigenstates do not satisfy ETH and nearby eigenstates look very different spatially. There is a local spectral gap [222, 162] such that a local operator can only couple states differing in energy by $W \sim O(1)$. Thus, if we locally drive

an MBL system with weak amplitude and frequency $\omega \gg W$, the states brought into resonance as a result of the drive do not effectively mix and the Floquet eigenstates can remain localized. Increasing the amplitude of the drive or reducing its frequency can lead to Floquet delocalization as before. In Chapters 5 and 6, we explore some of the consequences of this remarkable Floquet localization.

1.9 Open Problems

Despite remarkable progress over the last decade, our understanding of many-body localization and quantum thermalization is still in its infancy. We briefly discuss a few open questions that are active areas of current research, although this list is by no means exhaustive.

1. *Nature of the MBL-Ergodic transition:* The phase transition between the MBL and ergodic phases is not a thermodynamic phase transition, so it need not fit in to the usual classifications of phase transitions. This is a dynamical phase transition across which the nature of the system’s many-body eigenstates changes in a singular fashion from “volume-law” entangled eigenstates that obey the ETH to nonthermal and only boundary-law entangled eigenstates in the MBL phase. Since the MBL-to-ETH transition lies outside the purview of equilibrium statistical mechanics and scaling theory, very little is definitively known about its properties. A recent paper has derived a Harris/Chayes bound $\nu_{FS} \geq 2/d$ for the finite-size correlation length exponent ν_{FS} at this transition in a disordered system in d dimensions [68]. Recent approximate renormalization group (RG) studies, which are confined to one-dimensional systems, all find a continuous transition with a localization length exponent $\nu > 2$ satisfying this inequality [320, 254]. On the other hand, all exact diagonalization (ED) numerical studies [234, 182, 208] to date (which are limited to small system sizes

$L \sim 22$) have found exponents ν which violate the Harris bound. Interestingly, all these ED studies have observed a finite-size crossover only on the thermal side of the transition with no observed crossover between the MBL and quantum critical regimes.

Following Ref. [127], it is generally believed that the MBL-ergodic critical point looks thermal, although recent computations [170] suggest that this belief is most likely false. The derivation in Ref. [127] makes an important assumption that the entanglement entropy of small subregions with size $L_A \ll L$ remains continuous through the transition, a wholly reasonable assumption for conventional continuous transitions which do not show discontinuities in local observables. On the other hand, there is evidence which suggests that this assumption is false and the entropy of *local* subregions can vary discontinuously across the transition [170], with the critical region looking localized. Thus, some aspects of this transition look “first-order” like, even while many others look continuous. Understanding the nature, properties and scaling behavior of this unique transition with its peculiar asymmetries between the MBL/ergodic sides is an important open question.

2. *Nature of Many-Body Resonances in the MBL phase:* We have discussed how the stability of localization in the locator limit turns on bounding the probability of single-particle/many-body resonances between pairs of sites/configurations. We use the term “resonances” somewhat loosely to describe entanglement between different degrees of freedom in the system, which result in the eigenstates looking like superpositions over few-to-several basis states. The transition to the thermal phase is driven by a proliferation of many-body resonances, and understanding the structure and properties of these resonances remains an open question which is vital for better understanding the MBL phase and the transition. In fact, even the two RG schemes [320, 254] which describe the approach

to the ergodic phase present qualitatively different pictures for the resonances driving the transition.

3. *Structure of Quantum Entanglement in the MBL phase:* We have described how MBL eigenstates have area-law entanglement entropy. However, this is only true for *typical* entanglement cuts, while the full distribution of entanglement across cuts and eigenstates is much more involved due to the resonances discussed in the previous point [29]. Understanding the full structure of quantum entanglement in the MBL phase is important both for its accurate description, and, more practically, for refining and improving tensor-network based approaches for efficiently diagonalizing and representing MBL systems (*c.f.* Chapters 7, 8).
4. What is the best definition of a “localization length” ξ_{loc} which diverges as the delocalization transition is approached from the MBL side? There are arguments [223, 168] which suggest the existence of multiple length scales which diverge differently or not at all as the transition is approached. Which of these, if any, govern the finite-size scaling at the transition?
5. What is the nature of eigenstate phase transitions between different localized phases? Under what conditions does the MBL-MBL critical point look localized/partially delocalized/thermal?
6. What is the nature of the phase on the delocalized side of the localization transition? Are there alternatives to the ETH which permit delocalized but non-ergodic phases [69]?
7. Does MBL exist in higher dimensions? If so, which properties are dimensionality dependent [69]?

8. What are some definitive experimental signatures of MBL, both in driven and undriven settings? Can we observe MBL or signatures of it in real materials systems instead of synthetically engineered AMO settings?
9. Despite the results of Chapter 2, is it possible to carefully engineer MBL systems as platforms for a new generation of high-temperature quantum devices?

1.10 This Thesis

We now turn to the contents of this thesis. The balance comprises eleven chapters organized in five parts. In Part II, we study the dynamical response of many-body localized phases by considering the effects of driving an MBL system with a time-dependent field in two different limits. In Chapter 2, we consider the adiabatic limit of an extremely slowly varying field, while in Chapter 3 we consider the linear-response regime of a weak-amplitude drive. The two limits give different physical insights into the dynamics. In the first, we find, surprisingly, that a slow, gentle perturbation induces a highly non-local charge response in an otherwise localized phase, while the second limit elucidates the structure of the many-body resonances in the MBL phase which contribute to the linear response a.c. conductivity.

In Part III, we extend the notion of eigenstate order in localized systems. Chapter 4 shows that highly-excited eigenstates of MBL systems can display symmetry-protected topological order, while Chapters 5 and 6 discuss phase structure in a periodically driven Floquet setting. We show that not only can Floquet-localized eigenstates display nontrivial phase structure, but that some of these phases show a novel form of correlated spatiotemporal order and are *absolutely stable* to all generic perturbations in the same sense in which topologically ordered phases are stable.

Part IV exploits the low-entanglement nature of MBL eigenstates to develop tensor-network based algorithms for efficiently computing and representing highly-

excited MBL eigenstates. In Chapter 7 we describe a variational procedure which approximately diagonalizes the full MBL Hamiltonian in polynomial time and gives an approximate representation of the entire many-body spectrum. Then, in Chapter 8 we describe a complementary algorithm based on the density-matrix renormalization group which targets individual MBL eigenstates with much greater accuracy.

In Part V, we switch gears from disordered systems but still examine questions on entanglement and quantum statistical mechanics. In both chapters, we treat the entanglement Hamiltonian from a statistical mechanical lens. In Chapter 9, we show that the low-energy spectrum of the entanglement Hamiltonian is much less universal than assumed in the literature, while in Chapter 10 we examine questions about the eigenstate thermalization hypothesis applied to the eigenstates of the entanglement Hamiltonian.

We close in Section VI with two miscellaneous results on topologically ordered phases. In Chapter 11, we examine the nonequilibrium dynamics resulting from driving a system through a phase transition from a topologically ordered phase to a trivial one at a finite rate. This is a study of the well known Kibble-Zurek mechanism applied to topological order. Finally, Chapter 12 examines the four-state Potts model on the frustrated pyrochlore lattice and shows that the system lies in a “Coulomb Phase” characterized by three emergent gauge fields.

Part II

Dynamical Response of Many-Body Localized Systems

Chapter 2

Non-local Adiabatic Response of a Localized System to Local Manipulations

A standard technique for probing the dynamical properties of a system is to perturb it with time-varying fields and to examine the resultant response of the system to the perturbation. While this chapter and the next have different motivations and applications, both consider the general framework

$$H(t) = H_{\text{MBL}} + v \cos(\omega t).$$

In this chapter, we probe the extremely slow (adiabatic) limit of the drive above *i.e.* the limit $\omega \rightarrow 0$ for a finite v . In the next chapter, we look at the same protocol in the opposite order of limits, $v \rightarrow 0$ for a finite ω , in which linear response theory is applicable.

2.1 Introduction

As we saw in Chapter 1, MBL phases have a fascinating complex of properties including (i) vanishing long wavelength conductivities at finite temperatures [27], (ii) an extensive number of local conserved quantities [148, 283] leading to a breakdown of ergodicity, (iii) spectral functions of local operators that show a ‘mobility’ gap at all temperatures [222, 162], and (iv) highly excited MBL eigenstates that can exhibit localization protected order – both Landau symmetry-breaking and topological order – in dimensions and at energy densities normally forbidden by the Peierls-Mermin-Wagner theorem [149, 239, 319, 182, 29, 24, 64, 224].

MBL systems present the tantalizing possibility of using localization to protect high temperature quantum computation. Localized systems might serve as protected quantum memories since they undergo only slow (logarithmic) dephasing, and even this can be removed by spin echo procedures [29, 282, 306, 222]. Prima facie, one expects to be able to locally manipulate degrees of freedom in such systems without affecting distant q-bits, a property with various quantum control applications. Further, property (iv) above raises the interesting possibility of performing topological quantum computation at finite temperatures in the MBL regime by braiding excitations in topologically ordered MBL eigenstates. While there isn’t an energy gap at finite temperatures, the ‘mobility gap’ could serve to protect adiabatic braiding instead.

All these applications require local manipulation of quantum degrees of freedom. Motivated by these considerations, we study the adiabatic response of localized phases to local perturbations using a combination of analytic arguments and numerical exact diagonalization. In particular, we study the adiabatic time evolution of a system governed by the time dependent Hamiltonian

$$H(t) = H_L + V(t/\tau),$$

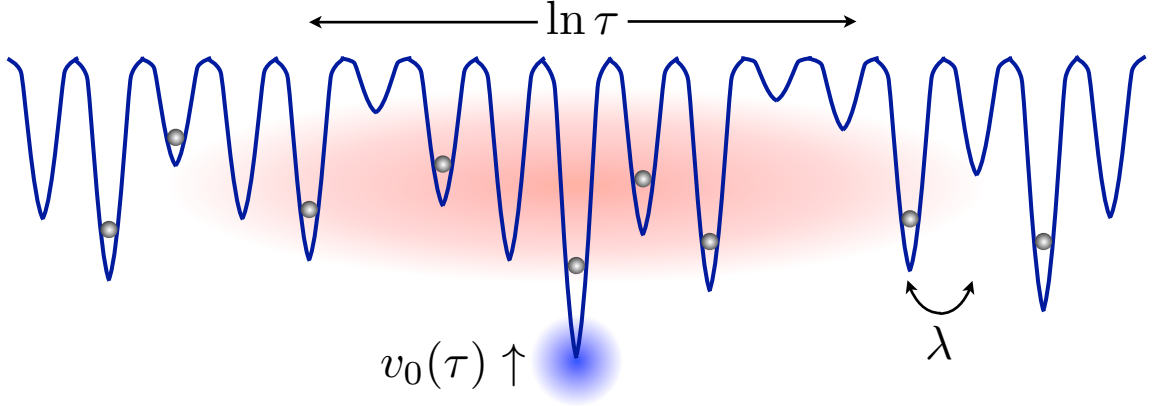


Figure 2.1: Schematic illustration of the time-dependent protocol. A *local* time-dependent potential $v_0(\tau)$ leads to a highly non-local adiabatic charge response in disordered insulators, causing a ‘zone of disturbance’ with radius $\sim \ln \tau$.

where H_L is a localized Hamiltonian, V is a time dependent local perturbation which acts only on a small compact subregion in real space, and which is zero in the distant past and future ($t \rightarrow \pm\infty$). Finally, τ sets the time scale on which the perturbation changes. In this work, adiabatic time evolution will be understood to mean

$$|\psi(t)\rangle = \lim_{L \rightarrow \infty} \lim_{\tau \rightarrow \infty} U(t/\tau)|\psi(0)\rangle$$

where $U(t)$ is the unitary time-evolution operator defined by $H(t)$, and the limit $\tau \rightarrow \infty$ is taken before the thermodynamic limit $L \rightarrow \infty$. We also discuss the opposite order of limits.

A naive understanding of localization suggests that the influence of the perturbation $V(t)$ should be spatially confined to within a localization length ξ of the region in space where V acts. The discovery [25, 284] of logarithmic dephasing and entanglement spreading in interacting, localized systems revises this understanding, but nonetheless leaves in place the intuition that conserved charges, such as number and energy, should not move over distances greater than the localization length. We will show that this understanding needs to be further revised.

Our main results are as follows: (a) A local perturbation remarkably induces a highly non-local adiabatic *charge* response in distant parts of the system. For an infinitely slow perturbation, $\tau \rightarrow \infty$, there is a “zone of disturbance” where charge rearrangement occurs over a length scale that diverges linearly with system size. For finite τ , charge transfer takes place over length scales $\sim \log(\tau)$. See Fig. 2.1. This effect is distinct from the logarithmic entanglement growth as the charge spreading occurs even in the non-interacting problem where there is no entanglement spreading. (b) This effect cannot be captured by linear response theory, and revises our understanding of susceptibility and transport in localized phases. Our results also modify our understanding of MBL in time dependent systems [96, 251]. And (c), there is a *statistical* Anderson orthogonality catastrophe [16] for both ground and highly-excited states in strongly localized systems, contrary to established wisdom for ground states [118]. Importantly, our work places strong constraints on possibilities for quantum control and topological quantum computation in disordered systems as we will discuss below. We note that there are parallels to our discussion of local manipulations of disordered systems in the field of optics [38, 194]. We emphasize that while our work is *motivated* by many body localization, our results apply also to *Anderson* localized systems, such as systems on a quantum Hall plateau.

2.2 The Anderson Insulator

We start with a disordered single-particle (SP) Anderson insulator in 1D with a time-dependent local potential where most of our results can be described in a transparent setting. Generalizations to higher dimensions is straightforward. Many-body (MB) eigenstates are constructed by simply filling the SP levels. To characterize the non-local charge response of MB eigenstates, define the adiabatic change in the charge density as:

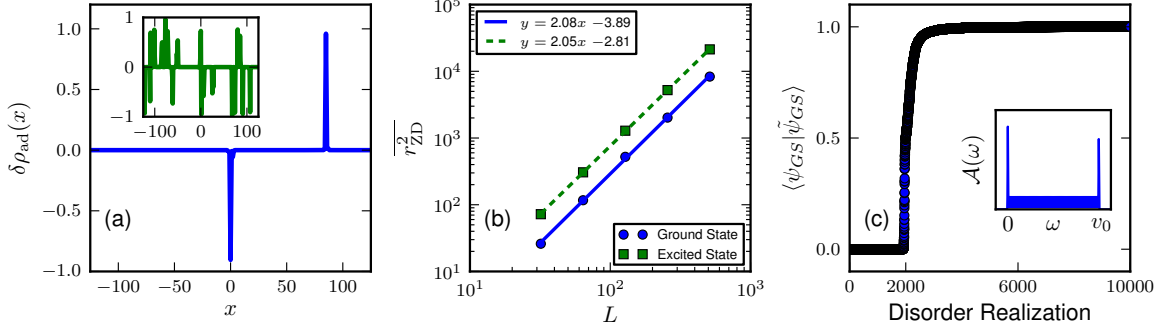


Figure 2.2: (a) Adiabatic change in the ground state charge density (Eq. (2.1)) in a given disorder realization in a 250 site Anderson model (Eq. (2.3)) subject to a repulsive time-dependent potential on site 0 with $\lambda/W = .1$. Charge is expelled from site 0 and transferred to a distant location (near site 75). Inset: Same for an excited state in the middle of the spectrum (colloquially, a $T = \infty$ excited state) showing a multi-particle rearrangement over a large ‘zone of disturbance’. (b) Scaling of the radius of zone of disturbance (Eq. (2.2)) with system size for the ground state (blue circles) and $T = \infty$ excited states (green squares) averaged over 10^4 disorder realizations showing a linear scaling $r_{ZD} \sim L$ in both cases. (c) Overlaps of the MB ground states in the presence ($|\tilde{\psi}_{GS}\rangle$) and absence ($|\psi_{GS}\rangle$) of a local potential of strength $v_0 = .4$ at site 0 sorted over 10^4 disorder realizations with $f = v_0/2W = .2$. The sorted values show a *statistical* orthogonality catastrophe with probability $f = .2$. Inset: Sketch of the disorder averaged spectral function (Eq. (2.6)) for Anderson insulators. The spectrum is pure point, and the diffuse, non-zero strength between $(0, v_0)$ is a signature of the long-distance charge rearrangement.

$$\delta\rho_{\text{ad}}(x) = \sum_{\alpha \text{ occ}} |\psi_{\alpha}(x, t = \infty)|^2 - |\psi_{\alpha}(x, t = -\infty)|^2 \quad (2.1)$$

where $\psi_{\alpha}(x, t)$ is the α -lowest instantaneous SP eigenstate of $H(t)$, and the sum is over occupied SP states in a given MB eigenstate. This expression can be applied quite generally to many-body states of both noninteracting fermions and hard-core bosons where all SP states can be occupied by at most one particle. Figure 2.2(a) shows $\delta\rho^{\text{ad}}$ for the MB ground state and an excited state (drawn randomly from the infinite temperature Gibbs ensemble) in a given disorder realization of the Anderson insulator; both show a long-distance rearrangement of charge. We emphasize that this transfer is mediated by the action of a strictly local potential in an insulator!

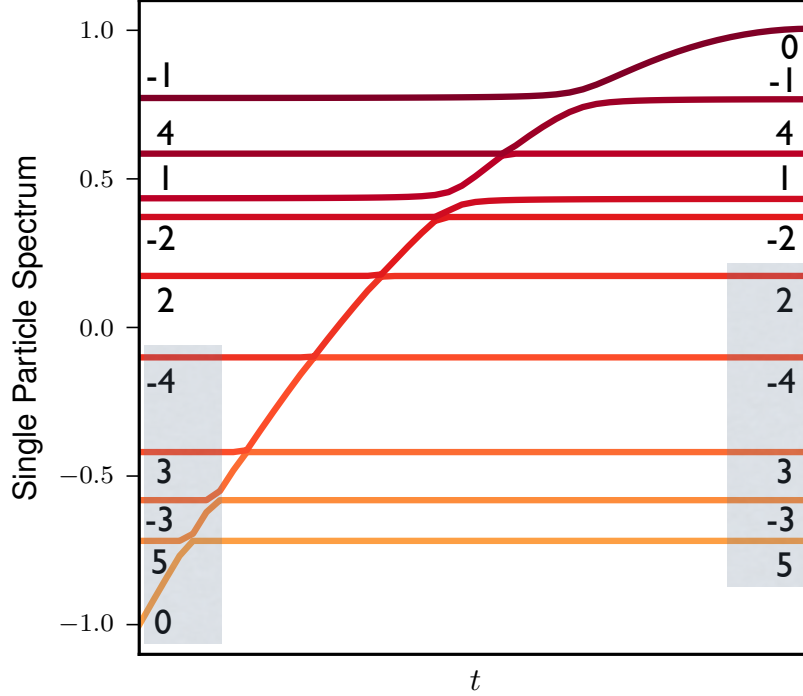


Figure 2.3: Single-particle spectrum of a 10 site Anderson insulator, Eq. (2.3), in a given disorder realization as a function of time. The numbers denote the localization centers of the corresponding eigenstates. The changing potential on site 0 brings $|\psi\rangle_0(t)$ into resonance with the other eigenstates and leads to a set of avoided crossings. The MB ground states at half filling (shaded levels occupied) in the distant past and future are related through the transfer of charge from site 0 to site $R_m = 2$.

More precisely, define

$$r_{\text{ZD}}^2 = \frac{\int_{-L/2}^{L/2} dx x^2 \delta\rho_{\text{ad}}^2}{\int_{-L/2}^{L/2} dx \delta\rho_{\text{ad}}^2} \quad (2.2)$$

where L is the system size and r_{ZD} quantifies the radius of the zone of disturbance over which charge rearrangement takes place. It would be natural to expect r_{ZD} to scale as the localization length ξ . Instead, we find that the disorder averaged radius diverges linearly with system size, $\sqrt{r_{\text{ZD}}^2} \sim L$, *i.e.* the zone of disturbance grows without bound in the adiabatic limit. Fig 2.2(b) shows the disorder averaged scaling of $\overline{r_{\text{ZD}}^2}$ with system size for both the MB ground state and $T = \infty$ excited states.

To understand these results, let's turn to the specific fermionic Hamiltonian in which our computations were performed:

$$\begin{aligned}
H(t) &= H_{\text{hopping}} + V_{\text{loc}}(t/\tau) \\
&= \sum_{i=-L/2+1}^{L/2} -\lambda(c_{i-1}^\dagger c_i + c_i^\dagger c_{i-1}) + v_i c_i^\dagger c_i + v_0(t/\tau) c_0^\dagger c_0
\end{aligned} \tag{2.3}$$

where λ is the nearest-neighbor hopping strength, the onsite potentials v_i are drawn uniformly from $[-W, W]$ and $v_0(t)$, the potential on site 0 is changed with time. We now focus on the strong disorder limit, $\lambda/W \ll 1$, where the localization length $\xi \sim 1$ is on the scale of a lattice constant and an especially simple picture emerges. Denote the eigenstate with localization center at site r as $|\psi\rangle_r$. As $v_0(t)$ is varied in time, the eigenenergy of $|\psi\rangle_0$ is affected most strongly. To leading order, as $v_0(t)$ sweeps the range from $-W$ to W , $|\psi\rangle_0(t)$ comes into resonance with each of the other eigenstates giving rise to a set of avoided crossings with gaps that scale as $\lambda \exp(-R \ln(W/\lambda))$, the effective coupling between $|\psi\rangle_0$ and $|\psi\rangle_{\pm R}$. Thus, the smallest gaps (due to a resonance between $|\psi\rangle_0$ and $|\psi\rangle_{O(N)}$) scale exponentially with system size ($\sim \lambda^N$) even though the system is non-interacting, a fact previously discussed by Altshuler et al [12] in the context of the global adiabatic optimization approach to quantum computation. Figure 2.3 shows the evolution of the spectrum for a given disorder realization in a 10 site chain with $W = 1$. We note that such resonances are also present in an unperturbed Anderson insulator with exponentially small probability; however, the local drive ensures that they occur with probability one.

The many-body ground state of fixed number, say $m = N/2$, is constructed by filling the m lowest single-particle states. Thus, if the system evolves adiabatically, a purely local perturbation on site 0 leads to a transfer of charge a distance R_m away, where $|\psi\rangle_{R_m}$ is the m^{th} lowest eigenstate in the distant future! See Fig. 2.3. The value of R_m differs between disorder realizations, but can take any value from

1 to $N/2$ with equal probability in a system with uniform disorder strength. Thus, the disorder averaged response to the local perturbation has a very wide spatial distribution, and shows no decay on scales longer than ξ_{loc} . When v_0 sweeps only a finite fraction f of the bandwidth ($\sim W$), distant charge transfer in the ground state happens with probability f , occurring only if an occupied state is swept through an avoided crossing with an unoccupied state. The disorder averaged response still shows no decay. For highly excited MB states, the adiabatic response leads to a multi-particle charge rearrangement in a diverging zone of disturbance as shown in Fig.2.2(b).

Having characterized the spatial spread of the adiabatic response, we now turn to the ramp time τ needed for adiabatic time evolution. In particular, we want to know whether τ is set by the exponentially small avoided crossing gaps or by an $O(1)$ mobility gap [222].

For the n^{th} SP eigenstate of $H(-\infty)$ to remain the n^{th} instantaneous eigenstate of $H(t)$, the adiabaticity condition

$$a_{mn}(t) = \hbar \frac{\langle \psi_m(t) | \frac{\partial V(t/\tau)}{\partial t} | \psi_n(t) \rangle}{(E_m(t) - E_n(t))^2} \ll 1 \quad (2.4)$$

must be satisfied at all times for all $m \neq n$, where the eigenstates are defined by $H(t)\psi_\alpha(t) = E_\alpha(t)\psi_\alpha(t)$. For a local $V(t/\tau)$, one might expect the numerator of a_{mn} to be significant only when $\psi_{m,n}$ are centered within a few localization lengths of each other and the potential; however, states within a localization volume in space are separated in energy by the mobility gap giving a large denominator. Thus, naively $a_{mn} \ll 1$ so long as \hbar/τ is smaller than the mobility gap.

This reasoning fails at the avoided crossings in our locally perturbed system. At an avoided crossing at time t between eigenstates $|\psi(t)\rangle_0$ and $|\psi(t)\rangle_R$ the energy gap is exponentially small in R , whereas the instantaneous eigenstates look like the symmetric

and antisymmetric combinations : $|\psi_{m,n}(t)\rangle \sim |\psi(t)\rangle_0 \pm |\psi(t)\rangle_R(t)$. Since $V(t)$ is also localized near site 0, the numerator of $a_{mn}(t)$ receives a substantial contribution from the diagonal piece ${}_0\langle\psi(t)|\dot{V}|\psi(t)\rangle_0$. Thus, the system remains adiabatic only if

$$\tau_{\text{ad}} \gg \frac{\hbar W^{2(R-1)} \partial_t V}{\lambda^{2R}}$$

i.e. the mobility gap does not protect adiabaticity. Thus in a system of size L , the drive is adiabatic for all levels only if the ramp is exponentially slow in the system size, even for a single-particle Anderson insulator.

The preceding discussion also implies that with a finite ramp time τ , the system is only able to adiabatically avoid level crossings with gaps $> \hbar/\tau$. Since the charge transfer is a consequence of avoided crossings and since the gaps decay exponentially with distance $W \exp(-R/\xi)$ (in the strong localization regime), with a finite ramp time τ , charge transfer occurs over a characteristic length scale

$$r_{\text{ZD}} \sim \xi \ln \left(\frac{\tau W}{\hbar} \right) \sim \ln(\tau) \quad (2.5)$$

This logarithmic transfer of charge is our key result. We predict a similar logarithmic spreading in the weak localization regime, on distances larger than the localization length.

2.2.1 Orthogonality Catastrophe

This non-local charge response implies a *statistical* Anderson orthogonality catastrophe (OC) in the Anderson insulator. Anderson's original work had shown that the many-body ground states of a clean (metallic) system of fermions in the presence and absence of a local impurity potential were orthogonal in the thermodynamic limit, even for arbitrarily weak (but finite) potentials. In the strongly disordered system under study, adding an on-site potential on site 0 of strength $v_0 = 2Wf$ with

$f < 1$ leads to a distant charge transfer and hence an orthogonal new ground state with probability f . Figure 2.2(c) shows the ground state overlaps with and without a potential, clearly showing an orthogonality with probability f (roughly when the starting potential on site 0 lies within v_0 of the Fermi energy). For highly excited states, we have a catastrophe with probability 1. Previous work [118] on the OC in ground states of strongly disordered systems only captured the non-orthogonal overlaps that occur with probability $1 - f$ to incorrectly conclude that strongly disordered insulators don't suffer from the OC.

The OC has important consequences for several dynamical phenomena in metals. Famously, it predicts an X-ray edge singularity [211], where the low-energy X-ray absorption spectrum in a metal has the singular form $\mathcal{A}(\omega) \sim \omega^{-1+2\eta}$ and η is derived from the Anderson OC. The primary spectral function characterizing local quantum quenches (such as a change in the potential) takes the form: s

$$\mathcal{A}(\omega) = \sum_n |\langle n|GS\rangle|^2 \delta(\omega - E_n + E_{GS} + \omega_0) \quad (2.6)$$

where $|GS\rangle$ is ground state of the system before the quench, and $|n\rangle$, E_n are the eigenstates and eigenvalues of the final Hamiltonian. For the Anderson insulator in the $\lambda/W \ll 1$ limit, $A(\omega)$ looks pure point, and is characterized by delta function peaks located between $\omega \in (0, v_0)$ for different disorder realizations with a catastrophe. In disorder realizations where there is no catastrophe and no long-distance charge transfer (probability $1 - f$), $\mathcal{A}(\omega)$ has a peak at either $\omega = 0$ or $\omega = v_0$. The inset in Fig. 2.2(c) shows a representative sketch of the disorder averaged spectral function – the non-zero weight between $(0, v_0)$ distinguishes the Anderson insulator response from that of ordinary band insulators and is a signature of long-distance charge rearrangement.

2.2.2 Failure of linear response

Before leaving the Anderson insulator it is instructive to compare our description of the adiabatic response to a local perturbation to the more standard account of such a perturbation in linear response (LR) theory in the $\omega \rightarrow 0$ limit. This response is governed by the density susceptibility which has been calculated using LR, for example, in the classic work by Vollhardt and Wölfle [314] and the LR answer *is* local on the scale of the localization length. As the standard computations are approximations carried out with disorder averaged Green's functions and done at fixed chemical potential, it is useful to revisit this question more carefully. For a single disorder realization the density susceptibility is given by a Kubo formula which involves matrix elements of the perturbation between the exact *unperturbed* eigenstates. We can estimate the density susceptibility in LR by a generalization of the arguments used in the derivation of the celebrated Mott formula for the AC conductivity of an Anderson insulator, $\sigma \sim \omega^2 \ln^{d+1} \omega$ [209] at small ω . Essentially, we translate those arguments from the global dissipative response for the conductivity to the local reactive response for the charge susceptibility. Accordingly, we estimate that the charge rearrangements to distance $r \gg \xi$ away from our chosen site are dominated by unperturbed states in which the site is resonant with another at that distance. As such a state is present with probability exponentially small in r/ξ , the disordered averaged linear response will indeed decay exponentially on the scale of ξ . This has been verified by numerical computations as shown in Fig. 2.4(a). The same figure also shows the exact response averaged over the same disorder realizations and it is clear that it is exponentially larger for $r \gg \xi$. This contrast vividly illustrates our central observation that while the states with long-range resonances that contribute to the Mott/ LR result are exponentially rare, even a local drive, surprisingly, *creates* resonances with high probability. For concreteness, we note that the linear-response result in Fig. 2.4 is obtained by evaluating Eq.(2.1) with the single-particle eigen-

states perturbed to first order in the local potential, while the exact result uses the exact eigenstates in the presence of the potential.

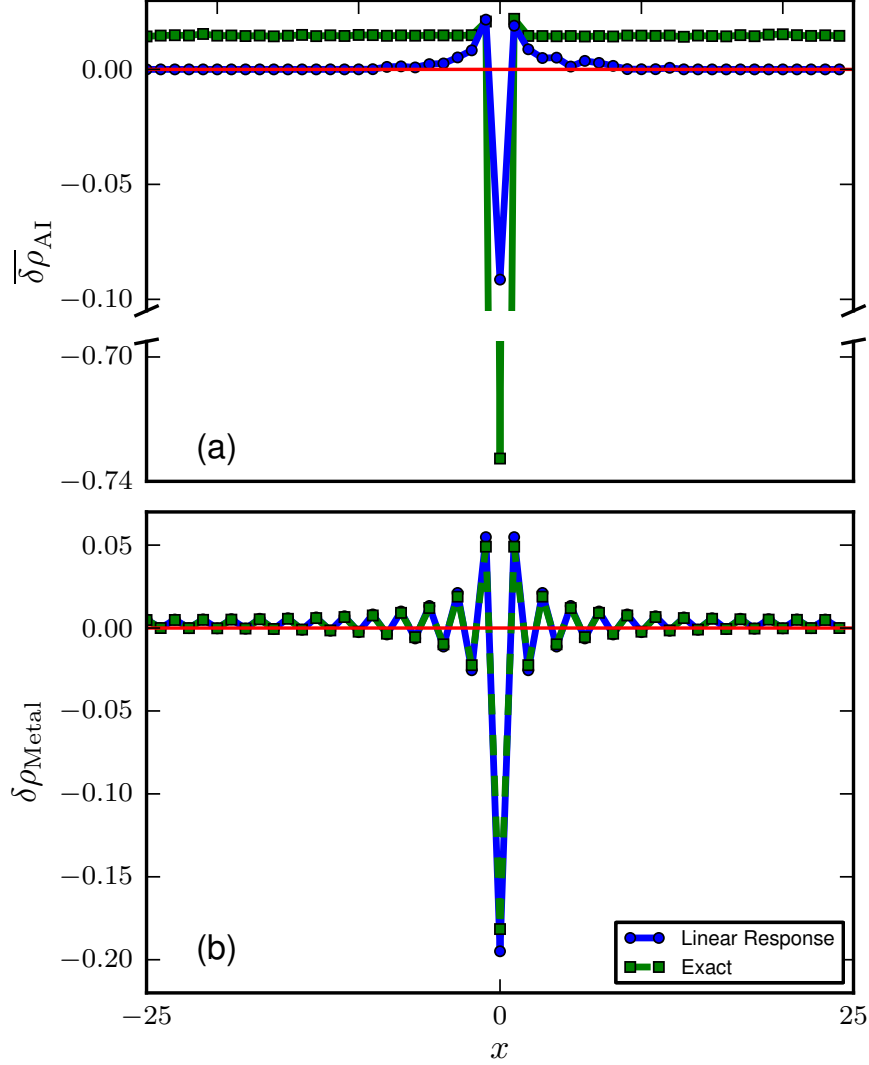


Figure 2.4: Exact (green, squares) and linear-response (blue, circle) answers for the ground-state charge density difference (Eq. (2.1)), $\delta\rho(r)$, in a system of size $L = 50$ due a perturbing repulsive potential of strength $v_0 = .4$ added to the center of the system in (a) an Anderson insulator with $\lambda/W = .1$ averaged over 10^5 disorder realizations. While $\delta\rho_{LR}(r)$ rapidly decays away from the location of the potential, the exact $\delta\rho(r)$ shows a uniform response everywhere (with amplitude scaling as $1/L$). (b) In a metal ($\lambda = 1, W = 0$), the linear-response charge response closely captures the exact answer.

2.3 Contrast with Clean Insulators and with Metals

At this point it is instructive to contrast the behavior we have found for the Anderson insulator with that of undisordered insulators (band and Mott) and that of metals. In an undisordered insulator the particles are again localized with a length scale that can be read off from correlation functions and which will scale inversely with the gap. Now a) the response to an adiabatically prepared local potential is indeed localized with this localization length, b) there is no orthogonality catastrophe, c) the adiabatic response is accurately captured by linear response/perturbation theory. The case of metals—ballistic and diffusive—is intermediate. In a metal a) charge can flow to infinity and thus the adiabatic charge transfer is not restricted to the vicinity of the applied perturbation, b) there *is*—famously—an orthogonality catastrophe with a scaling with system size that is modified in the diffusive case, c) the adiabatic response is accurately captured by linear response/perturbation theory as illustrated in 2.4(b). As a function of the time scale we can be more specific. In both ballistic and diffusive metals we will obtain a power law spreading of charge $R_\tau \sim \tau^\sigma$ with $\sigma = 1, 1/2$ respectively. Indeed, charge can continue to flow even long after the Hamiltonian stops changing ($t \gg \tau$) allowing the effects of a local perturbation to propagate out to infinity. This is in contrast to both undisordered insulators and Anderson localized systems, where charge transfer occurs *only* when the Hamiltonian is changing, and thus the influence of the perturbation is restricted to a finite region of space (with linear size τ^0 or $\ln \tau$ respectively). Moreover, the smallest gaps in non-interacting metals scale only polynomially with system and thus an adiabatic response can be achieved by much faster ramp rates τ as compared to localized systems. Finally it is interesting to note that in clean insulators and metals the adiabatic limit considered in this chapter yields the same charge response as the

opposite limit in which $L \rightarrow \infty$ before $\tau \rightarrow \infty$. In the Anderson insulator the latter limit fails to exist in the mathematical sense that the charge response does *not* converge to a fixed answer as τ is increased in an infinite system but instead continues to evolve erratically as increasingly small gaps become relevant.

2.4 Generalization to MBL

We now generalize our analysis to fully MBL interacting localized systems. Our principal results for the Anderson insulator carry over. MBL systems also exhibit a) a zone of disturbance that grows as $\ln(\tau)$, b) a statistical orthogonality catastrophe for the ground state and a certain orthogonality catastrophe for highly excited states and c) a failure of linear response to agree with this behavior. There are three new features that come into play. First, we can consider systems that lack a parent single particle description as they lack a conserved number and the non-local response now involves a rearrangement in the energy density alone. Second, the rearrangement process for highly excited states now exhibits a range of length scales from the ubiquitous $\ln(\tau)$ to the shorter, but still divergent, $(\ln \tau)^{1/(d+1)}$ at which much more comprehensive changes take place in the structure of the ground state. Third, the termination of the perturbation is now followed by the entanglement spreading discussed in [25, 284]. We note that the entanglement spreading is the dominant effect in work on quantum revivals [306] which considers sudden quenches and thus works in the opposite limit from the one considered here. These results can be derived within the “1-bits” formalism introduced in [283, 148]. For specificity consider a quantum spin system dominated by random fields:

$$H = \sum_{i=-L/2}^{L/2} h_i \sigma_i^z + \lambda H^{(2)} \quad (2.7)$$

where the h_i are taken from a distribution of width W , $H^{(2)}$ includes interaction terms that may or not conserve $\sum_i \sigma_i^z$ and λ is chosen appropriately small so that the eigenstates of H are localized at *all* energies. Such a fully MBL system can be recast via a unitary transformation into the form [283, 148]

$$H_0 = \sum_i \tilde{h}_i \tau_i^z + \sum_{i,j} \tilde{J}_{ij} \tau_i^z \tau_j^z + \sum_n \sum_{i,j,\{k\}} K_{i\{k\}j}^{(n)} \tau_i^z \tau_{k_1}^z \dots \tau_{k_n}^z \tau_j^z. \quad (2.8)$$

where the τ_i^z are exponentially localized emergent integrals of motion ('l-bits'), and the high order terms J_{ij} and $K_{i\{k\}j}$ fall off exponentially rapidly in the range, modulo exponentially rare resonant ones which can be ignored for the most part. To leading order in large W , the τ_i^z coincide with the σ_i^z , but with a 'dressing' of multi-spin operators that falls off exponentially in the range.

Let us now introduce a local perturbation by making the field on a particular site h_0 time dependent $h_0 \rightarrow h_0(t/\tau)$. With this change the new \tilde{h}_0 and the interaction terms involving τ_0 also become time dependent. Further, the other l-bits $\tau_{i \neq 0}$ will also be affected due to their overlap with σ_0 . In particular, the l-bits themselves will have to be redefined continuously in time, so that (written in terms of the l-bit operators τ_i^z at time zero), the Hamiltonian will acquire off diagonal terms:

$$\begin{aligned} H(t > 0) &= H_0 + \sum_i \tilde{h}_i \exp(-|i|/\xi_0) \tau_i^z + \sum_i \tilde{J}_{ij}(t) \tau_i^z \tau_0^z \\ &+ \sum_{n,i,\{k\}} K_{i\{k\}j}^{(n)}(t) \tau_i^z \tau_{k_1}^z \dots \tau_{k_n}^z \tau_0^z \\ &+ \sum_j (t_{j0}^x(t) \tau_j^x \tau_0^x + t_{j0}^y(t) \tau_j^y \tau_0^y) + \dots \end{aligned} \quad (2.9)$$

where the ... denotes higher order l-bit spin hopping terms which rearrange multiple l-bits and the off diagonal terms all fall off exponentially with distance from 0, both in the magnitude of individual terms and in the total weight.

Now, a slowly varying time dependent potential induces avoided crossings, with the minimum gaps controlled by the off diagonal terms. Range R single l-bit spin hops will then occur IFF the Hamiltonian varies slowly compared to the gap scale $\exp(-R/\xi_0)$, where ξ_0 is the characteristic length scale for decay of a typical off diagonal term. The effect of the higher order interaction terms is to modify the effective interaction length so that the gaps fall off as $\exp(-R/\tilde{\xi})$, where $\tilde{\xi}$ is the decay length of the total interaction. The largest gaps are typically set by *many spin* rearrangements. Thus, the size of the zone of disturbance (the region over which some l-bits are rearranged) grows as $\tilde{\xi} \ln \tau$, with $\tilde{\xi} \geq \xi_0$. For highly excited states we can also identify a “zone of total rearrangement” - a (smaller) region of size \tilde{R} over which a \tilde{R} independent fraction of the l-bits are rearranged. Since the number of l-bits that must be rearranged in the zone of total rearrangement grows as \tilde{R}^d , and the matrix element for flipping each l-bit is exponentially small in \tilde{R} , the gaps associated with total rearrangements will scale as $\exp(-\tilde{R}^{d+1})$. Thus, we expect the zone of total rearrangement to grow as $\tilde{R} \sim (\ln \tau)^{1/(d+1)}$. One can also establish the remaining results within the same framework.

2.5 Discussion and Ramifications

We conclude by discussing the implications of our work for experiments, other aspects of the physics of localized systems and for quantum engineering. Starting with experiments, it would be gratifying to directly observe the zone of disturbance created in response to a local perturbation and it seems to us that the cold atomic systems which have exhibited Anderson [20, 35, 190, 269] and, apparently, MBL [192] are the best places to look.

Alternatively experiments could look for the predicted form of the X-ray absorption spectrum sketched in Fig. 2.2(c). Apart from solids hosting disordered electron gases [231], cold atomic gases [184] are again plausible systems to observe this effect.

The tuned resonance behavior that underlies our chief results can, in principle, be produced in other ways—e.g. by sandwiching a localized system between two conducting leads and tuning the chemical potential in the conducting regions. Indeed, this is the well known setting of the Lifshitz-Azbel [23, 240, 206] resonances in Anderson localized systems. Quasiperiodic systems, with [157] and without [22] interactions, are known to exhibit localized states and are natural for studying our results in a setting without disorder.

Another problem for which our results have consequences is that of Floquet localization in MBL systems. It has been argued [96, 251] that MBL systems subject to a periodic local driving do not absorb energy indefinitely. In particular, the eigenstates of the Floquet operator for such systems are expected to be MBL. Here our results predict that slow, low-frequency local drives (or a slow perturbation of the amplitude of a fast drive) will give rise to a diverging ‘zone of disturbance’ in the Floquet eigenstates and lead to a transfer of energy deep into the system.

We now turn to the implications of our work for quantum control, engineering and computation where it might often be necessary to perform local manipulations in disordered environments while leaving distant regions untouched. At the broadest level, our results imply that such control will be problematic if we attempt to carry out such manipulations arbitrarily gently/slowly as one might wish to for a theoretical analysis of devices. We emphasize that such adiabaticity is implicit in thinking of ideal control by means of gates, for example, or even of small excitation currents which imply slow changes of various potentials.

We will now explain in more detail why this charge rearrangement is problematic for quantum computation. The discussion below pertains to two broad classes of

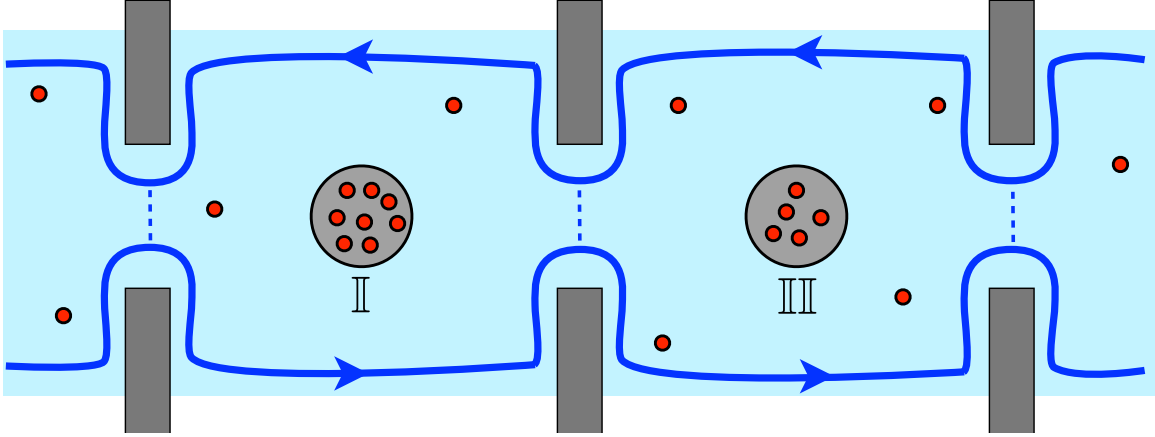


Figure 2.5: Schematic illustration of a proposal for topological quantum computation outlined in Ref. [226]. Regions I and III contain the intended non-Abelian quasiparticles whose joint state is measured by interferometric tunneling experiments of quasiparticles across the constrictions. In realistic experiments, there will be unintended quasiparticles in the shaded region outside of I and III which will rearrange over long distances in response to the changing potential on the constriction, thereby spoiling the braiding experiment.

systems. First, it applies to several of the most popular existing platforms for *low temperature* topological quantum computation in experimentally realizable systems, including the ground states of non-Abelian quantum Hall systems. Implementing quantum computing in these systems is an active and challenging area of current research that our work directly informs. Second, our results apply to the recent, novel possibility [149] of performing *high-temperature* quantum computation by using many-body localized systems which can stabilize topological order at finite energy densities. This nascent idea, while still speculative, represents an exciting new frontier which has attracted a lot of attention recently; our work places strong limits on the implementations of this idea and will inform future experiments and developments in this area.

2.5.1 Quantum computation with quantum Hall systems

For concreteness, let us analyze a well-known proposal which uses fractional quantum Hall systems as platforms for topological quantum computation by creating and braid-

ing localized excitations. The simplest operation for this system shown in Fig. 2.5, taken from Ref. [226], involves constructing a quantum bit from the non-Abelian quasiparticles and applying a NOT gate to flip the state of this bit. We summarize this construction here and refer the reader to Ref. [226] for more details. A two-state qubit is realized by localizing an odd number of target quasiparticles in small regions in each half of a Hall bar (regions I and III in Fig. 2.5). The bar has a manipulatable constriction in between regions I and III. As the constriction is narrowed, if a single quasiparticle (or an odd number) tunnels from the top edge of the bar to the bottom, its trajectory passes between the two sets of localized target quasiparticles which flips the state of the qubit.

In a perfectly clean sample, the only quasiparticles present are those created by the experimenter in regions I and III. In practice, all known experimental realizations are disordered and exhibit *broadened* quantum Hall plateaux with additional topologically charged quasiparticles that are Anderson localized by the disorder. Thus, there is a ‘background’ of localized quasiparticles in addition to those present in regions I and III as indicated by the red dots in Fig. 2.5.

The middle constriction is controlled through an electrostatic potential with a dipolar shadow leaking into the sample. Operating the gate involves adiabatically changing the potential at the constriction to braid a controlled number of quasiparticles around the target regions. Of course, in a realistic sample, this slowly varying potential is also felt by the localized ‘background’ quasiparticles which can respond by moving long distances. If the background quasiparticles move across the braiding path, the resulting braid will be different from the intended one, causing the computational step to fail. The problem is only worsened by operating the gate arbitrarily slowly, since that leads to an even more non-local response. Thus, there is no safe asymptotic limit, and braiding in these devices will require considerable engineering of time scales. The ideas laid out in this section generalize quite directly to various

experiments aiming to perform slow, local manipulations in disordered systems with localized (Anderson, or many-body) quasiparticles.

2.5.2 Other proposals for quantum computation

We now expand our discussion of the implications of our results in disordered environments by considering a few other proposals for topological quantum computation. Proposals for topological quantum computation draw their strength from the spatially extended character of their qubits which make them relatively immune to decoherence, but this spatially extended character makes them vulnerable to the non-local response discussed in this chapter. In the prior section, we considered a single motif that has been discussed as a gate for computation with quantum Hall systems. Here we comment on two more proposals which all involve electrostatic gating in some fashion:

- Measurement only computation with QH devices: In this proposal [41], the authors describe how to implement braids and carry out computations without actually physically transporting quasiparticles. Instead, the computational steps are carried out via a series of topological charge measurements. Prima facie, it might seem that such a proposal is immune to our effect since no charges are being transported. However, this method is also dependent on electrical gates to carry out measurements and thus susceptible to the same issues as more “conventional” approaches. In particular, electrical gates enter at two stages in this scheme. First in preparing the state to be measured wherein the idea is to prepare entangled pairs of quasiparticles by creating them from the ground state. This has to be done via gates and will be subject to uncertainty via our effect - extra quasiparticles will enter/exit the region to be measured in an uncontrolled fashion. The second place where gates need to be used is in selecting the quasiparticles to be measured - this requires directing the flow

of the measuring current via electrical gates. Once the gates are in place, the measurement itself can, in principle, be done asymptotically gently for our purposes.

- Computation with Majorana wires: The basic ingredient in these proposals (Ref. [32] and references therein) is to create qubits from the ends of superconducting wires in a topological phase and to move them around by the action of gates which cause segments of a longer wire or wire network to transition between topological and non-topological phases. In the presence of disorder, these gate potentials will cause quasiparticles to tunnel between different segments of the wire hosting the Majoranas, as well as between the wires and the proximate superconductor which is needed for their superconductivity—thus leading to bit flips. This effect in the absence of gate potentials has been discussed as quasiparticle poisoning [262]. Interestingly, as in the measurement only proposal discussed above, it is possible to read out the state of Majorana qubit by means of vortices [134] which themselves will be immune to our considerations.

Finally, we turn to the possibility of performing *high-temperature* quantum computation by using many-body localized systems. The discussion above unfortunately has a negative implication for MBL physics. As outlined in Ref. [149], highly excited MBL eigenstates with localized quasiparticles can still support topological order. This observation has led to the recent, novel possibility of performing *high-temperature* topological quantum computation using MBL systems. While still nascent, this exciting idea has attracted a lot of attention. The discussion for quantum computation using quantum Hall platforms directly generalizes to braiding in MBL systems since the localized background quasiparticles can again respond to the slow braid and spoil the computation; thus our work places strong limits on the implementations of this idea and will inform future experiments and engineering in this field. Further, our results here imply that since one *cannot* define an adiabatic process with a well defined

Berry phase, quasiparticle statistics are, as such, ill-defined in the localized setting. Instead the topological information in the excited MBL states must be reconstructed from other data.

Altogether, our results place natural limits on the manipulation of local degrees of freedom in localized phases and help further elucidate the remarkably subtle nature of localization.

Chapter 3

Low-Frequency Linear-Response Conductivity in Many-Body Localized Systems

3.1 Introduction

In the last chapter, we saw that the adiabatic response of MBL systems is governed by “induced” resonances which give predictions that are markedly different from linear response theory. This analysis holds in the limit of extremely slow drives, $\omega \rightarrow 0$. It is equally instructive to study the dynamical response of MBL systems by probing their low-frequency response in the linear response regime characterized by a vanishing drive amplitude $v \rightarrow 0$. This calculation will be sensitive to “pre-existing” resonances in the system as in Mott’s celebrated result on the a.c. conductivity of Anderson insulators [209].

We have seen that while the eigenstate properties of MBL systems are, in some respects, similar to those of noninteracting Anderson insulators, there are important

differences in the dynamics, such as the logarithmic spreading of entanglement in the MBL phase [152, 25, 318, 284, 148, 282, 172].

In this chapter we show that the MBL phase also differs sharply from noninteracting localized systems in its low-frequency response. We focus on the infinite temperature a.c. conductivity in the MBL phase, for concreteness and to make contact with previous literature on solid-state systems (e.g., Mott’s law [209]); however, as we argue below, our discussion directly extends to relaxation dynamics, which is more easily accessible in experimental studies using ultracold atoms [279], polar molecules [330], nitrogen-vacancy centers [91], and other forms of “synthetic” matter. We identify two physical mechanisms underlying the slow response: (a) the presence of resonant pairs of charge or spin *configurations*, connected by slow many-body rearrangements; and (b) the presence within an MBL system of rare thermalizing regions, or “inclusions”, that act as local heat baths for their surroundings. These mechanisms are absent in noninteracting systems: thus, the differences in transport between single-particle and many-body localization can be traced to the much larger *connectivity* of the many-body Hilbert space. The two mechanisms we discuss involve dissipative dynamics, and are thus distinct from the “pure dephasing” processes that cause the slow growth of entanglement within the MBL phase [148, 284].

Our results for the a.c. conductivity are as follows. Whereas in noninteracting systems the a.c. conductivity $\sigma(\omega) \sim \omega^2 \log^{d+1} \omega$ (Mott’s law [209] in d dimensions), in the interacting MBL phase at high temperature the conductivity goes as $\sigma(\omega) \sim \omega^\alpha$, where α is an exponent that varies continuously throughout the MBL phase, ranging from $\alpha = 1$ at the MBL transition to $\alpha \rightarrow 2$ deep in the MBL phase. The exponent α has two regimes of behavior, corresponding to the two mechanisms described above. Deep in the MBL phase, the conductivity is dominated, as in Mott’s law, by resonant transitions between localized configurations. It is enhanced relative to noninteracting localization because more such resonances are possible: in addition to single-particle

hopping, a MBL state can undergo multiple-particle rearrangements. We term this regime the “MBL-Mott” regime, and argue that response in this regime is dominated by rare regions that are still localized but with anomalously large localization length. Close to the transition, the conductivity is dominated by rare thermalizing or critical regions and their surroundings; we call this the “MBL-Griffiths” regime. As the system approaches the transition from the insulating side, thermalizing inclusions proliferate; we show that this leads to the conductivity exponent $\alpha \rightarrow 1$.

In two or more dimensions, the exponent $\alpha = 0$ throughout the thermal phase (i.e., there is presumably a nonzero d.c. conductivity). In one dimension, however, a subdiffusive phase with a continuously varying conductivity exponent $0 < \alpha < 1$ exists on the thermal side of the MBL transition [201, 8, 320]. Remarkably, therefore, the a.c. conductivity exponent α in one dimension is continuous and apparently smooth across the MBL transition, approaching the critical behavior $\sigma(\omega) \sim \omega$ from both sides (Fig. 3.1).

This chapter is structured as follows. In Section 3.2 we list our assumptions. In Sections 3.3 and 3.4 we introduce the MBL-Mott and MBL-Griffiths phases respectively; then in Section 3.5 we discuss the transition between these phases. In Section 3.6 we describe the numerical methods used to compare our theoretical predictions with data on random-field Heisenberg spin chains (details of the numerical analysis are given in Appendix 3.B). Section 3.7 connects the a.c. conductivity to the relaxation dynamics measured in ultracold atomic experiments. Finally, Section 3.8 summarizes our results and comments on their scope.

3.2 Assumptions

We work with a generic disordered lattice Hamiltonian having a conserved density (e.g., a particle number, or a particular projection of spin). The current associated

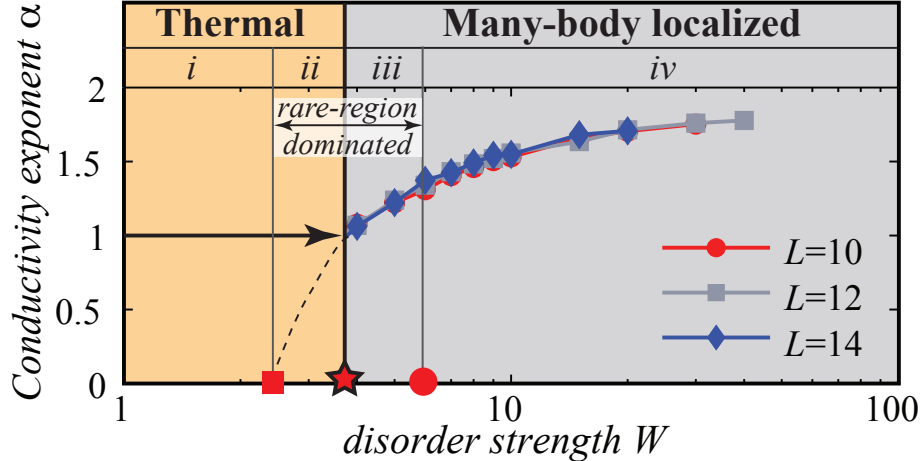


Figure 3.1: A.C. conductivity exponent α of a disordered one-dimensional system across the many-body localization transition, showing four regimes: (i) the diffusive thermal phase; (ii) the *subdiffusive* thermal phase [8], which exists only in one dimension; and (iii, iv) the MBL phase. The MBL phase is divided into an “MBL-Griffiths” regime (iii) in which low-frequency response is dominated by rare critical or thermal regions, and an “MBL-Mott” regime (iv) in which it is dominated by pairs of resonant configurations. Our main predictions are that the exponent $\alpha \rightarrow 1$ [i.e., $\sigma \sim \omega$] as the MBL transition is approached from the localized side, and that $1 \leq \alpha < 2$ throughout the MBL phase. These are consistent with numerical simulations of a nearest-neighbor random-field XXZ chain (shown in the plot). In the thermal phase, finite-size effects are strong, and a more careful analysis [8] is needed to extract the conductivity exponent.

with this charge is denoted \mathbf{j} . The a.c. conductivity tensor σ in the $T \rightarrow \infty$ limit is then given by the Kubo formula:

$$T\sigma_{\beta\gamma}(\omega) = \frac{1}{ZN} \sum_{mn} \langle m | j_\beta | n \rangle \langle n | j_\gamma | m \rangle \delta(\omega - \omega_{mn}) . \quad (3.1)$$

Here T is the temperature, N is the number of sites, Z is the partition function which in this infinite T limit is the dimension of the many-body state space; the indices m, n run over all Z many-body eigenstates; and the current j_β is the sum over local currents, viz. $j_\beta \equiv \sum_i j_{i,\beta}$. We shall only be concerned with the diagonal elements $\sigma_{\beta\beta}$, so henceforth we shall drop the index β . Our arguments should also apply to the frequency-dependence of the a.c. thermal conductivity, e.g., in systems

where the only conserved quantity is the energy. We can also consider the dynamics of a Floquet system with no conserved densities to be transported; for such systems in the MBL phase, the mechanisms we discuss give relaxation that is a power of time (see Section VII below).

When we consider the MBL phase, we specialize here to the case where all many-body eigenstates are localized, so we can discuss in terms of the localized conserved operators. However, the results we obtain should also apply to the MBL phase in systems with a many-body mobility edge. In the latter case, when we discuss ‘rare regions’ they are not only rare local disorder configurations in the system’s Hamiltonian, but also rare local configurations of the state that put it locally closer to, at, or across the mobility edge.

We consider the a.c. conductivity here at the level of linear response theory: i.e., we assume throughout that the drive is sufficiently weak and is present for a sufficiently short time that linear response applies. It was shown [172] in the last chapter that localized systems subject to a nonzero-amplitude drive go nonlinear and display a highly non-local response at low enough frequencies. Further, an MBL system subject to a finite-frequency drive for a long enough duration will eventually leave the linear response regime and enter instead a Floquet MBL steady state or even thermalize due to the a.c. drive [223, 172, 252, 251, 2, 199].

3.3 MBL-Mott regime

3.3.1 Many-body “Mott” conductivity

We begin by considering the generic behavior deep in the MBL phase. As discussed earlier, we specialize to the regime where all eigenstates of the system are localized. In this regime, the system Hamiltonian admits a representation in terms of effective spin-1/2 degrees of freedom labeled τ_k , which are frequently referred to as local integrals of

motion or “1-bits” [283, 148, 271]: in terms of these, $H = \sum_i h_i \tau_i^z + \sum_{i,j} J_{ij} \tau_i^z \tau_j^z + \dots$. Eigenstates of H are also simultaneously eigenstates of all the τ_k^z . These effective τ spins are related to the microscopic degrees of freedom (which need not be spin-1/2) by a unitary transformation that is local up to exponentially small tails. In terms of the effective τ spins, the current operator can be expressed as

$$j = \sum_{\beta,k} K_{\beta,k}^{(1)} \tau_k^\beta + \sum_{\beta,\gamma,k,l} K_{\beta\gamma,k,l}^{(2)} \tau_k^\beta \tau_l^\gamma + \dots, \quad (3.2)$$

where $\beta, \gamma = x, y, z$; τ^β is the appropriate Pauli matrix; and k, l run over effective spins. The coefficients $K^{(n)}$ for $n \geq 2$ fall off exponentially with the distance between the farthest effective spins in that term. Stability of the MBL phase further requires them to fall off exponentially with the order n [122]. Note that for a single-particle (noninteracting) Anderson insulator the τ^β operators are the creation, annihilation and number operators of the localized single-particle states, so the coefficients $K^{(n)}$ are zero for $n > 2$, i.e., the current operator only contains single-particle hops and no multiple-particle rearrangements.

We now briefly review Mott’s argument [209] for the a.c. conductivity in *noninteracting* localized systems at temperature $T > \omega$. For this noninteracting case, the transitions contributing to $\sigma(\omega)$ at low frequency involve rare pairs of resonant *sites* that hybridize to form pairs of nearly-degenerate eigenstates (i.e., symmetric and antisymmetric linear combinations of the wavefunctions centered at the two sites) with small energy splitting ω . Short-distance resonances, while common, typically have large splittings because of local level repulsion; these local processes give only a subdominant contribution to the conductivity in the low-frequency limit ¹. To find the resonant pairs of sites with energy splitting ω that dominate in $\sigma(\omega)$, one has to go a distance r_ω determined by the condition $W \exp(-r_\omega) = \omega$, where W is a

¹There are also random-matrix theory tails—i.e., short-distance resonances with anomalously small matrix element—whose contribution is subleading at low ω .

microscopic bandwidth. (We are assuming the single-particle localization length is of order one lattice spacing and do not include factors of it.) The number of such pairs is $\sim r_\omega^{d-1}$. The typical current matrix element between such pairs of eigenstates is $\omega r_\omega \simeq \omega \log(W/\omega)$ (because they involve moving a unit charge a distance r_ω at a rate ω). Putting these pieces together, we recover the Mott result:

$$\sigma(\omega) \sim \omega^2 \log^{d+1}(W/\omega). \quad (3.3)$$

Note that the contribution from more distant pairs is weaker, because the current matrix element falls off as $\exp(-R)$ whereas the phase space only grows as R^{d-1} .

This argument is fundamentally altered by many-body processes for the *interacting* MBL phase. Here the conductivity includes not only hopping resonances between pairs of *sites* but also many-body resonances between pairs of *configurations*. Hence the “phase space” factor is strongly enhanced. We now argue that this enhanced phase space factor grows exponentially in the number of effective spins flipped.

The many-body resonances that dominate the low-frequency dynamics flip n effective spins, with those spins typically having random spacings of order the localization length or less so that they do interact with each other. For $d > 1$ this set of spins will in general have a fractal geometry. Let γ collectively denote all the relevant parameters (shape, typical interparticle spacing, etc.) specifying the ensemble of possibly resonant ‘clusters’ of flipped spins. (Given a cluster, in other words, one can characterize it through its parameters γ ; different resonant n -spin clusters with the same γ will have the same hybridization strength.)

The typical current matrix element for a resonance with parameters γ that flips n spins is $\sim W \exp(-n/\zeta(\gamma))$. Here $\zeta(\gamma)$ is a dimensionless quantity that depends on γ and varies continuously in the MBL phase; $\zeta(\gamma)$ remains finite at the MBL transition and decreases as one moves deeper into the localized phase. $\zeta(\gamma)$ is larger for

resonances having more closely spaced and thus more strongly interacting spins. Let us fix these parameters γ . Then, analogous to the single-particle case, the frequency ω picks out an “optimal” n such that

$$W \exp(-n/\zeta(\gamma)) = \omega \Rightarrow n = \zeta(\gamma) \log(W/\omega). \quad (3.4)$$

The number of possible resonances (in the ensemble parameterized by γ) that flip n effective spins in the immediate vicinity of one particular real-space location is exponential in n , while the frequency bandwidth of such rearrangements is linear in n . Thus, to leading order the density of states of possible resonances at order n grows exponentially with n . Specifically, it grows as $\sim e^{s(\gamma)n}$, where $s(\gamma)$ is the configurational entropy per flipped spin of the possibly resonant clusters in the ensemble γ . This is the entropy of all the possible choices of the n spins flipped by the resonance. Using this and Eq. (3.4), the density of states of resonant configurations from ensemble γ at frequency ω grows as a power law, $\omega^{-\phi}$, where $\phi = s(\gamma)\zeta(\gamma)$, in contrast with the logarithmic growth in the noninteracting case. The dominant resonances at low frequency flip many spins and have their properties γ chosen so that the product $s(\gamma)\zeta(\gamma)$ is maximized ².

We now assume that we have maximized this product ϕ , and complete our estimate of the MBL-“Mott” conductivity. The current matrix elements remain $\sim \omega$, up to logarithmic factors. Putting this together with the phase space factor $\omega^{-\phi}$, the conductivity goes as

$$\sigma(\omega) \sim \omega^{2-\phi} \quad (3.5)$$

at low frequency.

²We need not be explicit about the nature of the dominant resonances to conclude that the phase space grows as $\omega^{-\phi}$ for $0 \leq \phi \leq 1$. For simple ensembles γ_0 of resonances (e.g., those that lie on a straight line with a given average spacing), one can check that the matrix element decreases exponentially in n and the phase space grows exponentially in n . Thus the density of *these* resonances goes as $\omega^{-s(\gamma_0)\zeta(\gamma_0)}$. At low frequencies, this is a lower bound, whereas $1/\omega$ is an upper bound, assuming the stability of the MBL phase.

For the MBL phase to be stable, we need that a typical eigenstate is, at a typical real-space location, not involved in many resonances. From the discussion above, the typical accessible phase space for final states with a matrix element of ω goes as $\sim \omega^{-\phi}$; thus the typical level spacing for these goes as $\sim \omega^\phi$. In order that long-range resonances remain rare and do *not* destabilize the MBL phase, the matrix element must vanish faster than the typical level spacing in the long-distance, small ω limit. Thus $0 < \phi < 1$ (and thus $2 > \alpha > 1$) in the MBL phase, with ϕ increasing (thus α decreasing) as the phase transition to the thermal state is approached.

Note that the above analysis for the MBL-Mott conductivity does not rely on randomness of the system’s Hamiltonian. Thus we expect it to also apply to nonrandom MBL systems where the localization is due to spatial quasiperiodicity, such as discussed e.g. in Refs. [157, 279].

3.3.2 Rare-region Mott resonances

In the above discussion, we argued that the low-frequency conductivity in the MBL phase is dominated by rare many-spin resonances, and goes as $\omega^{2-s\zeta}$, where s and ζ are properties of the MBL phase (optimized over families of resonances parameterized by γ). However, in a disordered system, ζ is itself a random variable, so there will be atypical clusters in which (for example) the random fields are small and therefore the system is locally closer to the delocalization transition. (We focus on ζ but the same argument can be applied to any other parameter.) In such segments, ζ will take a local value ζ_{loc} that deviates from its typical value $\bar{\zeta}$, and the matrix element for resonances involving n spins will be atypically large.

These rare local “regions” occur with a probability $\sim \exp[-rf(\zeta_{\text{loc}})]$, where $f(\zeta_{\text{loc}})$ is a nonnegative “rate function” [86] that vanishes quadratically at $\zeta_{\text{loc}} = \bar{\zeta}$. By the above arguments the contribution of such a rare local resonance to the ac conductivity will be $\sim \omega^2$, while the number of spins flipped by the rare resonance is

$n \approx \zeta_{\text{loc}} \log(W/\omega)$ (which sets a minimum “size” for the rare region). Therefore the density of such rare resonances will be $\sim \omega^{(\zeta_{\text{loc}} f(\zeta_{\text{loc}}) - \zeta_{\text{loc}}^s)}$. Because the initial ‘gain’ in conductivity by going to these rare local resonances is linear in $(\zeta_{\text{loc}} - \bar{\zeta})$ while the probability ‘cost’ is only quadratic in the deviations from typical, the generic situation in the MBL phase of a system with quenched randomness is that the low- ω conductivity is dominated by rare many-body resonances in rare regions that are locally atypically close to the delocalization transition (i.e., have an atypically large ζ_{loc}).

When the system is deep in the MBL phase, the dominant contributions to the low frequency conductivity are from resonant clusters in regions that are themselves in the localized phase; we call this regime the “MBL-Mott” regime. In the low frequency limit in this regime, each resonant cluster is large compared to its local value of the localization length. As the transition to the thermal phase is approached, at some point before reaching the transition these dominant rare clusters become instead locally critical or thermal quantum Griffiths regions. We now turn to such rare-region Griffiths effects, and show that they give rise to a conductivity exponent that approaches $\alpha = 1$ at the critical point.

3.4 MBL-Griffiths regime

We shall eventually be concerned with both thermal and critical rare regions, but to set up our discussion we begin by considering an inclusion that is locally deep in the thermal phase, embedded in a typical insulating environment. This thermal inclusion is of volume V , has a many-body level spacing Δ that decreases exponentially with V and a transport time (i.e., Thouless time) t_{Th} that increases polynomially with V (specifically, as $V^{2/d}$ for a compact internally diffusive inclusion and with a larger power for a fractal or critical inclusion). In general, $t_{Th}\Delta \ll 1$ for large thermal

inclusions. (We expect this also to be true for critical inclusions in $d > 1$.) Moreover, each inclusion thermalizes its immediate insulating surroundings. Thus the inclusion consists of two parts: first, the ‘core’ of the inclusion which is the rare region that is locally thermalizing (or critical), and second, the typical insulating region surrounding this core, which gets strongly entangled with the core in the many-body eigenstates (we call this the ‘periphery’). A more thorough discussion of these inclusions is presented in Appendix A.

Now we consider the a.c. response of this inclusion, probed at a frequency $\omega \sim \Delta \ll 1/t_{Th}$. Because the core relaxes rapidly compared with ω , it essentially adiabatically follows the applied electric field, and its response is reactive rather than dissipative [154, 288]. Specifically, to leading order, the core response goes as $\sigma(\omega) \sim \omega^2 t_{Th}$, which is subleading at low frequencies to the many-body Mott contribution. Thus transport within thermal inclusion cores does not dominate the low-frequency conductivity.

However, the *periphery* of an inclusion with core level spacing Δ does contribute strongly to its conductivity at frequencies down to Δ , as we now argue. This periphery consists of typical MBL regions that experience the core as a finite bath [222, 162] to which they are coupled with matrix elements that fall off as $\sim \exp(-R/\tilde{\zeta})$ (where R is the distance from the core and $\tilde{\zeta}$ is a decay length). We can estimate the decay rate of a peripheral spin, using the Golden Rule, as $\gamma(R) \sim W \exp(-2R/\tilde{\zeta})$. So long as $\gamma(R) \gg \Delta$, the Golden Rule is valid on these time scales and the core does indeed act as a ‘bath’ for these spins. Far from the inclusion core, however, $\gamma(R) \ll \Delta$; a spin at this distance resolves the discreteness of core levels and does not decay into them. The overall picture is as follows (Fig. 3.2): The core (with level spacing Δ) is surrounded by ‘shells’ of continuously decreasing $\gamma(R)$, with the outermost ‘active’ shell having a decay rate $\gamma(R) \simeq \Delta$. Beyond this distance the system is insensitive to the presence of the thermal core and remains fully localized.

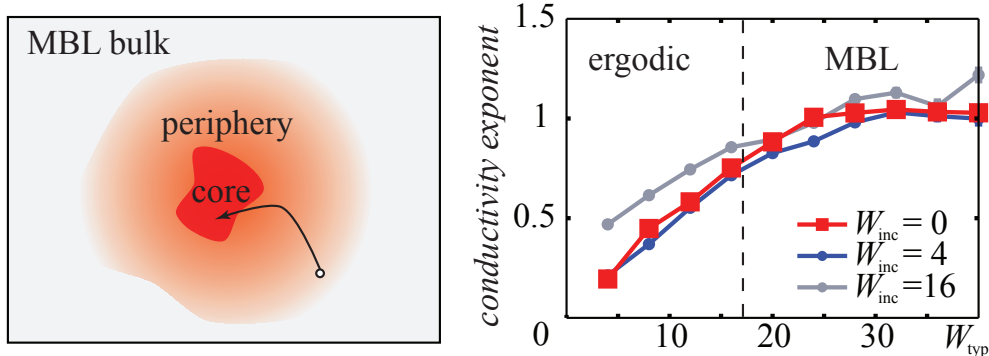


Figure 3.2: Left: schematic of the structure of a thermal inclusion in the MBL phase, showing its core (the microscopically rare thermal region), the periphery (the typical surroundings that get strongly entangled with the rare region), and the typical MBL surroundings where the core does not flip the local effective spins. Low-frequency transport occurs through transport between the periphery and the core. Right: numerically computed conductivity exponent α of an XXZ chain of size $L = 12$ with integrability-breaking next-to-nearest neighbor exchange coupling that contains a thermal or critical inclusion (i.e., a region that is locally thermal or critical) of four sites. W_{typ} is the typical value of disorder, and three different disorder values for the inclusion W_{inc} are shown. When the typical system is in the MBL phase ($W_{\text{typ}} > 8$), the conductivity exponent saturates to near one, consistent with the discussion in the main text.

This picture thus gives the behavior of the a.c. conductivity in the presence of a single such thermal inclusion. When one probes the system at a frequency $\omega \geq \Delta$, the conductivity is dominated by the shell at radius R_ω such that $\gamma(R_\omega) = \omega$. Shells closer to the core relax faster, and their response to a probe oscillating at ω is mainly reactive; meanwhile, shells that are farther do not respond at all at ω . The conductivity of the dominant shell is proportional to its Golden-Rule decay rate, so this shell gives $\sigma \sim \gamma(R_\omega) \sim \omega$ (up to $\log \omega$ factors due to size, dipole matrix element, etc.). The conductivity due to a single inclusion thus turns on at and above a frequency Δ and has the behavior $\sigma \sim \omega$ at intermediate frequencies. This reasoning extends directly to any inclusion whose core has an internal relaxation rate greater than its many-body level spacing, and is supported by numerical simulations (Fig. 3.2b) on inhomogeneous systems, in which thermal or critical inclusions are put

in by hand: the conductivity in the presence of an inclusion goes as $\sigma \sim \omega$ whenever the core is thermal or critical, as expected.

We now use the single-inclusion result to study the rare-region contribution to the a.c. conductivity of a generic MBL system, which contains some density of inclusions at all scales. The cores of these inclusions must be thermal, but there does not appear to be any constraint on how thermal they are, so the most common such cores of a given size will be cores that are locally arbitrarily close to the critical point. The inclusion cores that dominate the conductivity at low ω are thus rare locally critical regions with level spacing ω and consequently of volume $V \sim \zeta_c \log(W/\omega)$; the probability of such cores is therefore $\sim p^{\zeta_c \log(W/\omega)} \sim \omega^g$, where p is (heuristically) the probability that a unit-volume region is locally critical³. (One can define p more precisely as follows: the density of critical inclusions of volume V decreases exponentially with V , as p^V .) In the MBL phase $p < 1$, and p approaches one at the transition; thus the Griffiths exponent g , which is positive, approaches zero as the transition is approached. Since each such inclusion contributes $\sim \omega$ (up to logarithmic corrections) to the conductivity, the resulting conductivity of the Griffiths insulator goes as $\sigma \sim \omega^{1+g}$, where the Griffiths exponent g goes to zero at the critical point and rises smoothly in the MBL phase.

We briefly comment on how these Griffiths arguments connect with those in the thermal phase [8, 320]. In the MBL phase, as discussed above, thermal inclusions of large volume V become exponentially rare in V . On the thermal side, instead, it is *localized* inclusions that become exponentially rare at large scales. In one dimension, these rare localized inclusions act as transport bottlenecks, leading to a subdiffusive

³Here we are assuming that to make a rare inclusion core of volume V requires a number of rare “events” in the disorder configuration that is proportional to V . One can worry about the possibility that a fractal rare region with volume growing sublinearly in V can make an inclusion core of volume V by including nearby regions in to the core rather than the periphery (in the terminology of Appendix A). This scenario does not seem plausible to us.

Griffiths phase [8]. In higher dimensions, however, rare insulating regions in the thermal phase cannot block transport, and the d.c. conductivity is nonzero.

3.5 Transition between MBL-Mott and MBL-Griffiths regimes

The overall behavior of the low-frequency conductivity exponent α is shown in Fig. 3.1: everywhere in the MBL phase $1 < \alpha < 2$. Near the MBL phase transition, critical and thermal inclusions proliferate and the dominant mechanism is “Griffiths”; far from the MBL transition, such inclusions are too rare, and the dominant contributions to conductivity are instead from rare many-body Mott resonances within locally insulating regions (which are still less insulating than the *typical* region). These regimes transition into each other as follows: Within the “MBL-Mott” phase the dominant regions are still locally insulating; as one moves towards the transition, these dominant regions become less insulating. Eventually, before the MBL phase transition, the dominant regions become critical, and the system enters the “MBL-Griffiths” phase. Throughout the MBL-Griffiths phase, the dominant rare regions remain critical, and only their prevalence changes: as the critical point is approached, these rare critical regions become more common, and eventually proliferate. Thus the physics underlying the evolution of the conductivity exponent is qualitatively different in the two regimes, and we expect that the exponent is nonanalytic (though perhaps quite smooth) at the “Mott-Griffiths” transition between these two regimes. The location of the Mott-Griffiths transition line in Fig. 1 is schematic—determining the location of this transition within the MBL phase remains an interesting direction for future work.

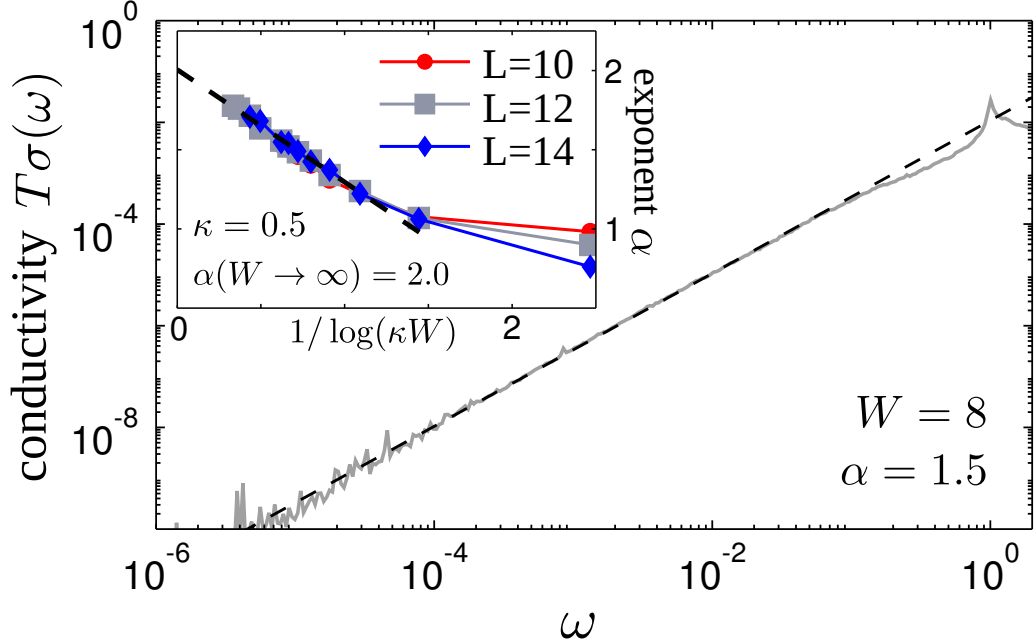


Figure 3.3: Main panel: conductivity as a function of frequency in the random field XXZ chain for system size $L = 14$ and disorder bandwidth $W = 8$, showing multiple decades of power-law behavior. Inset: behavior of the conductivity exponent deep in the MBL phase is consistent with the many-body Mott prediction (see main text) that $2 - \alpha \sim \zeta$, combined with the perturbative estimate $\zeta \sim 1/\log(W/J)$.

3.6 Numerical simulations

We have checked these expectations against simulations of the conductivity in the random-field XXZ chain, governed by the Hamiltonian

$$\hat{H} = \frac{J}{2} \sum_{\langle ij \rangle} (\hat{S}_i^+ \hat{S}_j^- + \text{h.c.}) + J_z \sum_i \hat{S}_i^z \hat{S}_{i+1}^z + \sum_i h_i \hat{S}_i^z, \quad (3.6)$$

where h_i is a local quenched random field drawn uniformly from $[-W, W]$, J is the spin exchange energy scale, and J_z the spin-spin coupling strength. We measure energies in units of J ; in all presented data, we also take $J_z = J = \hbar = 1$. We diagonalize the full Hamiltonian to calculate the conductivity $\sigma(\omega)$ at infinite temperature using Eq. (3.1) by binning it on a logarithmically spaced frequency grid which typically ranges from $\omega = 10^{-6}$ to 2. In Figs. 3.1 and 3.3 we have only nearest-neighbor exchange, while we

also have second-neighbor exchange of strength $J' = 1$ in Fig. 3.2. The rationale for the latter choice is that, while next-nearest neighbor exchange interactions exacerbate finite-size effects, they also break integrability and make the disorder-free delocalized phase behave thermally, even for relatively small system sizes. Thus they are essential for correctly simulating small thermal inclusions with $W_{\text{inc}} = 0$.

The conductivity exponent α , shown in Fig. 3.1, has been extracted from power-law fits to the low frequency response that hold over multiple decades, see Fig. 3.3 main panel for the example of $W = 8$ which yields $\alpha \sim 1.5$. The numerical results further confirm that the conductivity exponent $\alpha = 1$ at the MBL transition and that it asymptotes to $\alpha \sim 2$ in the strong disorder limit, see inset of Fig. 3.3. A more detailed discussion of some numerical issues and a comparison between noninteracting and many-body insulators is given in Appendix B.

3.7 Experimental aspects

The predictions in our work concern the finite-time dynamical properties of MBL systems; thus, they are robust against weak coupling to an external bath, which is present in all physical systems [222]; so long as $\omega > \Gamma$, where Γ is the bath-induced linewidth, the bath will not change these conductivity power laws. Therefore our predictions for conductivity can be tested experimentally, both in solid-state systems [231] and in ultracold atomic systems [279]. In electronic systems, a.c. conductivity is straightforward to measure, but the long-range nature of the Coulomb interaction will modify several of our conclusions.

In principle one can also measure a.c. conductivity in ultracold atomic systems such as optical lattices by applying a periodically modulated tilt to the entire lattice [101]. However, in the current optical-lattice MBL experiments [279] it is more convenient to study relaxation in the time domain; we now show how our results gener-

alize to such experiments. (Note: Ref [279] used a quasiperiodic potential, while here we mostly consider instead systems with quenched randomness. For the quasiperiodic systems the MBL-Mott regime should still be present, as discussed above; whether the MBL-Griffiths regime exists is unclear, however.) In general, these experiments involve creating a particular nonequilibrium initial configuration and measuring the evolution of its “contrast” (i.e., the overlap between final and initial deviations from thermal equilibrium). Note that the following analysis of the real time relaxation does not rely on there being a conserved density, so also applies to Floquet systems with no such transport. In the MBL phase, this contrast (which we denote $C(t)$) approaches a nonzero saturated value C_∞ ; we argue that it does so at long time t as

$$C(t) - C_\infty \sim t^{1-\alpha}, \quad (3.7)$$

where $\alpha > 1$ is the a.c. conductivity exponent discussed here and plotted in Fig. 3.1. This result holds in both the MBL-Mott and MBL-Griffiths regimes. In the Mott regime, at time t , resonant pairs of configurations with splitting $\lesssim 1/t$ are still in their initial state and retain their initial density deviation, whereas faster pairs oscillate and thus have “forgotten” their initial density deviation. Counting all Mott pairs with splitting $\lesssim \omega$, using the arguments above, we find that these go as $\omega^{1-\phi} = \omega^{\alpha-1}$, which gives Eq. (3.7). Likewise, in the Griffiths regime, the contribution at time t is due to the peripheral spins of inclusions with core level spacing $\Delta \lesssim 1/t$. The density of such inclusions is $\sim \Delta^{\alpha-1}$, which once again yields the result (3.7). Note that this decay becomes very slow as the transition is approached: the exponent $(1 - \alpha)$ goes to zero at the transition. These arguments apply to the long time behavior when $C(t)$ is near C_∞ ; the earlier time regime near the critical point when C_∞ is small should be governed by the dynamical critical behavior. Preliminary numerical simulations on XXZ chains suggest that, deep in the MBL phase, these contributions

might be difficult to detect in experiment, as their amplitude is small compared with steady-state fluctuations of the contrast in finite systems.

3.8 Discussion

In this chapter we have argued that the low frequency a.c. conductivity in the MBL phase goes as $\sigma(\omega) \sim \omega^\alpha$, with $1 \leq \alpha < 2$ throughout the phase, and $\alpha \rightarrow 1$ as the delocalization transition is approached. Deep in the MBL phase, the dominant processes involve transitions between rare configurations, in rare regions that are localized but have an anomalously large localization length. Near the transition, the dominant rare regions are locally thermal or critical instead. The power-laws we expect on general grounds are consistent with those seen in numerical results for the random-field XXZ model. We emphasize that the power laws we find in the optical conductivity are not related to those predicted for electron glasses [286, 81]: we are considering high-temperature behavior (i.e., $\omega \ll T$) in models with short-range interactions, whereas those works consider low-temperature behavior (i.e., $\omega \gg T$) in models with Coulomb interactions.

We conclude with some comments on the scope of our results. As already discussed above, our analysis of a.c. transport directly extends to relaxation dynamics. Moreover, our results here should also describe, e.g., thermal transport, in systems where the only conserved quantity is the energy. However, our analysis of the conductivity relies on the fact that the conductivity is related to the spectral function of a *current* (i.e., a quantity associated with a globally conserved charge) and does not extend to generic spectral functions, such as those probed using optical lattice modulation spectroscopy [101]. In fact for more general local spectral functions, the operator's matrix element between states within a MB Mott or Griffiths resonance is

not restricted to vanish in proportion to ω so may remain of order one, resulting in a divergent low-frequency spectral function $S(\omega) \sim \omega^{(\alpha-2)}$ in the MBL phase.

Our analysis also depends on both the disorder correlations and the interactions being short-range. Specifically, we assume that the effective interactions that mediate many-body resonances fall off exponentially with distance and with the number of effective spins involved. Thus our conclusions are modified in an essential way when the interactions instead fall off as a power law of distance; this case will be treated elsewhere. It is not presently clear whether or not the stretched-exponential effective interactions that occur at putative critical points within the MBL phase [318, 149, 239, 254, 307] substantially modify the above story. Also, our analysis of near-transition behavior assumes that the delocalized phase is thermal, and thus may not apply to hypothesized transitions between an MBL phase and a nonthermal delocalized phase [84, 127, 67].

3.A Structure of a thermal inclusion

A thermal inclusion core (i.e., a large region with rare microscopic parameters) in the MBL phase acts as a local, discrete “bath” for the peripheral insulating material around it. Thus, in the many-body eigenstates it is strongly entangled with the nearby (“peripheral”) typical regions. Because the inclusion is finite, sufficiently far from it the MBL phase with area-law eigenstate entanglement re-establishes itself. In this Appendix we discuss how this crossover takes place.

A naive estimate (which will turn out to be largely correct) is as follows: If one ignores the discreteness of the bath levels, a Golden Rule estimate [222] suggests that the decay rate of a typical degree of freedom (which for convenience we shall call a spin) a distance R from the inclusion core is $\sim \exp(-2R/\tilde{\zeta})$ where the decay length $\tilde{\zeta}$ remains finite as the MBL transition is approached. This rate must be compared with

the many-body level spacing $\Delta \sim e^{-\bar{s}V}$ of the inclusion core; when this putative decay rate is smaller than the many-body level spacing, the inclusion is actually unable to act as a bath [222] and no decay takes place. Thus, an inclusion core of *volume* V is surrounded by a thermal periphery of *linear size* $\sim V$. The characteristic relaxation rate decays from its value at the center of the core (which is of order the bandwidth for a strongly thermal inclusion) to its value at the edge of the periphery, which is $\sim \Delta$.

However, this argument is evidently incomplete. When the inclusion core thermalizes a spin, on sufficiently long time scales this additional spin is also “thermal”, and thus naively might be thought able to act as a bath for other, more distant, spins. If one iterates this reasoning, however, one arrives at an obviously incorrect result: an inclusion core of linear size L thermalizes a region of linear size $\sim L^d$ around it; and the combined level spacing of this full thermalized region is now $\sim e^{-sL^{d^2}}$ (s being the thermal entropy per spin), which naively allows it to thermalize yet further regions, and so on, until the entire MBL system is thermalized. To avoid this conclusion, one must understand why these peripheral regions that are “thermalized” by the core cannot act as a bath for more distant insulating regions.

One can see this as follows: Let us first remove all couplings that cross the boundary between the thermal inclusion core and the periphery. Then the Hamiltonian of the now MBL peripheral region can be written in terms of l-bits, in terms of which it takes the fully diagonal form $H = \sum_i h_i \tau_i^z + J_{ij} \tau_i^z \tau_j^z + \dots$; the thermal inclusion core is, of course, described by a generic thermalizing Hamiltonian. Now we reinstate the boundary couplings; these are local in terms of the physical spins, and thus generally consist of a strictly local physical operator O on the MBL side of the boundary, coupled to an operator on the thermal side. The operator O involves l-bit flips at all distances, but contributions from distant l-bits are exponentially suppressed. Because the intrinsic l-bit Hamiltonian is purely diagonal, an l-bit at a distance $l \gg \tilde{\zeta}$ from

the boundary can only thermalize through its exponentially weak contribution to the operator O ; in particular, the nearer l-bits do not act as a bath, and the ability of an inclusion to thermalize its surroundings is determined by the size of its core.

3.B Details of conductivity numerics

In this section, we discuss some of the subtler issues involved in numerically extracting the conductivity exponents. We begin with a discussion of finite-size effects and boundary conditions. We then compare our many-body a.c. conductivity numerics with a study of single-particle (i.e., noninteracting) insulators at similar system sizes. We find that the size- and disorder-dependence of the many-body conductivity is consistent with theoretical expectations, and qualitatively different from that of the single-particle conductivity. Finally, we present data elucidating the nature of transitions contributing to the low-frequency conductivity.

Boundary conditions and finite-size effects

In numerics on finite systems, the conductivity exponents discussed here only occur at intermediate frequencies, $\omega_L \ll \omega \ll J$, where $\omega_L \sim \exp(-L/\zeta)$ in the MBL phase [or $\exp(-L/\xi)$ in the single particle case] is a size-dependent low-frequency cutoff. ω_L sets the scale for level repulsion between states or configurations that differ on length scales on the order of the system size. The behavior below this frequency scale depends on whether the boundary conditions are open or periodic. In the case of open boundary conditions, the conductivity at the lowest frequencies goes as $\sigma(\omega) \sim \omega^3$. As in the Mott argument, two factors of ω are due to the current matrix element, which is constrained by the boundary conditions to vanish as ω at low frequencies. The third factor is due to level repulsion in the Gaussian Orthogonal Ensemble [288], and captures the phase space of pairs of states with these very small energy differences.

For periodic boundary conditions, on the other hand, the conductivity in the finite-size-dominated regime scales as $\sigma(\omega) \sim \omega$. In that case, there is still a factor of ω from level repulsion, but the current matrix elements do not vanish in the limit of low frequencies, because these currents “wrap around” the system and hence do not build up large charge imbalance even when they are at very low frequency. (The distinction between the two kinds of boundary condition can be intuitively understood by contrasting the behavior of (a) a finite metallic grain embedded in an insulator and subject to spatially uniform a.c. electric field, and (b) a conducting ring with an a.c. magnetic flux through it. The response of the former becomes essentially dielectric in the limit of low frequencies, whereas that of the latter remains dissipative.)

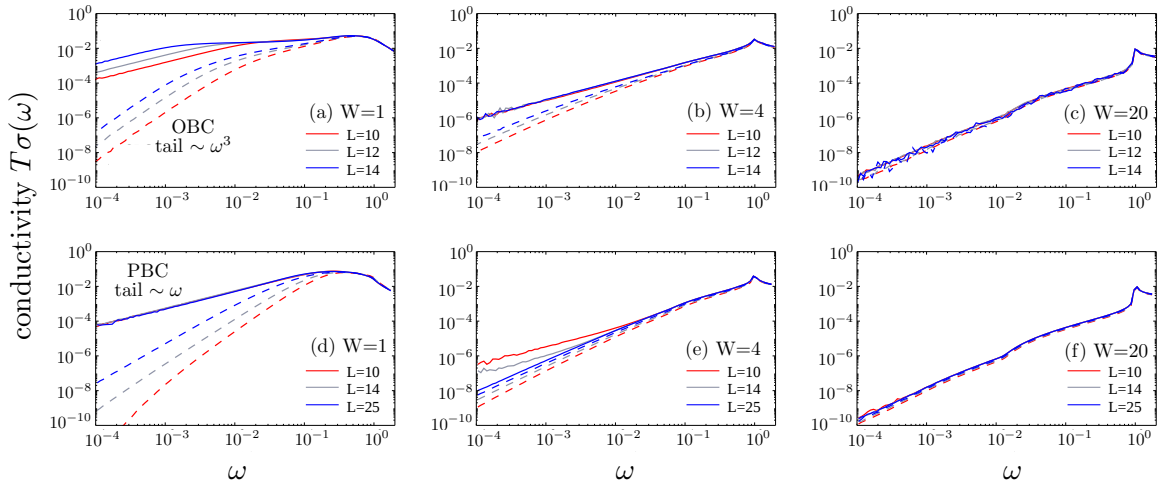


Figure 3.4: (a)-(c) Frequency-dependence of a.c. conductivity in the interacting system with periodic and open boundary conditions (solid and dashed lines respectively) for three values of disorder W , corresponding to the thermal phase (left), near-critical regime (center), and deeply localized phase (right). The lowest-frequency finite-size behavior in the thermal regime goes as $\sigma \sim \omega$ for periodic boundary conditions and $\sigma \sim \omega^3$ for open boundary conditions, as discussed in the text. (d)-(f) Frequency dependence of a.c. conductivity in noninteracting systems, for disorder values corresponding to those in panels (a)-(c). Again, solid lines represent periodic boundary conditions and dashed lines represent open boundary conditions.

This finite-size dominated regime is clearly seen in numerical simulations on the many-body system in the thermal regime [Fig. 3.4(a)]. Deep in the localized regime, $\sigma(\omega)$ is insensitive to boundary conditions in the frequency range we can access [Fig.

3.4(c)]; the finite size effects presumably appear only at even lower frequency $\omega_L \sim \exp(-L/\zeta)$. In the near-critical regime ($W = 4$), where α is near one, the finite-system behaviors for open and periodic boundary conditions are qualitatively different [Fig. 3.4(b)]: For periodic boundary conditions, the low frequency regime due to the finite size effect is expected to also have $\alpha = 1$. No finite size effect is apparent at $W = 4$ for periodic boundary conditions, which is possibly a consequence of the finite size regime having essentially the same scaling as the “bulk” regime. On the other hand, for open boundary conditions the low frequency finite size regime will have an effective exponent $\alpha_{\text{eff}} = 3$. The beginnings of the crossover in to this regime are apparent in Fig. 3.4(b), and we can see the results are converging with increasing L towards the periodic boundary condition results.

The analogous results for noninteracting systems are shown in Fig. 3.4(d)-(f). Deep in the localized phase at $W = 20$ the conductivity at these frequencies is dominated by short distance single-particle hops, so the interacting and noninteracting systems look similar and neither show finite-size effects. At $W = 4$, on the other hand, we see clear differences. The effective exponent α for the noninteracting system is well above one, so now the finite size effects are quite apparent for periodic boundary conditions.

These considerations can be sharpened by comparing the conductivity exponents extracted from the many-body (MB) interacting and single-particle (SP) noninteracting data, as shown in Fig. 3.5 (left). We consider systems with open boundary conditions, and extract the conductivity exponent from a fixed frequency range that is much smaller than the scales $J^2/W, J^3/W^2$ associated with short-distance hops. From our previous discussion, we expect that the limiting behavior for very small disorder is $\sigma \sim \omega^3$ (because of finite size effects), whereas that for large disorder is $\sigma \sim \omega^2$ (as finite size effects move to much lower frequencies and the Mott behavior is recovered). In the single-particle case, one expects the exponent α to cross over

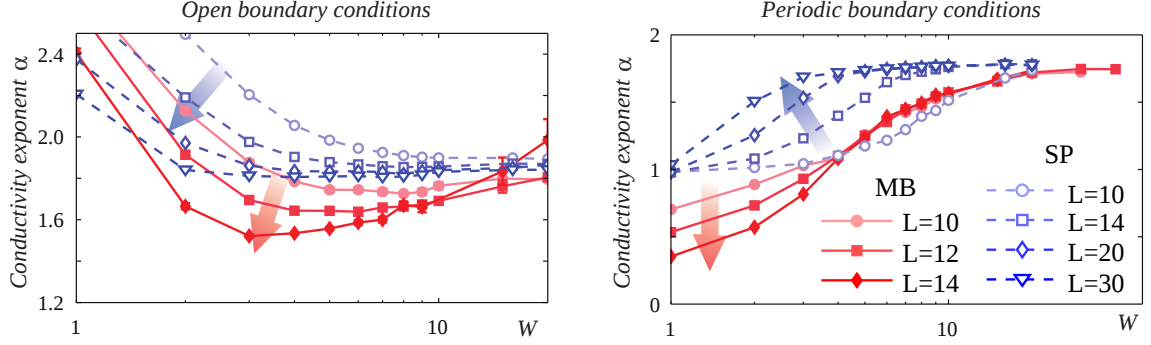


Figure 3.5: Conductivity exponent for interacting spin chains (solid red lines) and the corresponding noninteracting chains (dashed blue lines) as a function of disorder W , for various system sizes. The left panel shows data for open boundary conditions (OBCs); the right panel, for periodic boundary conditions (PBCs). Exponents are extracted from the frequency regime $10^{-4} \leq \omega \leq 5 \times 10^{-3}$ [OBC] and $10^{-4} \leq \omega \leq J^2/(4W)$ [PBC]. Arrows indicate the evolution of the exponent with increasing system size. For OBCs, the exponent crosses over from the finite-size value $\alpha = 3$ to the Mott value $\alpha \simeq 2$ with increasing disorder. The crossover is nonmonotonic for interacting systems but monotonic for noninteracting systems, as discussed in the text. For PBCs, noninteracting systems again exhibit a monotonic crossover from the finite-size exponent $\alpha = 1$ to the Mott exponent $\alpha = 2$. However, the exponent for interacting systems drops well below the finite-size value $\alpha = 1$, in the regime where these systems are thermal. Moreover, finite-size effects on α seem negligible throughout the MBL phase.

smoothly from a disorder-independent value slightly below 2 – on account of the logarithmic correction in Mott’s law – toward 3, and thus to increase monotonically as the disorder is decreased. On the other hand, for MBL, we expect that as the disorder is decreased two competing effects occur: the exponent decreases towards 1 for the reasons discussed in the main text; on the other hand, it is also pulled up toward 3 by finite-size effects. Thus, we expect it to exhibit a non-monotonic U-shaped disorder-dependence with a minimum near the MBL transition. These expectations are borne out by the numerical data (Fig. 3.5): the dip of the many-body exponent below 2 becomes *stronger* for larger system sizes, approaching the value for periodic boundary conditions, and thus supporting the view that the true exponent for the many-body case is disorder-dependent and dips well below 2.

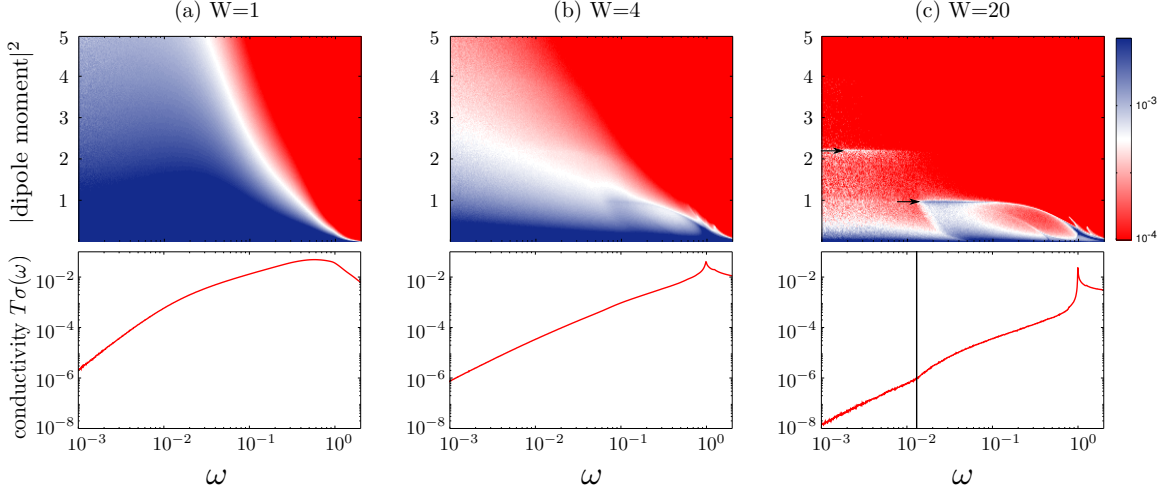


Figure 3.6: Distribution of squares of dipole moment matrix elements (i.e., $|\langle n | \sum_j j S_j^z | m \rangle|^2$) contributing to the conductivity at each frequency, for disorder corresponding to thermal phase (left), critical region (center), and MBL phase (right), all with open boundary conditions. In (c) the arrows mark the peaks corresponding to two-site and three-site hops in the MBL phase (see text); we expect the n -site peak to vanish at a frequency $\sim 1/W^{n-1}$, giving rise to a “shoulder” in the conductivity. Lower panel: frequency-dependence of the conductivity. Note that the different regimes of behavior in $\sigma(\omega)$ can be matched with features in the dipole moment distribution.

As a final point of comparison, Fig. 3.5 (right) shows the conductivity exponents for several different system sizes and as a function of disorder, extracted from the data with periodic boundary conditions. For these exponents, we do the fit over several decades of data between ω_L and the microscopic scales J^2/W . Thus, these exponents can be directly compared to the analogous MB ones plotted in Figs. 3.1 and 3.3. We see that for any given system size, the SP data look qualitatively similar to the MB data, showing a monotonic increase from the finite-size dominated exponent $\alpha \sim 1$ at low disorder (note that $\alpha \sim 1$ at the MB transition due to a completely different physical mechanism) to an exponent approaching 2 at larger disorders. However, unlike the MB system, the SP effective exponents are strongly finite-size dependent and approach a constant W -independent value on increasing system size. On the other hand, the MB exponents show no system size dependence in the localized phase

and converge to W -dependent values (significantly less than 2 for moderate disorder), further supporting our claim that the MB exponents are not finite-size effects.

Nature of transitions contributing to conductivity

We conclude with some details about the structure of the eigenstates contributing to the conductivity. The conductivity always exhibits a sharp feature near $\omega = 1$, which is due to nearest neighbor resonances. For strong disorder (Fig. 3.4c), the conductivity also develops a noticeable “shoulder” at a frequency $\omega \sim J^2/4W$ due to second-neighbor resonances. For frequencies above this shoulder, the dominant processes are these very short range hops and the power law fit does not work, not surprisingly. This can be seen by looking at the distribution of dipole moment matrix elements, Fig. 3.6, of transitions contributing to σ : above the shoulder in (c), a peak appears at about unity, corresponding to second-neighbor resonances, which is marked by the bottom horizontal arrow. Third-neighbor resonances can also be seen as a feature near $(3/2)^2 = 2.25$, indicated by the upper horizontal arrow. Data at lower values of W show more such peaks, but these “shoulders” become less and less pronounced until they disappear altogether for $W \lesssim 8$.

Part III

Eigenstate Order in Many-Body Localized Systems

Chapter 4

Many-body Localization and Symmetry Protected Topological Order

4.1 Introduction

In this chapter and the next two, we extend the notions of localization protected eigenstate order discussed in Section 1.6. As shown in Ref. [149], the eigenstates of MBL systems can spontaneously break or preserve global symmetries and exhibit or fail to exhibit topological order; these phenomena could violate the naive expectation from Peierls-Mermin-Wagner type arguments. Essentially, the localization of defects allows order to persist at energy densities where equilibrium arguments predict destruction of order.

In this chapter we extend the analysis of Ref. [149] to a case intermediate between symmetry-breaking and topological order. This is the case of symmetry protected topological order (SPT) [129, 73, 109, 280], wherein a symmetry is needed for the phase to exist but the order itself is topological in nature and cannot be characterized

by a local order parameter. Clean zero temperature SPT phases have a bulk gap to well-defined excitations whose quantum numbers are not fractional. Furthermore, SPT ground states cannot be continuously connected to trivial product states without either breaking the protecting symmetry or closing the energy gap; however, such a continuous path must exist if the protecting symmetry is explicitly broken. The canonical example of an SPT phase is the Haldane phase in $d = 1$ [130, 131] and the most celebrated one is by now surely the Z_2 topological insulator in $d = 3$ (reviewed in Ref. [133]).

With this background, we can now state our central question: Can highly excited eigenstates exhibit SPT order in the presence of MBL? We take such order to generalize the cluster of properties listed above. Specifically, we wish to examine Hamiltonians invariant under a protecting symmetry with highly excited eigenstates that lie in a mobility gap. We will require an eigenstate phase transition (at which the properties of the eigenstates change in some singular fashion) between the SPT region and the trivial region, which is well captured by product states as long as the protecting symmetry is intact. Further, there should be a path along which such a phase transition is absent when the symmetry is explicitly broken.

In the following, we address this question via two examples. The first is the Haldane phase protected by a discrete symmetry. We present strong evidence that the SPT order extends in an MBL version to highly excited eigenstates even though equilibrium considerations preclude such order. We do so by introducing an appropriate generalization of the AKLT model of Affleck, Kennedy, Lieb and Tasaki [6, 7] that allows the arguments of BAA to be brought to bear on highly excited states. We discuss various diagnostics of the Haldane phase that extend to this regime. We also note that the Haldane phase with continuous $SU(2)$ symmetry does not obviously extend to an MBL version and explain the obstacles involved in settling this question. Our second example is the topological Ising paramagnet in two dimensions [202, 74]. Here

again we adapt the BAA arguments to establish MBL and discuss the diagnostics needed to establish SPT order. We conclude with some comments on generalizations and open questions.

4.2 Haldane phase

4.2.1 Review of low energy physics

We begin with the Haldane phase of the spin-1 antiferromagnetic chain. Although usually understood in the context of continuous rotational symmetry¹, the Haldane phase is an SPT which may be protected by any one of the following discrete symmetries: inversion, time reversal or the dihedral group D of π -rotations around the x, y, z -spin axes [33, 250, 248]. At zero temperature, the clean phase is a gapped quantum spin liquid which breaks none of these symmetries. It has several defining characteristics. First, the bulk exhibits simultaneous long-range “string” order [87, 166] in the operators ($\alpha = x, y, z$)

$$\sigma_{ij}^\alpha = -S_i^\alpha \left(\prod_{k=i+1}^{j-1} R_k^\alpha \right) S_j^\alpha \quad (4.1)$$

where $R_j^\alpha = e^{i\pi S_j^\alpha}$ represents a rotation by π around the α spin axis of site j and S_i^α are the usual spin-1 operators. Second, the boundary exhibits protected spin-1/2 edge modes as a consequence of which the ground state is four-fold degenerate on open chains. Third, the presence of the protected spin-1/2 edge modes implies a two-fold degeneracy in the entanglement spectrum for virtual (Schmidt) cuts in the bulk of the chain. Further, the underlying spin-1 degrees of freedom do not fractionalize in the bulk, in consonance with the definition of an SPT. The low energy excitations are gapped spin-1 bosons called ‘triplons’, discussed later in the text. In contrast, in

¹It is interesting to note that Haldane discovered the phase that bears his name studying a dihedral-symmetric perturbation of the SU(2) invariant spin chains.

the trivial phase with the same discrete symmetries, the ground state can always be smoothly connected to a product state through a symmetric path [250]. The trivial phase has no string order, boundary modes or degenerate entanglement spectra; hence these properties signal the SPT order of the Haldane phase.

4.2.2 Ergodicity and localization in highly excited states

In the following, we will review how these signatures of the Haldane phase disappear at $T > 0$ in clean systems as a consequence of the delocalization of the triplons in highly excited states. On the other hand, in the presence of sufficient disorder, we will argue that individual triplons Anderson localize. At sufficiently small, but non-zero, energy density, the dilute gas of localized triplons interacts only weakly so that the perturbative arguments of BAA apply and the system is many-body localized. Finally, we will discuss how various defining characteristics of the Haldane phase persist to finite energy density in a suitably modified form in this MBL phase.

To be concrete, we introduce a frustration-free model for the Haldane phase. As the SPT order requires only the dihedral group $D = \{\mathbf{1}, R^x, R^y, R^z\} \equiv \mathbb{Z}_2 \times \mathbb{Z}_2$ to protect it, our model has precisely this symmetry, but is otherwise very closely related to the celebrated $O(3)$ -symmetric AKLT model [6, 7]. The Hamiltonian, which we refer to as the BKLT Hamiltonian, is

$$H_{BKLT} = \sum_{i,\alpha} P_{i,i+1}^{(2)} \left(J_i + c_i^\alpha (S_i^\alpha + S_{i+1}^\alpha)^2 + d_i^\alpha (S_i^\alpha + S_{i+1}^\alpha)^4 \right) P_{i,i+1}^{(2)} \quad (4.2)$$

where $P_{i,j}^{(2)}$ projects onto the spin-2 representation of the spins i and j , and $J_i, c_i^\alpha, d_i^\alpha > 0$ are coupling constants². The ground state space of H_{BKLT} is identical to that of the AKLT model: there are four ground states on open chains, each of which possesses an

²If $c_i^\alpha, d_i^\alpha > 0$, then each term is strictly positive. Note that in the spin-2 representation, the coupling constants are not all independent as $(S_i^\alpha + S_{i+1}^\alpha)^2 = 6$. Taking c_i^α, d_i^α to zero reduces BKLT to the traditional AKLT model.

explicit, compact matrix product state (MPS) representation simultaneously annihilated by all $P_{i,i+1}^{(2)}$ and therefore by H_{BKLT} . The excitation gap is of order J_i and the eigenstates may be labeled by the one-dimensional representations of $\mathbb{Z}_2 \times \mathbb{Z}_2$. Even though the ground states are exactly known, H_{BKLT} is not fully integrable. Its excited states should therefore be generic with respect to thermalization and many-body localization.

The A/BKLT ground states can be constructed by splitting each spin 1 site into two virtual spin 1/2 degrees of freedom. Pictorially,

$$|A; v_L, v_R\rangle = \begin{array}{c} \left. \vphantom{v_L} \right\} v_L \quad \left. \vphantom{v_R} \right\} v_R \\ \text{Diagram: A chain of four ovals, each containing two small circles. Solid lines connect the small circles of adjacent ovals. The first oval has a curly brace labeled } v_L \text{ above it, and the last oval has a curly brace labeled } v_R \text{ above it.} \end{array} \quad (4.3)$$

where each small circle represents a virtual spin 1/2, the solid lines denote singlet pairings and the ovals the symmetrization to reproduce a spin 1 physical degree of freedom. Here, v_L and v_R are the state vectors for the boundary spins that label the four-dimensional ground state space on the open chain. This picture immediately reveals the physical origin of the spin 1/2 boundary modes – they correspond to the unpaired virtual degrees of freedom left on either end of the open chain. The picture also suggests the origin of the 2-fold degeneracy in the entanglement spectrum as the cutting of the virtual Bell pair shared by a link.

The virtual spin structure of the A/BKLT state suggests a natural candidate for the low energy bulk excitations,

$$|j, \alpha\rangle = \begin{array}{c} \text{Diagram: A chain of four ovals, each containing two small circles. Solid lines connect the small circles of adjacent ovals. The second link (between the second and third ovals) is represented by a double line, labeled } j \text{ below it.} \end{array} \quad (4.4)$$

where the double line at bond j indicates a virtual pair in triplet state α . Note that we have suppressed the explicit boundary spin states v_L, v_R . The single ‘triplon’ states $|j, \alpha\rangle$ are non-orthogonal but linearly independent. They span the manifold studied in the single-mode approximation (SMA) provided by S_j^α operators acting

on $|A\rangle$ [19]³. These states are believed to be good variational approximations to the local excitations of H_{AKLT} , in part because the SMA calculations produce a single triplon band quantitatively in good agreement with numerical studies [19]. We note in passing that the bond triplon states provide a superior framework for the study of excitations in higher dimensional valence-bond solid states as well, where the SMA is inadequate.

In the $O(3)$ symmetric AKLT case, the three triplon states $|j, \alpha\rangle$ are strictly degenerate. Breaking the $O(3)$ symmetry down to the dihedral subgroup, as in BKLT, lifts the degeneracy and selects the dihedral-symmetric states $|x\rangle, |y\rangle, |z\rangle$ as an appropriate basis. In terms of virtual spins,

$$\begin{aligned} |x\rangle &= (|\uparrow\uparrow\rangle - |\downarrow\downarrow\rangle)/\sqrt{2} \\ |y\rangle &= (|\uparrow\uparrow\rangle + |\downarrow\downarrow\rangle)/\sqrt{2} \\ |z\rangle &= (|\uparrow\downarrow\rangle + |\downarrow\uparrow\rangle)/\sqrt{2} \end{aligned}$$

where $|x\rangle$ has eigenvalues $+1, -1, -1$ under R^x, R^y, R^z , $|y\rangle$ has $-1, +1, -1$ and $|z\rangle$ has $-1, -1, +1$. The reader should recognize that dihedral symmetry has picked out the maximally entangled Bell states!

Consider now the three diagnostics of the Haldane phase in the presence of a maximally localized triplon. (i) As the virtual spins in $|j, \alpha\rangle$ form a Bell state across every bond, the entanglement spectrum exhibits two-fold degeneracy across any real space cut. It is straightforward to confirm this using the explicit MPS representation of $|j, \alpha\rangle$ following from Eq. (4.4). (ii) The triplon excitation produces a topological

³On a periodic chain of length L , there are L linearly independent bond triplons as we have defined them. The spin operators S_j^α create superpositions of the form $S_j^\alpha |A\rangle \propto |j, \alpha\rangle - |j-1, \alpha\rangle$ and thus there are only $L-1$ linearly independent states in the traditional SMA calculation.

defect in the string order parameter σ_{ik}^β . Explicitly,

$$\langle j, \alpha | \sigma_{ik}^\beta | j, \alpha \rangle = \begin{cases} -(-1)^{\delta_{\alpha\beta} \frac{4}{9}} & i \leq j < k \\ \frac{4}{9} & \text{else} \end{cases} \quad (4.5)$$

That is, if the string operator crosses the triplon, it picks up a minus sign unless the flavors of the string and the triplon agree. (iii) On open chains, there remain four degenerate, linearly-independent variational states corresponding to the choice of boundary conditions (v_L, v_R) for the localized triplon state $|j, \alpha\rangle^4$.

The demise of the Haldane phase at finite energy density in the clean system is now apparent. Diagonalizing H_{BKLT} in the variational single triplon manifold gives rise to three delocalized bands of triplons corresponding to each of the flavors α . This follows from solving the generalized eigenvalue problem where H_{BKLT} is purely diagonal in the localized triplon basis while the overlap matrix $\langle j, \alpha | k, \beta \rangle \sim \delta_{\alpha\beta} (1/3)^{|j-k|}$ produces the off-diagonal dispersion. At low energy densities, we expect a dilute gas of these delocalized triplons in the eigenstates of H_{BKLT} . This fluctuating gas (i) produces an extensive entanglement entropy for macroscopic domains which precludes an MPS representation for the highly excited eigenstates and washes out the two-fold entanglement degeneracy. (ii) As the triplons act as defects in the string order Eq. (4.1), their spatial fluctuations suppress this order on the length scale of the inverse density. Finally, (iii) the spin-1/2 boundary modes decohere due to interaction with the delocalized bulk triplons on a time scale set by the density of triplons. This is all consistent with the expectation that there is no order, topological or otherwise, at finite temperature in one dimension.

⁴The issue of linear independence for bond triplon states is somewhat delicate. On an open chain of length L , there are naively $12(L-1)$ triplon states corresponding to the 4 boundary states, 3 triplon flavors and $L-1$ positions. These span only a $12(L-1) - 4$ dimensional space. On a closed chain, there are $3L$ linearly independent states.

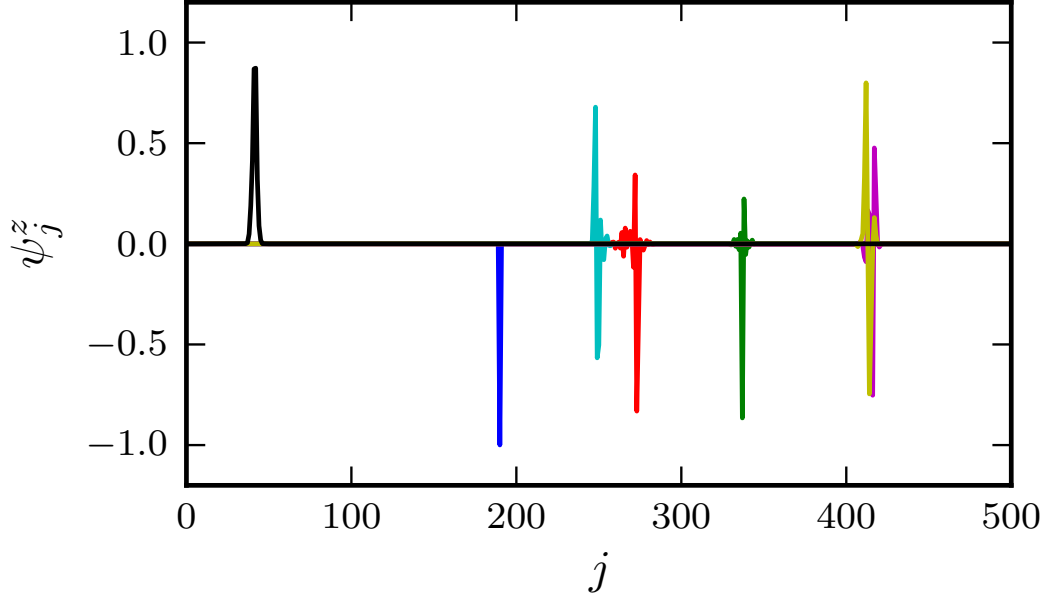


Figure 4.1: Seven typical eigenmodes of the Anderson problem in the single $\alpha = z$ triplon manifold in a 500-site chain with periodic boundary conditions. The coupling constants J_i are drawn uniformly from the interval $(0, 1)$.

The presence of sufficient disorder leads to an entirely different picture of the highly excited eigenstates – that they may many-body localize and thus retain their SPT character. Consider the introduction of disorder in the couplings of H_{BKLT} . So long as $J_i > 0$, the ground state is completely unperturbed by this variation, which is an extreme manifestation of the insensitivity of gapped phases to weak spatial disorder. The excitation spectrum, on the other hand, changes dramatically. Even for weak variations $\delta K \ll K$ for $K = J, c, d$, we expect the single triplon eigenstates to Anderson localize. This follows from analyzing the generalized eigenvalue problem described in the paragraph above with spatially varying diagonal matrix elements. Fig. 4.1 shows the typical localized triplon wavefunctions found by this analysis.

We now make the case for MBL following BAA. Consider the excited states with a low density of localized triplons. The interaction U between two triplons separated by a distance l scales as $Je^{-l/\xi}$, where ξ is the longer of the triplon overlap decay

length ($1/\log(3)$) and the localization length. When the typical spacing l between excitations is sufficiently large so that the typical energy splitting between nearby states (of order 1) is much larger than the interactions, $U \sim \pm J e^{-l/\xi}$, the perturbative BAA arguments protect triplon localization. That is, the system remains many-body localized up to a finite energy density ϵ such that the typical separation J/ϵ is small on the scale ξ .

The naive application of the same argument fails as one approaches the $O(3)$ symmetric AKLT point by taking c_i, d_i to zero. In this limit, the local fields splitting the triplet degeneracy vanish so that there is no regime where the typical interaction strength U is smaller than the typical local level spacing. Rather, the localized triplons carry spin-1 and the system of a dilute random array of non-interacting triplons is highly degenerate. From this point of view, the interactions (still of order $U \sim J e^{-l/\xi}$) split this large degeneracy according to a disordered system of both ferro- and antiferromagnetic exchanges. Whether such an effective $O(3)$ -symmetric random spin-1 chain can exhibit a MBL phase is an intriguing open question. The application of the real space renormalization group to such a system suggests that the system ought to grow large effective moments [326, 151] which, if they behave classically as one expects of large spins, would lead to thermal conduction and equilibration [228, 26].

Finally, we consider how the three signatures of the Haldane phase persist to finite energy density in the MBL regime. First, take the ‘caricatures’ of the excited states at low energy density given by the MPS with a low density of double lines at prescribed bonds as in Eq. (4.4). We have already noted that (i) the entanglement spectrum is doubly degenerate, (ii) the string order is ‘glassy’ (Eq. (4.5)), and (iii) the expectation value of $H_{A/BKLT}$ is independent of the virtual spins v_L, v_R on the boundary. Thus, if the ‘caricature’ states were the true excited eigenstates in the

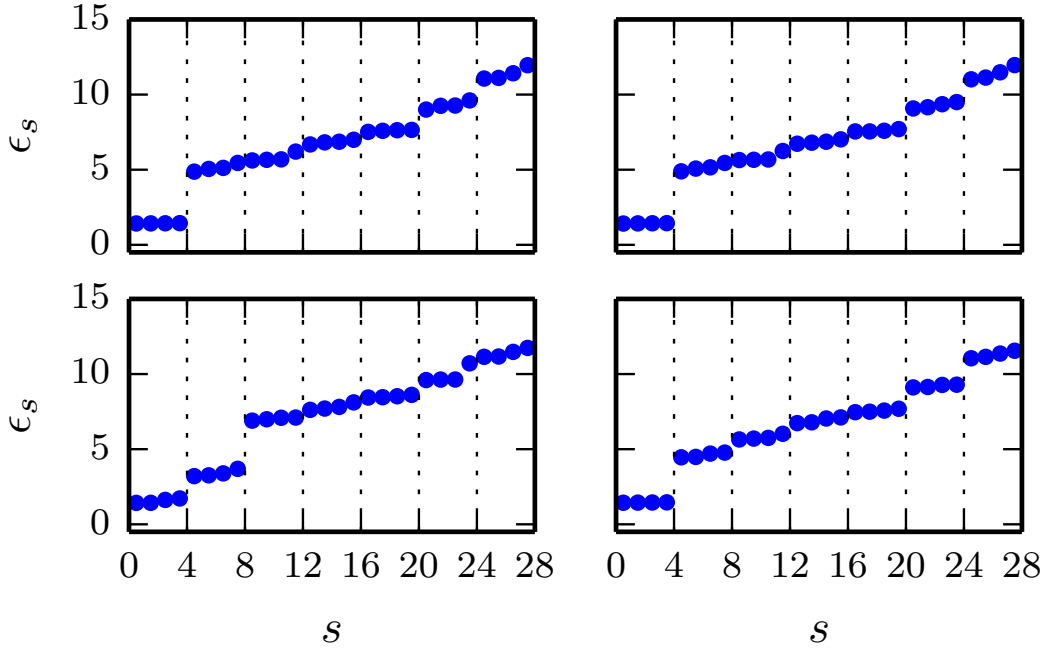


Figure 4.2: The entanglement spectra of four consecutive excited states, starting with the 60th state above the ground state, for a 12-site open BKLT chain with disorder in all coupling constants. Each state is decomposed into two equal halves.

presence of disorder, all of the characteristics of the Haldane phase would persist to low energy density.

Of course, the simple caricatures neglect the ‘fuzziness’ in the position of the triplons in Anderson localized single particle wavefunctions such as in Fig. 4.1. To construct multi-triplon ‘filled’ Anderson localized states, we define the bond triplon creation operators:

$$t_j^\alpha = \prod_{i \leq j} R_i^\alpha \quad (4.6)$$

These commuting, self-adjoint, unitary operators place triplons of type α at bond j when acting upon the A/BKLT ground state space. The single triplon localized

states are then created by

$$t_\psi^\alpha = \sum_j \psi_j^\alpha t_j^\alpha \quad (4.7)$$

acting on the A/BKLT vacuum, where ψ_j^α are the eigenmodes in the single triplon problem. We caution that the mode functions ψ_j^α are not orthonormal as they are coefficients with respect to a non-orthogonal basis, and neither do the t_j^α satisfy a canonical algebra. Nonetheless, for sufficiently dilute collections of triplons, we expect the Fock states $|\Psi\rangle = t_{\psi_1}^{\alpha_1} t_{\psi_2}^{\alpha_2} \cdots t_{\psi_N}^{\alpha_N} |A\rangle$ to be good approximate representations of the MBL eigenstates. Just as localized Fock states of normal bosons and fermions have entanglement entropy satisfying an area law, $|\Psi\rangle$ has an area law for localized ψ_j^α . Thus, such states can be recast to exponential accuracy as finite dimensional MPS states which in turn fall into the two-fold SPT classification of dihedral symmetric states [250, 304]. We recapitulate this argument in more detail in Appendix 4.A for non-translation invariant states. In the same appendix, we argue that the fuzzy Fock states above are in the same non-trivial class as the A/BKLT ground state, that is, they exhibit two-fold degenerate entanglement spectra in the bulk for a single spatial cut. Numerical exact diagonalization results are consistent with this prediction. In Fig. 4.2, we plot the entanglement spectra of a few excited states of the 12-site open BKLT chain with disorder. Dihedral symmetry forces the physical spin halves at the two boundaries to be maximally entangled; thus the spectrum should be 4-fold degenerate if the excited state has SPT order. There is evidence of this degeneracy in Fig. 4.2. In conclusion, states such as $|\Psi\rangle$ exhibit (i) two-fold degenerate entanglement spectra in the bulk, and (ii) long-range string glass order with softened frozen in domain walls and (iii) spin-1/2 boundary modes associated with the projective representation of the corresponding finite dimensional MPS.

In the presence of dihedral symmetry, the string glass order diagnoses the non-analyticity of the eigenstates at the transitions between the SPT MBL phase and the trivial MBL phase (or the ergodic phase). On the other hand, without dihedral symmetry, such an order parameter distinction disappears. For example, turning on a local Néel field induces a Néel magnetization, and as shown in Ref. [166], string order. Thus, the non-analyticity associated with the loss of the long range string glass order will be lost and the eigenstates in both MBL phases can be smoothly connected.

We end with a few comments. First, a numerical study in Ref. [24] probed the boundary modes of excited MBL states in a related one-dimensional model using spin-echo. Such numerical experiments are unavailable in the disordered BKLT model due to the large intrinsic correlation lengths as compared to accessible system sizes. Second, a consequence of the existence of boundary modes is a ‘pairing’ regime in the many-body energy spectrum of open chains. In this regime, the four boundary states can be identified by their small splitting relative to the exponentially small many-body spacing [149]. However, there is evidence from perturbative and numerical calculations in the non-integrable Majorana chain that this pairing may persist to the clean limit [197]. The relationship between pairing and coherent boundary modes is thus not settled and requires further study. Finally, the entire discussion in this section is not special to the A/BKLT point. The MBL phase at low energy densities continues away from these points.

4.3 Topological Ising paramagnet in $d=2$

4.3.1 Review of low energy physics

We now turn to discrete SPT phases in higher dimension. In particular, we consider two dimensional spin systems with \mathbb{Z}_2 symmetry, where there is a two-fold classification of SPTs: the trivial and the topological Ising paramagnets [202, 74, 71]. We

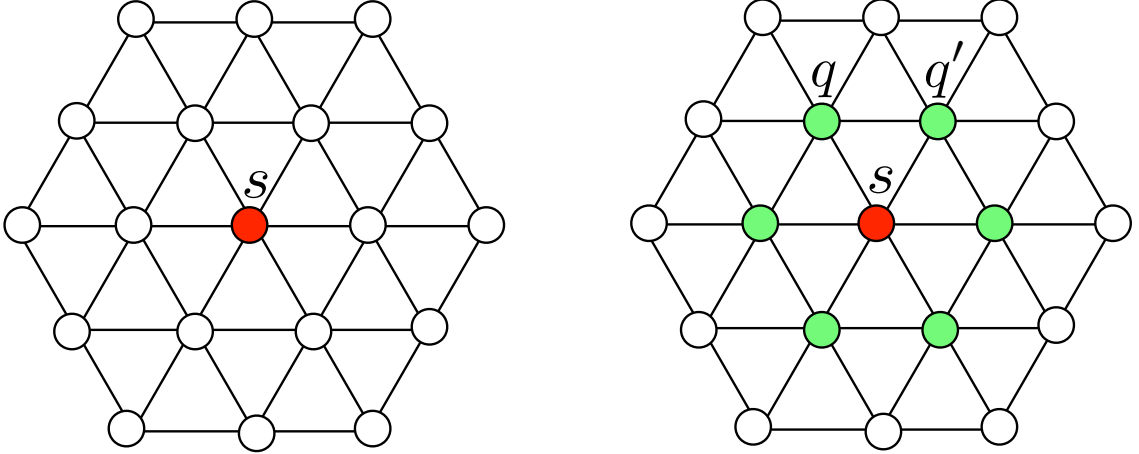


Figure 4.3: (Left) Trivial paramagnet H_0 defined in (4.9) is a sum of σ_s^x terms on sites s of the triangular lattice. (Right) Topological paramagnet H_{LG} defined in (4.8) is a sum of seven-spin terms involving a product of σ_s^x and a phase factor $\prod_{\langle sqq' \rangle} i^{\frac{1-\sigma_q^z \sigma_{q'}^z}{2}}$ from the six spins surrounding s .

work near an exactly solvable model in the topological SPT phase, first constructed by Levin and Gu [202]:

$$H_{LG} = - \sum_s \Lambda_s B_s, \quad B_s = -\sigma_s^x \prod_{\langle sqq' \rangle} i^{\frac{1-\sigma_q^z \sigma_{q'}^z}{2}}. \quad (4.8)$$

Here, Λ_s are coupling constants, σ_s are Pauli spin-1/2 operators living on the sites s of a triangular lattice, and the product in B_s runs over the six triangles $\langle sqq' \rangle$ intersecting the site s (see Fig. 4.3).

The Hamiltonian is invariant under the protecting Ising symmetry $S = \prod_s \sigma_s^x$. The B_s operators on different sites commute with each other, and the gapped paramagnetic ground state is the simultaneous $B_s = +1$ eigenstate $\forall s$. On closed manifolds, this ground state is unique and can be written explicitly in the σ^z basis as a superposition of all spin configurations each with amplitude $(-1)^{N_{dw}}$, where N_{dw} is the number of domain walls in the configuration. These non-trivial phase factors reflect the topological nature of the ground state.

The topological paramagnet (TPM) is to be contrasted with the better-known trivial paramagnet (TrPM) with exactly solvable model Hamiltonian

$$H_0 = - \sum_s \Gamma_s \sigma_s^x, \quad (4.9)$$

where Γ_s are coupling constants. The ground state of the trivial paramagnet is clearly a simple product state which, in the σ^z basis, corresponds to a uniform superposition of all spin configurations with amplitude 1.

The excitations in both models correspond to ‘spin flips’ which are sites s with either $B_s = -1$ or $\sigma_s^x = -1$, respectively. At the exactly solvable points, such spin flips are static and thus the highly excited eigenstates are already many-body localized analogous to the ‘caricature’ states of the previous section. Absent disorder, this form of MBL is non-generic: any non-commuting perturbations to the model Hamiltonians induce dispersion of the spin flips, which in turn destroys many-body localization. For specificity, we add a ferromagnetic coupling term to make the spin excitations dynamical and consider Hamiltonians of the form:

$$\tilde{H}_{0/LG} = H_{0/LG} - J \sum_{\langle ss' \rangle} \sigma_s^z \sigma_{s'}^z. \quad (4.10)$$

For J large enough, the ferromagnetic term drives a transition out of either paramagnet into a symmetry broken ferromagnetic phase.

4.3.2 Ergodicity and localization in highly excited states

Now include randomness in the couplings Λ_s and Γ_s . For simplicity, keep $\Lambda_s, \Gamma_s > 0$ to preserve the exact ground state. In this regime, the individual spin flip manifold remains Anderson localized even with small ‘hopping’ J . BAA arguments suggest that dilute gases of these weakly interacting point particles remain many-body localized.

It is intuitively clear that both paramagnets continue into MBL versions at finite energy density as the defects that would destroy the SPT order are localized. In the following, we will consider the extension of various SPT diagnostics to finite energy density MBL states to substantiate this intuition. We first distinguish the MBL topological and trivial paramagnets from the extended thermal paramagnetic phase, and then turn to diagnostics that differentiate the two MBL paramagnets.

The MBL paramagnets can be easily distinguished from their thermal counterparts at nonzero energy densities using the behavior of certain Wilson loops⁵. Recall that in 2+1 dimensions magnetic systems with site variables are dual to gauge theories with bond variables [187]. The spin models H_0/H_{LG} are respectively dual to the perturbed toric-code (t.c.)/ doubled-semion (d.s) \mathbb{Z}_2 gauge theories, with the t.c/d.s theories restricted to a static matter sector. These dual gauge theories live on the honeycomb lattice; their topologically ordered deconfined phases map to the paramagnetic phases of the spin models, while their confined phase maps to the ferromagnetic phase. The doubled semion model is discussed in [204].

As the dual models are pure gauge, their respective deconfined phases may be diagnosed by the celebrated perimeter-law of equal time Wilson loops. Each of the two deconfined phases, has a (different) canonical Wilson loop which minimally probes the confinement of charges without further exciting the gauge sector [204]. The Wilson loops of the dual gauge theories correspond to the following operators in the original spin variables σ_s , :

$$W_0[C] = \left\langle \prod_{s \in A[C]} \sigma_s^x \right\rangle \quad (4.11)$$

$$W_{LG}[C] = \left\langle \prod_{s \in A[C]} B_s \right\rangle \quad (4.12)$$

⁵The two paramagnets are smoothly connected when thermalized, so no distinction is necessary.

where the product is over all sites s lying within $A[C]$, the area enclosed by the curve C . These Wilson loops exhibit the “zero-law” $W_{0/LG}[C] = 1$ exactly at the pure trivial/topological paramagnetic points. The zero-law continues to a perimeter law $W[C] \propto e^{-c|C|}$ on perturbing away from the exactly solvable points. On the other hand, the Wilson loops exhibit an area law $W[C] \propto e^{-c'|A[C]|}$ in the ferromagnetic phase.

For clean, ergodic systems, both Wilson loops exhibit an area law at any finite temperature $T > 0$. This reflects the presence of a finite density of delocalized vortex excitations in the dual gauge theories.

The problem with disorder was discussed for the standard \mathbb{Z}_2 gauge theory by Huse et. al. [148]. In the presence of sufficient randomness in the couplings of the dual gauge theory, there exists a MBL topologically ordered phase for the \mathbb{Z}_2 gauge theory at finite energy density. The excited MBL eigenstates have a finite density of localized vortices, whence the Wilson loop W exhibits a “spin-glass” version of the perimeter law — the magnitude of W decays as the perimeter of C , but with a sign that depends on the number of localized vortices enclosed by C [148]. An analogous story holds for the doubled-semion gauge theory as well. By duality, the MBL highly excited eigenstates of the trivial and topological paramagnets exhibit a spin-glass perimeter law for $W_0[C]$ and $W_{LG}[C]$ respectively. By contrast, excited eigenstates for the thermal paramagnet exhibit area laws for these quantities just as in the clean limit. Thus, a sharp distinction exists between the MBL and thermal phases for the two paramagnets, diagnosed by the behavior of the Wilson loop operator.

We now turn to the question of diagnosing the two MBL paramagnets as distinct phases. One’s first instinct might be to use the Wilson loops and, for the ideal Hamiltonians, they work: $W_0[C] = 1$ for the TrPM and vanishes for the TPM, while $W_{LG}[C] = 1$ for the TPM and vanishes for the TrPM. Unfortunately this does not hold more generally; both Wilson loops exhibit a perimeter law in both paramagnetic

phases. Possibly the “correct” one is always dominant, but this is a topic for future work.

Instead, let us consider other possible diagnostics to separate the MBL TrPM and TPM phases. (i) At $T = 0$ in the ground state, the edge of the TPM must either be gapless or break the \mathbb{Z}_2 symmetry. (ii) If we gauge the models, the gauged TPM exhibits vortices with semionic statistics, which, (iii) in the presence of time reversal symmetry, bind Kramers doublets [335]⁶. We expect each of these properties to extend to the MBL phase, as we explore below.

The gaplessness of the symmetric edge is not a sharp diagnostic of the TPM, even at $T = 0$, as already alluded to by Levin and Gu in the clean case. The edges can always spontaneously gap by breaking Ising symmetry for arbitrarily weak perturbations; of course, gapped symmetry-broken edges can also be present in the TrPM. With disorder at finite energy the situation is even worse — the many-body spectrum is always gapless although local operators may exhibit a ‘mobility’ gap in localized states. Thus, we might expect ‘mobility gaplessness’ in the absence of symmetry breaking, but this is a delicate diagnostic at best.

At $T = 0$, Levin and Gu proposed a sharp distinction between the two paramagnets based on a different diagnostic. They coupled both paramagnets to a static gauge and then considered the statistics of braiding π flux vortex insertions. For the TrPM the statistics are bosonic while for the TPM they are semionic, as the gauged models are dual to the toric code and doubled semion theories, respectively. In a putative MBL state, a slow physical process of inserting fluxes, braiding and annihilating them should accumulate the same semionic statistical phase (on top of ‘spin glass’-like Aharonov-Bohm contribution from each of the encircled localized charges). The definition of ‘slow’ is subtle as the many-body spectrum is gapless, but again we expect a local $O(1)$ mobility gap. The exact mathematical operators which charac-

⁶We thank M. Zaletel for bringing this to our attention.

terize this process in the exactly solvable models do not have simple extensions to the general MBL state.

If the gauged paramagnet additionally has time reversal symmetry, then each vortex of the TPM binds a Kramers doublet (the semion and the anti-semion states). This can be seen in the exactly solvable model by defining a local charge operator on an area A , $Q[A] = \prod_{p \in A} B_p$, gauging it and noting that the gauged Q is time-reversal odd (even) if A encloses an odd (even) number of vortices. This implies an exact degeneracy for the entire spectrum. On the other hand, the TrPM vortices are bosonic and do not bind Kramers doublets (the gauged charge operators are always time-reversal even in the exact model). The degeneracy lifts exponentially in the separation between the vortices on perturbing away from the exactly solvable point and we expect this exponential degeneracy to persist into the MBL phase. The careful reader might note that the typical many-body level spacing for highly excited states is exponentially small in the system volume, and thus smaller than the separation between paired states. This is reminiscent of the paired MBL regime discussed by Huse et. al [148], and the ‘paired’ states share all their local properties unlike typical MBL eigenstates close in energy. A different but related diagnostic comes from measuring coherent ‘anyon oscillations’ between the semion and anti-semion states in the localized background with a timescale set by their separation.

We leave the detailed mathematical understanding of these last questions as open problems for future work.

Finally, we comment briefly on the requirement that there be a continuous path connecting the MBL phases of the TPM and the TrPM if Ising symmetry is broken along the path. Levin and Gu explicitly construct a local Ising symmetry-breaking unitary operator $U(\theta)$ which transforms H_0 into H_{LG} (with $\Lambda_s = \Gamma_s$) along a path in Hamiltonian space parameterized by the continuous variable θ ; the same unitary can also be used for random couplings Λ_s . The many-body energy spectrum, and hence

the level-statistics of $H(\theta)$ are identical everywhere along the path which strongly indicates the absence of a MBL to ergodic phase transition in accordance with work done by Huse et. al. [227]. More strongly, each localized excited eigenstate of H_0 continues to a localized eigenstate of $H(\theta)$ under the action of the local unitary, and there is a continuous mapping between MBL eigenstates everywhere along the path. This is to be contrasted with the eigenstate phase transition that we expect between the TPM and TrPM highly excited eigenstates when Ising symmetry is preserved.

4.4 Concluding remarks

Traditionally, the destruction of order and the proliferation of defects are closely intertwined in statistical mechanics. This has led previously to the idea that the localization of defects can improve order, e.g. in the case of superconductors in a magnetic field [147] and the quantum Hall effect away from the center of the plateau [158]. The work of Huse et al has generated the interesting possibility that this mechanism can operate also in many body localized quantum systems where statistical mechanics does not apply even for highly excited eigenstates. In this setting the sought after order has to be identified for individual many-body eigenstates and has a “spin glass” form or at least a spin glass component which is eigenstate specific.

In this paper we have considered whether SPT order can exist in highly excited eigenstates in the MBL setting by examining two specific models. In both cases it is not hard to see that thermal states differ qualitatively from the ground states exhibiting SPT order while MBL states qualitatively resemble the ground states thanks to the localization of defects. This is strong evidence for existence of an eigenstate phase transition that must separate the trivial and SPT regions at nonzero energy density. For the case of the Haldane phase in $d = 1$ we are able to go further and argue that highly excited MBL eigenstates in the SPT region can be directly distinguished from

highly excited MBL eigenstates in the topologically trivial region. For the topological Ising paramagnet in $d = 2$ this last step still needs to be taken. In both cases we have argued the absence of an eigenstate phase transition separating the regions when the preserving symmetry is allowed to be broken.

Evidently it would be interesting to extend this investigation to the larger zoo of SPT phases identified in recent work, including in $d = 3$ where SPT order can presumably survive to non-zero temperatures when the disordering defects have the topology of vortex lines. One immediate restriction suggested by our analysis is that we found it necessary to protect the Haldane phase via a discrete symmetry to invoke MBL. If that restriction is fundamental, it may be that SPT order is strengthened by MBL only if the protecting symmetry is discrete.

4.A Entanglement spectrum of dihedral symmetric MPS without translational symmetry

In Ref. [250], Pollman and co-authors demonstrated the entanglement spectrum of a spatial cut diagnoses the two dihedral symmetric translationally invariant phases of integer spins in one dimension. In the topological/Haldane phase, they showed that the entanglement spectrum is exactly double degenerate in the thermodynamic limit, while in the trivial phase, it is not. The two phases persist in the absence of translational invariance. In this appendix, we show that the classification of the entanglement spectrum of the MPS also holds without translational symmetry.

Our approach and notation closely follows that in Ref. [250]. Consider an open chain of a spin system with integer spin S in the thermodynamic limit. Let the wavefunction of the system have a MPS representation (as is the case for the ground state of the clean system or the highly excited MBL states in the dirty system). The

canonical form of such an MPS in the standard pictorial notation is:

$$|\Psi\rangle = \sum_{\{\sigma_i\}} \dots \text{---} \boxed{\Gamma_i} \text{---} \bigcirc{\Lambda_i} \text{---} \dots |\{\sigma_i\}\rangle$$
(4.13)

where i is the site label, σ_i is the physical spin index taking values $-S, -S + 1, \dots, S$, Γ_i is a matrix of dimension χ and Λ_i is a real, diagonal matrix, also of dimension χ , with non-negative values. χ is interpreted as the dimension of the virtual spins that make up the spin S ⁷. For a more detailed introduction to MPS, see [277, 310]. An important property of the canonical representation is that the transfer matrix at site i , defined as the tensor in the dashed box below, has a unique left (and right) eigenvector of eigenvalue one:

$$\begin{array}{c}
 \text{---} \bigcirc{\Lambda_{i-1}} \text{---} \boxed{\Gamma_i} \text{---} \\
 \text{---} \bigcirc{\Lambda_{i-1}} \text{---} \boxed{\Gamma_i^*} \text{---}
 \end{array}
 \quad = \quad
 \left[\begin{array}{c} \text{---} \\ \text{---} \end{array} \right]$$
(4.14)

The diagonal elements of Λ_i are the Schmidt numbers for a spatial cut between bonds i and $i + 1$; the entanglement energies are the negative logarithms of these diagonal elements. Properties of the entanglement spectrum therefore follow from the structure of Λ_i, Γ_i .

To prove that there is a two-fold classification of the entanglement spectrum, we proceed as follows:

1. Identify the action of the dihedral symmetry on the physical spins as a site-dependent gauge transformation of the virtual spins

⁷The proof may easily be extended to site-dependent χ ($\tilde{\chi}_i$). Then, the χ defined in the text is $\chi = \max \tilde{\chi}_i$.

2. Show that the gauge transformation is the identity up to a site-dependent phase
3. Determine that the smallest irreducible representation for the gauge transformation is either of dimension one, or two

When the smallest irreducible representation has dimension two, the Schmidt values are forced to come in degenerate pairs and the entanglement spectrum is doubly degenerate. When the dimension is one, there is no constraint on the entanglement spectrum. This then is the required classification.

We now go through the steps in turn. Consider the action of the dihedral group on the state $|\Psi\rangle$. The matrix, Γ_i in the MPS representation in Eq. (4.13) becomes:

$$\tilde{\Gamma}_i^\sigma = (R_i^\alpha)^{\sigma\sigma'} \Gamma_i^{\sigma'}, \quad \alpha = x, y, z \quad (4.15)$$

By definition, under the action of $\prod_i R_i^x$, $\prod_i R_i^y$ and $\prod_i R_i^z$, the given state goes back to itself, up to boundary effects that are not relevant in the thermodynamic limit. Thus, $\tilde{\Gamma}$ should be related to Γ by a gauge transformation:

$$\tilde{\Gamma}_i^\sigma = e^{i\theta_i^\alpha} (U_{i-1}^\alpha)^\dagger \Gamma_i^\sigma U_i^\alpha, \quad (4.16)$$

where U_i^α is a unitary matrix commuting with Λ_i and θ_i^α is real. Physically, the U matrices implement the action of the symmetry on the virtual spins. They form a χ -dimensional projective representation of the symmetry group of the wave function $|\psi\rangle$. Note that the MPS with matrices $(\tilde{\Gamma}_i^\sigma, \Lambda_i)$ is also in the canonical representation. As the dihedral operators square to identity, another action of the dihedral group provides a relation for Γ_i :

$$\Gamma_i^\sigma = e^{i2\theta_i^\alpha} (U_{i-1}^\alpha)^\dagger (U_{i-1}^\alpha)^\dagger \Gamma_i^\sigma U_i^\alpha U_i^\alpha, \quad (4.17)$$

Substituting Eq. (4.17) in Eq. (4.14), it is easily seen that:

The diagram shows a transfer matrix on the left, enclosed in a dashed box. It consists of two parallel paths. The top path has a circle labeled Λ_{i-1} followed by a square labeled Γ_i . The bottom path has a circle labeled Λ_{i-1} followed by a square labeled Γ_i^* . To the left of these paths is a square labeled $(U_{i-1}^{\alpha\dagger})^2$. To the right of the dashed box is an equals sign, followed by a phase factor $e^{-2i\theta_i^\alpha}$ and another square labeled $(U_i^{\alpha\dagger})^2$.

The input left vector to the transfer matrix and the output vector are different. However, the norm of both vectors is χ , equal to the norm of the unimodular eigenvector. As the transfer matrix has a unique unimodular eigenvector, both vectors have to be proportional to the identity eigenvector in Eq. (4.14) up to a phase. Thus,

$$(U_{i-1}^{\alpha\dagger})^2 = e^{i\phi_{i-1}^\alpha} \mathbf{1} \quad (4.19)$$

This gets us to the second step in the list above. Further, as the eigenvalue is one, we obtain a relationship between θ_i^α , ϕ_i^α and ϕ_{i-1}^α .

Finally, after a few steps of algebra, we find that:

$$(U_i^x)^\dagger (U_i^z)^\dagger = \kappa (U_i^z)^\dagger (U_i^x)^\dagger \quad (4.20)$$

$$\kappa = \pm 1 \quad (4.21)$$

That is, on every site i , U_i^x and U_i^z either commute or anti-commute. If U_i^x and U_i^z commute (anti-commute), the smallest irreducible representation has dimension one (two). Up to accidental degeneracies, U_i^x, U_i^z can then be expressed as direct sums of matrices with dimension one (two). Recall however that U_i^α and the diagonal matrix with the Schmidt numbers, Λ_i , commute. Thus, in the former case, there is no constraint on the entanglement spectrum, while in the latter, the entire entanglement spectrum (ES) has to be doubly degenerate.

In the ground states of the clean/disordered A/BKLT chains, $\kappa = -1$ and the (ES) is two-fold degenerate. Consider now the fuzzy Fock states defined below Eq. (4.7) using the localized single triplon wavefunctions, $|\Psi\rangle = t_{\psi_1}^{\alpha_1} t_{\psi_2}^{\alpha_2} \cdots t_{\psi_N}^{\alpha_N} |A\rangle$. In the extremely dilute limit, pick a bond m where the weight of all the single triplon states occupied in $|\Psi\rangle$ is small. The local action of the dihedral group on this bond is the same as in the ground state and $\kappa = -1$ on this bond. As κ is site-independent, U_i^x and U_i^z anti-commute for all i and the entanglement spectrum will be doubly degenerate for any spatial cut. Thus, these approximate MBL states have the topological order of the Haldane phase.

Chapter 5

Phase Structure Of Driven Quantum Systems

5.1 Introduction

We saw in Section 1.6 and the previous chapter that the lack of equilibrium in MBL systems allows for novel forms of eigenstate order and the possibility for nontrivial phases in regimes where they would be disallowed in equilibrium. In this chapter and the next, we continue this program of generalizing and extending ideas of equilibrium phase structure to the nonequilibrium setting.

In particular, we consider the following question: Is there a sharp notion of a phase in driven, interacting quantum systems? We find an affirmative answer for Floquet systems whose Hamiltonians depend on time t periodically, $H(t+T) = H(t)$ (see Section 1.8.1 for an introduction). Unlike in equilibrium statistical mechanics, disorder turns out to be an essential ingredient for stabilizing different phases; moreover, the periodic time evolution allows for the existence (and diagnosis) of phases without any counterparts in equilibrium statistical mechanics.

Naively, Floquet systems hold little promise of a complex phase structure. As discussed in Section 1.8.2, generic interacting Floquet systems absorb energy indefinitely from the driving field and heat up to a trivial “infinite temperature” state [198, 78, 251]. On the other hand, in the presence of disorder, weakly driven MBL systems can remain Floquet localized [199, 252, 2] and display a set of properties closely related to those exhibited by time-independent many-body localized systems.

In the following we show that such Floquet-MBL systems can exhibit multiple phases. Some of these are driven cousins of MBL phases characterized by broken symmetries and topological order. Remarkably, others are genuinely new to the Floquet setting, characterized by order *and* non-trivial periodic dynamics. Our analysis identifies a key feature of the Floquet problem, the existence of localized Floquet eigenstates (1.18), which permits us to extend the notion of eigenstate order [149, 239, 319, 64, 24] to time dependent Hamiltonians. Our work also builds on the discovery of topologically non-trivial Floquet single particle systems and recent advances in their classification [298, 229, 161, 181, 207, 180, 273, 225]. As we will explain, non-trivial single particle drives can yet lead to trivial many-body (MB) periodic dynamics even without interactions. Thus, the full framework of disorder and interactions is required for the MB problem.

We illustrate our ideas in the simple interacting setting of a one dimensional disordered spin chain with Ising symmetry,

$$H = \sum_i J_i \sigma_i^x \sigma_{i+1}^x + \sum_i h_i \sigma_i^z + J_z \sum_i \sigma_i^z \sigma_{i+1}^z. \quad (5.1)$$

Carrying out a Jordan-Wigner transformation on only the first two terms gives a p-wave superconducting free-fermion model, whereas the final term is a density-density interaction in the fermion language. The paramagnetic and symmetry-broken ferromagnetic phases of the Ising model are related by a well-known duality. We first show

that there are two Floquet phases, paramagnet (PM) and spin glass (SG), that connect smoothly to phases in the undriven systems. We then identify two *new* phases that do *not*, which we term the Floquet 0π -PM and the Floquet π SG. It turns out that the dynamics of the π SG phase show a novel form of correlated spatiotemporal order and the properties of this phase are remarkably robust to arbitrary perturbations—we will discuss these features in detail in the next chapter.

5.2 Floquet Paramagnet and Spin Glass

We begin with the two phases that *do* exist in undriven systems and demonstrate the stability of these to being (not too strongly) driven. Starting with the non-interacting limit, $J_z = 0$, we choose the J_i and the h_i to be log-normally distributed with a tunable mean $\overline{\log(J_i)} \equiv \overline{\log J}$, fixed $\overline{\log(h_i)} \equiv \overline{\log h} = 0$ and two fixed and equal standard deviations $\delta \log(h_i) = \delta \log(J_i) = 1$. Work on random, non-interacting Ising models culminating in Ref. [110] finds a ground state phase diagram which is a paramagnet for $\overline{\log J} < \overline{\log h}$ and a Z_2 breaking ferromagnet for $\overline{\log J} > \overline{\log h}$, separated by an infinite disorder fixed point at $\overline{\log J} = \overline{\log h}$. The work on eigenstate order has shown that, with disorder and localization, both phases exist at *all* energies with the symmetry-breaking phase exhibiting SG order in individual eigenstates instead of ferromagnetism. The eigenstates are also eigenstates of parity $P = \prod \sigma_i^z$, and deep in the PM phase, they (roughly) look like frozen spins along the z direction $|\uparrow\downarrow\downarrow\cdots\uparrow\rangle$ while deep in the SG phase they look like global superposition/cat states with spins in the x direction with frozen domain walls $|\pm\rangle = \frac{1}{\sqrt{2}}(|\rightarrow\leftarrow\rightarrow\cdots\rightarrow\rangle \pm |\leftarrow\rightarrow\leftarrow\cdots\leftarrow\rangle)$.

With weak interactions, $0 < J_z \ll 1$, the strongly localized PM and SG phases remain MB localized [239, 182]. The fate of the SG-PM transition is more sensitive to the inclusion of interactions. It was suggested that it would remain localized [149]

and exhibit the same scaling as the non-interacting fixed point [239]; we comment on the analogous question in the Floquet setting below.

We consider a periodic binary drive—computationally much simpler than a monochromatic modulation—switching between two static H s with $\overline{\log J}$ differing by 1:

$$H(t) = \sum_i f_s(t) J_i \sigma_i^x \sigma_{i+1}^x + \sum_i h_i \sigma_i^z + J_z \sum_i \sigma_i^z \sigma_{i+1}^z,$$

$$f_s(t) = \begin{cases} 1 & \text{if } 0 \leq t < \frac{T}{4} \text{ or } \frac{3T}{4} < t \leq T \\ e & \text{if } \frac{T}{4} \leq t \leq \frac{3T}{4} \end{cases}. \quad (5.2)$$

We set $J_z = 0.1$ in the following. For $-1 \leq \overline{\log J} \leq 0$ the drive straddles the undriven phase transition, up to small corrections to its location due to the interaction.

Drives consistent with Floquet localization require both small interactions and not too small frequencies. We arrange the latter by defining, for each set of $(\overline{\log J}, \overline{\log h})$ parameters, an effective “single-particle bandwidth”, $W = \max(\sigma_J, \sigma_h)$, where σ_h and σ_J are the standard deviations of h_i and J_i determined from the underlying log-normal distributions. The period is then defined by $\omega = 2\pi/T = 2W$. This choice ensures a roughly constant ratio of ω/W for different $\overline{\log J} - \overline{\log h}$ values and thus isolates the effect of tuning the means through the phase diagram. The lowest frequency in our drives is bigger than the estimated single particle bandwidth but much smaller than the MB bandwidth, so that localization is not a foregone conclusion.

Recall from Section 1.8.1 that the solutions of the time-dependent Schrodinger equation $|\psi_\alpha(t)\rangle = e^{-i\epsilon_\alpha t} |\phi_\alpha(t)\rangle$ are defined in terms of the periodic states $|\phi_\alpha(t)\rangle = |\phi_\alpha(t+T)\rangle$ which are obtained from the eigenstates $|\alpha\rangle$ of the time-evolution operator $U(T) = e^{-iH_F T}$ with eigenvalues $e^{-i\epsilon_\alpha T}$. The quasienergies ϵ_α are defined modulo ω .

In Fig. 5.1 we characterize the quasi-energy spectrum $\epsilon_n \in [0, 2\pi)$ using the level statistics of H_F . We define quasi-energy gaps by $\delta_n = \epsilon_{n+1} - \epsilon_n$ and the level-statistics

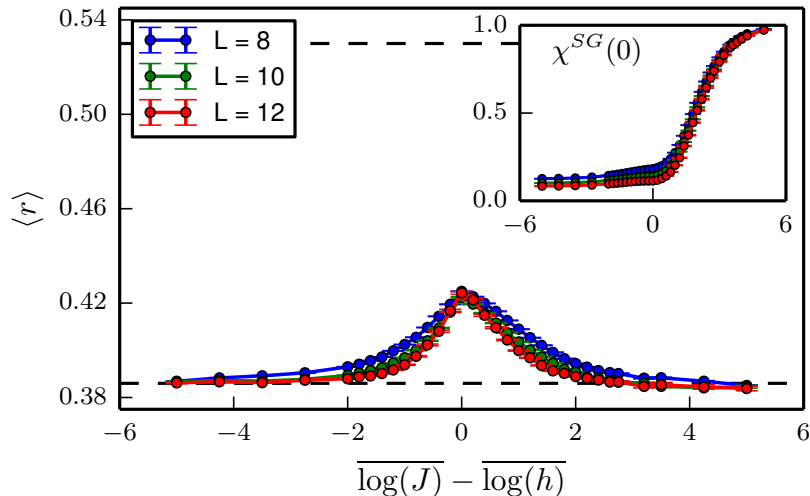


Figure 5.1: Disorder averaged level statistics $\langle r \rangle$ of H_F for the driven, disordered Ising model (5.2). $\langle r \rangle$ approaches the Poisson limit of .386 with increasing L deep in the PM and SG phases, showing that these remain well localized. There is a peak in $\langle r \rangle$ near the non-interacting critical point at $\overline{\log J} = \overline{\log h}$ indicating partial delocalization, although the value still remains well below the Circular Orthogonal Ensemble (COE) value of .527. (inset): The SG diagnostic χ^{SG} defined in (5.4) goes to 0 in the PM and approaches a non-zero value in the SG phase. All data is averaged over $2000 - 10^5$ samples depending on L .

ratio $r = \min(\delta_n, \delta_{n+1}) / \max(\delta_n, \delta_{n+1})$. Away from the critical region which—given the weak interactions and large frequency of the drive—is close to the undriven, non-interacting transition point $\overline{\log J} = \overline{\log h}$, the disorder averaged $\langle r \rangle$ approaches the Poisson limit of .386 with increasing system size L , signaling a lack of level repulsion and hence MBL. In the interacting critical region we find a peak in $\langle r \rangle$ which does not grow with system size and is much less than the delocalized COE value of .527; we return to this below.

With localization established, we turn to distinguishing the phases. Consider a pair of Z_2 invariant correlators (with $A = x$ or y)

$$C_{AA}^\alpha(ij; t) = \langle \phi_\alpha(t) | \sigma_i^A \sigma_j^A | \phi_\alpha(t) \rangle \quad (5.3)$$

for $i - j \gg 1$ in any given Floquet eigenstate. We find that for $\overline{\log J} < \overline{\log h}$ both correlators vanish with increasing system size L at all t , signaling a PM. For $\overline{\log J} > \overline{\log h}$, both are generically non-zero, though of random sign varying with eigenstate and location, signaling SG order. For the SG, our parameters give $|C_{xx}^\alpha(ij; t)| \gg |C_{yy}^\alpha(ij; t)|$ at all t although the more general signature is that $|C_{xx}^\alpha(ij; t)|$ and $|C_{yy}^\alpha(ij; t)|$ cross 0 mod 4 times within the period for $0 < t < T$. For our parameters, it suffices to compute

$$\chi_\alpha^{SG}(t) = \frac{1}{L^2} \sum_{i,j=1}^L (\langle \phi_\alpha(t) | \sigma_i^x \sigma_j^x | \phi_\alpha(t) \rangle)^2 \quad (5.4)$$

for $t = 0$. In Fig. 5.1 (inset) we plot the disorder averaged $\chi_\alpha^{SG}(0)$; the trend with system-size indicates that $\chi^{SG}(t) > 0$ in the spin-glass and $\chi^{SG}(t) \rightarrow 0$ in the paramagnet.

Three comments are in order. First, recall that it would be sufficient to establish the existence of the Floquet PM—the SG can be obtained by duality¹. Second, in chains with uniform couplings, both spin and dual spin order vanish in all but one of the Floquet eigenstates (the notion of the “ground-state” is not well defined in a Floquet system) even without interactions—this is the Landau-Peierls prohibition against discrete symmetry breaking in disguise. Localization is essential to avoid this. Third, the $|\pm\rangle$ MB Floquet eigenstates in the localized SG phase come in conjugate, almost degenerate pairs with different parity but with similar domain wall configurations. In the fermionic formulation of the problem, the PM is topologically trivial while the SG is non-trivial. The non-interacting SG phase has zero energy edge Majorana modes in open chains, and the two-fold degeneracy of the many-body SG spectrum (in this language) stems from the occupation/unoccupation of the bilocal Dirac mode formed from the edge Majoranas. With interactions, the

¹In the tails of the SG phase, $\overline{\log(J)} - \overline{\log(h)} \gtrsim 2$, the values of the couplings J are much bigger than the fixed interaction strength $J_z = 0.1$ so the problem effectively looks non-interacting. The PM does not suffer from this problem, and the strongly localized, interacting SG can be simply obtained by dualizing the PM.

edge mode remains coherent only in the MBL setting [64, 24]. Thus, the degenerate Floquet eigenstates can be connected by either (i) spectrum-generating operators localized near the edges which toggle the state of the coherent edge mode (fermionic language) or (ii) any spin operator that flips the parity of the eigenstates. Concretely, the spectral function of σ_i^+ , the spin raising operator on any site i , in the Floquet eigenbasis

$$\mathcal{A}(\omega) = \frac{1}{2^L} \sum_{\alpha\beta} \langle \phi_\alpha(0) | \sigma_i^+ | \phi_\beta(0) \rangle \delta(\omega - (\epsilon_\alpha - \epsilon_\beta)) \quad (5.5)$$

is a delta function peaked at $\omega = 0$ (this phase will hence also be labeled the ‘0’ phase below). Finally, we note that the SG displays long-range string order in all eigenstates regardless of boundary conditions. Without disorder, the string order vanishes even in the many body eigenstates of free fermion chains—despite the non-trivial momentum space topology present in their Hamiltonians.

5.3 Paramagnet-Spin Glass Phase transition

In the non-interacting problem we have strong evidence that the infinite disorder fixed point continues to control the physics. We have examined H_F and we find that all its eigenstates are localized even at the transition, and its structure differs from the canonical strong-disorder renormalization group form [110] by short ranged, irrelevant, terms. The ultimate fate of the critical region in the interacting driven problem is an interesting open question, but we note for now that our data on $\langle r \rangle$ suggests a partially delocalized interacting critical point.

5.4 π Spin Glass and 0π Paramagnet

We now present two new Ising phases which exist only in the driven system—the π -SG and the 0π -PM. Existing work on the band topology of translationally invariant Z_2

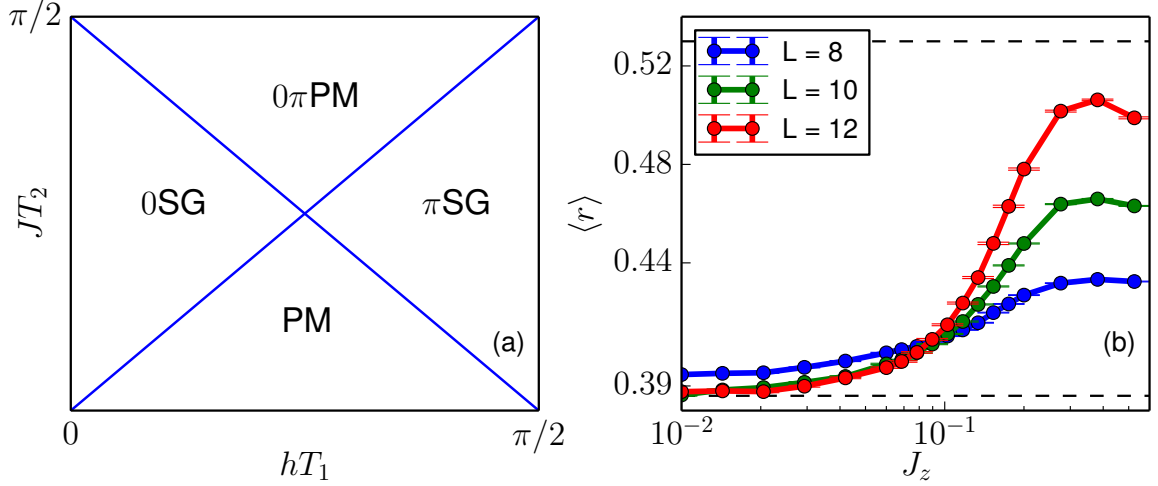


Figure 5.2: (a) Phase diagram for the binary Ising drive, Eq. (5.6) without interactions ($J_z = 0$) and disorder. (b) Level Statistics $\langle r \rangle$ of H_F in the π phase with parameters defined in the text and disorder averaged over 2000-100,000 realizations for different L s. H_F is localized for interaction strengths $J_z \lesssim 0.1$.

symmetric free-fermion chains [161, 28, 296] has shown that the Floquet eigenmodes for such chains with *open* boundary conditions can exhibit edge Majorana modes with $\epsilon_\alpha = \pi/T$ in addition to the better known edge modes with $\epsilon_\alpha = 0$. In the MBL setting in the ‘ π ’ phase, the MB Floquet eigenstates are long-range ordered and come in $|\pm\rangle$ cat pairs separated by quasienergy π/T . These can again be connected by either spectrum generating operators localized near the two edges (fermion language) or by local parity odd operators (spin language). Thus, the spectral function $\mathcal{A}(\omega)$ (5.5) now shows a delta function peak at $\omega = \pi/T$.

We now establish these phases for the binary periodic drive

$$H(t) = \begin{cases} H_z & \text{if } 0 \leq t < T_1 \\ H_x & \text{if } T_1 \leq t < T = T_1 + T_2 \end{cases} \quad (5.6)$$

$$\begin{aligned}
H_z &= \sum_{i=1}^L h_i \sigma_i^z + \sum_{i=1}^{L-1} J_z \sigma_i^z \sigma_{i+1}^z, \\
H_x &= \sum_{i=1}^{L-1} J_x \sigma_i^x \sigma_{i+1}^x + J_z \sigma_i^z \sigma_{i+1}^z.
\end{aligned}$$

Fig. 5.2(a) shows the uniform, non-interacting phase diagram with the four possible driven Ising phases. The phases labeled ‘0’ and ‘ π ’ have edge Majorana modes at quasienergies 0 and π/T respectively. With disorder and localization, these phases display long-range SG eigenstate order in the correlators (5.3) for both $A = x, y$. Moreover, in the π -SG phase, the time dependence of the C_{xx} and C_{yy} correlators over the period is non-trivially correlated: their magnitudes must cross twice (modulo 4) during a period. Thus, in this phase, the axis of SG order rotates by an angle π (modulo 2π) about the z -axis during the period which can be intuitively understood by thinking semi-classically about the drive (5.6) at the extremal boundaries of the phase diagram shown in Fig. 5.2(a). This sign reversal of the order parameter and thus doubling of the period (also found previously in [70]), provides a potential Floquet realization of a time crystal [328, 321]. Note that the issue at hand is a rotation of the order parameter about the z -axis, and thus one might imagine the existence of different Floquet phases (\mathbb{Z} classification) corresponding to rotations by all multiples of π . However, it was shown [316] that only the magnitude of the rotation modulo 2π is robust to continuous deformations of the unitaries, thus giving the two ‘0’ and ‘ π ’ phases. As before, without localization, only one of the Floquet eigenstates (analogous to the ground state) will display long-range order in the $0, \pi$ phases. The other two phases, labeled PM and 0π , have no long-range order and are respectively dual to the 0 and π phases.

We now turn to numerically identifying the localized π phase with disorder and interactions. We pick $T = 1, T_2 = \pi/2$ and $h_i T_1$ uniformly from the interval

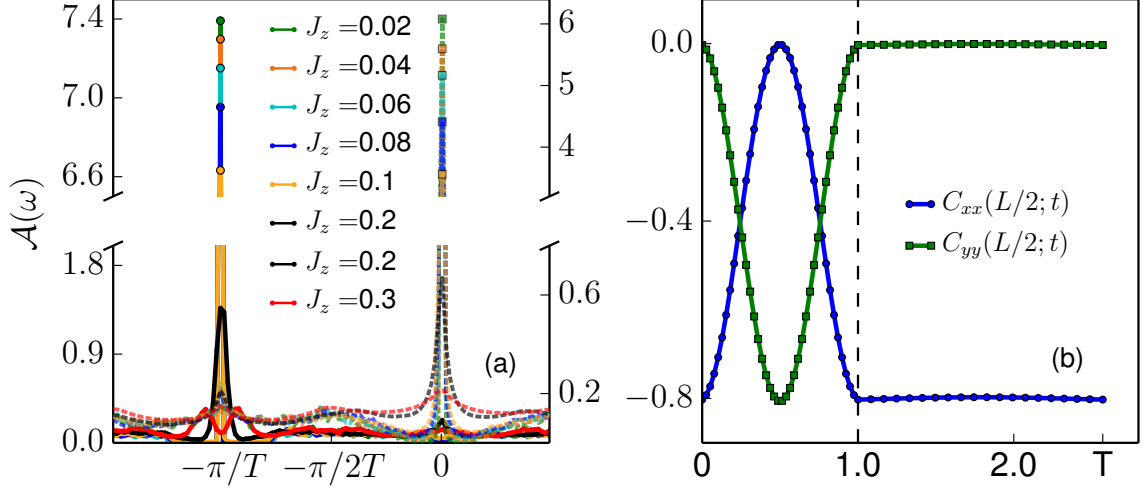


Figure 5.3: (a) Disorder averaged spectral function $\mathcal{A}(\omega)$ defined in Eq. (5.5). Solid (dashed) lines are for the π -SG (0-SG) phase showing a delta function peak at $\omega = \pi/T$ (0) for small interaction strengths which disappears as the interaction is increased. (b) Time dependence of the C_{xx} and C_{yy} correlators defined in Eq. (5.3) over one period for an eigenstate in the π phase; $L = 10$, $T_1 = 1$ and $J_z = 0.04$. The crossings are robust in the π phase.

(1.512, 1.551) and $J_i T_2$ from (0.393, 1.492), so that all pairs of values $(h_i T_1, J_j T_2)$ lie in the π/T Majorana region of the free uniform chains. We have confirmed that the free fermion disordered drive exhibits π/T Majoranas for open chains while all other modes are localized in the bulk. In Fig Fig. 5.2(b) we examine stability to interactions via $\langle r \rangle$ and clearly observe a transition around $J_z \approx 0.1$, with the small J_z regime being the MBL phase we seek.

Fig. 5.3(a) shows the appearance of the π/T peak in the disorder averaged spectral function (5.5) for system size $L = 10$ as the delocalization transition is crossed by decreasing the interaction strength. In contrast, the dashed lines show the spectral function for a similar drive in the 0-SG phase, clearly showing a peak at $\omega = 0$. Finally, Fig. 5.3(b) displays the anticipated time dependence of the SG order in the C_{xx} and C_{yy} correlators in a single eigenstate of the interacting system with $J_z = 0.04$ and $L = 10$. The crossings in the correlator within the period (modulo 4) are robust in the π -SG phase and topologically distinct from the correlators in the 0-SG phase

where there are no crossings (modulo 4). We emphasize that this is a true bulk diagnostic of the phase which, unlike the presence of an edge mode, is insensitive to boundary conditions. We also note that the non-trivial spin dynamics captured by it *cannot* be obtained without localization.

Finally we turn to the 0π -PM which is dual to the π -SG. This is an SPT phase with no bulk long-range order, but with coherent edge states. In the fermionic language, there are now two Majorana modes at each edge, one at quasienergy 0 and the other at π/T and thus MB spectrum is paired into conjugate sets of four MB states—two degenerate pairs of states separated by quasienergy π/T . The eigenstates in this phase do *not* look like global superposition states and the spectral function of bulk spin operators shows no structure. On the other hand, spectral functions of edge operators which toggle the state of the edge modes show a peak at both 0 and π/T .

5.5 Summary and open questions:

We have shown that MBL Floquet systems exhibit sharply defined phases bounded by parameter surfaces across which properties of their Floquet eigensystems change in a singular fashion. These phases include the trivial Floquet-ergodic phase and multiple non-trivial non-ergodic phases exhibiting various forms of ordering and dynamics, some of which are entirely new to Floquet systems. The net result is something quite striking given the contentious history of non-equilibrium statistical mechanics. Indeed, it is quite likely that Floquet systems constitute the maximal class for which such a definition of phase structure is possible; with generic time dependences it would not be surprising if heating to infinite temperatures is the inevitable result. Going forward we anticipate a more systematic search for Floquet phases and a better understanding of their phase diagrams. In this context we note two studies that

include disorder, but not interactions, in Floquet systems [300, 299]. It should also be possible to observe the new localized phases by the methods of Ref. [279].

Chapter 6

Absolute Stability and Spatiotemporal Long-Range Order in Floquet Systems

6.1 Introduction

In the previous chapter, we showed how Floquet localization allows phases to be defined for MBL-Floquet systems via a generalization of the idea of eigenstate order [169]. We now turn to a more detailed characterization of these Floquet phases.

In the undriven setting, an early paradigm for classifying phases, associated most with Landau, characterizes phases through the spontaneous breaking of global symmetries present in the microscopic Hamiltonian *i.e.*, phases are either paramagnetic, or spontaneously symmetry broken (SSB). In modern parlance, the phases obtained thereby are symmetry protected since their distinctions are erased if the symmetries are not present microscopically. More recently, it has been found that this characterization is too coarse — not all paramagnetic phases should be considered identical. Indeed, there exist paramagnetic symmetry protected topological (SPT) phases, such

as those discussed in Chapter 4, which do not break any symmetries, but which nevertheless cannot be adiabatically connected to one another in the presence of the protecting global symmetry [72]. Remarkably, we now know of other phases, such as those with topological order, which do not even require a global symmetry and are *absolutely stable*—their ground state (and sometimes even low temperature) properties are stable to arbitrary weak local perturbations [325, 178, 136]. Equally remarkably, we have seen that in MBL systems, the entire many body spectrum displays some absolutely stable property and is characterized by a full set of emergent local conserved quantities [148, 283, 153, 284, 66, 271, 238, 260]. As we have seen, one can also combine MBL with the above quantum orders to obtain MBL phases in which individual highly excited eigenstates show SSB, SPT, or topological order [149, 239, 29, 64, 24, 255].

We now consider these ideas in the driven setting. In the previous chapter, we showed that both paramagnetic and spin-glass phases can be defined for Floquet MBL systems. In very recent work, a classification was given for Floquet phases that either preserve [317, 100, 253] or spontaneously break [316] unitary global symmetries¹. In the present chapter we build on the latter work and show that a subset of the SSB phases identified therein are stable to arbitrary weak local perturbations, including those that explicitly break any of the defining global symmetries. Thus this subset is *absolutely stable*—a remarkable outcome for a driven system. The apparent puzzle that SSB phases can be stable absent Hamiltonian independent symmetries is resolved elegantly: at general points in these absolutely stable phases, the drives (in the infinite volume limit) are characterized by a set of Hamiltonian *dependent* emergent unitary and antiunitary symmetries. *Ex post facto*, we see that the symmetric models in the previous chapter and Refs. [169, 316] live in lower dimensional sub-manifolds (characterized by Hamiltonian independent symmetries) of a much higher

¹We use the term “spontaneously break unitary global symmetries” to mean that the eigenstates exhibit the long-range order characteristic of spontaneous symmetry breaking.

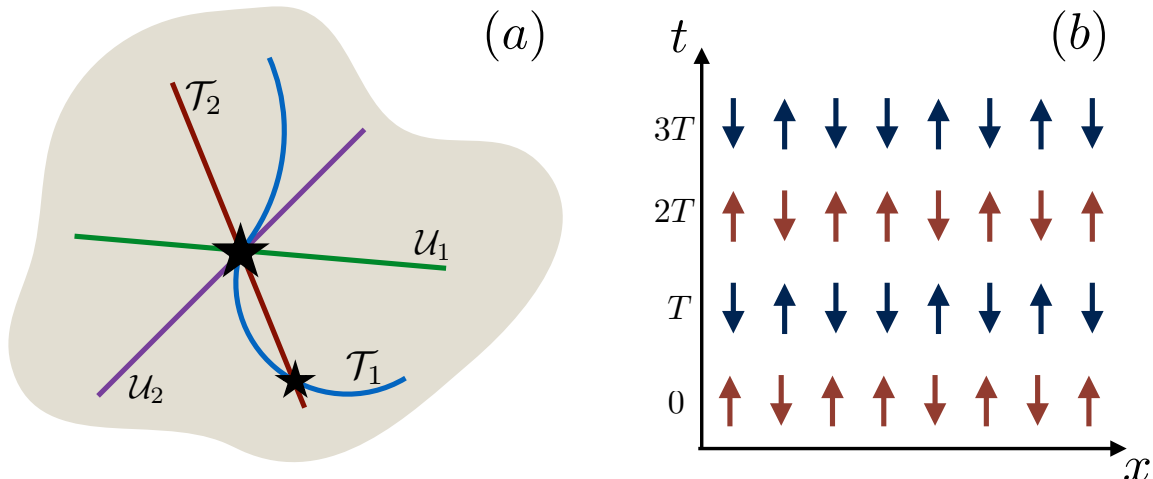


Figure 6.1: (a) Schematic depiction of the manifold of Floquet unitaries that are absolutely stable and characterized by Hamiltonian dependent emergent symmetries (grey area). Special sub-manifolds (colored lines) within the absolutely stable manifold are characterized by Hamiltonian *independent* unitary (\mathcal{U}_i) and antiunitary (\mathcal{T}_i) symmetries. Special models (black stars) can lie at the intersection of several sub-manifolds with exact symmetries. As an example, the π SG model defined in Refs. [169, 316] is absolutely stable and possesses the Ising unitary symmetry P and an antiunitary symmetry $\mathcal{T} = KP$ where K is complex conjugation. (b) Schematic depiction of the spatiotemporal long-range order found in absolutely stable phases—the order looks “antiferromagnetic” in time and glassy in space.

dimensional absolutely stable phase — we sketch the resulting structure in Fig. 6.1. This analysis uncovers a much richer symmetry structure than the global unitary symmetries used in previous work.

Strikingly, the out of equilibrium dynamics in these phases exhibits sharp universal signatures associated with oscillations of an emergent order parameter; these generalize the multiple period oscillations uncovered in previous work [169, 316] on symmetric drives. For example, we show that starting from arbitrary short range correlated initial states, the late time states show sharp oscillations of generic local operators at multiples of the fundamental period. This particular dynamical feature is a great boon to a future experimental detection of these phases as experimentalists are required neither to fine tune the Hamiltonian nor the starting state to observe a sharp signature!

These longer periods raise the question of whether they should be thought of as representing spontaneous breaking of yet another symmetry—that of time translations by a period of the drive². We note that the idea that time translations might be analyzed in this fashion was first mooted by Wilczek [328] for time independent Hamiltonians; there is, however, now a proof [321] that such “time crystals” do not exist for undriven systems in equilibrium. We analyze this question further and find that strictly speaking *all* MBL systems, driven or undriven, exhibit some eigenstate correlations characteristic of temporal *glasses*—an aperiodic breaking of time translation invariance (TTI). For the Floquet broken symmetry phases however, the long distance correlations simultaneously exhibit spin glass order in space and multiple period oscillation in time. These lead to the characteristic space-time snapshot illustrated for the simplest such phase in Fig. 6.1(b). Evidently the system exhibits spatiotemporal³ long-range order in both space and time. The modulation in time, which is antiferromagnetic, does indeed break time translation symmetry but it preserves the combination of a translation and emergent Ising reversal. We note that a similar spatiotemporal order—now ferromagnetic in space—was previously exhibited in the large N Floquet theory [70] and discussed in the terminology of a lack of synchronization with the drive.

We note that the discovery of these absolutely stable Floquet phases can also be viewed as the realization that while a Hamiltonian that lacks *any* symmetries (inclusive of time translation invariance) exhibits only a trivial phase, introducing discrete time translation invariance *alone* is sufficient to introduce a non-trivial phase structure. This would appear to be the minimum symmetry condition for this purpose.

In the rest of the chapter we describe these results in more detail. We begin with the simplest example of a SSB phase that is absolutely stable—this is the Ising

²We thank Ehud Altman for this incisive question.

³While spatiotemporal order has been discussed for classical systems out of equilibrium, e.g. Ref. [275], to our knowledge this is the first appearance of such order for quantum systems.

π spin-glass or π SG introduced in Chapter 5 and Refs [169, 316]. In Sec. 6.2 we establish its absolute stability and analyze its emergent symmetries, correlations and characteristic spectral features within the paradigm of eigenstate order. Next, in Sec. 6.3 we study the nature of dynamical correlations in the π SG in individual eigenstates and starting from generic short ranged entangled states, and discuss why the π SG should be identified as a Floquet space-time crystal. We then discuss the catalog of other absolutely stable Floquet phases in Sec. 6.4, and show how some Floquet SPT phases exhibit time crystallinity at their boundaries. We end with some concluding remarks in Sec. 6.5.

6.2 The π Spin glass: Absolute stability and emergent symmetries

6.2.1 Properties of the π SG phase

Chapter 5 and Refs. [169, 317, 316] discussed various SSB/SPT phases with Floquet eigenstate order, but not all of these phases are absolutely stable to arbitrary perturbations. In this work, our canonical example of an absolutely stable Floquet phase will be the π spin-glass (π SG) phase [169]. A concrete model Floquet unitary in this phase in 1d is

$$U_{f0} = P_x \exp[-i \sum_{r=1}^{L-1} J_r \sigma_r^z \sigma_{r+1}^z]; \quad P_x = \prod_r \sigma_r^x, \quad (6.1)$$

where L is the system size, the σ_r^α for $\alpha = \{x, y, z\}$ are Pauli spin 1/2 degrees of freedom on site r , $P \equiv P_x$ is the global Ising parity symmetry ($P_{y,z}$ analogously defined), and the J_r 's are random couplings drawn uniformly from $[\bar{J} - \delta J, \bar{J} + \delta J]$.

We note several properties of this model:

1. U_{f_0} commutes with the unitary symmetry P . Defining anti-unitary operators $\mathcal{T}_\alpha = P_\alpha K$ where K is complex conjugation, U_{f_0} also has $\mathcal{T} \equiv \mathcal{T}_x$ symmetry: $\mathcal{T}U_{f_0}\mathcal{T}^{-1} = U_{f_0}^{-1}$. It similarly has $\mathcal{T}_{y,z}$ symmetry for systems with an even number of sites⁴. Thus, this model lies at the intersection of several special submanifolds with Hamiltonian independent symmetries (Fig. 6.1) and is extremely robust to a large class of perturbations which preserve *some* exact symmetry. Note that the anti-unitary symmetries \mathcal{T} are a combination of K and a spatial Ising flip.
2. The eigenspectrum of U_{f_0} can be found by noting that all the domain wall operators $D_r \equiv \sigma_r^z \sigma_{r+1}^z$ commute with P_x , U_{f_0} and with one another. Thus, the eigenstates look like symmetric/antisymmetric global superposition states (also called cat states) of the form

$$|\pm\rangle \sim |\{d_r\}, p = \pm 1\rangle = \frac{1}{\sqrt{2}}|\{\sigma_r^z\}\rangle \pm \frac{1}{\sqrt{2}}|\{\overline{\sigma_r^z}\}\rangle,$$

where $\{\sigma_r^z\} = \{\uparrow\downarrow\downarrow \cdots \uparrow\}$ labels a frozen spin-glass configuration of z spins (and hence the domain wall expectation values d_r), $\{\overline{\sigma_r^z}\}$ is its spin-flipped partner, and $p = \pm 1$ is the Ising parity eigenvalue of the eigenstates.

3. The eigenstates above have corresponding unitary eigenvalues $u(d, p) = pe^{-i\sum_{r=1}^{L-1} J_r d_r}$. Note that the opposite parity cat-state partners have unitary eigenvalues differing by a minus sign $u(d, -1) = -u(d, 1)$ and hence quasienergies differing by π/T . We refer to this phenomenon as a π spectral pairing of cat states.
4. The Floquet eigenstates exhibit long range connected correlations (LRO) and spin glass (SG) order in σ_i^z , but show no long-range order in σ_i^x and σ_i^y .

⁴These symmetries have similar implications, which we do not discuss here for brevity.

5. The order parameter for the π SG model oscillates with frequency π/T or period $2T$, as indicated by the stroboscopic equation of motion $\sigma_r^z(nT) = (-1)^n \sigma_r^z$. This follows directly from the fact that σ_r^z anticommutes with U_{f0} . While $\langle \sigma_r^z(nT) \rangle = 0$ in the Floquet eigenstates, the observable shows a periodic time dependence with period $2T$ in short-range correlated states of the form $|\{\sigma_r^z\}\rangle \sim |+\rangle + |-\rangle$. On the other hand, the σ^x and σ^y operators do not show period $2T$ oscillations.

6.2.2 Absolute stability and emergent symmetries

How robust are the above properties to perturbations of the form $H(t) \rightarrow H(t) + \lambda V(t)$? Numerical results in the previous chapter have already demonstrated the stability of U_{f0} to weak Ising [169] symmetric perturbations. We will provide evidence that this phase is, in fact, absolutely stable to *all* generic weak perturbations — we will define dressed spin operators (Floquet l-bits) for the perturbed system and show that it displays *emergent* symmetries with the same effect on eigenspectrum properties as the exact Ising symmetry.

The first step in the argument is to observe that the stability of the localization of the unperturbed unitary to arbitrary weak local perturbations (for sufficiently strong disorder) is itself not a consequence of symmetries. More technically, call the corresponding perturbed Floquet unitary $U_{f\lambda}$ where λ is the strength of the perturbation. We expect that the stability of localization implies the existence of a family of local unitaries⁵ \mathcal{V}_λ which relate the eigenvectors of U_{f0} to those of $U_{f\lambda}$ for λ in some non-vanishing range [2, 252, 316, 99]. Note that the locality of such a unitary is a subtle business outside of the very strongly localized region due to proliferating resonances and Griffiths effects [29, 121].

⁵A local (or low depth) unitary is a unitary which can be written as $\mathcal{V} = \mathcal{T} e^{-i \int_0^t ds K(s)}$ for some local bounded Hamiltonian $K(t)$, with t finite in the thermodynamic limit.

Assuming that a low depth \mathcal{V}_λ exists, it relates the new eigenvectors of $U_{f\lambda}$ denoted $|\alpha\rangle_\lambda$ to the eigenvectors of U_{f0} via

$$|\alpha\rangle_\lambda = \mathcal{V}_\lambda |\{d_r\}, p\rangle.$$

The new quasienergies are similarly denoted as ϵ_λ^α . These local unitaries allow us to define a set of dressed, exponentially localized operators $\tau_{r,\lambda}$ (analogous to the l-bits [284, 283, 148, 271, 66] in static MBL systems) together with a dressed parity operator P^λ via

$$\begin{aligned} \tau_{r,\lambda}^\beta &= \mathcal{V}_\lambda \sigma_r^\beta \mathcal{V}_\lambda^\dagger \\ P^\lambda &= \prod_r \tau_r^x. \end{aligned} \tag{6.2}$$

We will often suppress the explicit λ dependence of $\tau_{r,\lambda}^\alpha$ for brevity and $\beta = x, y, z$. Defining (local) dressed domain wall operators as $D_r^\lambda \equiv \tau_r^z \tau_{r+1}^z$, we get

$$\begin{aligned} D_r^\lambda |\alpha\rangle_\lambda &= \mathcal{V}_\lambda (\sigma_r^z \sigma_{r+1}^z) |\{d_r\}, p\rangle = d_r |\alpha\rangle_\lambda, \\ P^\lambda |\alpha\rangle_\lambda &= \mathcal{V}_\lambda P |\{d_r\}, p\rangle = p |\alpha\rangle_\lambda. \end{aligned} \tag{6.3}$$

Thus, the perturbed eigenstates are also eigenstates of the dressed operators D_r^λ and P^λ which means these operators commute with $U_{f\lambda}$, and we can rewrite $|\alpha\rangle_\lambda$ more suggestively as $|\{\tau_r^z\}, p = \pm 1\rangle$ using the same notation as before. By definition, τ_r^z anticommutes with P^λ . Further we show in App. 6.A that it also anticommutes with $U_{f\lambda}$ in the large system limit

$$[\tau_r^z, U_{f\lambda}]_+ = O(e^{-cL}) \xrightarrow{L \rightarrow \infty} 0, \tag{6.4}$$

using only the assumptions of locality and continuity. This implies that the Floquet eigenvalues are odd in p . Together with the previous statements about the commutation properties of P^λ and D^λ with $U_{f\lambda}$, it is easy to show that the unitary eigenvalues take the form $u_\lambda(\{d_r\}, p) = pe^{-if(\{d\})}$. Re-expressing the eigenvalue dependence on conserved quantities in operator language gives

$$U_{f\lambda} = P^\lambda e^{-if(\{D_r^\lambda\})}, \quad (6.5)$$

where f is a functional of D^λ , or equivalently an even functional of the τ_r^z 's. One can moreover argue that f can be chosen to be local, using the fact that the Floquet unitary itself is low depth [317, 316]. Thus, f generically takes the form

$$f(\{D^\lambda\}) = \sum_{ij} J_{ij} \tau_i^z \tau_j^z + \sum_{ijkl} J_{ijkl} \tau_i^z \tau_j^z \tau_k^z \tau_l^z + \dots$$

where the couplings $J_{ij} \sim e^{-|i-j|/\xi}$ decay exponentially with distance reflecting the locality of the unitary.

Written this way, the Floquet unitary (6.5) clearly has a \mathbb{Z}_2 symmetry P^λ — although we say it is emergent because P^λ , in general, depends on the details of the underlying Hamiltonian. $U_{f\lambda}$ similarly has an emergent antiunitary symmetry $\mathcal{T}^\lambda \equiv P^\lambda K^\lambda$ where K^λ is complex conjugation defined with respect to the τ^α . Note that Eq. (6.5) takes much the same functional form as the model unitary Eq. (6.1), and correspondingly its eigenstates exhibit long-range order in the dressed order parameter τ_r^z (associated with spontaneous breaking of P_λ), and short range order in $\tau_r^{x,y}$. The statements about π spectral pairing and the temporal dependence of observables (in particular $\tau^z(nT) = (-1)^n \tau^z(0)$) also follow directly⁶.

⁶In principle we can now identify symmetry defined submanifolds based on keeping the emergent symmetries about *any* fixed point in the π SG which provides an “origin independent” view of the structure of the phase. The functional form of the perturbed unitary $U_{f\lambda}$ (6.5) and its implications are among the central results of this chapter.

Finally, we note that Refs [169, 317] also defined a 0SG phase with the model unitary $\exp[-i \sum_{i=1}^{L-1} J_i \sigma_i^z \sigma_{i+1}^z]$. Like the π SG, this is also a phase with long-range SSB Ising order, but one in which the cat states are degenerate instead of being separated by π/T . If we generically perturb about this drive, we must begin with Floquet eigenstates that explicitly break the Ising symmetry in order for the change of basis unitary \mathcal{V}_λ to be local. Implicitly this requires us to work in the infinite volume limit directly. In this case, one can show that τ^z commutes (rather than anticommutes) with the Floquet unitary, and one can readily use this to split the degeneracy between the Floquet eigenstates, rendering this phase unstable to arbitrary perturbations. By contrast, in the π SG phase, the cat states are π split and therefore non-degenerate — a fact which is essential to the stability of the SSB order to arbitrary perturbations.

6.2.3 Long range order and numerics

We now numerically check for the predicted π spectral pairing in a perturbed model of the form

$$U_{f\lambda} = P \exp[-i \sum_{r=1}^{L-1} J_r \sigma_r^z \sigma_{r+1}^z - i\lambda \sum_{r=1}^L h_r^x \sigma_r^x + h_r^y \sigma_r^y + h_r^z \sigma_r^z] \quad (6.6)$$

The fields $J_r, h_r^{x,y,z}$ are drawn randomly and uniformly with $\overline{J_r} = 1, \delta J_r = 0.5, \overline{h_r^x} = \delta h_r^x = 0.1, \overline{h_r^y} = \delta h_r^y = 0.15, \overline{h_r^z} = \delta h_r^z = 0.45$ and the notation $\overline{x}, \delta x$ means that x is drawn from $[\overline{x} - \delta x, \overline{x} + \delta x]$. The perturbation breaks all the unitary and anti-unitary symmetries present in the original U_{f0} model. To check for spectral pairing, we define the nearest neighbor gap between the perturbed quasienergies as $\Delta_0^i = \epsilon_{i+1}^\lambda - \epsilon_i^\lambda$ and the π gap as $\Delta_\pi^i = \epsilon_{i+\mathcal{N}/2}^\lambda - \epsilon_i^\lambda - \pi/T$ where $\mathcal{N} = 2^L$ is the Hilbert space dimension, and where the second equation follows from the fact that the quasienergy bandwidth is π/T and we expect states halfway across the spectrum to be paired at π/T (See Fig. 6.2 (inset) for an illustration of these definitions). The system shows spectral

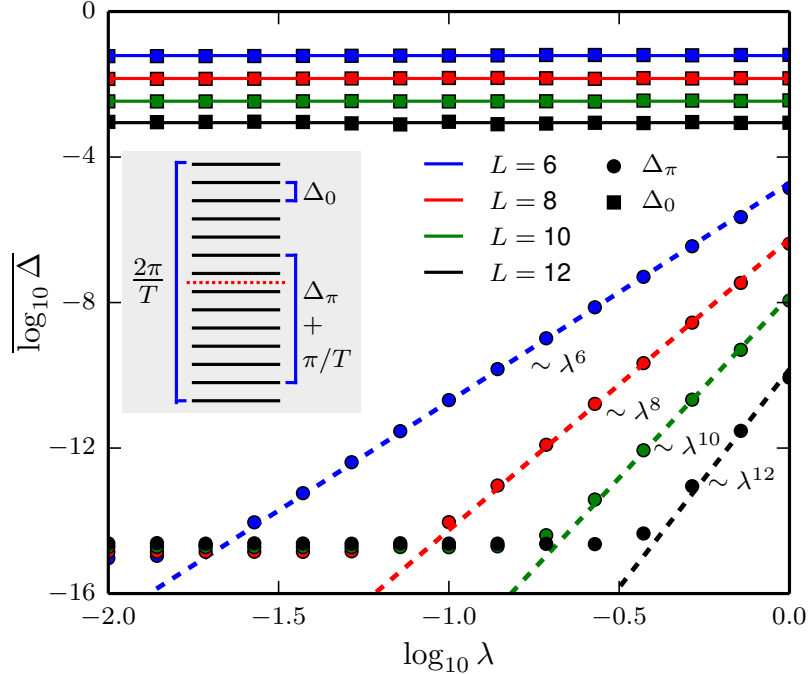


Figure 6.2: Disorder and eigenstate averaged spectral gaps for the generically perturbed model (6.6) without any P and \mathcal{T} symmetries plotted as a function of the perturbation strength λ and system size L . The nearest-neighbor quasienergy gap Δ_0 shows no λ dependence but decreases exponentially with L . On the other hand Δ_π which measures the spectral pairing of even-odd parity states scales as λ^L (fits to this form superimposed). Thus, there is a window of λ s for which $\Delta_\pi \ll \Delta_0$ and the system exhibits robust spectral pairing in the $L \rightarrow \infty$ limit. Gaps smaller than $\sim 10^{-14}$ are below numerical precision, thus the initial λ independent trend in the Δ_π data for larger L . (inset): Cartoon of the quasienergy spectrum illustrating the definitions of Δ_0 and Δ_π .

pairing at π if there is a range of λ 's for which $\Delta_\pi \ll \Delta_0$ as $L \rightarrow \infty$. Fig. 6.2 shows the mean Δ_π and Δ_0 log-averaged over eigenstates and several disorder realizations for different λ 's and L 's. We see that $\overline{\Delta_\pi} \sim \lambda^L$ whereas $\overline{\Delta_0} \sim e^{-sL}$ where $s \sim \log(2)$ is a λ independent entropy density. Thus, we can get robust pairing in the window $|\log \lambda| > s$.

Having shown how the robustness of the π SG phase is associated with spontaneously broken emergent symmetries and long-range order in the τ^z variables, we can now ask what effect this long-range order has on correlations in the physical σ^α degrees of freedom. Generically we expect the expansion of the physical spins in terms

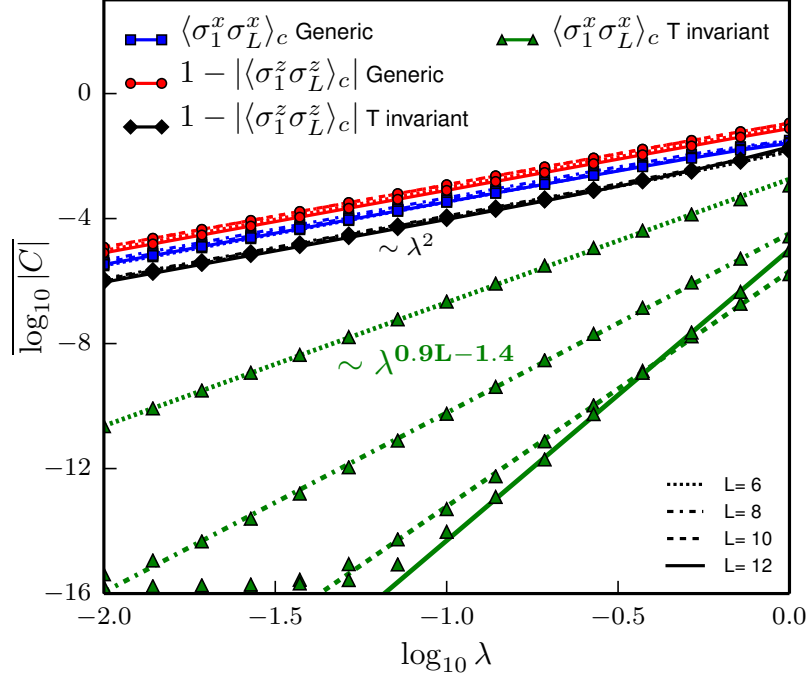


Figure 6.3: Disorder and eigenstate averaged end-to-end connected correlation functions for $\sigma^{x,z}$ in the “generic” model (6.6) with no P, \mathcal{T} symmetries (blue squares, red circles) and a model [99] with \mathcal{T} symmetry obtained by setting $h^y = 0$ in (6.6) (black diamonds, green triangles). As discussed in the text, the generic model shows long-range order for both operators which is signaled here by correlations scaling as λ^2 independent of system size. On the other hand, in the model with \mathcal{T} symmetry, only σ^z shows long-range order while the σ^x correlator scales as $\lambda^{f(L)}$ where $f(L) \sim 0.9L - 1.4$ (fits shown) and thus vanishes in the $L \rightarrow \infty$ limit. This is to be expected from symmetry constraints. The σ^y correlators (not shown here) also display long-range order in the generic model but not in the \mathcal{T} symmetric model.

of l-bits to have some components which are diagonal and odd in τ^z , for example $\sigma_r^\alpha = c^\alpha \tau_r^z + \dots$. As a result $\sigma_r^{\alpha=x,y,z}$ are all expected to have long range connected correlation functions, as well as a component exhibiting $2T$ periodic stroboscopic oscillations. These predictions agree with our numerical results Fig. 6.3 and Fig. 6.4 respectively.

On the other hand, when we perturb U_{f_0} in a manner that respects an explicit symmetry like P or \mathcal{T} , the resulting models reside in a special submanifold of the absolutely stable phase. The presence of the exact symmetries constrains the form of the dressed τ^α operators and leads to concrete predictions about the order in and

temporal dependence of different operators. For example, it was argued [316] that when the perturbation $\lambda V(t)$ is such that $U_{f\lambda}$ continues to have Ising symmetry, \mathcal{V}_λ can be chosen to commute with P . As a result, $P^\lambda = P$, and $\sigma^{y,z}$ are odd under P^λ whereas σ^x is even under P^λ . This means an operator expansion of σ_r^x in terms of the dressed τ_r^α operators can only involve even combinations of τ : $\sigma_r^z = \alpha_1 \tau_r^x + \beta_2 \tau_r^z \tau_{r+1}^z + \dots$. Hence the *connected* correlation functions of σ_{rs}^x should decay exponentially with $|r-s|$, and this operator is not expected to have robust period $2T$ oscillations. On the other hand $\sigma_r^{y,z}$ will generically exhibit both long range connected correlations as well as period $2T$ oscillations.

Similarly we can pick perturbations for which $U_{f,\lambda}$ respects antiunitary symmetries like $\mathcal{T} = PK$, i.e., for which $\mathcal{T}U_{f,\lambda}\mathcal{T} = U_{f,\lambda}^{-1}$. As an example, the model studied in Ref. [99] resembles Eq. (6.6) with $h^y = 0$, so has the effect of perturbing Eq. (6.1) by $\lambda V \sim h_r^z \sigma_r^z + h_r^x \sigma_r^x$. With this choice of V it is straightforward to verify that the corresponding $U_{f,\lambda}$ respects \mathcal{T} symmetry

$$\begin{aligned}
\mathcal{T}U_{f,\lambda}\mathcal{T}^{-1} &= (PK)U_{f,\lambda}(PK)^\dagger \\
&= (PK)P \exp\left[-i \sum_{r=1}^{L-1} J_r \sigma_r^z \sigma_{r+1}^z + h_r^z \sigma_r^z + h_r^x \sigma_r^x\right] (PK)^\dagger \\
&= \exp\left[i \sum_{r=1}^{L-1} J_r \sigma_r^z \sigma_{r+1}^z + h_r^z \sigma_r^z + h_r^x \sigma_r^x\right] P \\
&= U_{f,\lambda}^{-1}.
\end{aligned} \tag{6.7}$$

In this case, we can pick the change of basis matrix \mathcal{V}_λ to commute with \mathcal{T} (see App. 6.B) which implies that τ^x, τ^y, τ^z are even, even, and odd respectively under \mathcal{T} . In turn, the operator expansions of $\sigma^{x,y}$ can only contain terms with even numbers of τ^z s in their expansions. Hence neither should exhibit protected π/T oscillations, nor should they have long range connected correlations as demonstrated in Fig. 6.3. This

accounts for the absence of π/T oscillations for $\sigma_r^x(nT), \sigma_r^y(nT)$ in the data presented in Ref. [99].

6.3 The π Spin Glass: Spatiotemporal Long Range Order

We have already discussed above that at general points in the absolutely stable π SG phase the emergent order parameter operators, τ_i^z , change sign every period. Prima facie, this implies the spatiotemporal order sketched in Fig. 1b: spin glass order in space and antiferromagnetic order in time.

The aim of this section is to more sharply characterize this spatiotemporal order. As the π SG is a localized phase, unlike in the equilibrium context, there is not an obviously correct set of correlations one should examine to detect said order. We propose to examine the time dependent one and two point correlation functions of local operators in two families of states. The first are the Floquet eigenstates which are the basis of the eigenstate order paradigm of phase structure in Floquet systems. The second are the late time states reached by time evolving from general initial states; these are particularly relevant to experiments where the preparation of Floquet eigenstates is not feasible.

6.3.1 Eigenstate correlations and response

We start by considering Floquet eigenstates for the π SG. All single time operators $\langle O(t) \rangle$ in these are strictly periodic with period T —this is the analog of the time independence of single time operators in Hamiltonian eigenstates and hence the temporal component of the order is invisible to such operators. The invisibility of temporal order in the $\langle O(t) \rangle$ is analogous to the invisibility of Ising symmetry breaking in one point expectations of spatially local Ising-odd operators in globally Ising sym-

metric states. From this perspective [321] it follows that to detect temporal order we must either (a) examine a two time function of some operator or (b) explicitly add an infinitesimal field that selects the desired temporal order (much as we would examine long-range order in two-point functions of Ising-odd variables and/or add an infinitesimal Ising symmetry breaking term to detect spontaneously broken Ising symmetry).

We begin with (a) and examine time-dependent correlators

$$\begin{aligned}
C_\alpha(nT; r, s) &\equiv \langle \alpha | O_r(nT) O_s | \alpha \rangle \\
&= \sum_{\beta} e^{-inT(\epsilon_\alpha - \epsilon_\beta)} \langle \alpha | O_r | \beta \rangle \langle \beta | O_s | \alpha \rangle
\end{aligned} \tag{6.8}$$

of operators $O_{r/s}$ localized near sites r, s in the Floquet eigenstates $|\alpha\rangle = |\{d\}, \pm\rangle_\lambda$ (see Sec. 6.2 for notation). The operator expansion of $O_{r/s}$ in the τ^α basis will generically contain terms that are odd combinations of τ^z s. In the π SG phase, these have matrix elements between $|\alpha\rangle$ and its parity flipped partner and thus $C_\alpha(nT)$ generically has a frequency π/T component. In addition, the off-diagonal terms in the operator expansion involving $\tau^{\{x,y\}}$ will make local domain wall excitations near sites r/s . Now a crucial point: if r, s are held a fixed distance apart in the infinite volume limit, then $C_\alpha(nT)$ breaks TTI for *any* MBL-Floquet system. The reason is that one can crudely view a Floquet MBL system as a set of weakly interacting localized modes (the effective domain wall operators in this case) each with their own local spectra. As in the simplest case of 2-level systems whose physics is that of Rabi oscillations, these local subsystems (which are excited by $\tau^{x/y}$) exhibit response at frequencies incommensurate with the driving frequency. The presence of these incommensurate frequencies means $C_\alpha(nT)$ in *all MBL-Floquet systems always look glassy*, although for the π SG there is generically also a quantized response at π/T .

This short distance temporal glassiness however goes away when we examine long distances in space by placing the operators arbitrarily far apart in an infinite system, *i.e.*, by taking $\lim_{L \rightarrow \infty}$ before examining the limit $|r - s| \rightarrow \infty$. Since the operator expansions of $O_{r/s}$ are exponentially localized near sites r/s , the off-diagonal terms in the expansion of O_r which create domain-wall excitations near site r *cannot be annihilated* by the action of O_s in the limit $|r - s| \rightarrow \infty$ under the assumption of locality.

Thus, the only terms that contribute to $C_\alpha(nT; r, s)$ in this limit are diagonal in τ^z s. Terms odd in τ^z give a response at π/T while the even terms give a response at frequency 0. Thus we can write

$$C_\alpha(nT; r, s) \sim c_0(r; \alpha)c_0(s; \alpha) + c_1(r; \alpha)c_1(s; \alpha)(-1)^n$$

where the second piece reflects the spatiotemporal order of the odd τ^z terms, as well as the connected part of the correlation function. The dependence of the coefficients on r , s and α has been made explicit to emphasize the glassy nature of the order in space. This establishes a connection between the long range spatial order in the eigenstates and the period $2T$ temporal order.

The above analysis can be complemented by taking the approach (b) and adding to $H(t)$ a “staggered field” in time of the form $\epsilon \sum_n (-1)^n V \delta(t - nT)$, where V is odd and diagonal in τ^z . Now consider time-dependent expectation values of generic local operators O_r (which have a projection on odd τ^z terms) in the Floquet eigenstates $|\alpha\rangle_\epsilon$ for the new period $2T$ unitary which can be reshuffled to the form $U_{f,\epsilon}(2T) = e^{-i2\epsilon V} U_{f,0}^2$. This problem looks like the classic Ising symmetry breaking problem. At $\epsilon = 0$, $U_{f,\epsilon}(2T) = U_{f,0}^2$ has two degenerate states in the infinite volume limit. If V breaks the symmetry between two members of the doublet then

$$\lim_{\epsilon \rightarrow 0} \lim_{L \rightarrow \infty} \epsilon \langle \alpha | O_r(nT) | \alpha \rangle_\epsilon = b_0(r; \alpha) + b_1(r; \alpha)(-1)^n$$

since the perturbed period $2T$ eigenstates $|\alpha\rangle_\epsilon$ just look like product states of τ^z in this limit and are thus superpositions of the opposite parity eigenstates of $U_{f\lambda}$. On the other hand, the opposite order of limits gives $\lim_{L \rightarrow \infty} \lim_{\epsilon \rightarrow 0} \epsilon \langle \alpha | O_r(nT) | \alpha \rangle_\epsilon = b_0(r; \alpha)$. We emphasize that the measures discussed here are *eigenstate* measures. If averaged over all eigenstates the signatures vanish.

6.3.2 Quenches from general initial states

We now turn to the question of evolution from more general initial states rather than eigenstates. This is experimentally important, and more particularly so because the Floquet eigenstates for the π SG are macroscopic superpositions and thus hard to prepare. For concreteness, consider starting from a short-range correlated state like a product state of the physical spins. In the following we will adapt the analysis of dephasing in quenches in MBL systems [284, 149]. We will assume that the starting state exhibits a non-zero expectation value for the order parameter, i.e. $\langle \psi_0 | \tau_i^z | \psi_0 \rangle \neq 0$; if it does not the temporal features will be entirely absent. For simplicity we will only discuss one point functions as they are already non-trivial in this setting and the generalization is straightforward.

In a finite size system, τ^z only anticommutes with the Floquet unitary up to exponentially small in L corrections (6.4), which in turn introduce corrections to the equation of motion: $\tau^z(nT) = (-1)^n \tau^z(0) + O(e^{-L})$. This leads to exponentially small shifts in the spectral pairing at π/T which varies randomly between pairs of eigenstates. Ignoring these shifts for times $1 \ll t \ll O(e^{+L})$, one can readily show that for any finite system the one point functions will generically show glassy behavior with incommensurate Fourier peaks along with an additional peak at π/T ; see Fig. 6.4 for an illustration. More precisely, the logarithmic in time dephasing of correlations in MBL systems [284, 148] can be used to show that the correlators will show aperiodic behavior stemming from these additional Fourier peaks with a power law envelope

$\sim t^{-b}$, where $b > 0$ depends on the localization length [284]. *Thus, finite systems at large but not exponentially large times look like time-glasses with an additional quantized response at $\omega = \pi/T$.* However, if one waits a time $t \sim e^L$ that is long enough to (i) resolve the exponentially small many-body level spacings and (ii) to resolve the shifts in the spectral pairing away from π/T , both the peak at π/T and the extra incommensurate peaks almost entirely decay away due to usual dephasing mechanisms leaving behind aperiodic oscillations with a magnitude of $O(e^{-L})$. It is worth reminding the reader that the precise details of the time dependence will reflect the choice of the starting state and disorder realization.

We can formalize the above in two non-commuting limits: (a) $\lim_{t \rightarrow \infty} \lim_{L \rightarrow \infty}$ and (b) $\lim_{L \rightarrow \infty} \lim_{t \rightarrow \infty}$. While (a) characterizes the “intrinsic” quench dynamics of this phase, experiments will only have access to limit (b). In (b) the late time aperiodic oscillations with envelope $O(e^{-L})$ discussed above also go away, and the one-point functions are constants. In (a) we never reach times of $O(e^L)$ and instead observe persistent oscillations with period $2T$ out to $t \rightarrow \infty$ with all additional incommensurate oscillations decaying away as a power of time.

Thus, the intrinsic dynamical response of this phase is characterized by a single quantized Fourier peak at $\omega = \pi/T$ which goes along with formally exact spectral pairing at π/T and LRO in τ^z . In this limit, the late time state exhibits a precisely doubled period for every single realization of disorder and combined space-time measurements would lead precisely to the kind of snapshot sketched in Fig. 1b. More concretely, state-of-the-art experiments in ultracold atoms [279, 191, 42, 75] have convincingly demonstrated that a fingerprint of the initial state persists to asymptotically late times in the MBL phase. In a generalized experimental setup probing the π SG phase in the MBL Floquet problem⁷, the persistence of the starting fingerprint would measure localization and spatial spin glass order, while oscillations in time

⁷We thank Christian Gross for discussions on possible experiments.

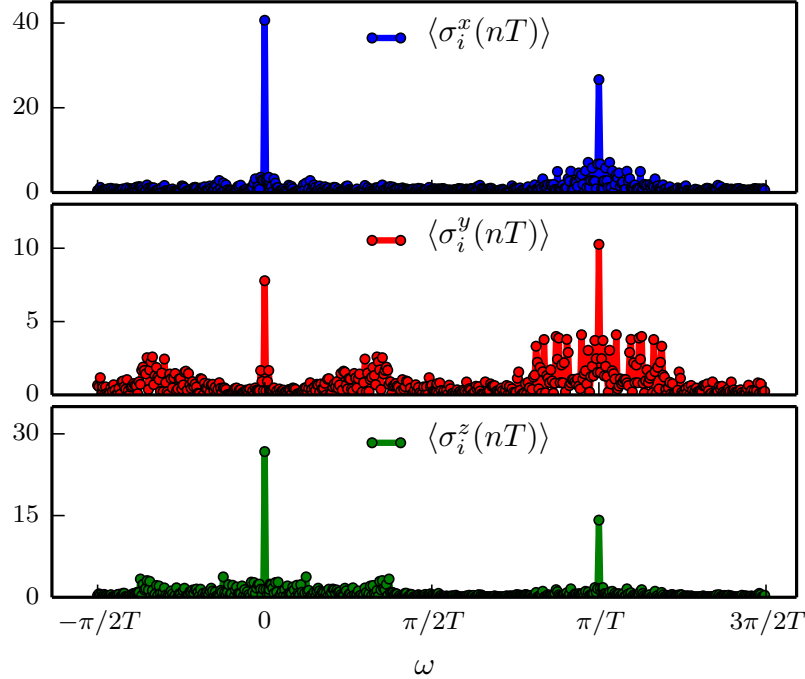


Figure 6.4: Fourier transform over time window $\Delta t = 500T$ of one point time-dependent expectation values $\langle \psi_0 | \sigma^{\{x,y,z\}}(nT) | \psi_0 \rangle$ in the “generically” perturbed model (6.6). The initial state $|\psi_0\rangle$ is a product state with physical spins σ^α randomly pointing on the Bloch sphere and uncorrelated from site to site. As discussed in the text, the response looks “glassy” with several incommensurate Fourier peaks in the addition to the peak at π/T , although we expect these to decay away in the $L \rightarrow \infty, T \rightarrow \infty$ limit. Data is shown for a single disorder realization in a system of length $L = 10$.

would measure the temporal response at π/T . We also note that a recent experiment demonstrated signatures of MBL in two dimensions [75] and, more generally, we expect our considerations to apply in all dimensions where MBL exists [69].

6.3.3 Comments

In the above discussion we have considered two settings, that of Floquet eigenstates and of late time states stemming from quenches. It is useful to contrast our findings with their analogs for general MBL phases (Floquet or undriven), and for ETH obeying phases (focussing on the undriven case, as the Floquet version has trivial infinite temperature correlations). We find that unequal time correlations in eigen-

states generically break TTI in all MBL phases, which thus generically look glassy. By contrast similar correlations in ETH systems do *not* generically break TTI. In the π SG we find that eigenstate correlations specifically designed to pick out the order parameter dynamics are “antiferromagnetic” in the time domain and thus break TTI while they are “ferromagnetic” for the OSG and thus do not. Turning now to the late time states coming from quenches, in MBL phases these are initial state dependent while in ETH phases these are not. Hence if we look for TTI breaking via these late time states we do not observe it in all ETH phases as well as MBL phases except the π SG (and its relatives which we discuss in the next section). We remind the reader though that in the π SG we need to quench from states that exhibit a macroscopic expectation value for the order parameter. All in all we conclude that the π SG exhibits a distinct and novel pattern of spatiotemporal order that is new to quantum systems.

6.4 Generalizations

Here we list a number of generalizations of the π SG phase. Ref. [316] presented a family of models with an explicit global symmetry group G which exhibit eigenstate long-range order, protected spectral pairing and temporal crystallinity. First we note that, much like the π SG, many of these models are absolutely stable to local perturbations, even those that break the global symmetry G . We then explain why bosonic SPT Floquet drives [317, 100, 253, 272] are not stable to the inclusion of symmetry breaking perturbations, although in the presence of the protecting symmetry they exhibit time crystallinity at their edges.

6.4.1 \mathbb{Z}_n and non-abelian models:

Consider first models with global \mathbb{Z}_n symmetry [316, 265]. There are n possible phases with completely spontaneously broken symmetry [316], labelled by $k = 0, 1, \dots, n-1$. The eigenvectors of the corresponding unitary are the \mathbb{Z}_n equivalents of cat states i.e., macroscopic superpositions of n spin configurations. In cases with $k \neq 0$, and in the presence of \mathbb{Z}_n symmetry, the spectrum consists of multiplets of n cat states appearing in n/g distinct groups each with degeneracy $g \equiv \text{gcd}(n, k)$. The n/g distinct groups are split by quasienergy multiples of $2\pi g/nT$. As for the π SG, some of these statements survive even when \mathbb{Z}_n symmetry is explicitly broken. In particular, while the g fold degeneracy for each group of cat states can readily be broken, it remains the case that each eigenstate is paired in a multiplet of n/g related cat states, separated by quasienergy $2\pi g/nT$. A similar statement holds for the non-abelian models in Ref. [316]. These more general drives have an explicit unitary non-abelian symmetry G , and are classified by an element of the center of the group $z \in Z(G)$. Let q denote the order of z . The spectrum consists of q groups of G/q degenerate cat-like states, and the q groups are separated by quasi-energies which are multiples of $2\pi/qT$. The $|G|/q$ degeneracy at each quasienergy can once again be lifted using symmetry breaking perturbations, but each eigenstate is still paired with q cat state partners, split by quasienergy multiples of $2\pi/qT$.

6.4.2 Stability of SPTs and boundary time crystallinity

While the π SG phase is absolutely stable, similar Floquet generalizations of bosonic SPT phases [316] are not. Before showing this, let us first note that some Floquet SPTs spontaneously break TTI at their boundaries. This boundary TTI breaking is not tied to bulk LRO and the phases are correspondingly *unstable* to symmetry breaking perturbations. We illustrate this with the simple example of an Ising Floquet SPT, the so-called 0π PM [169, 317]. In fact, as shown in the previous chapter,

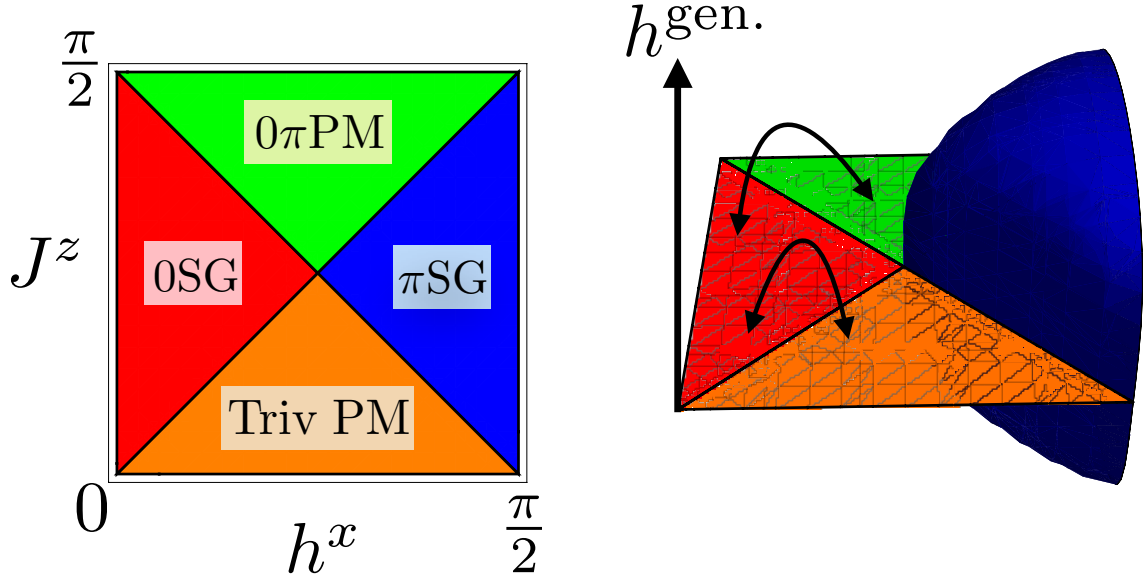


Figure 6.5: (left) Phase diagram for the MBL Ising symmetric drives presented in Refs. [169, 316] showing the 0SG and π SG phases which are long-range ordered and spontaneously break Ising symmetry, as well as the 0π PM and trivial paramagnetic phases which have no LRO. The 0π PM is an SPT with non-trivial edge modes and can spontaneously break time translation symmetry on its edges. (right): On perturbing with generic Ising symmetry breaking fields h^{gen} , only the π SG is absolutely stable and continues into a phase with LRO and an emergent symmetry. The other three phases can be continuously connected to the trivial MBL paramagnet in the presence of h^{gen} .

the 0π PM and π SG are neighbors on a common Floquet phase diagram [169, 317, 316] Fig. 6.5(left) which also contains the 0SG discussed earlier and a trivial MBL paramagnet. A simple Floquet unitary for 0π PM on a system with boundary is [317]

$$U_f = \sigma_1^z \sigma_N^z \exp[-i \sum_{r=2}^{N-1} h_r \sigma_r^x], \quad (6.9)$$

where the fields h_r are randomly distributed. This model has trivial bulk paramagnetic eigenstate order, but it also has non-trivial Ising odd “pumped charges” $\sigma_{1/L}^z$, using the parlance of Ref. [317]. As a consequence, the eigenspectrum exhibits “spectral quadrupling”. Labeling the simultaneous eigenvalues of U_f, P by $(u, p = \pm 1)$, it can be shown that states always appear in multiplets of the form $(u, 1), (u, -1), (-u, 1), (-u, -1)$ *i.e.*, there are two groups of degenerate states split

by exactly π/T quasienergy—hence the name $0\pi\text{PM}$. The π/T quasienergy splitting in πSG was associated with the breaking of TTI, so it is natural to also expect TTI breaking for the $0\pi\text{PM}$. Indeed, for the special model Eq. (6.9), the σ^x edge operators have stroboscopic equations of motion $\sigma_{1,N}^x(nT) = (-1)^n \sigma_{1,N}^x(0)$, with period $2T$. At generic points in the $0\pi\text{PM}$ phase obtained by perturbing (6.9) with Ising symmetric perturbations, dressed versions of these edge Pauli operators (and generic edge operators with non-zero projections on the dressed Pauli edge operators) will exhibit period $2T$ oscillations persistent for exponentially long time scales in system size (in the same spirit as Ref. [24]). Indeed, using Ising duality [169], statements about the dynamics of Ising even edge operators in the $0\pi\text{PM}$ paramagnet directly translate into statements about local bulk operator dynamics in the (Ising symmetric) πSG in Sec. 6.3. We emphasize, however, that for $0\pi\text{PM}$ generic local bulk operators will not show period doubling in the limit $L \rightarrow \infty$.

Despite the non-trivial dynamics in the $0\pi\text{PM}$, the spectral pairing properties of this phase (and the more general bosonic Floquet SPT phases discussed in Ref. [317]) are unstable to the inclusion of small, generic symmetry breaking perturbations at the boundary. To see how this works in more generality, note that Floquet MBL unitaries can be re-expressed in a certain canonical form [317]

$$U_{f0} = v_L v_R e^{-if}, \quad (6.10)$$

where f is a local MBL Hamiltonian functional of the l-bits in the bulk, and $v_{L,R}$ are unitaries localized at the left/right edges of the system respectively which commute with the bulk l-bits. Note that the model Eq. (6.9) is a special realization of this more general canonical form. The SPT order of U_{f0} is captured by two pieces of data: (i) The bulk SPT order, which is determined by the classification of f as an undriven Hamiltonian, and (ii) the “pumped charge”, characterized by the commuta-

tion relations between the $v_{L,R}$ and the global symmetry generators [317]. Note that Eq. (6.10) can readily be detuned – whilst maintaining locality and unitarity – to a form with trivial pumped charge, e^{-if} , through an interpolating family of unitaries $U_{f\lambda} = e^{-i\lambda \log v_R} e^{-i\lambda \log v_L} U_{f0}$ with λ being tuned from 0 to 1. Note further that if $v_{L,R}$ have non-trivial commutation relations with the global symmetry, this interpolating family of unitaries breaks the global symmetry. It may still occur that f , an MBL Hamiltonian, has a non-trivial SPT classification and therefore e^{-if} has spectral pairing and edge states. However, this SPT order is readily destroyed by perturbing f non-symmetrically as one would perturb an undriven SPT so as to gap out its edge states. This instability of the boundary-TTI breaking SPT phases reiterates our central message that the absolute stability of a TTI breaking phase is intrinsically tied to the coexistence of bulk spatial LRO.

The instability of 0π PM SPT combined with our prior statements on the instability of pairing in the 0SG leads to the picture depicted in Fig. 6.5(right)—in the presence of generic Ising symmetry breaking perturbations, the four Ising symmetric MBL-Floquet phases are reduced to two: the absolutely stable continuation of the π SG, and a trivial PM. The 0SG and the 0π PM can be continuously connected to the trivial PM without going through a phase transition in the presence of Ising symmetry breaking terms.

We end this section by briefly commenting on the stability of fermionic SPTs. Interacting SPTs protected by fermion parity are more robust. Let us focus on class D [161, 169, 317] for concreteness. While it is true that edge modes are unstable to fermion parity breaking perturbations, fermion parity is never broken for physical/local Hamiltonians $H(t)$ – hence, in the detuning argument above, $U_{f\lambda}$ is not a truly local unitary for intermediate values of λ when $v_{L,R}$ are fermion parity odd (we say the pumped charge is fermion parity odd [317]). However, as with all of the

examples discussed here, the Floquet edge modes can be removed by breaking time translation symmetry.

6.5 Concluding remarks

We have shown the existence of a family of phases of Floquet systems which are absolutely stable—a generic interior point in such a phase is stable to *all* weak local perturbations of its governing unitary. These phases are characterized by emergent, Hamiltonian dependent, abelian global symmetries and spatiotemporal long range order based on these. Submanifolds of these phases exhibit Hamiltonian independent symmetries which can be unitary or anti-unitary. At generic points in these phases, late time states evolved from randomly picked short ranged entangled states exhibit long range order in space and sharp oscillations of the emergent order parameter which can be used to identify the phases.

These Floquet phases join two previously established paradigms for such absolute stability—those of topological order and that of MBL for time independent Hamiltonians—and a comparison between these three is in order. Topological order, exemplified by the Z_2 order of the toric code and its weak local perturbations, is characterized by the absence of symmetry breaking and the presence of emergent gauge fields. Such phases are in a different language quantum liquids with long range (ground state) entanglement [72] which features account intuitively for their absolute stability.

MBL is characterized by a complete set of emergent, Hamiltonian dependent, local integrals of the motion (l-bits) and in its minimal form involves eigenstates that exhibit only short ranged entanglement. Its absolute stability can be attributed to the localization being unrelated to any spatial ordering—it is primarily a dynamical

phenomenon. By contrast, broken symmetries are *not* absolutely stable—symmetry induced degeneracies are lifted when symmetries are broken.

It is not hard to believe that one can mix topological order and MBL and still end up with an absolutely stable phase and this was discussed as an example of eigenstate order in Ref. [149]. By contrast it is also natural to conclude that MBL and symmetry breaking do not lead to absolute stability and this is also trivially the case. What is therefore striking is that a third ingredient, Floquet periodicity, allows broken symmetries and MBL to combine to yield absolutely stable phases. The resulting phases also exhibit long range entanglement in the form of the cat eigenstates and thus are stabilized by a relative of the mechanism which operates in the case of topological order.

Finally we note that the absolute stability of symmetry broken phases in this chapter can be put on a similar footing to the well known absolute stability of topological phases [325]. Recent work [163, 116] characterizes pure abelian gauge theories as spontaneously breaking 1-form global symmetries in their deconfined phases. In the presence of matter, the generators for these higher form symmetries are emergent and thus Hamiltonian dependent. For example, in the perturbed 2D toric code, the 1-form symmetries are generated by dressed line operators [136]. More generally, a large class of well known and undriven absolutely stable topologically ordered phases are characterized by spontaneously broken emergent 1-form global symmetries, while the Floquet drives in this work are characterized by emergent global (0-form) symmetries. In a related note, one can consider Floquet unitaries constructed from topologically ordered Hamiltonians, such as the toric code, which toggle states between different topological sectors. Such drives exhibit spatial topological order, do not break any global symmetries, but do break TTI because the Floquet unitary described does not commute with operators which measure the topological sector. Just as the cat states are split by π/T quasi-energy in the π SG, different topological sectors are split

by π/T in this topological example. It is somewhat a matter of taste whether these should be identified as Floquet time crystals.

6.A $\tau_{r,\lambda}^z$ either commutes or anti-commutes with $U_{f\lambda}$

To prove this assertion, we will use only the locality of the $\mathcal{V}_\lambda, U_{f\lambda}$. First note that we can express a product of any two τ_λ^z operators as a product of l-bits $\tau_{r,\lambda}^z \tau_{s,\lambda}^z = \prod_r^{s-1} D_r^\lambda$. This compound operator commutes with $U_{f,\lambda}$ because the D_r^λ do, i.e.,

$$U_{f,\lambda} \tau_{r,\lambda}^z \tau_{s,\lambda}^z U_{f,\lambda}^\dagger = \tau_{r,\lambda}^z \tau_{s,\lambda}^z \quad (6.11)$$

However note that the unitaries defined as

$$\theta_r \equiv \tau_{r,\lambda}^z U_{f,\lambda} \tau_{r,\lambda}^z U_{f,\lambda}^\dagger \quad (6.12)$$

$$\theta_s \equiv \tau_{s,\lambda}^z U_{f,\lambda} \tau_{s,\lambda}^z U_{f,\lambda}^\dagger \quad (6.13)$$

are local to r, s respectively. This follows from two observations. First $\tau_{r,\lambda}^z$ is local to r because \mathcal{V}_λ is assumed low depth. Second, $U_{f,\lambda} \tau_{r,\lambda}^z U_{f,\lambda}^\dagger$ is local to r because $\tau_{r,\lambda}^z$ is, and $U_{f,\lambda}$ is low depth (being the finite time ordered exponent of a bounded local Hamiltonian). Plugging Eq. (6.12) and Eq. (6.13) into Eq. (6.11) gives

$$U_{f,\lambda} \tau_{r,\lambda}^z \tau_{s,\lambda}^z U_{f,\lambda}^\dagger = \tau_{r,\lambda}^z \theta_r \theta_s^{-1} \tau_{s,\lambda}^z = \tau_{r,\lambda}^z \tau_{s,\lambda}^z \quad (6.14)$$

implying that

$$\theta_{r\lambda} = \theta_{s\lambda} \quad (6.15)$$

despite the fact that $\theta_{r\lambda}, \theta_{s\lambda}$ are exponentially localized to potentially distant sites r, s – in particular we could say choose $|r - s| = L/2$ to be of order the system size. The implication is then that, up to exponentially small corrections in system size, $\theta_{r,s\lambda}$ are pure phases. The corrections take the form $Ce^{-L/\xi}$, where C, ξ do not depend on the system size, and only depends on the details of $\mathcal{V}_\lambda, U_{f,\lambda}$ (such as their depth, which is assumed to be finite). The fact $(\tau_{r,\lambda}^z)^2 = 1$ and $\theta_{r\lambda}$ approximately a pure phase implies $\theta_{r\lambda}^2 = 1 + \epsilon$ where ϵ is a correction of the form $ce^{-L/\xi}$ and $c = O(1)$. This shows that

$$\theta_{r\lambda} = \pm 1. \tag{6.16}$$

to the same degree of a approximation. Supposing we know that $\theta_{r0} = -1$ exactly – as is the case for the fixed point π SG model Eq. (6.1). If $\mathcal{V}_\lambda, U_{f\lambda}$ is a continuous family of unitaries it follows by continuity that $\theta_{r\lambda} = -1$ in the large system limit, for all applicable λ .

6.B Symmetries and the \mathcal{V}_λ unitaries

Here we argue that diagonalizing unitaries \mathcal{V}_λ for families of unitaries $U_{f\lambda}$ respecting a fixed symmetry (e.g., Ising parity or time reversal) and exhibiting absolutely stable long ranged order, can themselves be chosen to commute with the fixed symmetry. For concreteness, focus on a system with an anti-unitary symmetry \mathcal{T} with $\mathcal{T}^2 = 1$ – the unitary symmetry case goes through similarly. Thus we consider a family of unitaries $U_{f\lambda}$ obeying $\mathcal{T}U_{f\lambda}\mathcal{T}U_{f\lambda} = 1$, with U_{f0} given by Eq. (6.1). Note first that the spectrum of U_{f0} generically has no degeneracies. Assuming the same is true of $U_{f\lambda}$ for now, consider the action of \mathcal{T} on eigenstates. As $\mathcal{T}U_{f\lambda}\mathcal{T}U_{f\lambda} = 1$, it follows that $U_{f\lambda}\mathcal{T} | \{d\}, p \rangle_\lambda = u_{d,p,\lambda} \mathcal{T} | \{d\}, p \rangle_\lambda$. Hence \mathcal{T} preserves eigenstates of $U_{f\lambda}$. As

the eigenstates are non-degenerate it follows that

$$\mathcal{T} | \{d\}, p \rangle_\lambda = e^{i\theta_{d,p}} | \{d\}, p \rangle_\lambda \quad (6.17)$$

for some state dependent phase $e^{i\theta_{d,p}}$. Eq. (6.17) immediately implies $d_{\lambda,r} = \mathcal{T} d_{\lambda,r} \mathcal{T}$ and $P^\lambda = \mathcal{T} P^\lambda \mathcal{T}$ which we can rewrite as

$$\begin{aligned} \mathcal{V}_\lambda d_r \mathcal{V}_\lambda^{-1} &= \mathcal{V}_{\lambda,\mathcal{T}} d_r \mathcal{V}_{\lambda,\mathcal{T}}^{-1} \\ \mathcal{V}_\lambda P \mathcal{V}_\lambda^{-1} &= \mathcal{V}_{\lambda,\mathcal{T}} P \mathcal{V}_{\lambda,\mathcal{T}}^{-1} \end{aligned}$$

where $\mathcal{V}_{\lambda,\mathcal{T}} \equiv \mathcal{T} \mathcal{V}_\lambda \mathcal{T}^{-1}$, and d_r, P are the undressed domain wall and parity operators. The upshot is that the unitary

$$\mathcal{Q}_\lambda \equiv \mathcal{V}_\lambda^{-1} \mathcal{V}_{\lambda,\mathcal{T}} \quad (6.18)$$

commutes with the commuting set of operators $\{d_r\}, P$. As these operators uniquely label a complete basis, \mathcal{Q}_λ is completely diagonal in $\{d_r\}, P$. In other words it can be expressed as

$$\mathcal{Q}_\lambda = e^{-iq_\lambda(d_r,P)} \quad (6.19)$$

for some real functional q_λ of the labels. In fact, using locality arguments similar to those in Sec. 6.A (and in the appendix to Ref. [317]) we find

$$\mathcal{Q}_\lambda = P^a e^{-is_\lambda(\{d\})} \quad (6.20)$$

up to exponentially small corrections in system size, where $a = 0, 1$, and s is a local functional of domain walls. We can use continuity of \mathcal{V}_λ again to argue moreover that $a = 0$. Therefore we have shown that $\mathcal{V}_{\lambda,\mathcal{T}} = \mathcal{V}_\lambda \mathcal{Q}_\lambda$. We now use this result to construct a new change of basis matrix which is invariant under time reversal.

We define a new change of basis unitary $\mathcal{W}_\lambda \equiv \mathcal{V}_\lambda e^{-is_\lambda(\{d\})/2}$. \mathcal{W}_λ indeed achieves the desired local change of basis, but is also time reversal invariant. We henceforth redefine $|\{d\}, p\rangle_\lambda \equiv \mathcal{W}_\lambda |\{d\}, p\rangle$. The operators $d_{\lambda,r}, P^\lambda$ are unaffected by this change in convention.

Part IV

Tensor-Network Approach to Many-Body Localization

Chapter 7

Efficient Variational Diagonalization of Many-Body Localized Hamiltonians

7.1 Introduction

In this chapter and the next, we take a quantum information theoretic view of many-body localization. In particular, we discuss two complementary ways in which the low entanglement in MBL eigenstates can be exploited for efficiently finding and representing these states.

In the Anderson problem, the many-body Fock/Slater states constructed from the single particle states have two important features. First, they exhibit an economical description— L single particle states for a system of size L are sufficient to construct all 2^L many-body states. Second, all many-body states exhibit an area law [290, 135, 311, 98] for the entanglement entropy stemming from the localized nature of the constituent single particle states.

As discussed in Section 1.5, it was noted early on [234, 29] that many-body eigenstates in the MBL regime have only local entanglement and thus also obey the area law. Further, the phenomenology of MBL systems was traced to an emergent set of L commuting local integrals of motion (the “1-bits”) which exist in fMBL systems [148, 283, 153] as discussed in Section 1.4.

These two developments invite a natural closure in which the full set of 2^L many-body eigenstates are explicitly constructed from $O(L)$ local ingredients, at least approximately. The well known connection of the area law to matrix-product state (MPS) / tensor network representations of many-body states [124, 281, 115] suggests that the latter are the correct language in which to carry out this program. The program has two components: showing that such a compact representation exists and providing a recipe for finding it without recourse to a knowledge of the exact eigenstates, potentially rendering a much larger range of system sizes computationally tractable.

In an important development, two groups have addressed the existence problem. Building on earlier work [239], Pekker and Clark (PC) [238] have shown that the unitary operators that exactly diagonalize fMBL systems can be represented by matrix products operators (MPOs) [309, 281] of bond dimensions that appear to grow very slowly with system size¹ —in contrast to delocalized systems where the dimension grows exponentially with system size. The slow growth that they do observe is presumably due to rare many-body resonances/Griffiths effects; in its absence, the MPOs would yield the sought after $O(L)$ local description of the full spectrum. Parallel work [61] argued for the congruent result that the presence of local integrals of motion implies the existence of a single “spectral tensor network” that efficiently represents the entire spectrum of energy eigenstates in the fMBL phase. These devel-

¹The PC prescription matches eigenstates obtained via exact diagonalization (ED) to the “best” (most local) diagonalizing unitary operator in a time that scales as $O(2^L)$ instead of the prohibitive worst case time which scales as $O(2^L!)$. Although it is not yet clear how to exhaust all gauge degrees of freedom to find the optimal representation and the truncation error yields a loss of unitarity.

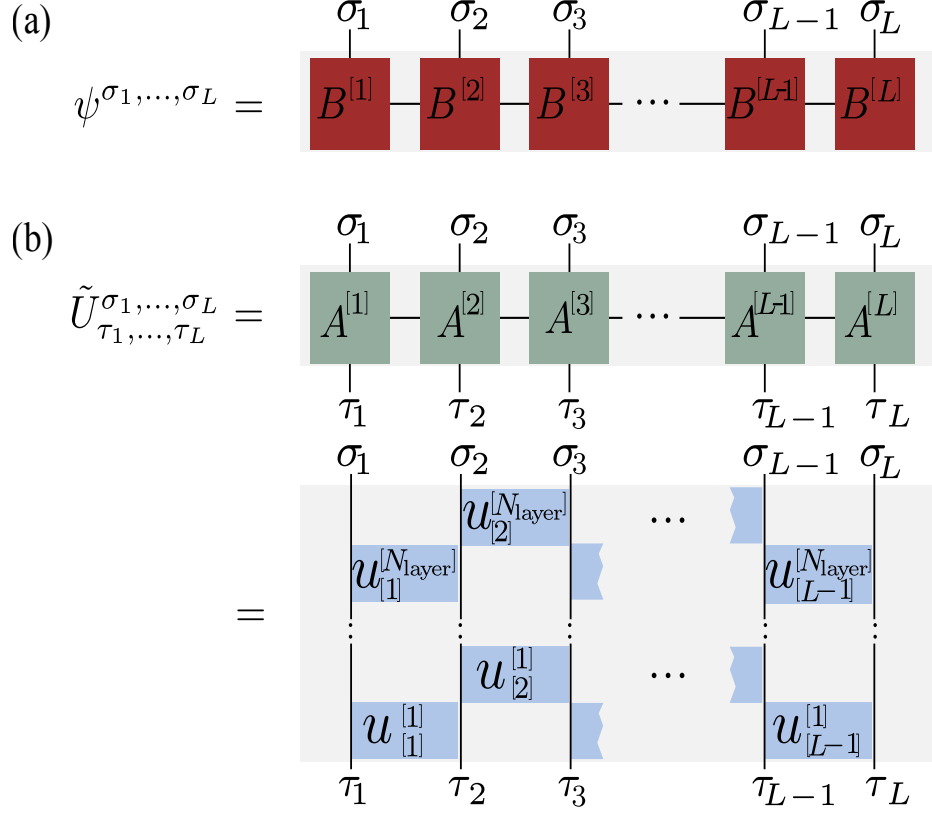


Figure 7.1: (a) Schematic representation of an MPS representation of a state $|\psi\rangle$. (b) Variational ansatz for the unitary U that encodes *all* eigenstates of a fully many-body localized Hamiltonian. The local unitaries $u_{[n]}^{[m]}$ are parametrized as $u_{[n]}^{[m]} = e^{iS_{[n]}^{[m]}}$ with real symmetric matrices $S_{[n]}^{[m]}$, $n = 1 \dots L - 1$ and $m = 1 \dots N_{\text{layer}}$.

opments however have not led to an algorithm for finding a compact representation directly without having to diagonalize the full system at a cost that scales exponentially with system size.

In this chapter we propose an approach to directly and efficiently find an approximate compact representation of the diagonalizing unitary by using a variational unitary MPO (VUMPO) ansatz. To this end, we construct a cost function whose minimum yields the exact unitary and, hence, the *entire* set of 2^L exact eigenstates of a system of L qubits. We show that for a fixed bond dimension of the approximate \tilde{U} , optimizing the cost-function in $d = 1$ can be performed at a computational cost

that is only *linear* in system size which, in theory, allows us to access system sizes far beyond those possible by ED.

7.2 MPS and MPO notation

An MPS representation of a quantum state living in a basis spanned by L qubits takes the form

$$|\psi\rangle = \sum_{\{\boldsymbol{\sigma}\}} \sum_{0 \leq \gamma_i < D} B_{\gamma_1}^{[1]\sigma_1} B_{\gamma_1 \gamma_2}^{[2]\sigma_2} \cdots B_{\gamma_{L-1}}^{[L]\sigma_L} |\sigma_1 \cdots \sigma_L\rangle, \quad (7.1)$$

whereas an MPO representation of an operator in the same Hilbert space takes the form

$$O = \sum_{\substack{0 \leq \gamma_i < D \\ \{\boldsymbol{\sigma}\}, \{\boldsymbol{\tau}\}}} A_{\gamma_1}^{[1]\sigma_1, \tau_1} \cdots A_{\gamma_{L-1}}^{[L]\sigma_L, \tau_L} |\sigma_1 \cdots \sigma_L\rangle \langle \tau_1 \cdots \tau_L|, \quad (7.2)$$

where $\sigma_i, \tau_i \in \{\uparrow, \downarrow\}$ and we use a compact notation in which $\boldsymbol{\sigma} = \sigma_1, \sigma_2, \dots, \sigma_L$ denotes the 2^L states (analogous for $\boldsymbol{\tau}$). Figure 7.1 shows a pictorial representation of these objects. The MPSs/MPOs are represented by rank three/four tensors $B^{[i]}/A^{[i]}$ on each site i (except the first and last tensors which are rank two/three); the external leg(s) σ_i, τ_i refer to the physical spin indices whereas the γ_i are the internal virtual indices that are contracted. Each $B^{[i]\sigma_i}/A^{[i]\sigma_i\tau_i}$ is a D^2 dimensional matrix where D is the bond-dimension of the matrix. Note that we do not put any constraints on the total magnetization and consider all 2^L states. Using standard methods [277] for the conservation of quantum numbers in tensor networks, a projection onto sectors with fixed magnetization is easily possible.

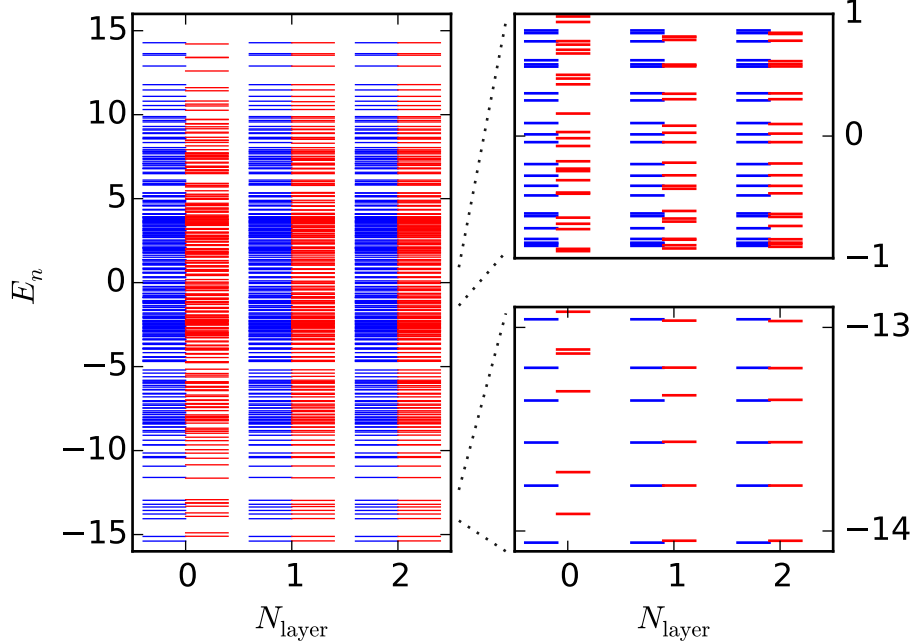


Figure 7.2: Comparison of the exact energy levels (blue lines) with the ones found by the variational optimization (red lines) for $W = 8$ and $L = 8$ as a function of the number of layers of two-site gates. The right panel shows a zoom of some energy levels at the bottom and in the center of the spectrum.

7.3 Method

We now introduce the VUMPO ansatz and an algorithm to numerically optimize it. Let us assume that H is an fMBL Hamiltonian defined on an L -site chain of spin $1/2$ operators. It is our goal to find a unitary MPO approximation \tilde{U} of the unitary that diagonalizes the Hamiltonian such that the 2^L eigenstates of H are given by $|\psi_{\tau}\rangle \approx \sum_{\{\sigma\}} \tilde{U}_{\tau}^{\sigma} |\sigma\rangle$. In the parlance of Refs. [148], the physical basis operators σ_i are the “p-bits” whereas the τ_i are the local “l-bits”. Each eigenstate is labeled by the occupation of l-bits $\tau = \{\uparrow\uparrow\downarrow \cdots \uparrow\}$, and is obtained by acting with the MPO representation of U on the product state $|\tau\rangle$. In this language of MPOs, it is clear how the 2^L MB eigenstates are constructed from the L matrices $A^{[i]\tau_i}$; further, if the bond-dimension of the matrices scales as $O(1)$ with the system size, the eigenstates are only locally entangled in the p-bit basis and a description of the full eigenbasis in terms of $O(L)$ local ingredients is possible.

The VUMPO is found by numerically minimizing the cost functional

$$f(\{A^{[n]}\}) = \sum_{\{\tau\}} \langle \psi_{\tau} | H^2 | \psi_{\tau} \rangle - \langle \psi_{\tau} | H | \psi_{\tau} \rangle^2 \geq 0, \quad (7.3)$$

with $\langle \psi_{\tau} | \psi_{\tau'} \rangle = \delta_{\tau, \tau'}$. The cost function is the variance of the energy summed over all approximate MB eigenstates. Naively, one might expect the time to evaluate the cost function Eq. (7.6) to scale exponentially with the system size L as the sum is performed over 2^L MB eigenstates. However, remarkably, the computation can be performed in a time scaling *linearly* with system size [309]! For example, the term $\sum_{\{\tau\}} \langle \psi_{\tau} | H | \psi_{\tau} \rangle^2$ can be evaluated by “doubling” the degrees of freedom and defining a state $|\phi\rangle = \sum_{\{\tau\}} |\psi_{\tau}\rangle |\psi_{\tau}\rangle |\tau\rangle$. With this notation we find that $\sum_{\{\tau\}} \langle \psi_{\tau} | H | \psi_{\tau} \rangle^2 = \langle \phi | H \otimes H \otimes \mathbb{1} | \phi \rangle$. This expectation value can be efficiently evaluated using the MPO formalism and the most expensive part of the evaluation scales, for a given Hamiltonian in MPO form, as $\propto LD^5$ (see 7.A for details). One can now iteratively minimize f by locally optimizing each $A^{[n]}$ using, for example, the conjugate gradient algorithm.

In general, an MPO compression of a unitary operator will not strictly respect unitarity. To get a valid positive-definite cost function in these cases, we need to add a Lagrange multiplier to enforce unitarity. In practice, this leads to either very unstable, or very computationally expensive optimizations.

The key to a stable optimization protocol turns on restricting our algorithm to the manifold of strictly unitary MPOs of a given bond-dimension. To achieve this, we parameterize the VUMPO as a finite depth circuit of two-site unitaries as shown in Fig. 7.1(b). This Ansatz incorporates two important properties: (i) The VUMPO is unitary for all parameters and (ii) it is local for any finite N_{layer} . We use a single unitary to obtain all eigenstates, but readers will note the obvious connection to the quantum computational notion [30]. Finally, we note that we can rewrite the unitary

network as a strictly unitary MPO with bond dimension $D \leq 2^{2N_{\text{layer}}}$, where N_{layer} is the number of layers of two-site gates². However, this step is not necessary and we can evaluate the cost function by directly contracting the unitaries circuit which, in fact, gives a considerable speed up for the systems we consider here³.

The algorithm to find the VUMPO is then similar in spirit to the density matrix renormalization group (DMRG) method [327], except instead of finding the lowest energy state, we minimize the cost function Eq. (7.6) by sweeping through the local unitaries:

- (i) Initialize the local unitaries $u_{[n]}^{[m]} = e^{iS_{[n]}^{[m]}}$ by choosing random symmetric matrices $S_{[n]}^{[m]}$, where $n = 1, 2, \dots, L$ and $m = 1, 2, \dots, N_{\text{layer}}$.
- (ii) Locally minimize the cost function by varying the elements of a given $S_{[n]}^{[m]}$ by using, e.g., a conjugate gradient method.
- (iii) Update the network and repeat the previous step for the next unitary.
- (iv) Continue the sweeping procedure by minimizing the local unitaries successively until convergence. A full sweep across all the unitaries has to scale as $O(L)$.

We find that the number of steps needed for convergence appears to be approximately independent of L . This gives an overall scaling of the algorithm as $O(LD^5) \sim O(Le^{N_{\text{layer}}})$. Once the algorithm has converged, the VUMPO can be used to obtain all the eigenstates of the system, and to efficiently compute observables using the MPS formalism.

²The maximum bond dimension follows from the fact that the maximum entanglement for a bipartition of an approximate eigenstate is bounded by the number of two layer gates extending across the entanglement cut.

³Using the locality of the unitary circuit, the cost function can be evaluated locally and thus it is, in principle, possible to generalize the approach to higher dimensions.

7.4 Results

We consider the Heisenberg model with random z -directed magnetic fields (1.5):

$$H = J \sum_n \vec{S}_n \cdot \vec{S}_{n+1} - \sum_n h_n S_n^z. \quad (7.4)$$

where \vec{S}_n are spin 1/2 operators, the fields h_n are drawn randomly from the interval $[-W, W]$, $J = 1$ and the MBL transition is at approximately $W \simeq 3.5$.

7.4.1 Energy Spectrum

We begin by comparing the energies obtained using the VUMPO approach with the exact spectrum (full diagonalization). The converged results for $W = 8$ and $L = 8$ with different numbers of layers N_{layer} are shown in Fig. 7.2. For $N_{\text{layer}} = 0$, the VUMPO is the identity (i.e, no variational parameters) and the resulting approximate eigenstates are simple product states of the form $|\sigma_1\rangle|\sigma_2\rangle \dots |\sigma_L\rangle$ with $\sigma_n = \uparrow, \downarrow$. The overall bandwidth in this case agrees relatively well with the exact results because W is the dominant energy scale in the problem. However, as shown in the zoomed in plots, the deviation of individual energy levels is relatively large compared to the mean-level spacing because the product states completely neglect local quantum fluctuations which are present in the exact eigenstates. Increasing N_{layer} strongly improves the agreement between the exact and approximate energy levels as the network successively adds entanglement over longer distances.

Next we turn to the mean variance of the energy, which is simply the disorder averaged cost function Eq. (7.6) divided by 2^L . Figure 7.5 shows this quantity disorder averaged over 50 realizations as a function of system size for different fixed N_{layer} . We observe a linear increase of the mean variance with system size, and find that the slope decreases as N_{layer} is increased. This tells us that for a given N_{layer} our approximate eigenstates involve a constant error per unit length which decreases as

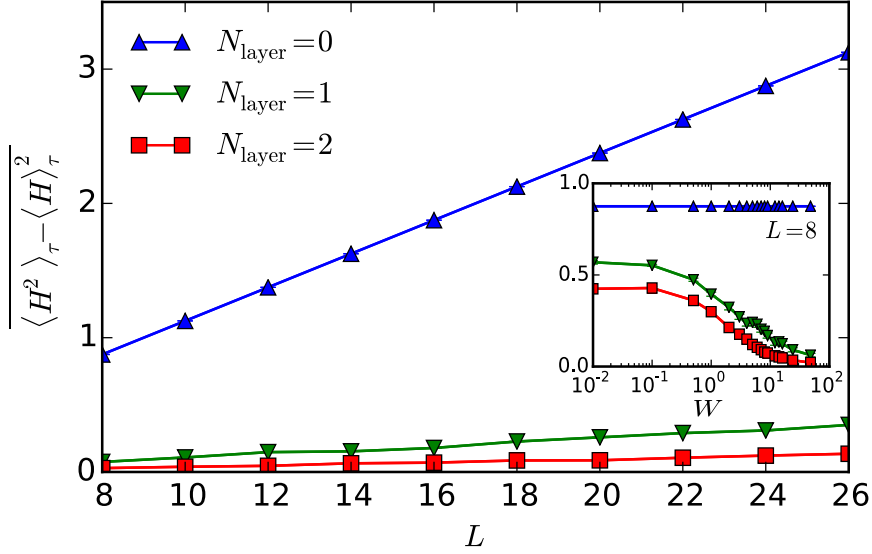


Figure 7.3: Mean variance of the energy as a function of system size for different number of layers for $W = 8$. Inset: Mean variance as function of W for a fixed $L = 8$.

N_{layer} is increased. When reducing the disorder strength W below the MBL transition, all excited eigenstates have a volume law and the MPO approximation, which is based on the locality of the eigenstates, breaks down (see inset of Fig. 3)

7.4.2 Spectral Functions

To examine the quality of our approximated eigenstates (with a view to capturing local properties), we use the VUMPO ansatz to obtain the infinite-temperature spectral function

$$A(\omega) = \frac{1}{2^L} \sum_{\{\tau_1\}, \{\tau_2\}} |\langle \tau_1 | S_{L/2}^z | \tau_2 \rangle|^2 \delta(\omega - E_{\tau_1} + E_{\tau_2}). \quad (7.5)$$

Spectral functions can again be efficiently evaluated using matrix-product techniques and it is also possible to efficiently target different energy densities by considering finite-temperature spectral functions [309, 343]. Figure 7.4 compares $A(\omega)$ obtained using the VUMPO approach for $L = 10$ with different disorder strengths and $N_{\text{layer}} = 0, 1, 2$ with the exact results. The large peak at $\omega = 0$ reflects the strongly localized

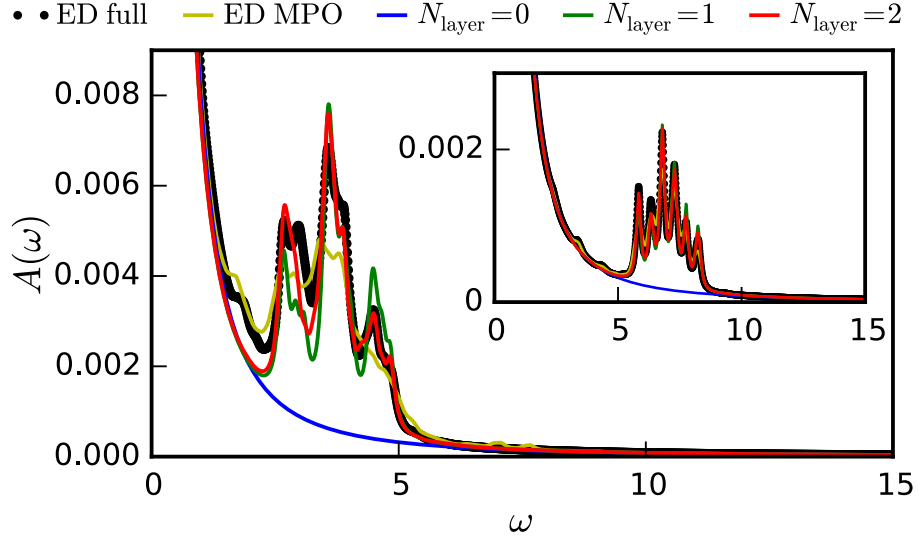


Figure 7.4: Comparison of the exact spectral function $A(\omega)$ (black dots) with those obtained using different approximations (see text for details) for $L = 10$ and $W = 8$. Spectra are shown using a Lorentzian broadening with an imaginary part of $\epsilon = 0.1$. Inset: Same data with $W = 16$.

nature of the eigenstates, i.e., the eigenstates of H are close to being eigenstates of local S^z operators. It is interesting to compare the peaks at $\omega > 0$ which are due to local fluctuations in the eigenstates. Clearly, $N_{\text{layer}} = 0$ does not show any features because the VUMPO is diagonal in S^z . When additional layers of unitaries are taken into account, the peak structure of $A(\omega)$ is well approximated. The agreement in both the frequencies and the intensities rapidly improve with increasing N_{layer} , and the results match almost perfectly for $W = 16$. Note that despite the extremely strong disorder, simply approximating the eigenstates as product states fails to capture any of the interesting features.

7.4.3 Comments on accuracy

We have presented some evidence above for the accuracy of the VUMPO obtained by our method. It remains to establish more precise theorems on what values of N_{layer} it would take to calculate various physical quantities to a specified accuracy. In a step in that direction, PC have looked at the bond dimension needed to ensure that the

smallest singular value in the Schmidt decomposition across any cut in U is less than some fixed ϵ . This ensures that the discarded weight on truncating the unitary to bond dimension D is small. They found a slow growth of the D_{\min} needed to achieve a desired ϵ with L . In the absence of rare resonances or Griffiths regions, D_{\min} would presumably saturate at a fixed $O(1)$ value for a fixed error density independent of system size implying that we would need only $O(1)$ layers to represent the entire spectrum to the desired accuracy. As it is, with the resonances/Griffiths regions present, D_{\min} is expected to grow as $\text{poly}(L)$ whence N_{layer} will grow logarithmically.

Let us return to our spectral function computation above but this time we first obtain the exact $2^L \times 2^L$ dimensional unitary that diagonalizes H and then compress it to an MPO of a given bond dimension D . We do this by iteratively maximizing the “overlap” of an MPO with a fixed bond dimension with the “most local” and “most positive” diagonalizing unitary obtained by following the PC prescription [238]. As seen in Fig. 7.4 (labeled ED MPO), when compressing U_{PC} to $D = 16$ (which can exactly represent our $N_{\text{layer}} = 2$ results), the spectral functions $A(\omega)$ are reproduced in a comparable accuracy as in our VUMPO approach.

7.5 Summary and discussion

We have introduced an algorithm to find a variational unitary MPO that approximately diagonalizes fully many-body localized Hamiltonians. Our method finds an approximation to all 2^L eigenstates of the Hamiltonian in a time that remarkably scales only linearly with system size! We have benchmarked the method by comparing the results to exact diagonalization for small systems and studied the scaling of the mean variance as a function of system size. For a Heisenberg model in a strongly disordered field we find good qualitative and quantitative agreement of the obtained energies and spectral functions for a fixed N_{layer} and, importantly, rapid improvement

with increasing N_{layer} . With this work we have provided a proof of principle that we can efficiently (i.e, polynomially in system size) perform a variational calculation that provides a complete diagonalization of fMBL systems. As the VUMPO encodes the entire set of eigenstates for fMBL Hamiltonians, many relevant observables such as spectral functions and conductivities can be evaluated efficiently at zero and finite temperatures.

A few comments are in order. First, it is intuitively clear that our VUMPOs should capture most of the structure of the eigenfunctions, or equivalently l-bits, out to a fixed “lightcone” radius, set by N_{layer} . In terms of the dynamics this should allow accurate inclusion of local excitations on the same length scale and via the recently discussed connection between the energy and size of many-body resonances [121] down to a related frequency scale. Indeed, this feature can be effectively used to study different “slices” of the response function as more layers are added. For example, Figure 7.4 shows that the exact solution in the case of $W = 8$ shows certain features at lower frequencies which are absent in the variational solution. Second, for a given VUMPO, one can construct [294] a family of parent Hamiltonians $H = U^\dagger H^{\text{diag}} U$ with the same eigenstates by picking different energy distributions for diagonal Hamiltonians in the “l-bit” basis, H^{diag} .

Going forward we can visualize many possible avenues for improving our method. Initially it may be possible to choose the same number of two-qubit gates in a different architecture [278, 195] to get a softer cutoff on the entanglement. More ambitiously we could allow for some two-qubit gates with a longer range and optimize over *both* the architecture of the unitary network, and the particular gates used. It is also possible to engineer the cost function to target a desired energy density via a pseudo-thermal weighting which could improve such focused results for fixed resource use and also allow MBL systems exhibiting mobility edges to be treated. Of course the most desired improvement would be to run at $N_{\text{layer}} > 2$ which is currently stymied by the

exponential scaling of the cost function. As the diagrams to be contracted now start resembling 2D tensor-network graphs, algorithms from this field could presumably be used to improve the scaling of contraction times.

7.A Efficient evaluation of the cost functional

In this section we discuss some details of how to efficiently evaluate the cost function

$$f(\{A^{[n]}\}) = \sum_{\{\tau\}} \langle \psi_{\tau} | H^2 | \psi_{\tau} \rangle - \langle \psi_{\tau} | H | \psi_{\tau} \rangle^2 \geq 0, \quad (7.6)$$

using the MPO formalism. Due to the unitarity of U , the first term, $\sum_{\tau} \langle \psi_{\tau} | H^2 | \psi_{\tau} \rangle$, is simply $\text{Tr} H^2$. If H is represented by a χ dimensional MPO, the trace can be evaluated with a cost scaling as $\sim Ld^3\chi^2$ as shown in Fig. 7.5 (top); d is the dimension of the local Hilbert space on each site and is equal to 2 for the spin-1/2 operators considered in this work. The second term, $\sum_{\tau} \langle \psi_{\tau} | H | \psi_{\tau} \rangle^2$, is somewhat more challenging. We first “double” the system by taking two identical copies and form a tensorproduct with a state $|\tau\rangle$ (which is simply a product state of the “l-bits”),

$$|\phi\rangle = \sum_{\tau} |\psi_{\tau}\rangle |\psi_{\tau}\rangle |\tau\rangle. \quad (7.7)$$

Using the state $|\phi\rangle$ and that $\langle \tau | \tau' \rangle = \delta_{\tau, \tau'}$, we find that

$$\sum_{\tau} \langle \psi_{\tau} | H | \psi_{\tau} \rangle^2 = \langle \phi | H \otimes H \otimes \mathbf{1} | \phi \rangle. \quad (7.8)$$

This expectation value can again be evaluated efficiently using the MPO formalism as demonstrated in Fig. 7.5 (bottom). Given that $D > \chi > d$, the most expensive part of the contraction scales as $\sim LD^5\chi^2d^4$.

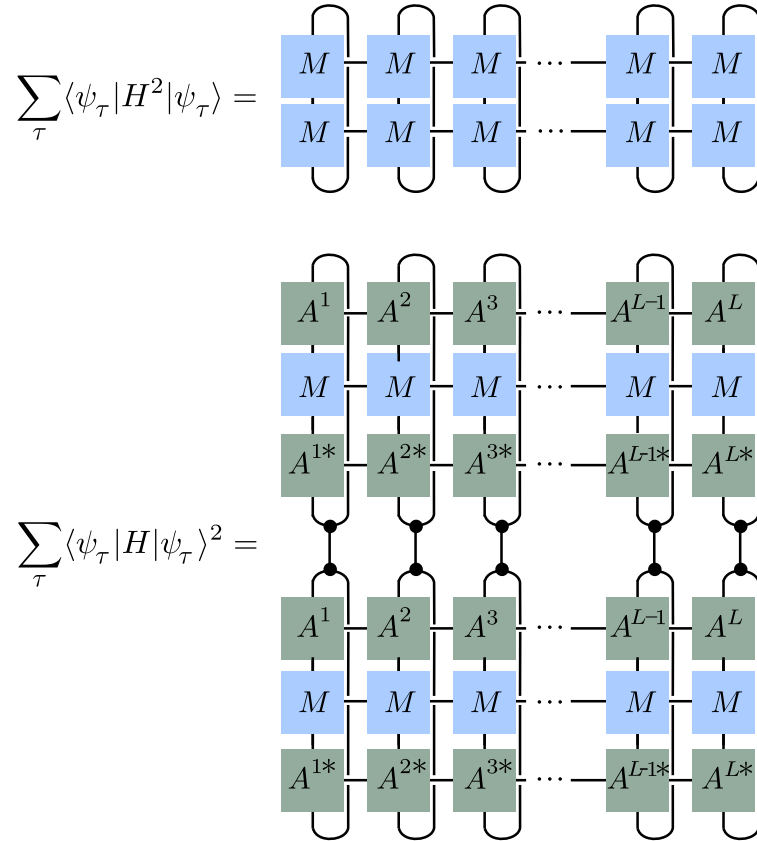


Figure 7.5: Diagrammatic representation of the tensor contractions required to evaluate the terms in the cost function Eq. (7.6). The tensors $A^{[n]}$ represent the unitary and M the Hamiltonian. The back dots are delta functions $\delta_{a,b,c}$.

Chapter 8

Obtaining Highly-Excited Eigenstates of MBL Hamiltonians by the Density Matrix Renormalization Group

8.1 Introduction

We have, by now, emphasized multiple times the centrality of many-body eigenstates in the MBL phase for understanding a regime where quantum statistical mechanics simply does not apply. Since typical MBL eigenstates have only local, area law, entanglement [234, 29]—although deviations from the area law due to rare many-body resonances and Griffiths effects are a complication to bear in mind—the well known connection between area laws and matrix-product state (MPS)/tensor-network representations of many-body states [124, 281, 115, 308] implies that they can be efficiently described, even at large L . Indeed, the previous chapter developed an efficient variational algorithm [249] to actually *find* an approximate, compact representation of the

diagonalizing unitary for fully MBL systems—and hence obtain *all* the eigenstates. This algorithm captures the gross features of the spectrum very well, but does not target individual eigenstates to high accuracy. Here we describe an alternative, complementary, procedure that can be used to obtain specific excited MBL eigenstates to high accuracy for large system sizes.

Our approach is directly inspired by the density matrix renormalization group (DMRG) [277, 327] which has been used to great effect to obtain modestly entangled ground states in low-dimensional systems. In the MPS formalism, the DMRG algorithm variationally optimizes the MPS to minimize the ground state energy of a given Hamiltonian H . Naively, we could modify this algorithm for MBL systems by targeting the eigenstate with energy closest to a specified excitation energy. However this is, in its simplest form, problematic due to the extremely small— $O(e^{-L})$ —generic many-body level spacings as we will explicitly show below.

We show that this problem can be overcome by making use of a defining characteristic of MBL phases, namely the existence of the l-bits discussed in Section 1.4. Importantly, since neighboring eigenstates with respect to the energy differ extensively in their spatial properties—we must typically flip $O(L)$ l-bits to go between them—there is a (soft) gap to excitations with finite numbers of l-bit flips. This leads to a natural algorithm in which we select excited eigenstates based on their overlap with particular, localized spatial patterns instead of their proximity to particular energies. By this overlap metric, “nearby” states differ by a few [$O(1)$] flips of local “l-bits. But such states are typically far separated in energy and thus the danger of mixing in eigenstates with exponentially small energy splittings is minimized.

We start with a brief review of the ground state DMRG method before describing our modified *DMRG-X* procedure. We then apply the method to the random field Heisenberg chain and evaluate our results using various metrics like energy variances and overlaps with exact eigenstates. For strong enough disorder, we obtain

eigenstates with machine-precision variance and find a rapid convergence of variances with bond dimension. Finally, we use our eigenstates to efficiently compute local-expectation values and demonstrate the failure of the eigenstate thermalization hypothesis (ETH) [89, 291, 267] in the MBL phase. We note related work [334] that also generalizes DMRG to highly excited states using a more complex energy based targeting approach.

8.2 DMRG-X Method

The proposed method is a reformulation of the standard DMRG algorithm [327, 277] to find highly-excited states of MBL systems. For a one-dimensional system of L sites, a general quantum state $|\Psi\rangle$ can be written in the following MPS form:

$$|\Psi\rangle = \sum_{j_1, \dots, j_L} B^{[1]j_1} B^{[2]j_2} \dots B^{[L]j_L} |j_1, \dots, j_L\rangle. \quad (8.1)$$

Here, $B^{[n]j_n}$ is a $\chi_n \times \chi_{n+1}$ matrix and $|j_n\rangle$ with $j_n = 1, \dots, d$ is a basis of local states at site n (for a spin 1/2 system, $d = 2$). Each matrix product $\prod_i B^{[i]j_i}$ in Eq. (8.3) produces a complex number which is the amplitude of $|\Psi\rangle$ on the basis state $|j_1 \dots j_L\rangle$. The key insight behind the success of DMRG is that ground states of one dimensional systems are efficiently approximated by MPS [308]. Starting from an initial random MPS, the DMRG algorithm sweeps through the system and iteratively optimizes the matrices $B^{[n]j_n}$ by locally minimizing the energy with respect to a given Hamiltonian H^1 . For the commonly used two-site update which simultaneously updates the matrices $B^{[n]j_n}$ and $B^{[n+1]j_{n+1}}$, an effective Hamiltonian \mathcal{H} is constructed by projecting H to a mixed $\chi_n \chi_{n+2} d^2$ dimensional basis. Here, the local basis states $|j_n\rangle|j_{n+1}\rangle$ represent the two updated sites, and the eigenstates of the reduced density matrix $|\chi_n\rangle_L$ and $|\chi_{n+2}\rangle_R$ compactly represent the environment to the left and right of the

¹See 8.A for details.

updated sites. The ground state of \mathcal{H} is found and the matrices on sites $n, n + 1$ are updated. The procedure is then repeated for all sites until convergence is achieved.

The DMRG-X method for finding excited eigenstates proceeds similarly to the standard DMRG algorithm in that we iteratively optimize an MPS. The key difference is that the algorithm does not attempt convergence in the energy of \mathcal{H} but instead in the local spatial structure of the eigenstate. We start by initializing the algorithm with a product state that has a finite overlap with some l-bit state, e.g., for the random-field Heisenberg model discussed below, we choose random states in the σ^z basis of the form $|\psi\rangle_0 = |\uparrow\downarrow\downarrow\uparrow \dots \downarrow\uparrow\rangle$. We start our DMRG-X algorithm with the following local two-site update : (i) Construct the effective Hamiltonian \mathcal{H} . (ii) Pick the eigenstate of \mathcal{H} that has *maximum overlap* with the current MPS. (iii) Update the tensors $B^{[n]j_n}$ and $B^{[n+1]j_{n+1}}$. To produce the data below, we use a full diagonalization of \mathcal{H} which scales as χ^6 with χ being the mean bond dimension. Alternatively, it is also possible to find a small set of k eigenstates of \mathcal{H} near the energy of the current MPS and then pick the eigenstate with largest overlap. This yields an algorithm that scales approximately as χ^3 , but an optimal k has to be found for each case.

This DMRG-X prescription ensures that no individual update step of the MPS matrices results in a large spatial reorganization, which is appropriate for a localized phase. By contrast, if we pick excited eigenstates of \mathcal{H} that are closest in energy to some target energy, the exponentially small energy gaps mean that we could be picking very different eigenstates (as labeled by their l-bit quantum numbers) at each step. This will, in general, result in a slow convergence and/or a final state that is a superposition of many nearby eigenstates.

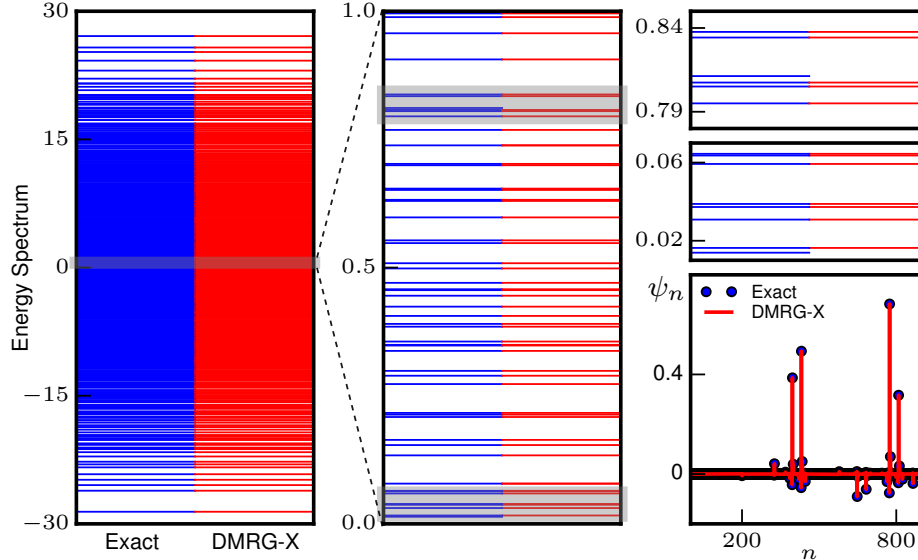


Figure 8.1: Comparison between eigenenergies obtained using exact diagonalization (blue) and variational DMRG-X (red) for a system of size $L = 12$, disorder strength $W = 8$ and bond dimension $\chi = 16$. The successive panels which zoom into the shaded regions of the spectrum show that all individual eigenenergies are obtained extremely accurately. The bottom right panel shows the exact and variational amplitudes for a particular eigenstate with Mott-resonances, showing that the method successively captures resonant states.

8.3 Comparison with ED for small systems

We now benchmark our method against the Heisenberg model with random z -directed magnetic fields (1.5):

$$H = J \sum_n \vec{S}_n \cdot \vec{S}_{n+1} - \sum_n h_n S_n^z. \quad (8.2)$$

where $J = 1$, \vec{S}_n are spin 1/2 operators and the fields h_n are drawn randomly from the interval $[-W, W]$. At strong disorder, typical eigenstates look like product states in the σ^z basis with small fluctuations. Equivalently, the “l-bits” τ_i^z look like σ_i^z with exponentially decaying corrections from operators away from site i . As the disorder is lowered, the probability of many-body “Mott-type” resonances [121, 209], wherein the eigenstates are approximately equal-weight superpositions of a few basis states,

increases. These resonant states have energy splittings that decay exponentially with the maximum distance involved in the resonance. At even smaller W s, the approach to the ergodic transition is marked by a “Griffiths” region [121, 320] in which locally ergodic/critical inclusions start to proliferate.

Figure 8.1 shows a comparison between eigenenergies obtained using exact diagonalization (blue) and variational DMRG-X (red) for a system of size $L = 12$, disorder strength $W = 8$ and bond dimension $\chi = 16$. To obtain the full spectrum, we feed the algorithm all possible σ^z product states as initial states. We find that the variance in the energy of all variationally obtained DMRG-X eigenstates is less than machine precision ($\sim 10^{-12}$), and the overlap of these states with the exact eigenstates is unity up to machine precision.

The zoomed in energy levels show that the method successively resolves the exponentially small splittings in the spectrum extremely accurately. However, a few exact eigenenergies have no DMRG-X partner—when two or more eigenstates of H have maximum weight on the same input basis state, the input state converges to one of these eigenstates leaving the other unpaired. We can avoid this duplication by requiring every new state to be orthogonal to the prior ones, but this will not be necessary in larger systems where our goal will never be to obtain every eigenstate.

One might worry that this is method biased towards product states and fails to capture resonant eigenstates. The bottom-right panel of Fig. 8.1 shows a representative eigenstate with a many-body “Mott” resonance involving a few distant basis states which is exactly captured by the variational state. We emphasize that the algorithm only uses a product state as an initial input; after that, the algorithm converges to the previously chosen eigenstate of \mathcal{H} . As long as the bond dimension χ is sufficiently large for the eigenstates of \mathcal{H} to capture resonances, it is easy for the algorithm to converge to a resonant superposition starting from one of the product states with significant weight in the resonant eigenstate.

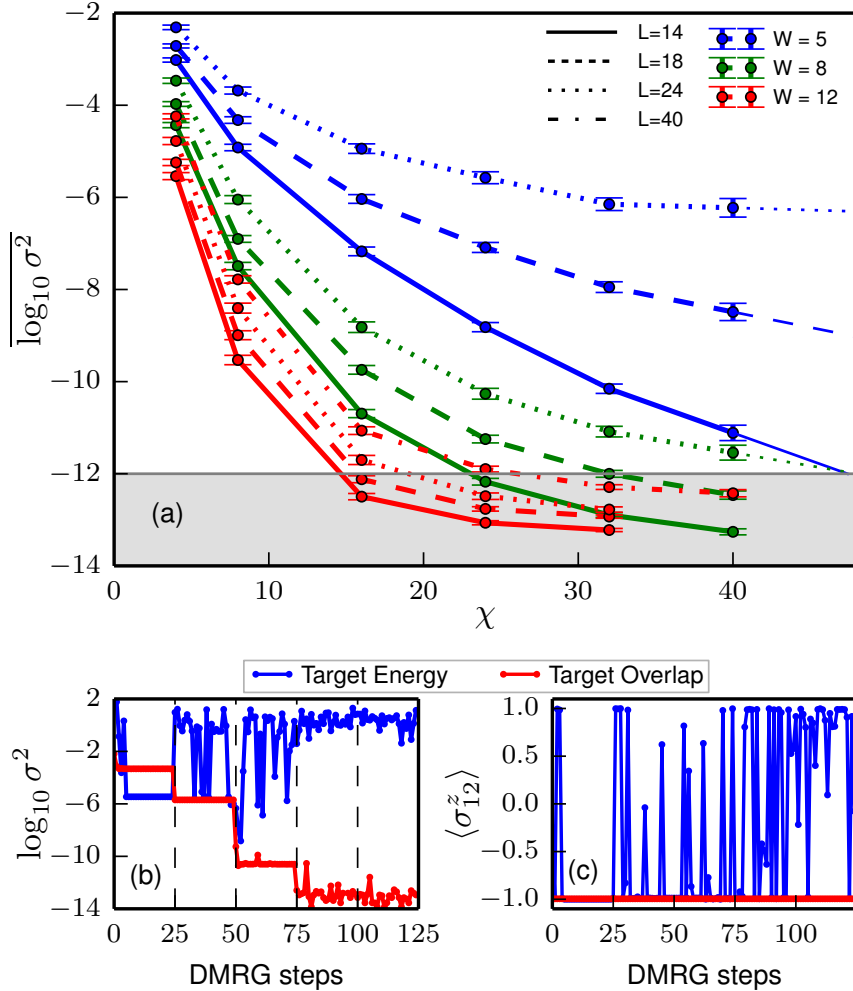


Figure 8.2: (a) Disorder averaged logarithm of the energy variance σ^2 plotted against bond-dimension χ for different disorder strengths W and system sizes L . We see a rapid decrease of the typical σ^2 with χ for moderate-strong disorder, with variances falling below machine precision (shaded grey region below 10^{-12}) at small $\chi \ll 2^{L/2}$. (b), (c) Variance and $\langle \sigma_{12}^z \rangle$ plotted against DMRG time-steps for a typical run in which χ is successively increased after each 25 steps to obtain a single eigenstate with $L = 24, W = 12$ using our overlap-based DMRG-X method (red), and a more naive energy-targeting method (blue) showing vastly better convergence for the overlap method.

8.4 Larger systems

We now turn to an evaluation of the algorithm for system sizes inaccessible to ED by examining typical variances in the energy, $\sigma^2 = \langle H^2 \rangle - \langle H \rangle^2$ for approximate eigenstates of the Hamiltonian (8.2) obtained using DMRG-X at different disorder

strengths W and system sizes L . Figure 8.2(a) shows the disorder averaged value of $\log_{10} \sigma^2$ as a function of bond-dimension χ for randomly chosen excited states from 200-1000 disorder samples at different values of W and L . The grey line at 10^{-12} marks the approximate value of machine-precision and we average $\log \sigma^2$ to capture typical behavior instead of deviations due to rare eigenstates.

At strong and moderate disorder ($W = 8, 12$), we see an initial rapid decrease of σ^2 with χ followed by a saturation—the saturation is expected to happen when the bond dimension becomes large enough to capture entanglement over a correlation length $\log_2 \chi \sim \xi$. Even at moderate disorder $W = 8$, the bond dimension saturates quickly and $\chi \sim 40 \ll 2^{L/2}$ is already sufficient to capture states to machine precision accuracy! In this regime, this method can be used to really push the boundaries on the system sizes that we have been able to study through ED. As the transition to the ergodic phase is approached, locally thermal Griffiths regions become more probable and the eigenstates become more entangled. We see that the accuracy of the method for the small bond dimensions considered starts to break down around $W = 5$, though a rough extrapolation suggests that we can still make significant improvements by using larger χ . The increase in variance with system-size at fixed χ is to be expected since even clean ground state DMRG methods make a constant error per unit length and yield a variance that grows with system size.

At even larger sizes or/and small W , inevitable locally thermal/ critical Griffiths inclusions will require special handling as a subset of the l-bits now look more delocalized and the eigenstates have a very different structure from product states within the inclusions. A comparison with ED (not shown) on a system with an artificially engineered thermal inclusion shows that the variationally obtained states correctly capture local observables away from the inclusion, but make superpositions between eigenstates that differ primarily in the inclusion region. In principle, it is possible to purify these states to obtain an eigenstate by using a hybrid energy-overlap method;

an inclusion of length ℓ occurs with probability [121] p_W^ℓ with $p_W < 1$ and has a level spacing $\Delta \sim 2^{-\ell}$. We identify the Griffiths inclusion by looking for a diminished value of the frozen moment $|\langle \sigma_i^z \rangle|$ in the states obtained by DMRG-X. We then feed these states into a hybrid algorithm which picks states at a chosen energy from the subset of states which have large overlap with the starting state away from the inclusion. This ensures that we're only trying to resolve the larger level spacing $\Delta \ll 2^{-L}$, while also maintaining the integrity of the state away from the inclusion.

Note that for a *typical* cut somewhere along the chain, the entanglement entropy scales as an area law with co-efficient ξ proportional to the localization length since the state looks thermal on length scales shorter than ξ [127]. This implies that the typical bond dimension scales exponentially with ξ . On the other hand, the *maximum* entanglement entropy across all cuts in the chain scales logarithmically with L (a thermal region of size ℓ is exponentially rare in ℓ , but has $O(L)$ chances for occurring *somewhere* in a system of size L , thereby giving $\ell \sim \log(L)$). This implies a polynomial scaling with L for the maximum bond-dimension χ_{\max} . Combining this with the $\chi^6 L$ scaling of the cost of the DMRG-X algorithm means that the algorithm scales exponentially in ξ and linearly in L if the maximum χ is fixed at some $O(1)$ number $\sim e^\xi$. On the other hand, if the bond dimension is allowed to grow to achieve a certain accuracy, then the cost scales polynomially in L with a power larger than 1 and dependent on W .

We end with two comments. First, for large system sizes, we can randomly sample from the spectrum and approximate the underlying density of states by randomly choosing initial product states. Even though the DMRG-X sweep does not use energy targeting, we can still effectively target different energy densities. Deep in the disordered phase, the initial product state is exponentially close to an actual eigenstate, and thus $\langle H \rangle$ is almost constant during a run.

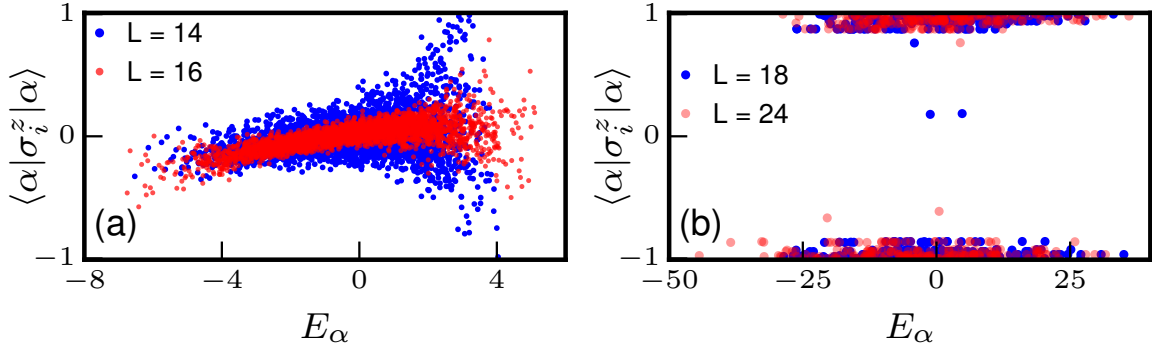


Figure 8.3: (a) $\langle \alpha | \sigma_i^z | \alpha \rangle$ plotted against $E_\alpha = \langle \alpha | H | \alpha \rangle$ for an ergodic system with $W = 1.5$ and eigenstates $|\alpha\rangle$ obtained via ED. This is an ETH obeying phase where the observable varies smoothly with energy and the fluctuations decrease with increasing L . (b) Same quantity evaluated with ~ 500 variationally obtained eigenstates $|\alpha\rangle$ of an MBL Hamiltonian with $W = 8$ and $L = 18, 24$ showing a clear violation of ETH

Second, since the variationally obtained states are MPSs, few-point observables can be computed extremely efficiently. In Fig 8.3(b) we show $\langle \alpha | \sigma_i^z | \alpha \rangle$ plotted against $E_\alpha = \langle \alpha | H | \alpha \rangle$ for ~ 500 variationally obtained eigenstates $|\alpha\rangle$ of an MBL Hamiltonian with $W = 8$ and $L = 18, 24$. We see a clear violation of ETH since the local observable does not vary smoothly with E_α and the fluctuations do not decrease with L . This also lends additional support that our method is correctly capturing MBL eigenstates since the violation of ETH would have been much weaker if the states $|\alpha\rangle$ were superpositions of actual eigenstates. Such a test is especially useful at large L s where the average level spacing is smaller than machine precision and we need to rely on methods other than the variance to diagnose the goodness of the variational states. Figure 8.3(a) shows the analogous calculation in an ergodic system with $W = 1.5$ and eigenstates obtained via ED. Here we do see a smooth variation of the observable with E_α , and the characteristic decrease in fluctuations [34] with increasing L .

8.5 Energy targeting

We now compare the convergence of our overlap method with the simplest energy targeting method which picks the eigenstate of \mathcal{H} closest to a chosen energy. Figure 8.2(b) shows a typical DMRG-X run with $L = 24$ and $W = 12$ to obtain a single eigenstate. The bond dimension is increased every 25 steps and takes the values $\chi = (4, 8, 16, 24, 32)$. We see that the overlap method (shown in red) converges extremely quickly each time the bond-dimension is increased and rapidly reaches machine precision. On the other hand, the energy targeting method (shown in blue) run for the same disorder realization and a target energy equal to the energy of the state obtained via the overlap method (upto 4 digits of precision) shows an extremely poor convergence and very large variances. In Fig. 8.2(c) we plot the expectation value of σ^z for a site in the middle of the chain evaluated using the states at each DMRG step. As expected, the overlap method shows very little fluctuation in this quantity, while the naive energy approach is clearly seen to be rattling between states with extremely different local quantum numbers.

8.6 Summary and Outlook

In summary, we have developed a DMRG-X method that successfully obtains *highly excited* eigenstates of MBL systems to machine precision accuracy at moderate-large disorder in a time that scales only polynomially with L . This method explicitly takes advantage of the local spatial structure and order characterizing MBL eigenstates, thereby moving away from traditional energy based DMRG algorithms.

A natural next step is to use the DMRG-X method to obtain phase boundaries between localized phases with different kinds of eigenstate order present. The nature of the phase transition between different localized phases is an important open

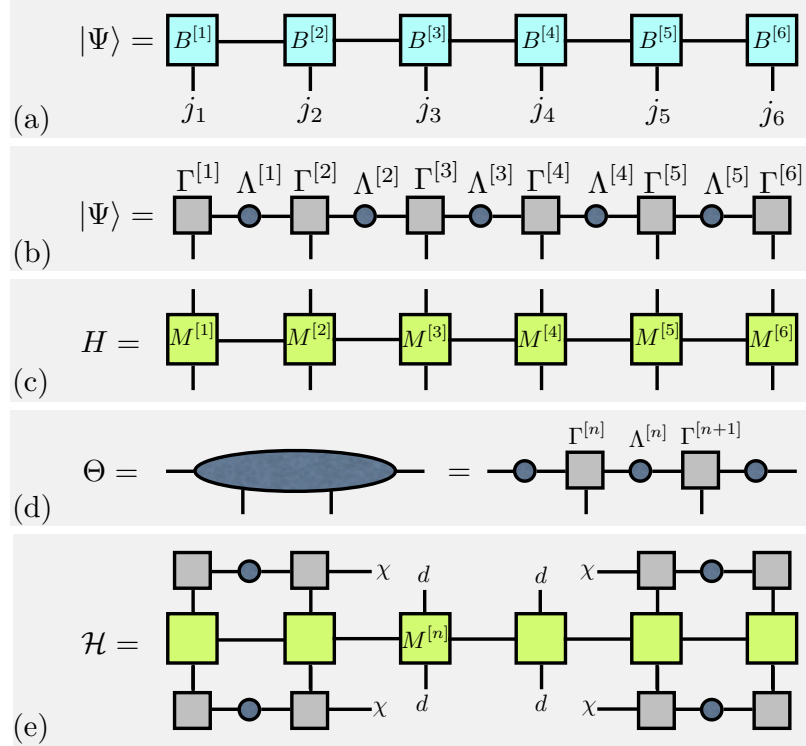


Figure 8.4: Diagrammatic representation of (a) the state $|\Psi\rangle$ as an MPS, (b) $|\Psi\rangle$ as a canonical MPS, (c) the Hamiltonian H as an MPO, (d) co-efficients Θ of $|\Psi\rangle$ in the variational basis and (e) the effective Hamiltonian \mathcal{H} in the variational basis.

question, and refining this technique to access these transitions at larger system sizes should help settle some of these questions.

8.A Details of the DMRG-X Method

In this section, we briefly recapitulate the standard DMRG algorithm [327] implemented in the language of matrix-product states (MPSs) [277], before providing more details on the DMRG-X method. Section IV in Ref. [183] also provides a very clear exposition of these numerical methods and some of our discussion closely follows this reference.

A general quantum state $|\Psi\rangle$ for a one-dimensional system of L sites can be written in the following matrix-product state (MPS) form:

$$|\Psi\rangle = \sum_{j_1, \dots, j_L} \sum_{0 < \gamma_n \leq \chi_n} B_{\gamma_1}^{[1]j_1} B_{\gamma_1 \gamma_2}^{[2]j_2} \dots B_{\gamma_{L-1}}^{[L]j_L} |j_1, \dots, j_L\rangle. \quad (8.3)$$

where $|j_n\rangle$ with $j_n = 1, \dots, d$ is a basis of local states at site n (for a spin 1/2 system, $d = 2$ and $|j_n\rangle = |\uparrow\rangle, |\downarrow\rangle$), and the $B^{[n]}$ are rank three tensors (except on the first and last sites where they are rank two tensors). Figure 8.4(a) shows a pictorial representation of an MPS. The external legs j_n are the “physical” spin indices whereas the internal legs γ_n are the virtual indices that are contracted. Each $B^{[n]j_n}$ is a $\chi_n \times \chi_{n+1}$ matrix (at the boundaries $\chi_1 = \chi_{L+1} = 1$) and each matrix product $\prod_i B^{[i]j_i}$ in Eq. (8.3) produces a complex number which is the amplitude of $|\Psi\rangle$ on the basis state $|j_1 \dots j_L\rangle$.

The maximum dimension χ of the $\{B^{[n]}\}$ matrices is called the bond-dimension of the MPS and low entanglement states can be efficiently represented by MPSs of bond dimension $\chi \ll d^{L/2}$. The relationship between χ and the entanglement can be made more precise by considering the Schmidt decomposition of the state $|\Psi\rangle$. For a given bipartition of the system into left and right halves, a singular value decomposition can be used to rewrite $|\Psi\rangle$ as

$$|\Psi\rangle = \sum_{\alpha} \Lambda_{\alpha} |\alpha\rangle_L |\alpha\rangle_R$$

where the $|\alpha\rangle_{L/R}$ form orthonormal bases for the left and right halves respectively, ${}_L\langle\alpha|\beta\rangle_L = {}_R\langle\alpha|\beta\rangle_R = \delta_{\alpha\beta}$, and the entanglement entropy of the bipartition is defined through the Schmidt values Λ_{α} as $S_E = -\sum_{\alpha} |\Lambda_{\alpha}|^2 \ln |\Lambda_{\alpha}|^2$. Following a prescription by Vidal [312], it is possible to define a *canonical form* (Fig.8.4(b)) for the MPS by rewriting each matrix $B^{[n]j_n}$ as a product of a $\chi_n \times \chi_{n+1}$ dimensional complex matrix $\Gamma^{[n]j_n}$ and a square diagonal matrix $\Lambda^{[n]}$ such that matrices $\Lambda^{[n]}$ matrices contain the

non-zero Schmidt values for a bipartition between sites n and $n + 1$

$$|\Psi\rangle = \sum_{j_1, \dots, j_L} \Gamma^{[1]j_1} \Lambda^{[1]} \Gamma^{[2]j_2} \Lambda^{[2]} \dots \Lambda^{[L-1]} \Gamma^{[L]j_L} |j_1, \dots, j_L\rangle = \sum_{\alpha=1}^{\chi_{n+1}} \Lambda_{\alpha\alpha}^{[n]} |\alpha_n\rangle_L |\alpha_n\rangle_R, \quad (8.4)$$

and the states

$$\begin{aligned} |\alpha_n\rangle_L &\equiv \sum_{j_1 \dots j_n} (\Gamma^{[1]j_1} \Lambda^{[1]} \dots \Lambda^{[n-1]} \Gamma^n)_\alpha |j_1 \dots j_n\rangle \\ |\alpha_n\rangle_R &\equiv \sum_{j_{n+1} \dots j_L} (\Gamma^{[n+1]j_{n+1}} \Lambda^{[n+1]} \dots \Lambda^{[L-1]} \Gamma^L)_\alpha |j_{n+1} \dots j_L\rangle \end{aligned} \quad (8.5)$$

define the orthonormal Schmidt states for the left and right halves of the bipartition respectively. This canonical form clearly relates the bond dimension of the MPS χ to the number of Schmidt values contributing significantly to the entanglement entropy.

A standard two-site DMRG algorithm tries to find the ground state $|\psi_0\rangle$ by variationally optimizing the MPS matrices on neighboring sites to minimize the energy $\langle \psi_0 | H | \psi_0 \rangle$ while keeping the rest of the chain fixed. We define a matrix-product operator (MPO) representation of H exactly analagous to Eq. 8.3 but now using 4-index tensors M as shown in Fig. 8.4(c), and then implement the following steps:

- To update the MPS between sites n and $n + 1$, rewrite the state $|\Psi\rangle$ in the basis spanned by the states $|j_n\rangle$, $|k_{n+1}\rangle$ and the left and right Schmidt states $|\alpha_{n-1}\rangle_L$ and $|\beta_{n+1}\rangle_R$

$$|\psi\rangle = \sum_{j,k,\alpha,\beta} \Theta_{\alpha\beta}^{jk} |\alpha_{n-1}\rangle_L |j_n\rangle |k_{n+1}\rangle |\beta_{n+1}\rangle$$

where the definition of Θ is shown pictorially in Fig. 8.4(d) and follows directly from the definitions (8.5).

- Define an effective Hamiltonian \mathcal{H} as the Hamiltonian projected to the $|\alpha j k \beta\rangle$ basis. This is a $d^2 \chi^2 \times d^2 \chi^2$ dimensional operator, again best seen pictorially in Fig. 8.4(e).

- Find the ground state of \mathcal{H} , denoted by $\tilde{\Theta}_{\alpha\beta}^{jk}$. This is the optimal state for minimizing $\langle\psi_0|H|\psi_0\rangle$ in this subspace.
- Do an SVD on $\tilde{\Theta}$ to put the MPS back in canonical form with the matrices $\Gamma^{[n]}, \Lambda^{[n]}, \Gamma^{[n+1]}$ updated.
- Repeat for the next pair of sites and iteratively sweep through the chain till the state converges.

The only difference between the ground-state DMRG algorithm outlined above and DMRG-X is in step 3. In the DMRG-X algorithm, we find *all* the $d^2\chi^2$ eigenstates of \mathcal{H} instead of just its ground state. We then pick $\tilde{\Theta}$ as the eigenstate of \mathcal{H} with the maximum overlap with the previously found state in the iterative scheme. The algorithm is initialized with an appropriate initial state which is perturbatively “close” to the true eigenstates of the MBL Hamiltonian (such as a product state in the σ^z basis).

Part V

Statistical Mechanics with the Entanglement Hamiltonian

Chapter 9

How Universal is the Entanglement Spectrum?

9.1 Introduction

A set of ideas from quantum information has revitalized the study of phase structure in condensed matter [14]. Amongst these is the elucidation of the entanglement in wavefunctions. As we saw in Sections 7 and 8, the area-law entanglement entropy in highly excited eigenstates is a key signature of the MBL phase and plays a crucial role in tensor-network approaches to diagonalizing MBL Hamiltonians. More conventionally, the entanglement entropy has been studied in ground states of quantum systems. This quantity obeys an area law in gapped phases [98] with a subleading universal correction indicating the presence of topological order [177, 203].

In a striking development, Haldane and Li [205] found that the largest eigenvalues of the reduced density matrix in a subregion A could contain more universal signatures than just the entanglement entropy. Consider a bipartition of the system into two parts, A and B . The reduced density matrix for A , $\rho_A = \text{Tr}_B |\psi\rangle\langle\psi|$ is obtained for the wavefunction $|\psi\rangle$ by tracing over the degrees of freedom in part B . Haldane and

Li defined the “entanglement Hamiltonian” H_E as $\rho_A = \exp(-H_E)$, and its energy spectrum as the “entanglement spectrum” (ES). They found that the low-energy ES of the Pfaffian quantum Hall state resembled the minimal edge excitation spectrum, and proposed the ES as a fingerprint of topological order. A large literature followed [44, 196, 332, 256, 297, 305, 108, 250, 164, 140, 92, 264, 63, 235, 145, 259, 244, 295], and the idea has been applied to broken symmetry [77, 214, 9, 10, 188, 243, 146, 242, 159] and near critical points [51, 274, 82, 200, 119]. Broadly speaking, this body of work suggests that a) the low-energy ES contains universal information about the phase that goes beyond the entanglement entropy and b) this information reflects the actual excitation spectrum of the systems at issue.

In this chapter, we offer a critique of these beliefs and show that the low-energy ES contains much less universal information than assumed. Define the canonical ensemble of H_E as $\rho_E = e^{-H_E/T_E}$, where T_E is the entanglement temperature. For any operator O_A in A , $\langle O_A \rangle = \text{Tr}(\rho_A O_A) = \text{Tr}(e^{-H_E} O_A)$. *Thus, all physical observables in the parent wavefunction are derived from the canonical ensemble of H_E at entanglement temperature $T_E = 1$.* On the other hand, the low-energy ES probes the limit $T_E \rightarrow 0$. For generic Hamiltonians, these two limits need not be in the same phase, and the exponentially fewer eigenstates near the ground state contribute vanishingly to physical canonical averages at $T_E = 1$.

We show that, as a consequence, H_E can exhibit quantum phase transitions (QPT) with accompanying singular changes in the ES that are entirely spurious. These ES rearrangements take place away from actual phase boundaries and all *physical* observables remain completely analytic. This implies that previously used diagnostics of phase structure based on the low-energy ES, such as the “tower of states” in broken symmetry systems, quasi-degeneracies of the excitation spectrum and the entanglement gap as an order parameter can fail. We first present simple, general arguments in the context of broken symmetries and then illustrate them by explicit

computation for a 2D Ising model. We then give an analogous treatment for the $\sigma_{xy} = 1$ phase of the Chern insulator which will bring us full circle to the work of Li and Haldane.

A few results in the literature already suggest the need for caution in using the ES. The ES is a purely ground state property. More than one local Hamiltonian can have the same ground state and thus the same ES, and examples where the spectrum is gapped in one case and gapless in another are known [106]. Further, by the area-law, H_E lives in one dimension less than H so the two spectra cannot easily match unless the low energy excitations are at the boundary. The failure mode of the ES discussed here is new and cuts across both considerations.

9.2 Systems with symmetry breaking

The belief in the literature is that symmetry breaking in H_E (and the related “tower of states” spectrum for continuous symmetries) reflects order in the underlying ground state. We show that this belief is mistaken.

Consider the Ising model in a transverse field δ (TFIM). In $d \geq 2$ dimensions, the TFIM is ferromagnetic for $\delta < \delta_c^P$ and paramagnetic for $\delta > \delta_c^P$. We use P and E to denote physical and entanglement related quantities. By the area law, the entanglement Hamiltonian associated with a cut in real space describes a $d - 1$ dimensional boundary system. The generic phase diagram of H_E as a function of T_E and δ (Fig. 9.1) must satisfy the following constraints: a) the $T_E = 1$ cut must coincide with the physical phase diagram, b) as $\delta \rightarrow 0$, H_E projects onto the ideal ferromagnetic state and hence is ordered at all T_E , c) as $\delta \rightarrow \infty$, H_E projects onto the ideal paramagnetic state and cannot support order at any T_E . Together (a) and (b) imply the existence of the ordered region FM₁ wherein the boundary spins in H_E exhibit ferromagnetic order; the bulk spins far from the cut will be trivially ordered

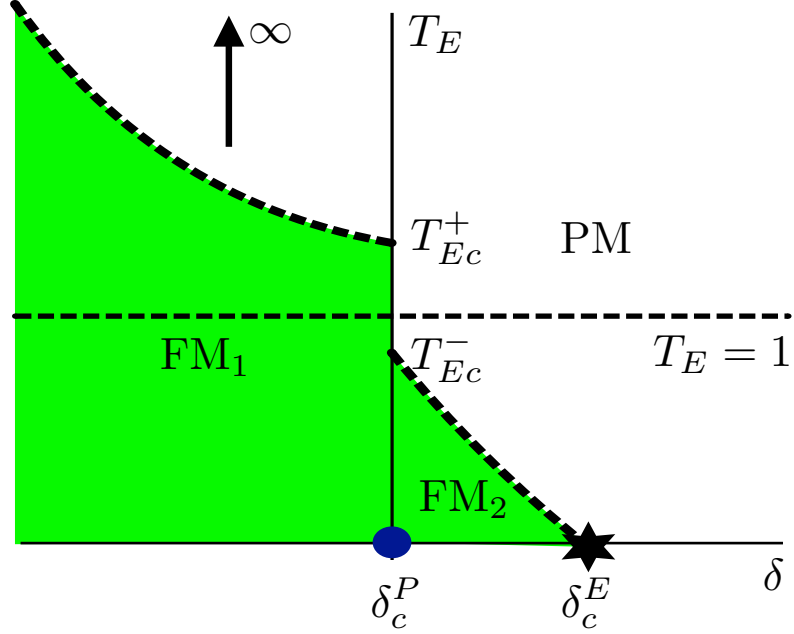


Figure 9.1: Phase diagram of the entanglement Hamiltonian $H_E(\delta)$ for an Ising model. Blue dot at δ_c^P : physical transition. Black star at δ_c^E : pseudo QPT. FM_2 : spurious ordered phase. Dashed line separating FM_2 and PM: pseudo transition in $d \geq 3$. If generic, $T_{Ec}^+ = \infty$.

at any T_E . Now (a) *also* implies that the boundary correlation length diverges as $\delta \rightarrow \delta_c^P$ at $T_E = 1$. The correlation length at $T_E = 0$ is even longer at any δ near δ_c^P . Thus, at small T_E , FM_1 should continue into a second ordered region FM_2 for $\delta > \delta_c^P$. The phase FM_2 is spurious as, in this regime, the low-energy ES is ordered when the physical state is paramagnetic. At $\delta_c^E > \delta_c^P$, there is a ‘pseudo’ QPT from FM_2 into the paramagnet, accompanied by singular rearrangements in the ES.

A few comments about Fig. 9.1 before we turn to a computation. First, *microscopic* couplings in H_E exhibit singularities in the vicinity of the critical point δ_c^P [77]. Thus, the two ordered phases on either side, FM_1 and FM_2 , need not connect smoothly¹. Second, for the generic TFIM, $T_{Ec}^+ = \infty$ as the boundary H_E is always ordered when the bulk is. For the PEPS/Rokhsar-Kivelson wavefunction we

¹In higher dimensions, the simplest hypothesis is that $T_{Ec}^- = 1$ on the critical line; the computations reported in Ref. [213] bear on what happens in $2 < d < 3$, but they currently deal only with subleading terms in the thermodynamics of H_E .

consider below, the evidence appears consistent with $T_{E_c}^+ < \infty$. Third, in $d = 2$, by the Peierls-Mermin-Wagner theorem, FM_2 only exists at $T_E = 0$.

We demonstrate the above scenario through an explicit calculation in a 2D Ising model. We work with the Rokhsar-Kivelson (RK) Ising wavefunction [270],

$$|\Omega\rangle = \sum_{\sigma} e^{-E_{cl}/2} |\vec{\sigma}\rangle, \quad (9.1)$$

where E_{cl} defines the classical anisotropic Ising model for spins $\sigma_{i,j}^z = \pm 1$ on sites (i, j) of a 2D square lattice

$$E_{cl}(\vec{\sigma}) = \sum_{i,j} -\beta_x (\sigma_{i,j}^z \sigma_{i,j+1}^z - 1) - \beta_y (\sigma_{i,j}^z \sigma_{i+1,j}^z - 1). \quad (9.2)$$

The probability of a given configuration is $e^{-E_{cl}(\vec{\sigma})}$. Thus, the quantum RK wavefunction reproduces classical probabilities in the z -basis. The RK wavefunction is the ground state of a *local* Ising-symmetric parent Hamiltonian $H_{RK}(\beta_x, \beta_y)$, which is quantum critical on the same critical line as the classical 2D Ising model [137, 55, 18]: $\sinh(2\beta_x^c) \sinh(2\beta_y^c) = 1$. This critical line defines the analog of δ_c^P in the preceding discussion.

To compute H_E , we place the system on an open cylinder of length L_x and circumference L_y and trace out half the cylinder (Fig. 9.2). Consider the limit $\beta_x \gg 1$, $\beta_y = 0$ in the PM phase. This corresponds to L_y decoupled classical Ising chains parallel to the x axis. As $|\Omega\rangle$ obeys a strict area law, the basis states of H_E can be labelled by the spins at the boundary of the entanglement cut. For chain i , the two states are

$$|\sigma_{i,n}^z; A\rangle \equiv \sum_{\substack{\sigma_{i,j}^z \\ j=0,\dots,n-1}} e^{\sum_{j=0}^{n-1} \frac{\beta_x}{2} (\sigma_{i,j}^z \sigma_{i,j+1}^z - 1)} \prod_{j=0}^n \otimes |\sigma_{i,j}^z\rangle \quad (9.3)$$

where $n = L_x/2$ and $\sigma_{i,n}$ is the spin to the left of the cut. A small value of β_y couples the chains. Using perturbation theory, we can systematically calculate H_E in powers

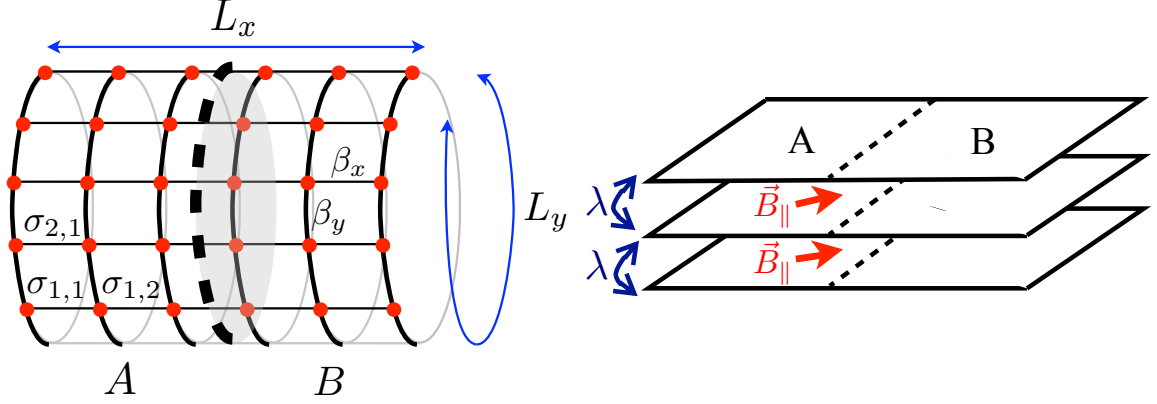


Figure 9.2: Left: the RK Ising model on the square lattice. Right: the three layer Chern insulator model with magnetic flux between the layers. Region B is traced out in the ground state to obtain the entanglement Hamiltonian in A .

of β_y (keeping $\beta_x \gg 1$). To first order,

$$H_E = -2e^{-\beta_x} \sum_{i=1}^{L_y} \tilde{\sigma}_{i,n}^x - \frac{\beta_y e^{2\beta_x}}{2} \sum_{i=1}^{L_y} \tilde{\sigma}_{i,n}^z \tilde{\sigma}_{i+1,n}^z,$$

where $\tilde{\sigma}^{x,z}$ act on the basis states in Eq. (9.3) in the usual way. The condition for our perturbative result to be valid is $\beta_y e^{2\beta_x} \ll 1$. Although the states of H_E are labelled by the boundary, they have weight in the 2d bulk.

We now present our central result. As H_E is a 1D TFIM, it undergoes a pseudo QPT transition at a critical value of β_y^E

$$\beta_y^E \sim 4e^{-3\beta_x}. \quad (9.4)$$

This critical point lies within the regime of validity of our perturbation theory $\beta_y^E e^{2\beta_x} \ll 1$. The physical transition in H_{RK} is however at

$$\beta_y^P \sim e^{-2\beta_x}. \quad (9.5)$$

Thus, $\beta_y^E \ll \beta_y^P$ with the inequality getting parametrically better for larger β_x ; the zero temperature entanglement transition in H_E precedes the physical one in a controlled limit. Essentially, the ground state of H_E undergoes a surface ordering transition at β_y^E before the bulk orders at β_y^P .

These pseudo transitions can be diagnosed by the oft-studied Renyi entropies. The Renyi entropy S_n is proportional to $F_{1/n} - F_1$, where $F_T = -T \log(\text{Tr } e^{-H_E/T})$ is the entanglement free energy at temperature T . Therefore, whenever H_E has a pseudo $T_E > 0$ phase transition, the S_{1/T_E} Renyi exhibits unphysical singularities in the PM. In the (2+1)D TFIM, Singh et. al. [287] show that S_2 is analytic for $\delta \neq \delta_c^P$. This is consistent with the proposed phase diagram as only S_∞ is singular in the PM phase in $d = 2$. Previous Renyi studies of the RK Ising model have only focused on sub-leading terms [293], while the relevant signature here is in the leading term.

Recent studies in systems with continuous symmetry breaking [214, 10, 188, 243] have reported that the ES shows the characteristic “tower of states” (ToS) structure of finite-size systems in the ordered phase. Our arguments show that the ES can be ordered even when the ground state is disordered in $d \geq 3$ (FM_2 in Fig. 9.1), with XY symmetric systems exhibiting Kosterlitz-Thouless order even in $d = 2$. In this spurious region, the ES exhibits ToS structure, falsely diagnosing order. If the symmetry is successively broken in stages (e.g. $O(4) \rightarrow O(3) \rightarrow O(2)$), then a spurious ToS may also appear in the putative ordered phase. However, we note that for non-RK wavefunctions, the spacing in the ToS in H_E scales with system size L as $e^{-L^{d-1}}$ in the spurious FM_2 phase, and as e^{L^d} in FM_1 . In principle, this identifies the spurious ToS in this case, though it requires more numerically intensive work. For RK wavefunctions, the scaling is the same in both ferromagnets.

9.3 Chern Insulator/QH Hall fluid

The quantum Hall (QH) fluids are incompressible in the bulk, but support chiral, gapless edge excitations. The topological order in these fluids is manifest in the universal content of the edge theory. In the ideal $\nu = 1/3$ fractional QH Laughlin state, the edge is a single chiral boson with a universal compactification radius. The low-energy ES of such ideal states (and more realistic states) mimics the edge spectrum [205].

However, the edges of realistic states can exhibit edge reconstruction in which one or more non-chiral modes get added to the spectrum [59, 165, 331]. This leads us to conjecture that the ES can *also* exhibit additional non-chiral modes. Further, there exist phase transitions in which the ES reconstructs while the system remains in the same topological phase. For related comments, see [295]. While the traditional discussion of edge reconstruction in the QHE requires interactions, we substantiate our conjecture below with an example involving a free fermion Chern insulator.

The connection between the physical and the virtual edge is direct for free fermions [108]. First, H_E for the ground state of a free fermion Hamiltonian is quadratic [241]². Thus, the ES vs the momentum along the cut, k_y is a band spectrum. Second, the single particle entanglement energies, ξ_i , are monotonically related to e_i , the energies of a “flat-band” Hamiltonian restricted to region A :

$$e_i = (1/2) \tanh(\xi_i/2) \tag{9.6}$$

The “flat-band” model on $A+B$ is in the same phase as the original Hamiltonian and has the same eigenstates, but with flattened bands [179]. Thus, the transitions at the physical edges of A in the flat-band model appear in the ES of the ground state of H . We plot (Fig. 9.3) e_i vs k_y instead of the actual many-body ES for clarity.

²More generally, H_E is quadratic for any Slater determinant many-body state.

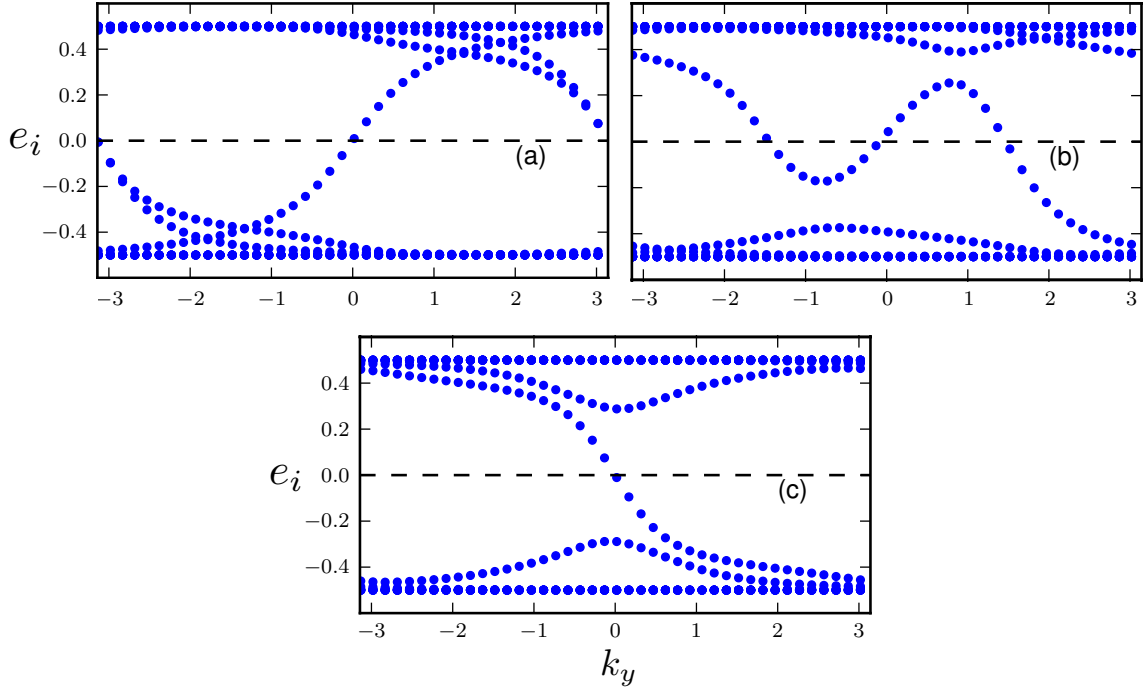


Figure 9.3: Entanglement spectra (Eq. (9.6)) of the ground states of the three layer model with $M_1 = -2.5$, $M_2 = -1$, $M_3 = -3.5$ and $L_x = L_y = 200$. (a) $\lambda = 0$, $\vec{A}_l = 0$. (b) $\lambda = 1/2$, $\vec{A}_1 = -\vec{A}_3 = (-\pi/2, -\pi/2)$, $\vec{A}_2 = (0, 0)$. (c) $\vec{A}_1 = -\vec{A}_3 = (-\pi, -\pi)$, $\vec{A}_2 = (0, 0)$.

Consider the $C = 1$ Chern insulator on a periodic lattice. To allow for multiple edge modes, we take three independent bipartite layers in which the lower bands have $C = 1$ in two layers and $C = -1$ in the third layer. In the ground state, all three low energy bands are occupied and the system exhibits net $C = 1$ with two right moving and one left moving chiral edge modes, i.e. the edge content exceeds the minimal edge content (central charge $c = 1$) by one non-chiral mode (whence $c = 3$). This appears in the ES in Fig. 9.3(a) as well. By deforming the Hamiltonian without closing the gap to the three high energy bands, we can modify the Chern numbers of the three lower bands to $C = 1, 0, 0$. The ES then exhibits one chiral mode with $c = 1$ and there has to be a QPT in H_E *en route*.

For simplicity, we give a different deformation in which we perturb the starting problem with a combination of interlayer hopping and uniform magnetic fields parallel

to the layers (Fig. 9.2). The Hamiltonian is:

$$H = \sum_{l=1}^3 h_l(\vec{A}_l, M_l) - \lambda \sum_{l=1}^2 a_{\vec{k}}^\dagger(l+1)a_{\vec{k}}(l) + h.c. + b_{\vec{k}}^\dagger(l+1)b_{\vec{k}}(l) + h.c. \quad (9.7)$$

where l is the layer index, λ the hopping amplitude between identical sites on adjacent layers and

$$h_l(\vec{A}_l, M_l) = \sum_{\vec{k}} \begin{pmatrix} a_{\vec{k}}^\dagger(l) & b_{\vec{k}}^\dagger(l) \end{pmatrix} (\vec{d}(\vec{k} + \vec{A}_l, M_l) \cdot \vec{\sigma}) \begin{pmatrix} a_{\vec{k}}(l) \\ b_{\vec{k}}(l) \end{pmatrix}$$

$$\vec{d}(\vec{k}, M_l) = \begin{pmatrix} \sin(k_x), & \sin(k_y), & 2 + M - \cos(k_x) - \cos(k_y) \end{pmatrix}$$

is the single layer Hamiltonian on layer l . Each layer is bipartite and $a_{\vec{k}}^\dagger(l), b_{\vec{k}}^\dagger(l)$ create Bloch waves on the two sublattices. \vec{A}_l are constant vector potentials corresponding to magnetic fluxes parallel to and between the layers. The phase diagram of one layer at half filling is a function of M_l only: for $M_l > 0$ or $M_l < -4$, the ground state is a trivial insulator. When $-2 < M_l < 0$, the ground state is a Chern insulator with Chern number $C = -1$, while $C = 1$ corresponds to $-4 < M_l < -2$. At $M_l = 0, -2, -4$, the system is gapless with Dirac fermion excitations.

At $\lambda = 0, \vec{A}_l = \vec{0}$, we pick M_l so that layers 1 and 3 are in the $C = 1$ phase and layer 2 is in the $C = -1$ phase. On turning on weak inter-layer coupling and magnetic fluxes, this point extends into a $C = 1$ phase. The location of the Fermi points in the ES depends on a combination of λ and the fluxes. We can therefore arrange for the Fermi points of opposite chirality to be far apart in the starting configuration with the two left moving ones degenerate (Fig. 9.3(a)), then evolve into a configuration where they are all at distinct locations (Fig. 9.3(b)), and finally arrive at a configuration where an oppositely charged pair can meet and annihilate (Fig. 9.3(c)).

The transition in the ES is a genuine QPT, as the central charge changes. However, the net chiral central charge, $C_c = C_{left} - C_{right}$, is unchanged. More physically, there

is a residual universality in the edge (or ES) structures for a given bulk QH state as the conductance is the same at any T (or T_E). In principle, this can be extracted from the low-energy ES of sufficiently large systems (much larger than currently accessible in computational studies). All the methods to date to extract C_c rely on the entire spectrum [338, 76, 336].

We end with three comments. First, the quasi-degeneracies of particle-hole excitations as a function of momentum δk_y relative to the ground state of H_E —the commonly employed diagnostic for topological order—change. In Fig. 9.3(c), they take the values $\{1, 1, 2, 3, 5 \dots\}$ for $\delta k_y = 0, 1, 2 \dots$, while in the middle and left panels, they are modified to $\{1, 2, 5 \dots\}$ for $\delta k_y = 0, 1, 2$. This modified counting is not universal; by changing the speeds of the movers on the left edge, almost any sequence is possible. Second, the arguments above should apply to fractional QH states, as they exhibit edge reconstruction. Recent work [52] has shown that for sufficiently complex abelian quantum Hall states, even the minimal edge structure is not unique and there can be phase transitions between distinct stable edge structures. The ES should exhibit analogous phase transitions. Third, while our general arguments apply to isotropic states, we work with anisotropic states for convenience.

9.4 Conclusions

This chapter has two central messages about the low-energy entanglement spectrum. First, H_E can exhibit spurious quantum phase transitions that have *nothing* to do with any physical phase transitions. All physical observables are derived from H_E at $T_E = 1$ and can remain analytic even as the low-energy ES exhibits singular changes. Second, previously used diagnostics of phase structure based on the low-energy ES, such as the tower of states, quasi-degeneracies, and the entanglement gap, either fail

completely or require much more careful analysis. Altogether our work indicates the need for caution in interpreting the results of ES computations.

Chapter 10

Eigenstate Thermalization and Representative States on Subsystems

10.1 Introduction

In Chapter 9, we employed the strategy of doing statistical mechanics with the entanglement Hamiltonian H_E to study the limits of the universality of the low-energy entanglement spectrum. This chapter continues in this vein and discusses the implications of applying the eigenstate thermalization hypothesis to H_E .

We consider the following problem. Let $|AB\rangle$ be a pure state of the quantum system $A \cup B$ made up of degrees of freedom that can be partitioned into spatially disjoint regions A and B with A being the smaller subregion. We wish to find a pure state on region A , $|\psi_A\rangle$, which we can use for practical purposes to reproduce expectation values of typical operators of interest in region A . We will call such a state a “representative state” (RS) on A .

Evidently, proceeding axiomatically would require us to define which operators are “typically of interest” and what error is acceptable for “practical purposes”. With these defined we can then ask for what states $|AB\rangle$ and bipartitions A and B such RS can be found. We will not try to carry out such an exercise in the abstract. Instead we will use ideas from quantum statistical mechanics, notably the equivalence of ensembles and the eigenstate thermalization hypothesis (ETH) [89, 291, 267] to discuss several broad classes of states for which one can usefully define RS. Possibly future work can fold our concrete examples into a more general account.

The striking feature of a RS description of subsystems is that it dispenses with the entanglement between the degrees of freedom in A and those outside. This entanglement is at the root of the exact description by means of the reduced density matrix

$$\rho_A = \text{Tr}_B |AB\rangle\langle AB|$$

which is the textbook prescription for describing a subsystem. We are interested in replacing this exact description with an RS description.

The intuition for why it may be possible to replace ρ_A with a single state on A comes from writing ρ_A in the suggestive form [205]

$$\rho_A = e^{-H_E}$$

which defines the entanglement Hamiltonian H_E on A . In this form, ρ_A is the canonical density matrix of H_E at entanglement temperature $T_E = 1$, and all physical observables in A are derived from this ensemble: $\langle O_A \rangle_{T_E=1} = \text{Tr}(\rho_A O_A) = \text{Tr}(e^{-H_E} O_A)$. If H_E is assumed to be “generic” – in the sense that we can do quantum statistical mechanics with it – we can replace canonical averages with a single quantum state via the ETH. More concretely, the ETH assumes that eigenstate expectation values (EEVs) of few-body observables computed from individual eigenstates in an energy

window match canonical or microcanonical averages in the thermodynamic limit. It follows that if H_E satisfies the ETH, we can replace the canonical ensemble of H_E with eigenstates of H_E drawn from the right entanglement energy window. These states are the desired “representative states”. Further, in cases where H_E doesn’t satisfy the ETH (e.g. H_E is integrable/free or many-body localized [227]), RS can be found for a smaller, more restricted class of observables in a manner to be discussed later. We note that a similar line of reasoning in subsequent work by Garrison and Grover [117] shows that a single many-body eigenstate can be used to encode the full Hamiltonian for the purposes of reproducing few-body observables in small subsystems.

In this article we will discuss three families of quantum states for which an RS description can be provided. These are a) ground states of local quantum Hamiltonians, b) highly excited states (those with a finite energy density) of local Hamiltonians, and c) randomly picked states in Hilbert space. For (a) and (b) we will consider subsystems A such that both A and B are simply connected domains, while for (c) we will consider arbitrary subsystems of $A \cup B$. In all three cases we use the number of spins/qubits in A , denoted by $|A|$, as our control parameter with the implicit ordering $1 \ll |A| \leq |B|$. In this limit we will argue that we can reproduce the expectation values of few-body operators¹ on A to controlled accuracy by means of RS.

In detail, we start with a free fermion system for which H_E is known to be free (and hence integrable) [241]. While this is a “non-generic” case which doesn’t permit us to use the full machinery of ETH, it nonetheless provides a transparent illustration of our ideas for a special class of operators that are “orthogonal” to the conserved quantities. We consider RS descriptions of both the ground state and highly-excited states of the free-fermion system. We then generalize our results to ground and excited states of generic gapped, local quantum Hamiltonians. In this case, we provide evidence that H_E will also be generic and we can use the ETH to argue for RS. Finally, we consider

¹One question we leave open is the meaning of “few”, where the corresponding question regarding ETH is still open.

randomly picked vectors in Hilbert space where the RS can be obtained quite directly. We conclude with some comments on generalizations and open questions.

10.2 Free fermions

We begin with a gapped free fermion model in 2D which illustrates the ideas and errors involved in a representative states description. Consider the dimerized hopping model in 2D:

$$H = - \sum_{i,j} t_{i,i+1}^x c_{i,j}^\dagger c_{i+1,j} + t^y c_{i,j}^\dagger c_{i,j+1} + h.c. \quad (10.1)$$

where $c_{i,j}$ are fermionic operators on sites (i,j) of a 2D square lattice, the hopping in the x direction, $t_{i,i+1}^x$, alternates between $1 \pm \delta$, and t^y is the hopping in the y direction. The Hamiltonian is readily diagonalized in momentum space, and there are two bands with momenta in the reduced Brillouin zone. At half filling, the model is gapped for either $t^y < \delta < 1$ or $\delta > 1$ and $t^y < 1$.

The entanglement Hamiltonian for free fermion systems is itself quadratic [241]:

$$\rho_A = \frac{1}{Z} e^{-H_E}, \quad H_E = \sum_{i=1}^{|A|} \epsilon_i f_i^\dagger f_i \quad (10.2)$$

where the operators f_i live in A and are related to the original fermionic operators by a canonical transformation, and $Z = \text{Tr} \rho_A$. The single-particle entanglement energies $\{\epsilon_i\}$ are easily calculated through their monotonic relation with the eigenvalues ξ_i of the correlation matrix $C_{\mathbf{r}\mathbf{r}'} \equiv \langle c_{\mathbf{r}}^\dagger c_{\mathbf{r}'} \rangle$ restricted to region A :

$$\epsilon_i = \log \left(\frac{1 - \xi_i}{\xi_i} \right). \quad (10.3)$$

Evidently, H_E is also integrable, with the set of conserved quantities $f_i^\dagger f_i$.

We will show that we can find representative states in A that reproduce canonical averages computed using ρ_A . However, the RS cannot be used to reproduce all few-body observables in A . Since H_E is integrable (and thus non-generic for the purposes of the ETH), we must restrict ourselves to few-body observables that are roughly uniformly “spread” over all conserved quantities in H_E . As our underlying Hamiltonian is translationally invariant, we expect that momentum conservation is broken in H_E by boundary effects alone so that the $f_i^\dagger f_i$ have a fair degree of locality in momentum space. This indicates that operators which are local in real space are good candidates for an RS description and we study these below.

We do this in turn for the system at zero and finite temperatures.

10.2.1 $T = 0$

Pick a set of parameters t^y and δ such that the Hamiltonian H is gapped at half filling. At zero temperature, the system is in the ground state of H on $A \cup B$. We trace over half the system with the entanglement cut along the y axis to obtain ρ_A and H_E in the usual fashion. Gapped ground states are believed to satisfy an area law for the entanglement entropy [98]:

$$S_E = -\text{Tr} \rho_A \log \rho_A \sim s L_A^{d-1}$$

where L_A is the linear size of region A and d is the spatial dimension. In $d = 1$, a rigorous proof of the above scaling exists [135, 17]. The entanglement entropy is the thermal entropy of H_E at $T_E = 1$; as this scales only with the area of the boundary, H_E is morally a $(d - 1)$ -dimensional Hamiltonian whose low-energy excitations live on the boundary between A and B .

The many-body eigenstates of H_E are Slater determinants in terms of the f operators in (10.2). For spatially local observables, the canonical ensemble of H_E at

$T_E = 1$ can be replaced by individual eigenstates: we pick representative states $|\psi_A\rangle$ by filling single particle states $f_i^\dagger|0\rangle$ with the Fermi-Dirac (FD) probability distribution at $T_E = 1$ and $\mu_E = 0$. Thus the representative states lie in an energy window that scales as $\sqrt{L_A^{d-1}}$ about the mean entanglement energy $\langle H_E \rangle_{T_E=1}$.

Drawing states using the FD distribution ensures that averages for operators $\hat{\mathcal{A}}$ computed using the ensemble of RS agree with the canonical average of H_E . However, there are fluctuations from eigenstate to eigenstate within the energy window which can be shown to scale as

$$\langle \hat{\mathcal{A}} \rangle_{T_E=1} = \langle \psi_A | \hat{\mathcal{A}} | \psi_A \rangle + O\left(\sqrt{\frac{1}{L_A^{d-1}}}\right). \quad (10.4)$$

The scaling follows from the expansion of the $\hat{\mathcal{A}}$ in the mode occupation basis: $\hat{\mathcal{A}} = \frac{1}{L_A^{d-1}} \sum_i \hat{n}_i a(i)$, where $\hat{n}_i = f_i^\dagger f_i$ and $a(i)$ is a smooth function of the mode index i . In each RS, $\hat{n}_i = 0, 1$, while the probability that $\hat{n}_i = 1$ is given by the FD distribution. Further, the occupation numbers of different modes in the RS ensemble are uncorrelated. Thus, Eq. (10.4) follows from the central limit theorem. Observe that the fluctuations go to zero in the infinite volume limit for $d > 1$.

We now present numerical evidence supporting our claims. For simplicity, we study expectation values of local density operators $\hat{\mathcal{A}}_i = c_{i,0}^\dagger c_{i,0}$, though more complicated m -local operators could also be considered. Note that translation invariance is preserved along the y direction so operators are only labeled by i , their position along the x axis. The main plot in Fig. 10.1(a) shows $\langle \psi_A | \hat{\mathcal{A}}_i | \psi_A \rangle$ for 100,000 representative states $|\psi_A\rangle$ randomly picked with FD probabilities. We work in a system of length $L = 256$ and $L_A = 128$, and consider $\hat{\mathcal{A}}_i$ for all sites i along the x axis. The red line is the canonical average $\langle \hat{\mathcal{A}}_i \rangle_{T_E=1} = \text{Tr} \rho_A \hat{\mathcal{A}}_i$. We see that the EEVs in representative states $\langle \psi_A | \hat{\mathcal{A}}_i | \psi_A \rangle$ follow the canonical average $\langle \hat{\mathcal{A}}_i \rangle_{T_E=1}$ quite closely, with the error being maximum for operators near the boundaries of A . This is consis-

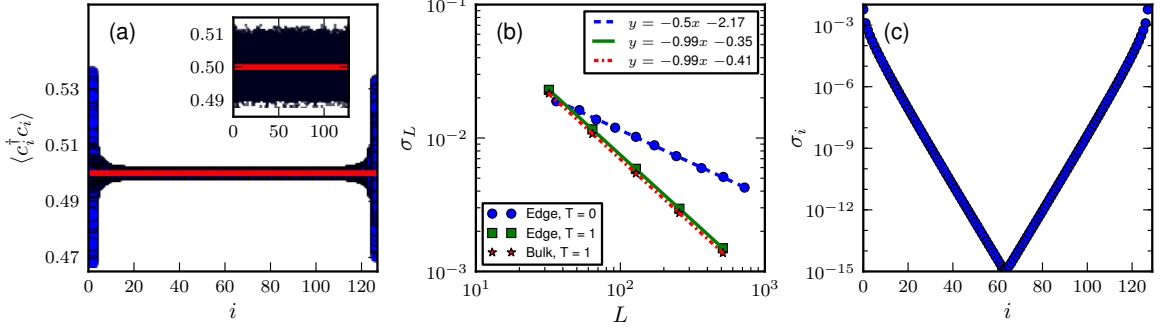


Figure 10.1: (Color online) (a) $\langle \psi_A | c_i^\dagger c_i | \psi_A \rangle$ plotted against the position i for 100,000 randomly picked representative states $|\psi_A\rangle$ in a dimerized free-fermion system of linear dimension $L = 256$, $L_A = 128$ and temperature $T = 0$. The thick, red (grey) line denotes the canonical average. The error is maximum for boundary operators. Inset: Same results for a system at temperature $T = 1$. In this case there is no discernible difference in the variance between boundary and bulk operators consistent with the volume law. (b) Standard deviation of $\langle \psi_A | c_i^\dagger c_i | \psi_A \rangle$ for i at the boundary at $T = 0$ (blue circles), i at the boundary at $T = 1$ (green squares) and i deep in the bulk at $T = 1$ (red stars) plotted against system size. The best-fit lines confirm the $\sqrt{\frac{1}{L^{d-1}}}$ scaling of the error for boundary operators at $T = 0$, and the $\sqrt{\frac{1}{L^d}}$ scaling for both boundary and bulk operators at finite T . (c) standard deviation of $\langle \psi_A | c_i^\dagger c_i | \psi_A \rangle$ as a function of position i , showing exponential decay with distance from the boundary.

tent with the picture that the $O(L^{d-1})$ eigenstates of H_E that contribute to canonical averages resemble the starting ground state in the bulk of A and only differ on the boundary. Fig. 10.1(b) (blue circles) shows the standard deviation of $\langle \psi_A | \hat{\mathcal{A}}_i | \psi_A \rangle$ for i at the boundary of A for various system sizes confirming the $\sqrt{\frac{1}{L^{d-1}}}$ scaling of the error posited in (10.4). Finally, Fig. 10.1(c) shows that for a fixed system size, the error decreases exponentially with distance from the boundary.

We note that even though we picked representative states by filling single-particle orbitals with Fermi-Dirac probabilities at $T_E = 1$, our results also apply to other reasonable prescriptions for picking RS. For example, we can equally consider all states in some fixed $O(1)$ window about $\langle H_E \rangle_{T_E=1}$ and with some fixed spread in particle number. This prescription will still give a $\sqrt{\frac{1}{L^{d-1}}}$ scaling of the error, but now with an improved coefficient.

10.2.2 $T > 0$

We repeat the analysis of the previous subsection, now starting with $|AB\rangle$ as an excited eigenstate of the hopping Hamiltonian H . We work at a finite physical temperature $T = 1$, and we can construct $|AB\rangle$ by filling single-particle orbitals with Fermi-Dirac probabilities at $T = 1$ and $\mu = 0$. However, for computational ease, we prefer to start with the Gibbs state on $A \cup B$ instead of individual eigenstates. It is easy to check that selecting RS for the Gibbs state and excited eigenstates are equivalent upto an error of $O(1/L^d)$.

The entanglement entropy for such finite temperature states shows a volume law scaling $S_E \sim sL_A^d$, and H_E acts as a genuine d - dimensional Hamiltonian with excitations living everywhere in the bulk of A . This changes the scaling of various estimates in the previous section from L^{d-1} to L^d , leading to an improved convergence. Since H_E is still a free-fermion Hamiltonian, we pick RS according to FD probabilities at $T_E = 1, \mu_E = 0$ as before.

The inset in Fig. 10.1(a) shows $\langle \psi_A | \hat{\mathcal{A}}_i | \psi_A \rangle$ for 10,000 randomly picked representative states $|\psi_A\rangle$ in a system of linear dimension $L = 256, L_A = 128$. In this case, the spread in eigenstate expectation values appears equal for operators at all positions. Boundary operators are not special, consistent with the volume law for the entanglement entropy of excited states. Fig. 10.1(b) (boxes and stars) shows the standard deviation of $\langle \psi | \hat{\mathcal{A}}_i | \psi_A \rangle$ for sites i lying deep in the bulk of A and on the boundary, confirming the $\sqrt{\frac{1}{L^d}}$ scaling of the error in both cases. Note the improvement in the convergence of the EEVs at the boundary compared to zero-temperature case.

In summary, we have found RS $|\psi_A\rangle$ in free fermion systems that typically reproduce the EEVs of spatially local observables computed with ρ_A in A . The typical error in replacing ρ_A with $|\psi_A\rangle$ scales as $O(\sqrt{1/L_A^{d_{\text{eff}}}})$, where d_{eff} is the effective dimensionality of H_E and equals $d - 1$ at $T = 0$ and d for $T > 0$. For $T > 0$, the convergence is independent of the distance from the boundary, while at $T = 0$, the

convergence is exponentially suppressed with the distance from the boundary. Thus, the boundary operators at $T = 0$ exhibit the slowest convergence with system size L_A . Three aspects deserve re-emphasis. First, not *all* states drawn from the FD distribution at $T_E = 1$ (or from an energy window about $T_E = 1$) are good RS. The scaling of error results are for *typical* states drawn from such ensembles. Second, the convergence depends on the choice of ensemble for the RS, and can be optimized. Third, for this free fermion example, RS can be found only for a restricted class of few-body operators that live in *position* space and are spread over all conserved quantities.

At this point, it is instructive to delineate two systematic trends in error estimates. The first is the scaling of error with system size as a function of temperature. We have seen that the effective dimensionality of H_E changes from $d_{\text{eff}} = d - 1$ at $T = 0$ to $d_{\text{eff}} = d$ for $T > 0$. Since the error scales with d_{eff} , the RS description for a given system is more accurate at higher temperatures. In the second case, we keep the temperature (and hence d_{eff}) fixed and compute the dependence of the error on some physical parameter Γ in the Hamiltonian. In particular, we can imagine tuning Γ in a way that evolves the ground-state of $H(\Gamma)$ from a product state to a more generic area-law entangled state. In this case, the error scales as $c(\Gamma)\sqrt{\frac{1}{L^{d_{\text{eff}}}}}$, where $c(\Gamma)$ is parameter dependent and depends on the coefficient s of the entanglement entropy scaling $S_E \sim sL^{d_{\text{eff}}}$. For product states, $|\psi\rangle = |A\rangle|B\rangle$, both s and $c(\Gamma)$ are zero, consistent with the fact that the best RS is simply $|A\rangle$ with no error.

Before moving on to more generic examples, let us briefly consider the implications of our free-fermion study for disordered, localized entanglement Hamiltonians that also fail to satisfy ETH. If H_E is non-interacting and Anderson localized [15], its eigenstates are localized in position space. Analogous to the free-fermion example, we now expect few-body operators in a suitably defined “momentum” space to have an RS description². Many-body localized H_E deserve further thought, but here again

²Translation invariance is broken by disorder. By “momentum” we just mean a set of variables obtained by an appropriate Fourier transform of the position coordinates

we might expect to find RS for observables that are spread over the local integrals of motion [148, 283] of H_E .

10.3 Generic eigenstates

The previous section provided a transparent illustration of representative states for the case where $|AB\rangle$ is a Slater determinant eigenstate of a free fermion Hamiltonian. Now we turn to eigenstates of more generic, local quantum Hamiltonians which will not be Slater determinants. For such states, we expect H_E to be non-integrable and we can bring the full machinery of quantum statistical mechanics and ETH to bear on our RS description. This has three important consequences:

1. Representative states can be used to reproduce expectation values of a much wider class of few-body operators. Unlike the free fermion case, we are no longer restricted to operators orthogonal to conserved quantities.
2. Fluctuations in EEVs for states that are close in energy are exponentially suppressed as $O(e^{-L_A^{d_{\text{eff}}}})$, where $d_{\text{eff}} = d$ (or $d - 1$) is the effective dimensionality of H_E for states obeying the volume (or area) law for the entanglement entropy [267, 34]. This is to be contrasted with the free fermion case where conserved quantities led to a much larger fluctuation of $O(\sqrt{1/L_A^{d_{\text{eff}}}})$ from eigenstate to eigenstate.
3. The total error in replacing ρ_A with $|\psi_A\rangle$ scales as $O(1/L_A^{d_{\text{eff}}})$ for reasons that will be explained below. Again, this is to be compared to a larger error that scales as $O(\sqrt{1/L_A^{d_{\text{eff}}}})$ for the free fermion case.

Points 2 and 3 above warrant further elucidation. If H_E satisfies the ETH, then EEVs of an operator $\hat{\mathcal{A}}$ are hypothesized to have the form [291, 292]:

$$\langle n | \hat{\mathcal{A}} | n \rangle = \mathcal{A}(E) + e^{-S(E)/2} f(E) R_n \quad (10.5)$$

where $|n\rangle$ are eigenstates of H_E with entanglement energy eigenvalue E and $S(E)$ is the entropy (computed using H_E) at E . Here, $\mathcal{A}(E), f(E)$ are smooth functions of E and R_n is a random sign. Since $S(E) \sim sL_A^{d_{\text{eff}}}$, Eq. (10.5) implies that the dominant contribution to the EEVs comes from $\mathcal{A}(E)$. Thus, the EEVs vary smoothly with energy between neighboring eigenstates and fluctuations between eigenstates ($\sim e^{-S/2}$) are exponentially suppressed, which is the content of point 2. Eq. (10.5) is the fundamental assumption of ETH, and the steady state properties under unitary evolution by H_E and the emergence of statistical mechanics as the correct equilibrium description follow from it.

Turning now to point 3, observe that

$$\begin{aligned} \langle \hat{\mathcal{A}} \rangle_{T_E=1} &= \frac{\text{Tr } \mathcal{A} e^{-H_E}}{\text{Tr } e^{-H_E}} \\ &= \frac{\int dE e^{S(E)-E} \mathcal{A}(E)}{\int dE e^{S(E)-E}} + O(e^{-S/2}) \end{aligned}$$

where the integral is over the entanglement energies. For $d > 1$ and $d_{\text{eff}} > 0$, $S(E)$ and E are extensive in L_A . Thus, the integrals can be evaluated by steepest descent and expanding about the saddle point gives

$$\langle \hat{\mathcal{A}} \rangle_{T_E=1} = \mathcal{A}(\langle E \rangle) + O\left(\frac{1}{L_A^{d_{\text{eff}}}}\right) \quad (10.6)$$

where $\langle E \rangle = \langle H_E \rangle_{T_E=1}$ is the mean entanglement energy.

Let us now put together the various ingredients. First, a reasonable, operator independent prescription for picking representative states involves drawing eigenstates of H_E with some probability in an energy window ΔE about $\langle E \rangle$. For example, $\Delta E \sim \sqrt{L_A^{d_{\text{eff}}}}$ if states are drawn with canonical probabilities, or we can equally well pick a fixed $O(1)$ energy window. If $\mathcal{A}(E)$ varies systematically with E , then

$$\mathcal{A}(E) \simeq \mathcal{A}(\langle E \rangle) + \frac{d\mathcal{A}}{dE} \left(\frac{\Delta E}{L_A^{d_{\text{eff}}}} \right) \quad (10.7)$$

for energies within ΔE of $\langle E \rangle$, and we have been careful to include the fact that we're interested in local operators that depend on the energy *density*. To optimize the error in the RS, let's specify an $O(1)$ energy window so the second term in Eq.(10.7) scales as $O(1/L_A^{d_{\text{eff}}})$. Then, from Eqs. (10.5), (10.6) and (10.7), we get that

$$\langle \hat{\mathcal{A}} \rangle_{T_E=1} = \langle n | \hat{\mathcal{A}} | n \rangle + O \left(\frac{1}{L_A^{d_{\text{eff}}}} \right) \quad (10.8)$$

when $|n\rangle$ are eigenstates of H_E lying within ΔE of $\langle E \rangle$. This is the statement of point 3 with $|n\rangle$ acting as the representative states $|\psi_A\rangle$.³

As in the free-fermion case, we would like to support our claims with numerical evidence for some example cases. Proceeding as before would require numerically obtaining eigenstates of generic, interacting Hamiltonians which is severely limited by system size. Instead, our strategy will be to obtain H_E for a particular example wavefunction and present evidence of its non-integrability by examining its level statistics. This provides strong, albeit indirect, evidence since our result, Eq. (10.8), follows more or less axiomatically from non-integrability and ETH.

³ One can improve matters for a single operator by carefully selecting an RS which reproduces its exact expectation value to higher accuracy but not for the full set we wish to reproduce.

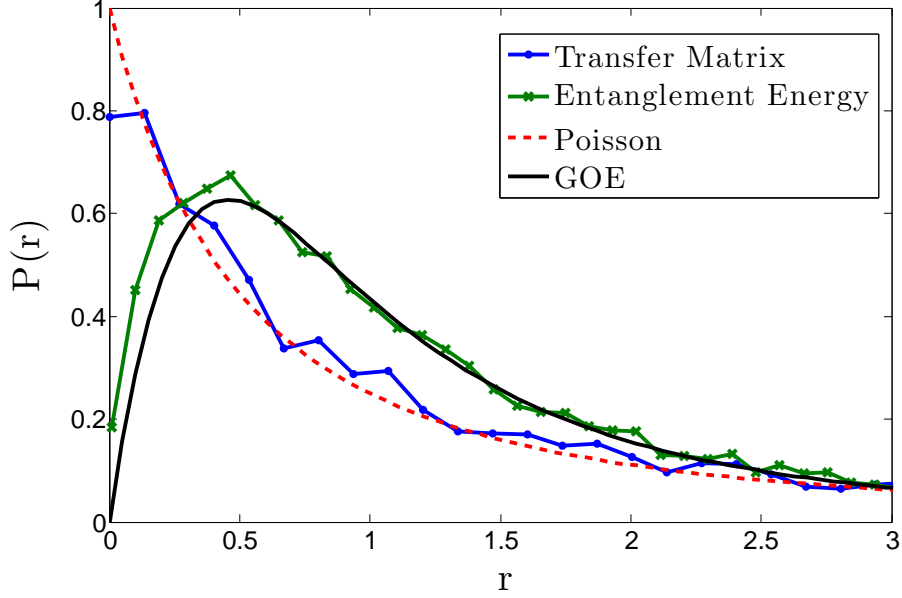


Figure 10.2: (Color online) Level spacing ratio statistics of H_E for the Rokhsar Kivelson state (green crosses) (10.9) compared to the Poisson (red dashed line) and GOE (black solid line) distributions. The statistics clearly look GOE consistent with a non-integrable H_E . This is to be contrasted with the Poissonian statistics of the integrable transfer matrix (blue dots) T_{σ_i, σ_j} in (10.11). r refers to the ratio of subsequent level spacings, and $P(r)$ is the probability of obtaining a given r . The GOE form is derived in Ref. [21].

To this end, consider the Rokhsar-Kivelson (RK) Ising wavefunction [270],

$$|AB\rangle = \sum_{\sigma} e^{-E_{cl}/2} |\vec{\sigma}\rangle, \quad (10.9)$$

where E_{cl} defines the classical anisotropic Ising model for spins $\sigma_{i,j}^z = \pm 1$ on sites (i, j) of a 2D square lattice

$$-E_{cl}(\vec{\sigma}) = \sum_{i,j} \beta_x (\sigma_{i,j}^z \sigma_{i,j+1}^z) + \beta_y (\sigma_{i,j}^z \sigma_{i+1,j}^z). \quad (10.10)$$

The probability of a given configuration is $e^{-E_{cl}(\vec{\sigma})}$. Thus, the quantum RK wavefunction reproduces classical probabilities in the z -basis. The RK wavefunction is the ground state of a *local* Ising-symmetric parent Hamiltonian $H_{RK}(\beta_x, \beta_y)$, which is

quantum critical on the same critical line as the classical 2D Ising model [137, 55, 18]: $\sinh(2\beta_x^c) \sinh(2\beta_y^c) = 1$. To compute H_E , we place the system on a cylinder of length L_x and circumference L_y and trace out half the cylinder with the cut parallel to the y axis. The system obeys a perfect area law and $S_E \sim sL_y$. For simplicity, we take the limit $L_x \rightarrow \infty$. We can rewrite $|AB\rangle$ in the more convenient form

$$\begin{aligned}
|AB\rangle &= \sum_{\sigma_L} \sum_{\sigma_R} \sqrt{\frac{T_{\sigma_L, \sigma_R} \langle \sigma_R | \lambda \rangle \langle \lambda | \sigma_L \rangle}{\lambda^2}} |\sigma_L\rangle |\sigma_R\rangle \\
&\equiv \sum_{\sigma_L} \sum_{\sigma_R} M_{\sigma_L, \sigma_R} |\sigma_L\rangle |\sigma_R\rangle
\end{aligned} \tag{10.11}$$

where σ_L (σ_R) labels the spins in the column immediately to the left (right) of the entanglement cut in A (B), and $|\sigma_L\rangle$ ($|\sigma_R\rangle$) is the RK Ising wavefunction in A (B) with the boundary spins fixed to be σ_L (σ_R). T_{σ_i, σ_j} is the (integrable) transfer matrix of the 2D Ising model. It is 2^{L_y} dimensional, “transfers” from column to column, and the indices $\sigma_{i/j}$ label the states of the L_y spins in columns i/j of the lattice. λ is the largest eigenvalue of T with corresponding eigenvector $|\lambda\rangle$. The entanglement Hamiltonian is related to the matrix M through $H_E = -\log(M^\dagger M)$ and the entanglement energies are obtained via a singular value decomposition of the matrix M .

Fig. 10.2 shows the statistics of the ratio of adjacent level spacings of the transfer matrix T_{σ_i, σ_j} , and the entanglement Hamiltonian for a paramagnetic system of size $L_y = 16$ and with $\beta_x = \beta_y = 0.43$ ⁴. Level spacings of integrable systems are known to show Poissonian statistics, while those of non-integrable systems show Gaussian Orthogonal Ensemble (GOE) statistics [39]. The figure clearly shows that H_E is non-integrable, even though it is so closely related to the integrable transfer matrix.

⁴ The entanglement Hamiltonian has translation, Ising and inversion symmetry. We break translation symmetry by using open boundary conditions, and take the even sector with respect to both Ising and inversion symmetries to access the largest matrix size for level spacing statistics. The statistics are the same for each symmetry sector and do not depend on the boundary condition.

In general, we expect generic states to give generic, non-integrable entanglement Hamiltonians which are susceptible to the analysis of this section.

10.4 Random states

Another limit in which we can apply the idea of representative states is when $|\psi_{AB}\rangle$ is a randomly picked pure state with respect to the Haar measure on the Hilbert space of $A \cup B$. In this sense, one can find RS for almost all states!

For simplicity, we consider the “random sign” states introduced in Ref. [128] below, although the same results also apply to states drawn from the Haar measure on the space of unit vectors in the entire Hilbert space as the reader can readily check.

Let $|c_{AB}\rangle$ represent a state in the computational basis on $A \cup B$. In this basis, we define the set of “random sign” states via

$$|AB\rangle = \frac{1}{\sqrt{\mathcal{N}_{AUB}}} \sum_{c_{AB}} \text{sgn}(c_{AB}) |c_{AB}\rangle \quad (10.12)$$

where the sgn function is a random variable that equals ± 1 with equal probability over the \mathcal{N}_{AUB} configurations in Hilbert space. We use \mathcal{N}_L to denote the Hilbert space dimension of region L . Hence for spin-1/2s, $\mathcal{N}_{AUB} = 2^N$, where N is the total number of sites in the system, $\mathcal{N}_{AUB} = \mathcal{N}_A \mathcal{N}_B$, and $|c_{AB}\rangle = |c_A\rangle |c_B\rangle$.

For observables $\hat{\mathcal{C}}$ in some finite bounded region $C \subset A$ it is a straightforward application of the central limit theorem to show that

$$\begin{aligned} \langle AB | \hat{\mathcal{C}} | AB \rangle &= \langle \hat{\mathcal{C}} \rangle_{T_E=1} \\ &= \text{Tr} \rho_A \hat{\mathcal{C}} = \text{Tr} \rho_C \hat{\mathcal{C}} \\ &= \text{Tr}_\infty \hat{\mathcal{C}} + O\left(\frac{\mathcal{N}_C}{\sqrt{\mathcal{N}_{AUB}}}\right) \end{aligned} \quad (10.13)$$

where ρ_C is the reduced density matrix of region C and $\text{Tr}_\infty \hat{\mathcal{C}} = \frac{1}{\mathcal{N}_{A \cup B}} \sum_{c_{AB}} \langle c_{AB} | \hat{\mathcal{C}} | c_{AB} \rangle$ is the infinite temperature canonical average of observable $\hat{\mathcal{C}}$. Observe how $\langle \hat{\mathcal{C}} \rangle$ is just $\text{Tr}_\infty \hat{\mathcal{C}}$ upto exponentially small corrections in the system size L_{AB} . Hence our randomly picked states behave like infinite temperature states on the full system. Our first guess might be to use the results of the previous section on generic eigenstates to find representative states for $|AB\rangle$. However, those results do not apply here since $\rho_A \sim \mathbb{I}$ (up to exponentially small corrections in L) for such random-sign states, and $H_E = 0$ is highly degenerate and non-generic.

Fortunately we can get around this problem by simply taking a representative state on region A , $|\psi_A\rangle$, which is itself a random sign state. The same considerations as above imply that in such a state

$$\langle \psi_A | \hat{\mathcal{C}} | \psi_A \rangle = \text{Tr}_\infty \hat{\mathcal{C}} + O\left(\frac{\mathcal{N}_C}{\sqrt{\mathcal{N}_A}}\right), \quad (10.14)$$

which says that $\langle \hat{\mathcal{C}} \rangle$ in representative states is again $\text{Tr}_\infty \hat{\mathcal{C}}$ upto exponentially small corrections in L_A . Thus, the RS captures the same physics as the canonical ensemble of H_E if the size of region C is much smaller than that of A . For a finite region C , the error in replacing the canonical ensemble with the RS is exponentially small in the size of A .

Note that unlike the previous two sections, we were able to pick RS for random sign states without taking into account the specific state $|AB\rangle$. This is because of the particularly simple form that all observables take in these states. However, lest the reader be worried that these states are just trivial, we note that subsystems of such randomly picked states are close to maximally entangled with their environment as evidenced by the work of Page [233].

10.5 Concluding Remarks

In this chapter we have demonstrated that for few-body observables, the reduced density matrix of a subsystem A entangled with a larger system can be replaced by a “representative” pure state on A alone for three different classes of states: low entanglement ground states of local quantum Hamiltonians, highly entangled randomly picked states, and highly excited eigenstates of local quantum Hamiltonians which interpolate between these two limits in the amount of bipartite entanglement they exhibit. The error in such a replacement is well controlled and quantified for these families of states, and vanishes as the volume of A approaches infinity. We have provided both numerical data and general arguments from quantum statistical mechanics and the ETH in support of this picture. Further, we expect that when H_E is non-generic with respect to the ETH, the RS description should continue to hold for a limited set of observables and we have demonstrated this explicitly for free fermions.

Future work could provide a more general account of classes of states $|AB\rangle$ that do, and do not, lend themselves to a description of this kind. Natural generalizations include applying these ideas to states $|AB\rangle$ with topological or symmetry-breaking order, and the reader can readily verify that the RS description naturally generalizes for local observables in these cases.

The ideas in this chapter present an interesting hierarchical onion-like picture. We can replace a pure state on $A \cup B$ with a pure state on A alone, which in turn can be replaced by a pure state on a subset $A_1 \subset A$, which itself can be replaced by a pure state on $A_2 \subset A_1$, and the process can be continued *ad infinitum* in the limit that the volume of each subsystem approaches infinity.

Finally, we observe that the RS description is not entirely an exercise in the abstract. Isolated quantum systems in pure states form the starting point in the description of many physical phenomena. Isolated systems are of course an idealization

since some degree of entanglement with the environment is inevitable, in which case the system is properly described by a density matrix. Our work suggests that the pure state description is still useful, with an error that vanishes as the system is made larger.

Part VI

Miscellaneous Results on Topological Phases

Chapter 11

Kibble-Zurek Scaling and String-Net Coarsening in Topologically Ordered Systems

11.1 Introduction

This chapter lies at the intersection of two interesting streams of contemporary research: the study of the non-equilibrium dynamics of quantum systems, and the study of topologically ordered phases of matter. Consider driving a topologically ordered system through a phase transition to a topologically trivial, or relatively trivial, phase by changing some parameter in the Hamiltonian at a slow, but finite rate. This work investigates the ensuing non-equilibrium dynamics resulting from this “trans-critical protocol” [62], with particular emphasis on universality and the non-Landau character of the transition.

The Kibble-Zurek (KZ) mechanism [174, 340, 341] is a scaling theory of the defects generated by slowly cooling a classical system through a continuous symmetry-breaking phase transition. Kibble originally formulated this problem as a cosmo-

logical theory of the phase transitions in an expanding universe, and Zurek later applied it to condensed matter systems. The central physical insight is that sufficiently distant parts of the system settle into independently seeded local broken symmetry “directions” whence the mismatch must be accommodated by a finite density of defects. The mechanism has since been generalized to quantum phase transitions [245, 95, 342, 79]. Although several experiments are consistent with the predictions of Kibble-Zurek [93, 212, 219], decisive confirmation of the scaling law of defect densities is still lacking. A recent experiment in an inhomogenous system of trapped ions [258] provides the most compelling evidence in this regard¹. Polkovnikov and co-workers have also studied the scaling theory of the excess heat density and the interplay between the ramp velocity and finite size [245, 83]. For a recent review of the broader context of these developments in the study of non-equilibrium quantum phenomena, see Ref. [247] .

A few observables [83, 88, 36, 80] other than the universal non-equilibrium defect density have been studied in the KZ problem, now defined more broadly as the non-equilibrium temporal evolution of a system in the vicinity of a critical point. Recently, Chandran et. al. [62] have systematized the universal content in the KZ problem in a scaling limit, and written non-equilibrium scaling functions for *all* physical observables in this limit. The scaling functions describe the entire time history, and asymptote to equilibrium and coarsening scaling regimes in the appropriate limits. The universal content depends only on the pairing of the dynamical universality class of the critical point, and the particular protocol through parameter space.

The KZ scaling theory also provides an elegant framework within which to investigate ramp dynamics of phase transitions beyond those of traditional symmetry breaking. These transitions could involve the destruction of the topological order of states of matter like spin liquids and the fractional quantum Hall phases. Topo-

¹Confirmation is still lacking in transitions in thermodynamic systems that are not described within mean field theory.

logically ordered phases are *not* locally distinguished by any order parameter, but are characterized by emergent gauge fields and fractionalized excitations. Their non-local structure makes them particularly robust to local perturbations and well-suited to perform “topological” quantum computation [226]. Despite their robustness, a strong enough perturbation can drive a transition from a topologically ordered phase to a trivial or relatively trivial (i.e. one with a smaller gauge group) phase. For appropriately selected perturbations, this transition will be continuous.

This chapter addresses the KZ problem when a system is driven from a topologically ordered phase to a proximate trivial or relatively trivial phase. We do so for a class of topological phases that possess lattice realizations where the gauge degrees of freedom are manifest: these are the toric code/lattice \mathbb{Z}_2 gauge theory [187, 178] and the string-net models of Levin and Wen [204] that realize doubled non-Abelian Chern-Simons theories. By a combination of duality and perturbative arguments, we show that KZ scaling in the generalized sense of Ref. [62] holds for various observables even though the canonical KZ signature of a density of topological defects is not meaningful. We further provide strong arguments that the late time dynamics in the scaling regime exhibits a slow coarsening of the string-net that is condensed in the starting topologically ordered state. To our knowledge, this is the first treatment of a quantum coarsening regime in the dynamics of an isolated quantum system. As the extended string-nets are central to the topological character of the starting phase², their slow decay outside the phase is a (potential) signature of the physics of the parent phase. In the same spirit, we find that the exponentially small energy splitting of topologically degenerate ground states on closed manifolds can be amplified in the KZ process to a splitting linear in the system dimension. The restriction to the scaling limit always brings simplification as particular gapped degrees of freedom

²Sensitivity to the topology of the lattice manifold requires extended degrees of freedom like strings. The strings form nets as the phase is a liquid.

are, at worst, dangerously irrelevant. That is, they do not affect the scaling regime but do alter the asymptotically long time behavior of the KZ process.

The most relevant precursor to our work is found in the cosmology literature in the papers of Rajantie and Hindmarsh [142, 263]. They studied the non-equilibrium dynamics of ramps through the finite temperature phase transition in the non-compact Abelian Higgs model; their protocol moves between the gapless Coulomb phase with gapped matter to the fully gapped Higgs phase. However, there are three important differences. First, their work involves finite temperature in an essential way. The zero temperature limit of their protocol would involve exciting the system in the gapless phase even before the transition is reached. Second, the non-compactness of their gauge field makes the physics of their Higgs phase qualitatively different from that of the compact gauge models considered by us. This difference is quite visible in our choice of observables. Third, we work on the lattice in the “electric flux” representation, a natural choice in the condensed matter setting, while they work in the continuum with the vector potential. Thus our discussion of string-net coarsening has no analog in their formulation. In the condensed matter literature, ramps across topological transitions [85] in (1+1)D and sudden quenches in one of our model systems, the perturbed toric code, have been studied before [261, 302]. The sudden quenches are in a completely different limit from the slow ramps we study here as they inject a large amount of energy into the system. Finally, low temperature spin ice exhibits topological order in a classical limit [56] and its dynamics following quenches is dominated by monopoles of the gauge field. However in this case, non-universal lattice effects turn out to dominate the long time behavior [57].

We turn now to the contents of the chapter. We begin in Sec. 11.2 by reviewing the phase diagram of the \mathbb{Z}_2 gauge theory coupled to matter and describing the transitions out of its topologically ordered phase. Readers literate in the canon of topological phases can skim this section for our notation. Section 11.3 describes the KZ ramp

across the pure matter sector of the \mathbb{Z}_2 theory which has a conventional symmetry-breaking transition. This section contains a new analysis of coarsening in the (2+1)D transverse field Ising model and summarizes our previous understanding of KZ. In 11.4, we discuss our results on the KZ scaling functions and string-net coarsening for ramps in the pure gauge sector of the theory, which has a confinement transition without a local order parameter. We then generalize the scaling theory to a ramp across an arbitrary point on the critical line in the phase diagram in 11.5. In Sec. 11.6, we turn to generalizations of these results to phases with non-Abelian topological order; specifically, we discuss a particular transition from the $SU(2)_k$ ordered phases. We end with a discussion of generalizations to other theories.

11.2 Review of the phase diagram of the \mathbb{Z}_2 Gauge Theory

The phase diagram of the $(d + 1)$ dimensional \mathbb{Z}_2 gauge theory with matter [112] contains a topologically non-trivial (deconfined) phase and a topologically trivial (confined-Higgs) phase. The topological order in the deconfined phase is described by the BF theory [132]. We work in $d = 2$ for which the \mathbb{Z}_2 theory is precisely (the topologically ordered) Kitaev's toric code with perturbations [178]. We start by reviewing the key features and the excitation spectrum of the toric code. We then discuss two perturbations that drive a continuous transition to a topologically trivial phase.

11.2.1 The perturbed toric code

The toric code [178, 176] is defined in terms of spin-1/2 degrees of freedom that live on the links l of a 2D square lattice:

$$\begin{aligned} H_{TC} &= -K \sum_P B_P - \Gamma_M \sum_s A_s \\ &\equiv -K \sum_P \prod_{l \in \partial P} \sigma_l^z - \Gamma_M \sum_s \prod_{l: s \in \partial l} \sigma_l^x \end{aligned} \quad (11.1)$$

where the A_s and B_P are “star” and “plaquette” operators. s and P denote the sites and elementary plaquettes of the lattice, while ∂P and ∂l are the boundaries of plaquettes and links. H_{TC} can be rewritten as a gauge theory with matter by identifying the σ_l variables as the gauge degrees of freedom, and introducing new spin 1/2 ‘matter’ variables, τ_s , on the sites of the lattice. Upon restricting the expanded Hilbert space to the ‘physical’ subspace of gauge-invariant states

$$G_s |\psi\rangle = |\psi\rangle, \quad G_s = \tau_s^x \prod_{l: s \in \partial l} \sigma_l^x, \quad (11.2)$$

the toric code Hamiltonian (11.1) is equivalent to the gauge-invariant Hamiltonian:

$$H_0 = -K \sum_P \prod_{l \in \partial P} \sigma_l^z - \Gamma_M \sum_s \tau_s^x. \quad (11.3)$$

Note that G_s defines a set of local symmetries at each site since $[H_0, G_s] = 0 \forall s$.

In the x basis of the spin operators, it is useful to think of τ and σ as the electric ‘charges’ and ‘fluxes’ in the theory respectively: $\tau_s^x = -1$ (+1) if an electric charge is present (absent) at site s , while $\sigma_l^x = -1$ denotes the presence of electric flux on link l . In this language, we recognize the gauge-invariant condition (11.2) as the lattice \mathbb{Z}_2 version of Gauss’s law. In the conjugate z basis, the operator $B_P \equiv \prod_{l \in \partial P} \sigma_l^z$ measures the magnetic flux through the plaquette P .

The model is exactly solvable as both terms in H_0 commute with each other and the gauge constraint G_s . The ground state is charge-free and vortex-free: a simultaneous $+1$ eigenstate of τ_s^x and B_P for all s, P . As the ground state is free of charge, it is a loop gas of electric flux. That is, it is an equal amplitude superposition of configurations where links with $\sigma_l^x = -1$ form closed loops. The degeneracy of the ground state manifold depends on the topology of the lattice; on the torus, it is four-fold degenerate. The four ground states cannot be distinguished locally. They are labelled by the eigenvalues ± 1 of the non-local Wilson loop operators $W^{nc} \equiv \prod_{l \in C_{nc}} \sigma_l^z$ along the two distinct non-contractible loops C_{nc} on the direct lattice.

The elementary excitations of the model are gapped and are of two types: e and m . e denotes the presence of electric charge on site s , while m is a magnetic vortex on plaquette P characterized by $B_P = -1$. e and m are individually bosonic, but have mutual semionic statistics. The non-local string operators

$$W^e(s, s') = \prod_{\substack{l \in C: \\ s, s' \in \partial C}} \tau_s^z \sigma_l^z \tau_{s'}^z, \quad W^m(\bar{s}, \bar{s}') = \prod_{\substack{l \in \bar{C}: \\ \bar{s}, \bar{s}' \in \partial \bar{C}}} \sigma_l^x \quad (11.4)$$

defined respectively on the curves C and \bar{C} on the direct and the dual lattice, create a pair of electric charges and vortices at their ends as shown in Fig. 11.1.

H_0 is robust to small local perturbations and extends to a topological phase. Nevertheless, a strong enough perturbation will eventually drive a transition into a trivial phase. The toric code Hamiltonian perturbed by transverse fields is $H = H_{TC} - \sum_l \Gamma \sigma_l^x + J \sum_l \sigma_l^z$; both perturbations drive continuous transitions to trivial (spin-polarized) phases when made large. In the gauge-invariant formulation of the \mathbb{Z}_2 gauge theory with matter, the perturbed Hamiltonian takes the form

$$-H = K \sum_P B_P + \Gamma_M \sum_s \tau_s^x + J \sum_l \sigma_l^z \prod_{s \in \partial l} \tau_s^z + \Gamma \sum_l \sigma_l^x. \quad (11.5)$$

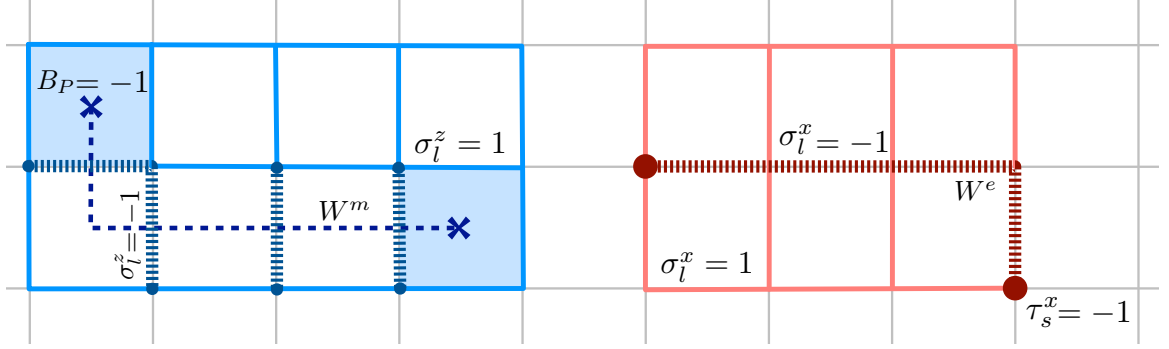


Figure 11.1: A section of the toric-code lattice with operators in the magnetic (left) and electric (right) bases. Matter (τ) and gauge (σ) variables are located on the sites and links respectively. The W^m operator (11.4) flips a string of σ^z variables and creates a pair of magnetic vortices at its endpoints, while the W^e operator flips spins in the x basis to create a pair of electric charges linked by electric flux.

The phase diagram of this theory was explained in detail in the seminal paper by Fradkin and Shenker [112] and has more recently been confirmed in several numerical studies [94, 303, 313, 301, 329]. We will now briefly review this model in different parameter regimes.

11.2.2 Pure matter theory ($\Gamma = 0$)

For $\Gamma = 0$, the gauge degrees of freedom are static and frozen into a vortex-free configuration in the ground state sector. It is therefore convenient to diagonalize H in the gauge-variant subspace where $\sigma_l^z = 1$ for all l and project the eigenstates to the gauge-invariant subspace afterwards. The Hamiltonian then maps to the (2+1)D transverse field Ising model (TFIM) for the matter spins:

$$H_{TFIM} = -J \sum_{\langle ss' \rangle} \tau_s^z \tau_{s'}^z - \Gamma_M \sum_s \tau_s^x. \quad (11.6)$$

On tuning J , the TFIM undergoes a conventional ‘Higgs’ phase transition from a paramagnetic phase to a symmetry-broken ferromagnetic phase. In a complementary view, the static electric excitations e defined at the toric code point ($\Gamma = J = 0$)

acquire dynamics when $J \neq 0$ and eventually condense at a critical value of J . The transition is in the 3D Ising universality class and is detected by the local order parameter, $\langle \tau^z \rangle$ in the gauge-variant subspace. In the gauge-invariant subspace, τ_z maps on to a non-local string operator.

After projection, the state with $\{\sigma_l^z = 1\}$ is the vortex-free configuration in the topological sector defined by the Wilson loop $W^{nc} = 1$ for both non-contractible loops on the torus. This choice maps to a TFIM with periodic boundary conditions in both directions of the torus; the remaining three topologically inequivalent vortex-free configurations generate TFIMs with different boundary conditions (periodic-antiperiodic etc.). The four-fold degeneracy of the topological phase vanishes in the Higgs/ferromagnetic phase.

11.2.3 Pure Gauge Theory ($J = 0$)

In this case, matter is static. The ground state is in the charge-free sector ($\tau_s^x = 1$), and the Hamiltonian for the gauge variables in this sector is:

$$H_{\mathbb{Z}_2} = -K \sum_P B_P - \Gamma \sum_l \sigma_l^x. \quad (11.7)$$

When Γ/K is small, the gauge variables are weakly fluctuating and the elementary excitations are well-described as vortex pairs. At some critical Γ/K , the vortices condense and the gauge variables strongly fluctuate past this point. This transition cannot be diagnosed by a local order parameter. Instead, the vortex condensate phase is marked by the vortex pair creation operator, $\langle W^m \rangle \neq 0$ for vortices separated by long distances. In the conjugate electric field basis, flux loops become costly as Γ is increased; hence the transition is from a topological loop gas phase at the toric code point to a phase in which flux loops become confined.

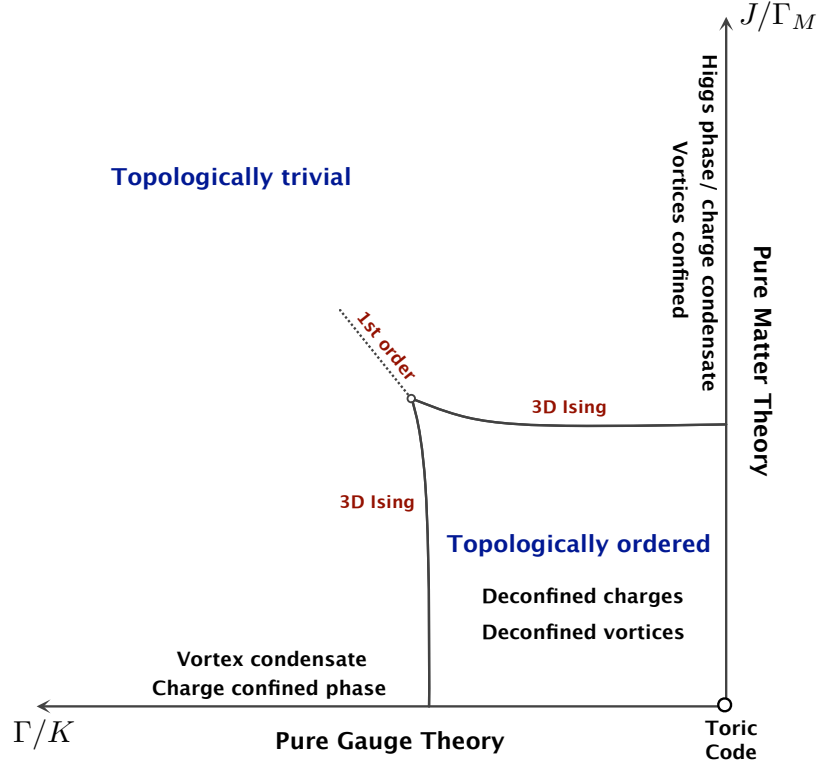


Figure 11.2: $T = 0$ phase diagram of the \mathbb{Z}_2 theory in $d = 2$ dimensions. The matter and gauge axes are dual, and the Higgs and charge confined phases are smoothly connected.

In a different language, the transition is understood as a deconfinement-confinement transition for the static electric charge [112] and is diagnosed by the free energy cost of creating a pair of (infinitely separated) charges. The cost is finite in the deconfined phase, but infinite in the confined phase, and is equivalent to the change in behavior of the expectation of the contractible Wilson loop:

$$W(L) \equiv \left\langle \prod_{l \in C} \sigma_l^z \right\rangle \quad (11.8)$$

from a perimeter law ($W(L) \sim \exp(-L)$) to an area-law ($W(L) \sim \exp(-L^2)$). C is a contractible loop and L is its perimeter.

In $d = 2$, the \mathbb{Z}_2 Ising gauge theory is self dual [323, 187]. Thus the pure gauge theory also maps to a (2+1)D TFIM and the confinement-deconfinement transition

belongs to the 3D Ising universality class. The details of this duality are explained in Ref. [187], and have been summarized in Fig. 11.3. We emphasize that despite the duality, the transition is *not* described by a local order parameter, as will be even clearer in Sec. 11.6.

11.2.4 The full phase diagram

The full $T = 0$ phase diagram of the Ising gauge theory in (2+1)D is shown in Fig. 11.2. Fradkin and Shenker [112] have shown that the confinement/Higgs transitions are stable on moving away from the pure gauge/matter axes. Further, the Higgs and confined phases are smoothly connected. However the diagnostics previously discussed, like the Wilson loop, no longer differentiate between the two phases. In a recent paper [126], Gregor et. al. have shown that an appropriately defined line tension, related to the Fredenhagen Marcu [113, 114] order parameter studied by lattice gauge theorists, can be used to diagnose the transition everywhere in the phase diagram. We will use this quantity in combination with the topological ground state degeneracy to study ramps across generic points on the critical line in the phase diagram.

11.3 Kibble Zurek I - Ramp across the Higgs transition

We begin by reviewing the Kibble-Zurek (KZ) formalism for linear ramps (a Trans-Critical-Protocol in the parlance of Ref. [62]) across the conventional 3D Ising transition along the pure matter line at $\Gamma = 0$ in Sec. 11.3.1. The late time evolution of the system is naturally described as “coarsening”: a dynamical process previously discussed only in classical systems. We take the first steps to apply these ideas to an isolated quantum system in Sec. 11.3.2.

11.3.1 Scaling theory: Review

The system is in equilibrium in the paramagnetic phase at $t = -\infty$ and is driven to the ferromagnetic phase by changing the transverse field $\Gamma_M(t)$ linearly: $\delta(t) \equiv (\Gamma_M(t) - \Gamma_{Mc})/\Gamma_{Mc} = -t/\tau$. The critical point (CP) is at $\delta = 0$ and τ is the ramp time. The response of the system to slow ramps is characterized by three chronological regimes: adiabatic evolution at early times, ‘critical’ or diabatic evolution near the CP, and a late-time regime that we argue to be domain-growth.

At early times, the system is far from the CP and evolves adiabatically. Critical slowing down implies that the instantaneous correlation time diverges as $\xi_t \sim |\Gamma_M - \Gamma_{Mc}|^{-\nu z}$ near the CP and adiabaticity must break down before the CP is reached. ν and z are respectively the correlation length and dynamic exponent with $\nu = 0.627$ and $z = 1$ in this case [107]. The system falls out of equilibrium at the KZ time, $t = -t_K$, when the time remaining to reach the critical point, t_K , becomes equal to ξ_t :

$$\xi_t(-t_K; \tau) = t_K \quad \Rightarrow \quad t_K = \tau^{\frac{\nu z}{\nu z + 1}}. \quad (11.9)$$

At $t = -t_K$ the evolution of the system become diabatic and, to zeroth order, the system remains frozen until it emerges on the other side of the CP at $t = t_K$. The KZ time, t_K , defines a KZ length, $l_K = t_K^{1/z}$ which is the correlation length at the time the system falls out of equilibrium. Finally, for $t \gg t_K$, we get coarsening.

Recently, Chandran et. al. [62] formulated a scaling limit in which the physics described above becomes universal for a given pairing of a critical point and a ramp protocol. This limit is defined as $\tau \rightarrow \infty$ with time and length scales measured in units of the diverging scales t_K and l_K . As $\delta(t_K) \rightarrow 0$ in this limit, the out-of-equilibrium response of the system is completely controlled by the critical point. The content of the scaling theory is not just the critical exponents, previously discussed by Kibble

and Zurek, but also scaling functions for various physical observables. For example, the equal-time two-point correlation function of the order parameter defined as:

$$\langle \tau_s^z(t) \tau_{s'}^z(t) \rangle_\tau \equiv G_{\tau\tau}(|\mathbf{s} - \mathbf{s}'|, t; \tau), \quad (11.10)$$

has the KZ scaling form

$$\lim_{\tau \rightarrow^* \infty} l_K^{2\Delta} G_{\tau\tau}(x, t) = \mathcal{G}_{\tau\tau} \left(\frac{x}{l_K}, \frac{t}{t_K} \right) \quad (11.11)$$

where $\tau \rightarrow^* \infty$ is defined as the limit $\tau \rightarrow \infty$ with $\frac{x}{l_K}$ and $\frac{t}{t_K}$ held fixed, x is the distance between sites s and s' , and Δ is the scaling dimension of the operator τ^z . Δ is equivalent to β/ν , and is numerically found to be 0.518 in the (2+1)D TFIM [107].

The scaling function should asymptote to the correct equilibrium form in the limit $t/t_K \rightarrow -\infty$ with $x/\xi(t; \tau)$ fixed

$$\mathcal{G}_{\tau\tau}(\hat{x}, \hat{t}) \sim \hat{t}^{2\nu\Delta} \mathcal{G}_{\tau\tau}^{eq}(\hat{x}\hat{t}^\nu) \quad (11.12)$$

where \hat{x} and \hat{t} are defined as x/l_K and t/t_K respectively, \mathcal{G}^{eq} is the equilibrium scaling function, known to decay exponentially in the Ising model, and $\hat{x}\hat{t}^\nu = x/\xi(t)$. *For the rest of this article, the hat superscript will be reserved for the variables scaled by l_K or t_K , depending on their units.*

A full description of the diabatic regime, previously termed ‘critical coarsening’ [36], is much harder. The difficulty surpasses static computations in the analogous quantum critical regime as it involves real time.

As the scaling content at late times has not appeared in the literature before, we devote the next subsection to it. We can also investigate the scaling functions for thermodynamic quantities like the excess energy density above the ground state [83],

q , and the entropy density [62, 246] s :

$$q(t; \tau) \sim l_K^{-d} t_K^{-1} \mathcal{Q}(\hat{t}) \quad (11.13)$$

$$s(t; \tau) \sim l_K^{-d} \mathcal{S}(\hat{t}) \quad (11.14)$$

Both quantities tend to zero as $t/t_K \rightarrow -\infty$ when the evolution is adiabatic and become non-zero when the system falls out equilibrium. The evolution at late times is therefore best understood through the finite excess energy density ($q > 0$) or finite temperature phase diagram.

11.3.2 Coarsening

We now address the late time dynamics of the KZ ramp. It is generally believed that a *classical* system quenched to an ordered phase with multiple vacua undergoes coarsening, whereby each local broken-symmetry region grows in time and the system is asymptotically statistically self-similar on a characteristic length scale, $l_{\text{co}}(t)$. Put another way, the two-point function heals to its equilibrium value on the scale ξ within each domain, and is exponentially suppressed between domains, each of growing length $l_{\text{co}} \gg \xi$. In the late time regime, dynamical scaling is expected to hold when there are no growing scales competing with l_{co} . For more details, see Ref. [43].

We now generalize this idea to the KZ ramp in the *quantum* TFIM. For simplicity, let us stop the ramp in the ordered phase at some $t/t_K = \hat{t}^s \gg 1$, while continuing to measure time and length on the scales set by t_K, l_K . The superscript s denotes stopping. The system initially appears disordered. At infinitely long times however, we expect that the system is thermal and ordered, as the (2+1)D TFIM is not known to be integrable. Further, we expect the approach to equilibrium to be through domain growth or coarsening, driven by the lack of long range order at late times. The system then locally breaks the symmetry but is globally disordered, with long

domain walls past the growing length scale, $l_{co}^s(t) \gg l_K$. Assuming local equilibration, the physics of coarsening can be captured in a hydrodynamic theory with two slow modes: the non-conserved, scalar order parameter and the conserved energy density³. We shall call this Model C in a slight abuse of language (properly it refers to the theory with thermal noise included [143]). As $\hat{t} \rightarrow \infty$, we therefore predict that the system obeys the dynamic scaling hypothesis, that is, it looks self-similar on the scale of a growing length $l_{co}^s(t; \tau)$ and that $\mathcal{G}_{\tau\tau}^s$ has the late time form:

$$\mathcal{G}_{\tau\tau}^s(\hat{x}, \hat{t}) \sim (\hat{t}^s)^{2\nu\Delta} \mathcal{G}_{\tau\tau}^{co}(\hat{x}l_K/l_{co}^s), \quad (11.15)$$

where $l_{co}^s(t; \tau) = l_K \left(\frac{t}{t_K}\right)^{1/z_d}$ and $z_d = 2$.

The value of the dynamic exponent, z_d , quoted above is only known numerically [186, 185]. $\mathcal{G}_{\tau\tau}^{co}$ is a scaling function that can also be computed within Model C [186, 185, 339, 215].

The above discussion hinges on two key assumptions. First, the infinite time state of the system should have long-range order, that is, the late time evolution should be in the ordered phase. More precisely, we require the excess energy density (11.13) at the stopping time $q(\hat{t}^s; \tau)$ to be smaller than critical energy density $q_c(\hat{t}^s; \tau)$, below which the system will be ordered in equilibrium. The dominant contribution to q (at \hat{t}^s) is from the defect density on the scale l_K frozen in at $t \approx t_K$. Assuming that these defects evolve adiabatically for $t > t_K$, we may conservatively estimate q to scale as the single-particle gap $1/\xi(\hat{t}^s; \tau)^z$. As promised, this density is much smaller than the instantaneous critical density, $q_c \sim 1/\xi^{d+z}$:

$$\frac{q}{q_c} \sim \xi^d \sim \left(\frac{1}{\hat{t}^s}\right)^{\nu d} \ll 1. \quad (11.16)$$

³The momentum density appears as an additional conserved quantity in this field theory. It is our current belief that this does not change the relevant power in the coarsening regime, but we are investigating this.

For all $\hat{t} > \hat{t}^s$, the energy of the system is conserved and q and q_c do not change in time. Thus, the system evolves in the ordered phase at late times.

The second assumption is that of local equilibration over hydrodynamical time-scales. In Model C, the latter is the time-scale for domain growth by l_K . It can be inferred from Eq. (11.15) to be $\delta t_{co} \sim t_K \hat{t}^{1-1/z_d}$. On the other hand, the time-scale for local equilibration processes on the scale l_K is set by t_K . The validity of Model C as the late-time dynamical description relies on the equilibration time being much smaller than δt_{co} . As the inequality $t_K \ll \delta t_{co}$ is parametrically controlled by \hat{t} , the coarsening behavior in Model C is a better and better approximation to the quantum dynamics as $\hat{t} \rightarrow \infty$.

Finally, in the original KZ problem (where we don't stop the ramp), the late time evolution is also in the finite-temperature ordered phase as the relation $q/q_c \ll 1$ holds for every $t/t_K \gg 1$. However, the continuously changing parameter in the Hamiltonian affects the local equilibration argument in two important ways. First, the characteristic size of the domains grows at a slower rate:

$$l_{co}(t; \tau) = l_K \left(\frac{t}{t_K} \right)^\theta \quad \text{where } \theta = \nu \left(\frac{z}{z_d} - 1 \right) + \frac{1}{z_d}. \quad (11.17)$$

In the (2+1)D TFIM, $\theta = (1 - \nu)/2$ and is smaller than $1/z_d$. This slowing down can only help in the argument given above. The second effect is that the single particle gap Δ grows as $1/t_K (t/t_K)^{\nu z}$ at late times. This, however, increases various scattering times (and consequently various equilibration times) in the problem and the applicability of hydrodynamics here becomes a delicate affair. In Appendix 11.A, we argue that the process that drives coarsening and increases entropy involves the interaction of the long domain walls with the bulk quasiparticles within each domain. As the bulk quasi-particles scatter off the walls parametrically many times before the system parameters are changed, coarsening can at least self-consistently be justified.

We therefore conjecture that the two point function as $\hat{t} \rightarrow \infty$ holding $x/l_{co}(t)$ fixed obeys dynamic scaling:

$$\mathcal{G}_{\tau\tau}(\hat{x}, \hat{t}) \sim \hat{t}^{2\nu\Delta} \mathcal{G}_{\tau\tau}^{co}(\hat{x}l_K/l_{co}). \quad (11.18)$$

In this process, the entropy density increases weakly in time. The late time asymptotes reflect this:

$$\begin{aligned} \mathcal{Q}(\hat{t}) &\sim q_0 \hat{t}^{\nu z} + q_1 \hat{t}^{\nu z - \theta} \\ \mathcal{S}(\hat{t}) &\sim s_0 - s_1 \hat{t}^{-\theta}. \end{aligned} \quad (11.19)$$

The leading terms in \mathcal{S} would be present even if the evolution were adiabatic. The sub-leading term is the thermodynamic signature of coarsening. From this point, every time we invoke results from coarsening, the reader should keep in mind the subtleties presented in this section.

11.4 Kibble Zurek II - Ramp across the confinement transition

We now ramp across the pure gauge theory Eq. (11.7) by tuning Γ . In this case, the transition is from a topologically ordered deconfined phase to a confined one, and there is no description in terms of a local order parameter. Nevertheless, we will now show that the KZ mechanism for Landau transitions discussed in the previous section can be generalized to these transitions. Additionally, the loops and strings characterizing the topological phase (string-nets) will coarsen.

Our main tool is the duality in $(2+1)$ D between the pure gauge theory and the TFIM summarized in Fig. 11.3. Importantly for us, the presence of electric flux on a

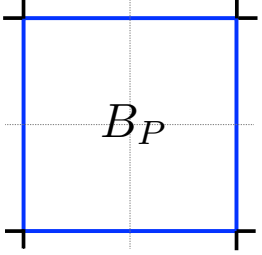
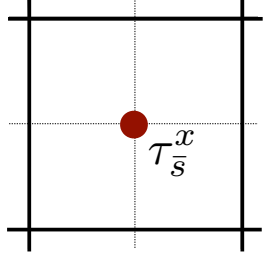
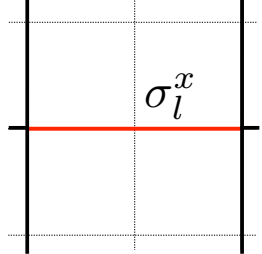
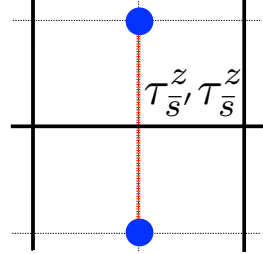
| | | |
|---|-----------------------|--|
| Pure \mathbb{Z}_2 gauge theory | \longleftrightarrow | Transverse field Ising Model |
|  | \longleftrightarrow |  |
| Magnetic Flux | | Transverse field |
|  | \longleftrightarrow |  |
| Electric Flux | | Domain wall |
| Confined/ Deconfined phase | \longleftrightarrow | Ferromagnetic/ Paramagnetic phase |

Figure 11.3: Table summarizing the duality between the pure \mathbb{Z}_2 gauge theory (11.7) and the TFIM in $d = 2$. Dark and light lines denote the direct and dual lattice respectively.

link (of the direct lattice) maps to a domain wall between the TFIM spins (on the dual lattice), while the vortex operator B_P maps to the dual transverse field. The duality also ensures that a finite temperature confined phase exists, and that coarsening is described by the hydrodynamics of Model C.

For specificity, we begin the ramp at the deconfined toric code point in one of the ground state sectors. The ground state is a loop gas of the electric flux lines in the σ^x basis. By duality, these are the domain walls of the paramagnetic phase of the TFIM. The system falls out of equilibrium in the deconfined phase before it is taken

through the transition, with a network of loops of minimum size l_K . In the confined phase, flux loops map to the costly domain walls of the dual ferromagnetic phase. Post the diabatic regime in the confined phase, this network of loops (string-nets) is diluted (average size increases as l_{co}) as the system coarsens. More generally, we can imagine string-nets being diluted in a generic topological theory and we will show some examples of this in Section 11.6.

As before, energy conservation requires the decreasing electric flux density to be compensated for by an increasing bulk energy density. Essentially, the system arrives in the confined phase (which is a vortex condensate) with a greater electric field density and a smaller magnetic vortex density as compared to the instantaneous ground state. The subsequent evolution through coarsening increases the typical size of the electric flux loops to $l_{co}(t)$, thereby decreasing the electric field density and increasing the bulk energy density of the vortex condensate.

Next, the two-point correlator that detects long-range order in the dual TFIM, $\langle \tau_{\bar{s}}^z \tau_{\bar{s}'}^z \rangle$, maps to the vortex pair creation operator (11.4), $\langle W^m(\bar{s}, \bar{s}') \rangle$ that detects vortex condensation. As the condensed phase is also a confining phase for charge, a non-zero value of $\langle W^m \rangle$ for long strings detects charge confinement. The scaling form for $\langle W^m \rangle$ is given by Eq. (11.11), and its asymptotic behavior is identical to that of the two-point function discussed in the pure-matter theory. In particular, in the coarsening regime, the dual TFIM is ordered on length scales less than $l_{co}(t)$. Correspondingly, $\langle W^m \rangle$ is also non-zero on scales shorter than $l_{co}(t)$ but decays exponentially on longer length scales. Thus, the non-local string operator $\langle W^m \rangle$ probes the crossover scale from confinement to deconfinement as a function of time. Fig. 11.4(a) shows the scaling for $\langle W^m \rangle$.

Finally, we can consider an interesting observable that we did not discuss in the TFIM. This is the Wilson loop (11.8), $W(R, t; \tau)$ on a curve of radius R . Were the evolution to be adiabatic, $W(R, t; \tau)$ for large R would obey a perimeter law when

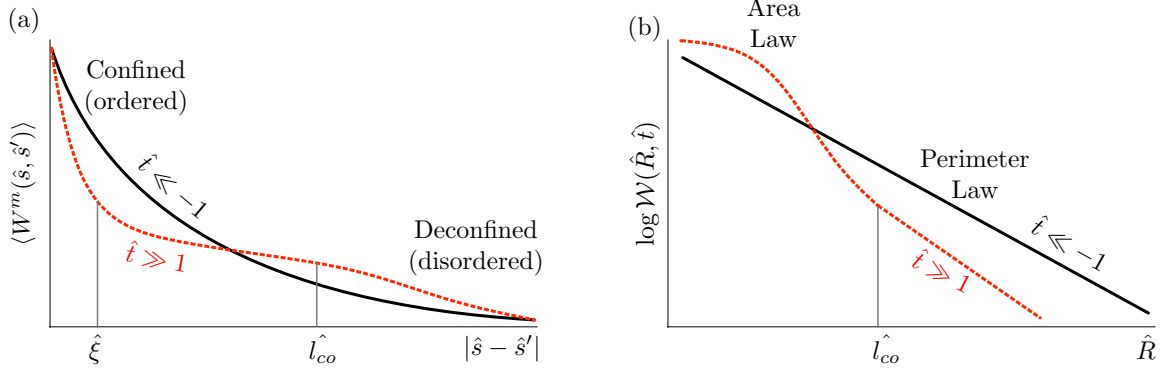


Figure 11.4: An illustration of two scaling functions showing adiabatic behavior in the deconfined phase at early scaled times (black) and coarsening behavior in the confined phase at late scaled times (red). The crossover on the scale $\hat{l}_{co} \equiv l_{co}/l_K$ in the red curves is a signature of string-net coarsening. The hat superscript denotes scaled variables like $\hat{t} = t/t_K$ etc. (a) The scaling function of the string operator that creates a pair of vortices at \hat{s} and \hat{s}' ($\langle W^m \rangle$ defined in Eq. (11.4)) as a function of the scaled vortex separation $|\hat{s} - \hat{s}'|$. This operator is dual to the two-point correlator $\langle \tau_s^z \tau_{\hat{s}'}^z \rangle$ in the TFIM. (b) The logarithm of the scaling function of the Wilson loop as a function of the scaled radius illustrating Eq. (11.20). The time dependence of $\hat{\xi}$ and \hat{l}_{co} is respectively $\hat{t}^{-\nu}$ and \hat{t}^θ .

$t < 0$ and an area law when $t > 0$. In the KZ scaling limit, the scaling of the Wilson loop takes the form $W(R, t; \tau) \sim \mathcal{W}(\hat{R}, \hat{t})$, where $R/l_K = \hat{R}$. Its asymptotic behavior is:

$$\mathcal{W}(\hat{R}, \hat{t}) \sim \begin{cases} \exp(-\hat{R} \hat{t}^\nu), & \text{if } \hat{t} \ll -1 \\ \exp(-(\hat{R} \hat{t}^\nu)^2), & \text{if } \hat{t} \gg 1 \text{ and } \hat{R} \ll \hat{t}^\theta \\ \exp(-(\hat{R}/\hat{t}^\theta)), & \text{if } \hat{t} \gg 1 \text{ and } \hat{R} \gg \hat{t}^\theta. \end{cases} \quad (11.20)$$

These scaling forms follow simply from the picture of adiabatic evolution when $\hat{t} \ll -1$ and a growing length $l_{co}(t)$ separating confinement from deconfinement when $\hat{t} \gg 1$. The Wilson loop therefore also probes the crossover scale from confinement to deconfinement as a function of time. Fig. 11.4(b) shows the scaling of the Wilson loop.

11.5 Kibble Zurek III - Ramp across a generic transition in the \mathbb{Z}_2 theory

We will now see how the discussions of the previous two sections can be generalized to ramps crossing any critical point in the full \mathbb{Z}_2 phase diagram. First, consider moving off the pure gauge line by introducing a small, but non-zero J . The coupling to matter is irrelevant to the $T = 0$ transition; hence, the confinement-deconfinement transition in Fig. 11.2 persists for non-zero J and remains in the same universality class. Since the gap to charge excitations does not close on making J non-zero, we can re-write the Hamiltonian as one with no gauge-matter coupling (to any fixed order in J) through a canonical unitary transformation. The transformation defines “dressed” charge and gauge operators – in the dressed variables, the ground state is charge-free and Δ_c is the non-zero gap to charge excitations.

As we heat the system in the process of the ramp, we also need to consider the finite temperature phase diagram and the excited spectrum when $J \neq 0$. Although the ground state is (dressed) charge-free, the excited states have an exponentially small density of charge, $e^{-\Delta_c/T_{eff}}$, at any effective temperature T_{eff} corresponding to an excess energy density q . The presence of charge at finite temperatures is extremely significant for the late-time coarsening picture for two reasons. First, it destroys the finite temperature confined phase at any non-zero J , without which a coarsening description is not meaningful. Synergistically, a finite density of charge implies that the electric field lines naturally end somewhere. Thus, the pictures of flux-loops/domain walls coarsening are no longer sensible at the longest length scales.

Fortunately, the Kibble-Zurek scaling limit saves us from the problems raised above. This is because the ratio q/q_c goes to zero as $t/t_K \rightarrow \infty$ (Eq. (11.16)) or equivalently, the effective local temperature, T_{eff} , computed from q goes to zero in the scaling limit (T_{eff} is well-defined as the system is locally in equilibrium. See

Sec. 11.3.2). Δ_c , on the other hand, remains finite. This implies that the ratio of the average distance between charges to the KZ length, $e^{\Delta_c/T_{eff}}/l_K$, is formally infinite in the scaling limit. Thus, while the dressed charges modify the *true* long-time behavior by ending coarsening, the scales on which they do so lie outside the KZ scaling regime: in this way, the coupling to matter is a dangerously irrelevant variable in the KZ problem (in the scaling limit).

While we can write scaling functions for dressed observables, the results are not very elegant since the Hamiltonian dependent dressed operators are different at different points in time. A crisper solution is to use the line tension [126]/ Fredenhagen-Marcu (FM) order parameter [113, 114] alluded to previously. This is defined as

$$R(L) = \frac{W_{1/2}(L)}{\sqrt{W(L)}} = \frac{\langle \tau_s^z (\prod_{l \in C_{1/2}} \sigma_l^z) \tau_{s'}^z \rangle}{\sqrt{\langle \prod_{l \in C} \sigma_l^z \rangle}}, \quad (11.21)$$

where C is a square loop of side L and $C_{1/2}$ is the open rectangle of sides L and $L/2$ obtained by cutting C in half, s, s' are the endpoints of $C_{1/2}$ and W is the contractible Wilson loop.

As $L \rightarrow \infty$, $R(L)$ is zero in the deconfined phase and non-zero otherwise. In this way, $R(L)$ acts as a test of long range “order”, and appropriately generalizes the two-point spin correlator $G_{\tau\tau}$ from the pure matter theory (11.10), and the vortex pair creation operator W^m (11.4) from the pure gauge theory. In fact, in the gauge-variant subspace $\{\sigma_l^z = 1\}$ on the pure matter line, $R(L)$ exactly reduces to $G_{\tau\tau}$. The scaling form and asymptotes of $R(L)$ therefore follows from Eq. (11.11) and the discussion below it. Of course, by duality, an identical analysis can be carried out by perturbing away from the pure-matter line as long as we interchange the gauge and matter degrees of freedom.

11.6 Extension to generalized Levin-Wen models

In this section, we generalize the Kibble-Zurek problem to transitions in which topological order is reduced as opposed to destroyed. Specifically, we consider transitions out of a broader, non-Abelian, class of topological phases in lattice spin models of the Levin-Wen [204] type. Along special lines in the phase diagram, we show that the dynamics and scaling properties are exactly equivalent to those of the \mathbb{Z}_2 gauge theory. We identify analogous observables and the coarsening degrees of freedom of the string net that is condensed in the starting topological phase. However, we will see that the mapping of the dynamics is not an equivalence. We then consider perturbations away from this line, finding that as for the \mathbb{Z}_2 gauge theory, in the scaling limit these other perturbations do not alter the coarsening dynamics, but can be either irrelevant or dangerously irrelevant perturbations.

We restrict our discussion to the subset of $SU(2)_k$ models whose topological order is that of a doubled, achiral, Chern-Simons theory with gauge group $SU(2)$ and a coupling constant of k in appropriate units, though the construction of Ref. [204] is more general. We also restrict to particular transitions that change the topological order by condensing bosonic vortex defects; the transitions we consider here were shown [49] to be dual (in a certain limit) to the TFIM.

11.6.1 Levin-Wen Hamiltonians with Ising transitions

The $SU(2)_k$ models we study live in a Hilbert space built from tensoring a finite set of spin variables on each link of a honeycomb lattice, $\sigma_l \in \{0, \frac{1}{2}, 1, \dots, \frac{k}{2}\}$. These are analogous to the set of possible electric fluxes ($\sigma_l^x = \pm 1$) in the \mathbb{Z}_2 gauge theory. The idealized Levin-Wen Hamiltonians are similar in spirit to the toric code, and are

constructed from a set of commuting projectors

$$H_{LW} = -K \sum_P \mathcal{P}_P - \Gamma_M \sum_s \mathcal{P}_s \quad (11.22)$$

where P represents a plaquette, and s a site. These models can be viewed as deformations of lattice gauge theories with a continuous gauge group. They are ‘deformed’ in the sense that their representation theory is truncated, even though the gauge group is not discrete. In our context, a lattice $SU(2)$ theory would have electric fluxes corresponding to all allowed spin values $0, 1/2, 1, \dots$, while the models in question have a maximum spin $k/2$. (We refer to the link spins as ‘electric flux’ though, more accurately, they are the representations of the lattice gauge/quantum group). Instead of describing our analysis for general values of k , we will now specialize to $k = 2$ in the interests of pedagogical simplicity and return to comment on the generalization subsequently.

We now discuss the detailed form of the Hamiltonian (11.22) for $SU(2)_2$. The vertex projector \mathcal{P}_s penalizes violations of angular momentum conservation, analogous to the Gauss’s law constraint $G_s = 1$ in the \mathbb{Z}_2 theory. If the three links entering a vertex have spins i, j and l , angular momentum conservation requires $l \in i \times j$. The rules for adding angular momentum have to be modified to be consistent with the truncation, however. For the $SU(2)_2$ model, the result is [40]:

$$\mathcal{P}_s |i, j, k\rangle = \begin{cases} 1 & \begin{array}{cccc} \text{---} & \text{---} & \text{---} & \text{---} \\ \diagup & \diagdown & \diagup & \diagdown \\ \text{---} & \text{---} & \text{---} & \text{---} \\ (0, 0, 0) & (0, 1, 1) & (\frac{1}{2}, \frac{1}{2}, 1) & (\frac{1}{2}, \frac{1}{2}, 0) \end{array} \\ 0 & \text{otherwise} \end{cases} \quad (11.23)$$

where it is understood that the eigenvalue of \mathcal{P}_s is independent of interchanging the spins on the three links entering the vertex.

The plaquette term \mathcal{P}_P projects onto states in which P has no magnetic flux, and is written as a superposition of “raising operators”: $\mathcal{P}_P = \frac{1}{\mathcal{D}}(\mathbf{1} + \sum_{\sigma=1/2}^{k/2} a_{\sigma} B_P^{\sigma})$, where B_P^{σ} raises all spins on the plaquette P by σ in the truncated spin space. By “raising” , we mean a combination of raising and lowering angular momenta in the truncated spin space. \mathcal{D} is the total quantum dimension, equal to 2 here, while the coefficients a_{σ} depend on the quantum dimension [204] of the spin representation σ . In $SU(2)_2$, they are $a_0 = 1$, $a_{1/2} = -\sqrt{2}$, $a_1 = 1$. B_P^{σ} raises all spins in P by raising the spin on each link $l \in \partial P$. The action of B_l^{σ} on a link l with spin $i \in \{0, 1/2, 1\}$ is:

$$\begin{aligned} B_l^i |0\rangle &= |i\rangle \\ B_l^{1/2} |1/2\rangle &\propto |0\rangle \pm |1\rangle & B_l^{1/2} |1\rangle &\propto |1/2\rangle \\ B_l^1 |1/2\rangle &\propto |1/2\rangle & B_l^1 |1\rangle &\propto |0\rangle \end{aligned}$$

The numerical coefficients are chosen such that the amplitude for creating any configuration with a 0-eigenvalue under \mathcal{P}_s is 0, ensuring that the vertex and plaquette projectors commute. Their precise value is related to the $6j$ symbols of the quantum group $SU(2)_2$, but we will not require their detailed form here. Interested readers can consult Ref. [204] for more details.

As \mathcal{P}_P and \mathcal{P}_s commute, the spectrum of the Hamiltonian can be determined exactly. The ground state is a generalization (a string-net) of the loop gas ground state of the toric code, though there can be relative sign differences between terms in the Levin-Wen ground state wavefunction. As in the toric code, the excited eigenstates of (11.22) consist of “matter” excitations of energy Γ_M , and “vortex” excitations, of energy K . In the $SU(2)_2$ model there are anyonic spin-1/2 charges, fermionic spin-1 charges, and spin-1/2 or spin-1 vortices, both of which have bosonic statistics. The spectrum can be made to correspond exactly to that of the doubled $SU(2)_2$ Chern-

Simons theory. Accordingly the topological ground state degeneracy is known [144] to be 9, as in the doubled Chern-Simons theory.

We can drive a phase transition in our system by perturbing the model (11.22) with transverse fields which create pairs of charges or vortices, as we did for the toric code by adding σ_l^x and σ_l^z . The vortex excitations have bosonic statistics and hence transverse fields which create vortex pairs can drive a transition to a vortex condensed phase in which string-nets are confined. On the other hand, the analogue of the Higgs transition is not evident for our problem as both charges are non-bosonic.

To drive the Ising transition that we are interested in, we add a transverse field which will condense spin-1 vortices. The Hamiltonian that we will tune through this transition is

$$\begin{aligned}
 H_{\text{SU}(2)_2} = & \quad -K \sum_P \frac{1}{2} (\mathbf{1} + B_P^1) - \Gamma_M \sum_s \mathcal{P}_s \\
 & \quad -K \sum_P \frac{1}{\sqrt{2}} B_P^{1/2} - \Gamma \sum_l (-1)^{2\sigma_l} \quad (11.24)
 \end{aligned}$$

where we have separated \mathcal{P}_P into operators that “raise” spins by integer and half-integer amounts, and added a transverse field perturbation, $\Gamma(-1)^{2\sigma_l}$. The transverse field creates a pair of spin-1 vortices on the plaquettes adjacent to l , and has eigenvalue 1 on integer spin links, and -1 on half-integer spin links. Because the transverse field term squares to the identity (and all vortex creation operators commute), the vortices are Ising like.

On every plaquette P and site s , the eigenvalues of B_P^1 and \mathcal{P}_s are conserved, since these operators commute with $H_{\text{SU}(2)_2}$. Thus, we can consider the transition engendered by varying the ratio K/Γ in the subspace of the Hilbert space where the conditions

$$\mathcal{P}_s |\Psi\rangle = |\Psi\rangle, \quad B_P^1 |\Psi\rangle = |\Psi\rangle \quad (11.25)$$

are always satisfied. In this subspace, the transition can be mapped onto the transition in the pure \mathbb{Z}_2 gauge theory discussed in Sect. 11.2.3, and is therefore in the 3D Ising universality class as discussed in Ref. [49]. Here we give a different derivation of this result which focuses on the ground state wavefunctions and is better adapted to our purposes in this chapter.

To understand the mapping between $H_{\text{SU}(2)_2}$ and $H_{\mathbb{Z}_2}$ (11.7), notice first that the condition $\mathcal{P}_s|\psi\rangle = |\psi\rangle$ ensures that we are always working in the “charge-free” sector where the (deformed) angular momentum is conserved at each vertex. This, together with Eq. (11.23), stipulates that we only need to consider configurations where the number of half-integer spins entering each vertex is even - or equivalently, configurations in which half-integer spins form closed loops. Similarly, in the absence of charge in the pure \mathbb{Z}_2 theory (11.7), the gauge constraint G_s in Eq. (11.2) ensures that links with electric flux ($\sigma^x = -1$) form closed loops. The Levin-Wen transverse-field operator $(-1)^{2\sigma_l}$ assigns an energy penalty to the spin 1/2 edges that form these loops, similar to the action of the transverse-field term σ_l^x on links with electric flux in the \mathbb{Z}_2 theory. *Thus both models describe a transition in which loops (of half-integer spin variables in the Levin-Wen case or $\sigma^x = -1$ variables in the \mathbb{Z}_2 gauge theory case) become confined, and vortices become condensed as Γ/K increases.*

There is, however, a qualitative difference between the operators $\prod_{l \in \partial P} \sigma_l^z$ and $B_P^{1/2}$, both of which change the number of loops in a given configuration. While σ_l^z simply flips the spin on the link l , the operator $B_P^{1/2}$ maps a spin 0 or 1 link to a spin 1/2 link, but a spin 1/2 link to a superposition of a link in the state 0 and a link in the state 1. Thus one might worry that the two operators generate the same set of configurations (after identifying $s = 0, 1$ with $\sigma^x = 1$, and $s = 1/2$ with $\sigma_x = -1$), but with different statistical weights.

We show in Appendix 11.B that this is in fact not the case. Specifically, we prove that for any Γ , the ground state wave-function of either model can be expressed in

the form

$$|\Psi\rangle = \sum_{\{l\}} \beta_{\{l\}}^\Gamma |\Psi_{\{l\}}\rangle \quad (11.26)$$

where $\{l\}$ denotes a set of links on which $\sigma_l = 1/2$ in the Levin-Wen model restricted to (11.25), or $\sigma_l^x = -1$ in the pure \mathbb{Z}_2 gauge theory. Crucially, we find that $\beta_{\{l\}}$ is the same for each set $\{l\}$ in both models. Operators in the Levin-Wen model which commute with the conditions (11.25) are either diagonal in the vortex basis, or diagonal in the spin basis and sensitive only to the spin on each edge modulo 1. The expectation value of any such operator is therefore identical to that of its \mathbb{Z}_2 analogue, cementing the equivalence of the two models.

We conclude that within the sub-sector (11.25), the transition is equivalent to that of the pure \mathbb{Z}_2 gauge theory, and dual to that of the TFIM. It follows that our previous discussion of string net coarsening, and the scaling of vortex creation operators, applies *mutatis mutandis* to the model at hand.

Note, however, that the topological order of the initial and final phases of Eq. (11.24) is not the same as in the \mathbb{Z}_2 gauge theory; there are additional deconfined excitations on both sides of the transition. (In fact, the confined phase of $H_{\text{SU}(2)_2}$ is a \mathbb{Z}_2 gauge theory [50]). There must therefore be some operators in the Levin-Wen model whose behavior through the ramp is not captured by the mapping to the Ising gauge theory.

To make this more explicit, we consider the fate of Wilson loop operators. In the Levin-Wen model there are two of these:

$$\begin{aligned} W_{1/2}(R, t; \tau) &= \left\langle \prod_{l \in C} B_l^{1/2}(t) \right\rangle \\ W_1(R, t; \tau) &= \left\langle \prod_{l \in C} B_l^1(t) \right\rangle. \end{aligned} \quad (11.27)$$

In order not to create vortices along the curve C , these raising operators must act with appropriate configuration-dependent complex coefficients, as discussed in Refs. [204, 48]. $W_{1/2}(R, t; \tau)$ is clearly the analogue of the Wilson loop operator in the \mathbb{Z}_2 gauge theory; its expectation value obeys a perimeter law in the small Γ/K phase, and an area law in the large Γ/K phase, and its universal scaling in a linear ramp is given by Eq. (11.20). However, as the spin-1 variable remains deconfined throughout the phase diagram, $W_1(R, t; \tau)$ always obeys a perimeter law. Its expectation remains constant in the scaling limit as the system passes through the critical point.

A related effect can be seen in the amplification of the energy splitting between ground states in different topological sectors discussed in the previous section. The $SU(2)_2$ Levin-Wen model has 9 ground states on the torus. It can be shown [49] that 6 of these obtain an energy cost of order L in the condensed phase, while one new ground state sector emerges, leaving a total of 4 topologically distinct ground states. These 4 correspond to the two possible eigenvalues of $W_1^{nc}(R, t; \tau)$ along each non-contractible curve.

Though we have primarily discussed the $SU(2)_2$ Levin-Wen model, the main results apply to a large family of models in which there is an excitation that behaves like the Ising vortex [49]. Specifically, all the $SU(2)_k$ models exhibit Ising transitions in which the half-integer spins (integer spins) can be mapped onto \mathbb{Z}_2 gauge configurations with $\sigma^x = -1$ ($\sigma^x = 1$). They have two families of Wilson-line operators: the half-integral Wilson line operators, which obey an area law in the confined phase, and scaling relations analogous to those of Eq. (11.20); and the integral Wilson line operators, whose expectation values do not depend on t, τ and which remain perimeter law throughout the ramp⁴.

It is worth mentioning that the Ising transition we have discussed here is but one of a variety of confining transitions that can be realized in Levin-Wen models [49, 120].

⁴The Higgs transition may survive when k is a multiple of 4 as some of the charges are bosons. Little is known about these transitions.

In the $SU(2)_2$ model discussed above, for example, we could also add a transverse field term of the form $\cos \pi s_l$ (which has eigenvalues $(1, 0, -1)$ for $s_l = (0, 1/2, 1)$, respectively). This confines both spin-1/2 and spin 1 labels, engendering a transition to a completely confined phase where both Wilson loop operators in Eq. (11.27) obey an area law. In this case the vortices that proliferate are not Ising-like, however, since the operator $\cos \pi s_l$ does not square to 1. Very little is known about the critical theory in this case, and we expect that the transition is not in the 3D Ising universality class, so that the scaling functions and coarsening behavior will be fundamentally different from those of the \mathbb{Z}_2 gauge theory.

11.6.2 Away from the pure \mathbb{Z}_2 limit

Thus far, we did not concern ourselves with the other excitations in the $SU(2)_2$ Levin-Wen model as their number was conserved in the ramp and we remained in the subspace (25) at all times. However, the other excitations, charges of spin 1 and 1/2, and vortices of spin 1/2, will be created in a ramp if we perturb away from the limit of Eq. (11.24) by adding terms to the Hamiltonian which break the local conservation laws. In particular, the spin 1/2 charge has anyonic statistics relative to the condensing vortices, so that a finite density of these destroys confinement (these are analogous to the matter sources of the Ising gauge theory). Once again, the KZ scaling limit saves the day. These spin 1/2 charges remain gapped throughout the transition. Thus, as for the Ising gauge theory with matter, in the scaling limit we expect that the density of all of these excitations is vanishingly small throughout the coarsening regime; terms violating the conservation of the spin-1/2 charge at each vertex then act as dangerously irrelevant variables in the manner described in Section 11.5.

Spin 1 charges and spin-1/2 vortices, however, have bosonic statistics relative to the spin 1 vortex, and do not have analogues in the \mathbb{Z}_2 theory. Once again, for small

perturbations which violate the exact local conservation of these excitations, they remain gapped throughout the transition and hence do not affect coarsening in the KZ scaling limit. Since a dilute density of such charges does not destroy confinement, however, we expect that they will not destroy coarsening even outside of the scaling limit.

11.7 Concluding Remarks

In this chapter, we have initiated the study of the Kibble-Zurek problem for topologically ordered phases by studying the linear ramp across a transition that reduces/breaks topological order and written down a scaling theory for it. Interestingly, unlike broken symmetry cases where it is natural to ramp from less to more order, here it is more natural to ramp from more to less order. The latter leads to our identification of the slow dynamics of string net coarsening much as the former leads to defect coarsening *à la* Kibble and Zurek. Of course, one *can* study the reverse protocol and the associated scaling although we have not done so here in the interests of not taxing the reader’s patience unduly.

The basic framework here can be easily generalized to other transitions out of topological phases; although for string-net coarsening to be visible, the gauge degrees of freedom must have a ready identification. Examples are transitions out of \mathbb{Z}_n phases with $n \geq 3$ in $d = 2 + 1$ and with $n \geq 2$ in $d = 3 + 1$. The Levin-Wen models also offer a “target rich” domain, although the analysis is likely to prove more complicated for more general condensation transitions. It will also be interesting to move to contexts with conserved currents where one can study the temporal and spatial evolution of transport coefficients, such as the Hall conductance.

Finally, for the statistical mechanically inclined, we would like to draw attention to our identification of gapped matter as a dangerously irrelevant variable in the

dynamical KZ context. This is clearly a more general idea—e.g. irrelevant departures from integrability will be similarly dangerous—and it suggests that in the KZ problem, more couplings will be classified as such than in the standard equilibrium analysis.

11.A Scattering times in coarsening

Here, we identify the dynamical process enabling coarsening at late times alluded to in Sec. 11.3.2, and justify that it remains in equilibrium during the KZ ramp. The criterion to remain in equilibrium is that the time-scale for such a process, t_{co} , is parametrically smaller than the time-scale for the change in the transverse-field t_Γ . Using $(\Gamma_M - \Gamma_{Mc}) = -t/\tau$, we estimate t_Γ to be:

$$t_\Gamma \equiv \frac{\Gamma_M - \Gamma_{Mc}}{d\Gamma_M/dt} = t.$$

The system at late times has two kinds of excitations that are remnants of the paramagnetism at early times: 1) The long domain walls of average size l_{co} and 2) The bulk gapped quasi-particle excitations about each ferromagnetically ordered state. As $t/t_K \rightarrow \infty$, the latter can be treated as classical particles. The average density of these particles and their momentum is essentially determined at $t \sim t_K$ and is fixed to be $\sim 1/l_K^2$ and $1/l_K$ respectively. Their mass is determined by the gap $\Delta(t)$. The growing mass and the long inter-particle distances as compared to the instantaneous correlation length ξ justify the classical particle approximation. An average velocity of these particles can be determined as

$$v_p \sim \frac{p}{m} \sim \frac{1/l_K}{\Delta},$$

where p is the average momentum and m the mass. The mechanism of coarsening proceeds through the transfer of energy between the long domain walls and these

particles. To wit, the relevant time-scale t_{co} is the scattering time between these particles and the wall:

$$t_{co} \equiv \frac{l_{co}}{v_p}.$$

Recall that the growth law when ξ is a function of time is (Eq. (11.17)):

$$l_{co}(t; \tau) \sim \xi(t; \tau) \left(\frac{t}{\xi(t; \tau)^z} \right)^{1/z_d} \sim l_K \left(\frac{t}{t_K} \right)^{\frac{1-\nu}{2}},$$

where in the last step, we have substituted the critical exponents of the (2+1)D TFIM, $z = 1$, $z_d = 2$. Putting the pieces together, we see that $t_{co} \ll t_\Gamma \Rightarrow \nu < 1$. This certainly holds at the 3D Ising critical point where $\nu \approx 0.6$. Thus, we conclude that coarsening described by Model C is indeed the correct long time asymptote for the KZ scaling functions in a linear ramp.

Finally, we observe that all dynamical processes in the (2+1)D TFIM do not remain in equilibrium in the KZ ramp at late times. The scattering time between quasi-particles, t_{pp} , grows as Δ^2 in this limit and is parametrically larger than t_Γ . A hydrodynamical description, if it exists, is therefore more delicate than the case when the ramp is stopped at some $t/t_K = \hat{t}^s$.

11.B Mapping of general $SU(2)_k$ models to the \mathbb{Z}_2 gauge theory

In this Appendix, we will discuss in more detail the mapping from the confining transition in the $SU(2)_2$ Levin-Wen model to the pure \mathbb{Z}_2 gauge theory (11.7). As discussed earlier, the transition in question involves varying K/Γ in Eq. (11.24), while restricting the Hilbert space to states with eigenvalue 1 under the vertex projector,

and the integer part of the plaquette projector. In this subspace, links with half-integer spins form closed loops. The mapping to the pure gauge \mathbb{Z}_2 theory involves mapping half-integer (integer) spins to the presence (absence) of \mathbb{Z}_2 electric flux $\sigma^x = -1$ (+1). The transverse field operator $(-1)^{2\sigma_l}$ maps to σ_l^x , and $B_P^{1/2}$ to $B_P = \prod_{l \in \partial P} \sigma_l^z$. We will now show that the probability to be in any loop configuration is the same in both theories for every choice of K/Γ .

We will begin with some notation. Let C denote the collection of links on the lattice that form closed loops, and $\langle \alpha_{1/2}(C) \rangle$ the probability for a configuration in C . We will work here in the restricted Hilbert space of states for which

$$\mathcal{P}_s |\Psi\rangle = |\Psi\rangle \quad B_P^1 |\Psi\rangle = |\Psi\rangle \quad (11.28)$$

and assume that our lattice has no boundary. To make the analogy to the \mathbb{Z}_2 gauge theory, we also define the analogous operator, $\alpha_x(C)$, whose expectation value gives the probability for a closed loop configuration of links with $\sigma_l^x = -1$.

Our objective is to prove that, for every Γ and K , $\langle \alpha_{1/2}(C) \rangle = \langle \alpha_x(C) \rangle$. Since operators that commute with the conditions (11.28) are either diagonal in the spin basis and sensitive only to $s_l \bmod 1$, or diagonal in the vortex basis (dual to the basis of spin-1/2 loops), this is sufficient to prove that their critical behavior is identical.

We will carry out the proof in two steps. First, we will show the equality for the two solvable points $\Gamma = 0, K > 0$ and $K = 0, \Gamma > 0$, where we can construct exactly the ground-states in both models. We will then use perturbation theory to argue that the result holds throughout the phase diagram.

11.B.1 Equal weighting of loops in the ground states at the solvable points

For $K = 0, \Gamma > 0$, the ground state has $\sigma_l^x \equiv 1$ in the \mathbb{Z}_2 gauge theory, and $\sigma_l \in \{0, 1\}$ for the Levin-Wen model. In this limit, for any C we have trivially that $\langle \alpha_{1/2}(C) \rangle = \langle \alpha_x(C) \rangle = 0$ and the result holds.

Focusing on the opposite limit ($\Gamma = 0, K > 0$), let us construct the exact ground states in the two models. We begin with the \mathbb{Z}_2 gauge theory. Let $|0\rangle$ denote the state with $\sigma^x = 1, \tau_s^x = 1$ on all links and sites. This satisfies the Gauss law, but is not an eigenstate of the plaquette projector. To construct such an eigenstate, we take

$$|\Psi_{TC}\rangle = \frac{1}{\sqrt{N}} \sum_{n=1}^{N_P} \sum_{*\mathbb{P}_n} \prod_{P \in *\mathbb{P}_n} B_P |0\rangle = \frac{2}{\sqrt{N}} \sum_{\{C\}} |\Psi_C\rangle \quad (11.29)$$

where $*\mathbb{P}_n$ runs over all possible distinct choices of n plaquettes on the lattice, and N is a normalization. This sum generates all possible configurations C of loops with $\sigma^x = -1$, weighted equally (each configuration is in fact generated twice, since $\prod_P B_P = 1$). Since $B_P^2 = 1$, $B_{P_i} \prod_{P \in *\mathbb{P}_n} B_P = \prod_{P \in *\mathbb{P}'_n} B_P$, where $*\mathbb{P}'_n$ is $*\mathbb{P}_n$ with P_i either added (if it was not originally in the set) or deleted (if it was). It follows that

$$\frac{1}{\sqrt{N}} \sum_{n=1}^{N_P} \sum_{*\mathbb{P}_n} B_{P_i} \prod_{P \in *\mathbb{P}_n} B_P |0\rangle = \frac{1}{\sqrt{N}} \sum_{n=1}^{N_P} \sum_{*\mathbb{P}_n} \prod_{P \in *\mathbb{P}_n} B_P |0\rangle$$

and $|\Psi_{TC}\rangle$ is a ground state.

A similar construction can be used in the Levin-Wen models. Let $|\Psi^e\rangle$ be a state satisfying (11.28), with σ_l an integer for every link l (careful inspection of these two conditions reveals that $|\Psi^e\rangle$ is a superposition of configurations of closed spin-1 loops). Now consider:

$$|\Psi_{LW}\rangle = \frac{1}{\sqrt{N}} \sum_{n=1}^{N_P} \sum_{*\mathbb{P}_n} \prod_{P \in *\mathbb{P}_n} \frac{1}{\sqrt{2}} B_P^{1/2} |\Psi^e\rangle \quad (11.30)$$

We will show presently that

$$\left(B_P^{1/2}\right)^2 = 1 + B_P^1 \quad B_P^{1/2}B_P^1 = B_P^1B_P^{1/2} = B_P^{1/2} \quad (11.31)$$

Using this fact, we have

$$B_{P_i}^{1/2} \prod_{P \in * \mathbb{P}_n} B_P^{1/2} = \begin{cases} \prod_{P \in * \mathbb{P}_n - P_i} B_P^{1/2} (1 + B_{P_i}^1) & P_i \in * \mathbb{P}_n \\ \prod_{P \in * \mathbb{P}_n \cup P_i} B_P^{1/2} & P_i \notin * \mathbb{P}_n \end{cases}$$

It follows that

$$\frac{1}{\sqrt{2}} B_{P_i}^{1/2} |\Psi_{LW}\rangle = |\Psi_{LW}\rangle \quad (11.32)$$

and $|\Psi_{LW}\rangle$ is a ground state.

Now, for any closed loop L , we can generate a configuration with $\sigma_l = 1/2$ on all links in L , and no other links, by acting on $|\Psi^e\rangle$ with the product of $B_P^{1/2}$ on all plaquettes inside the loop or all plaquettes outside the loop (these are the only such configurations on the right-hand side of Eq. (11.30)). In the \mathbb{Z}_2 gauge theory the same holds for closed loops of $\sigma^x = -1$. Hence given C , we have

$$\begin{aligned} \langle \alpha_{1/2}(C) \rangle &= \frac{1}{N} \langle \Psi^e | \left(\prod_{P \in * \mathbb{P}(C)} \frac{1}{\sqrt{2}} B_P^{1/2} \right)^2 | \Psi^e \rangle \\ &= \frac{1}{N} \langle \Psi^e | \prod_{P \in * \mathbb{P}(C)} \frac{1}{2} (1 + B_P^1) | \Psi^e \rangle \\ &= \frac{1}{N} \end{aligned} \quad (11.33)$$

where $* \mathbb{P}(C)$ contains either all plaquettes inside, or all plaquettes outside, the closed loops in configuration C , and the last equality is a result of imposing (11.28). Thus for $\Gamma = 0$ all possible configurations of spin-1/2 loops occur with equal probability in the ground state of the $SU(2)_2$ Levin-Wen model.

We note that these results carry over directly to the more general case of an $SU(2)_k$ Levin-Wen model, upon replacing spin-1/2 (spin-1) with the set of all half-integer (integer) spins, and $B_P^{1/2}$ (B_P^1) with the sum of all half-integer (integer) spin-raising terms in the plaquette operator (weighted by their respective quantum dimensions).

It remains to show that Eq. (11.31) holds, which we will do for general k . We let $\mathcal{P}_P^{1/2} = \frac{1}{\mathcal{D}} \sum_{\sigma=1/2,3/2,\dots} a_\sigma B_P^\sigma$ denote all half-integer raising terms in the plaquette operator, and $\mathcal{P}_P^1 = \frac{1}{\mathcal{D}} \left(\mathbf{1} + \sum_{\sigma=1,2,\dots} a_\sigma B_P^\sigma \right)$ denote all integer terms. Following Levin and Wen, we choose the constant \mathcal{D} such that $\mathcal{P}_P \equiv \frac{1}{2} \left(\mathcal{P}_P^1 + \mathcal{P}_P^{1/2} \right)$ is a projector. We then have

$$\begin{aligned} (\mathcal{P}_P^1 + \mathcal{P}_P^{1/2})^2 &= (\mathcal{P}_P^1)^2 + (\mathcal{P}_P^{1/2})^2 + \mathcal{P}_P^{1/2} \mathcal{P}_P^1 + \mathcal{P}_P^1 \mathcal{P}_P^{1/2} \\ &= 2(\mathcal{P}_P^1 + \mathcal{P}_P^{1/2}) \end{aligned}$$

Now, $(\mathcal{P}_P^{1/2})^2$ and $(\mathcal{P}_P^1)^2$ both contain only terms that raise the spins in P by an integer amount, while $\mathcal{P}_P^1 \mathcal{P}_P^{1/2} = \mathcal{P}_P^{1/2} \mathcal{P}_P^1$ contains only half-integral raising operators. It follows that

$$(\mathcal{P}_P^1)^2 + (\mathcal{P}_P^{1/2})^2 = 2\mathcal{P}_P^1, \quad \mathcal{P}_P^1 \mathcal{P}_P^{1/2} = \mathcal{P}_P^{1/2}. \quad (11.34)$$

We also have

$$(\mathcal{P}_P^1 + \mathcal{P}_P^{1/2})(\mathcal{P}_P^1 - \mathcal{P}_P^{1/2}) = 0 \quad (11.35)$$

since it can be shown [49] that $(\mathcal{P}_P^1 + \mathcal{P}_P^{1/2})$ projects onto flux-free states, while $(\mathcal{P}_P^1 - \mathcal{P}_P^{1/2})$ projects onto states with an Ising vortex. It follows that

$$(\mathcal{P}_P^{1/2})^2 = (\mathcal{P}_P^1)^2 = \mathcal{P}_P^1 \quad (11.36)$$

This also implies that \mathcal{P}_P^1 is a projector, and thus that the eigenvalues of \mathcal{P}_P^1 are 0 and 1. (From Eq (11.36) and the fact that \mathcal{P}_P is a projector, it follows that the eigenvalues of $\mathcal{P}_P^{1/2}$ are $0, \pm 1$; when restricted to configurations where $\mathcal{P}_P^1 |\Psi\rangle = |\Psi\rangle$,

they are ± 1 , as one expects from the correspondence of $\mathcal{P}_P^{1/2}$ to the plaquette term of the toric code.)

11.B.2 Away from the solvable points

Next, we wish to show that the result of the previous section holds true throughout the phase diagram. One way to do this is to invoke the result of Ref. [49], where it was shown that within the subspace of states satisfying (11.28), the $SU(2)_k$ Levin-Wen models are exactly dual to the transverse-field Ising model. We can identify all states in this Hilbert space by the configuration of dual Ising spins (together with their topological ground-state sector, in periodic boundary conditions). The duality relation— which also holds for the \mathbb{Z}_2 gauge theory — ensures that the probability amplitude to be in a given vortex configuration is identical in both models. The physical operators in this Ising subspace are either diagonal in the vortex (or dual Ising spin) basis, or diagonal in the basis of spin-1/2 loops. (These are precisely the operators that do not cause violations of (11.28), and cannot distinguish between edges of spin 0 and spin 1). It follows that all expectation values of such operators — including $\langle \alpha_{1/2}(C) \rangle$ — must also be identical to their \mathbb{Z}_2 analogues (such as $\langle \alpha_x(C) \rangle$).

Here we will take an alternative, perturbative approach to prove the desired result. We will begin at an arbitrary point in the deconfined phase, and consider constructing the wave-functions in both theories to some finite order in perturbation theory. These wave functions are linear combinations of the unperturbed (Levin-Wen or toric code) ground state, together with excited states of the form

$$|\Psi_{\{l\}}\rangle = \prod_{l \in \{l\}} h_l |\Psi_0\rangle \quad (11.37)$$

where we have defined the transverse field operator $h_l \equiv \sigma_l^x$ for the toric code, and $(-1)^{2s_l}$ for the Levin-Wen model, and $|\Psi_0\rangle$ denotes the unperturbed ground state. If

l_1 and l_2 are two links bordering plaquette P , we have

$$\begin{aligned}\sigma_{l_{1,2}}^x B_P &= -B_P \sigma_{l_{1,2}}^x \\ (-1)^{2s_{l_{1,2}}} B_P^{1/2} &= -B_P^{1/2} (-1)^{2s_{l_{1,2}}} \\ [\sigma_{l_1}^x \sigma_{l_2}^x, B_P] &= \left[(-1)^{2s_{l_1}} (-1)^{2s_{l_2}}, B_P^{1/2} \right] = 0\end{aligned}$$

Thus $|\Psi_{\{l\}}\rangle$ is a state with vortices on each plaquette with an odd number of edges in the set of links $\{l\}$. It also follows that choices of $\{l\}$ which differ by a product $\prod_{l \in C^*} h_l$, where C^* is a set of closed curves on the dual lattice, create identical excited states, as $\prod_{l \in C^*} h_l |\Psi_0\rangle = |\Psi_0\rangle$. Finally, we have

$$\langle \Psi_{\{l\}} | \Psi_{\{l'\}} \rangle = \delta_{\{l\} \cup \{l'\}, C^*} \quad (11.38)$$

In other words, the inner product is 1 if the combination of the two sets $\{l\}$ and $\{l'\}$ of links forms a set of closed curves on the dual lattice, so that $|\Psi_{\{l\}}\rangle$ and $|\Psi_{\{l'\}}\rangle$ have vortices on the same plaquettes. Similarly, we may compute matrix elements of the Hamiltonian within these excited states via:

$$\langle \Psi_{\{l\}} | \prod_{l \in \{l''\}} h_l | \Psi_{\{l'\}} \rangle = \delta_{\{l\} \cup \{l'\} \cup \{l''\}, C^*} \quad (11.39)$$

The crucial point is that for any choice of $\{l\}, \{l'\}, \{l''\}$, these matrix elements are identical in both models. Since the weight of each unperturbed excited state in the exact ground state can be constructed perturbatively using only matrix elements of this form, it follows that

$$|\Psi\rangle = \sum_{\{l\}} \beta_{\{l\}}^\Gamma |\Psi_{\{l\}}\rangle \quad (11.40)$$

with $\beta_{\{l\}}$ the same for each set $\{l\}$ in both models.

Finally, we observe that $\alpha_{1/2}(C)$ and $\alpha_x(C)$ both have the form

$$\alpha_\nu = \prod_{l \in C} \frac{1}{2} (1 - h_l) \quad (11.41)$$

and, in particular, commute with h_l on every link. (Here $\alpha_\nu = \alpha_{1/2}(C), \alpha_x(C)$ as appropriate). This, together with the relation (11.39), implies that

$$\langle \alpha_\nu \rangle_\Gamma = \sum_{\{l\}, \{l'\}} \bar{\beta}_{\{l\}}^\Gamma \beta_{\{l'\}}^\Gamma \langle \Psi_0 | \prod_{l \in \{l\}} h_l \alpha_\nu \prod_{l \in \{l'\}} h_l | \Psi_0 \rangle$$

in both models. We have already shown that the coefficients $\beta_{\{l\}}^\Gamma$ are the same, and the possible choices of $\{l\}, \{l'\}$ on which the δ function has support are a geometric property of the lattice. Invoking the result of the previous subsection, we can thus conclude that for all Γ in the deconfined phase,

$$\langle \alpha_{1/2}(C) \rangle_\Gamma = \langle \alpha_x(C) \rangle_\Gamma \quad (11.42)$$

Our derivation has implicitly relied on the fact that we can construct the exact ground state perturbatively, starting from the ground state of the toric code or Levin-Wen solvable point. Thus the above argument fails at the critical point, and in the phase where Γ/K is large. In this regime, however, we may make essentially the same argument, by replacing h_l with the plaquette operator, and $|\Psi_{LW}\rangle, |\Psi_{TC}\rangle$ (denoted by $|\Psi_0\rangle$ in the derivation above) with $|\Psi^e\rangle$ and $|0\rangle$ respectively. In this case, the basis of excited states generated will be an eigenstate of σ^x (toric code) or $(-1)^{2s}$ (Levin-Wen). There is no need to define an analogue of C^* , since if two distinct products of plaquette projectors produce the same loop configuration state, then their product is the identity operator.

In each phase, we can thus argue that Eq. (11.42) holds to arbitrary order in perturbation theory. It follows that as the phase transition is second order, it must also hold at the critical point, proving the result.

Chapter 12

A Bionic Coulomb Phase on the Pyrochlore Lattice

12.1 Introduction

Much recent activity in condensed matter physics has involved the study of “topologically ordered” phases which characteristically exhibit emergent gauge fields and deconfined fractionalized excitations at low energies. Canonical quantum examples of these are the various fractional quantum Hall phases [324, 337] and much of the physics is present in the elegant classical physics of the spin ice compounds [56].

Gauge fields are intimately connected to local constraints, as in the textbook example of Maxwell electromagnetism wherein Gauss’s law reflects a constraint at each point in space that must be obeyed by the dynamics. In a condensed matter setting, the analogous constraints arise as a low-energy effective truncation of the space of configurations; examples range from the dimer configurations of short range RVB theory [217] to the string nets of Levin and Wen [203].

A subclass of these constraints literally take the form of lattice versions of the familiar Gauss’s law for abelian gauge fields, albeit with restricted microscopically

realizable values for the lattice electromagnetic fields. The introduction of an appropriate classical statistical mechanics that consists of averaging over all allowed configurations with uniform weight leads to the so-called Coulomb phase [139] with dipolar correlations, whose coarse-grained description realizes a Euclidean Maxwell theory. More elaborately, the introduction of a quantum dynamics in the constrained manifold can lead to a version of Maxwell electrodynamics coupled to electric charges and magnetic monopoles. An elegant point of intersection between the classical and quantum Coulomb phases is an appropriate Rokhsar-Kivelson point where the ground state wavefunction is itself an equal amplitude superposition of allowed configurations [141, 218].

In this chapter we expand the catalog of Coulomb phases. We study the antiferromagnetic four-state Potts model on the highly frustrated pyrochlore lattice and show that its ground state manifold exhibits correlations characterized by *three* abelian gauge fields. We find that the fundamental excitations/defects above this ground state manifold are charged under these gauge fields in an unusual way—they carry nonzero charges for two of the three gauge fields whence we refer to them as bions. (The term dyon is already reserved for particles charged under dual electric and magnetic fields whereas here both fields are of the same species.) In the classical setting, which is our primary interest in this chapter, the import of the charge assignments is that it predicts the entropic force between different bions and more generally the free energy/entropy for any configuration of multiple bions. Our evidence for these assertions comes from a Monte Carlo simulation that agrees with the correlations predicted by the triple Maxwell theory, and which yields statistics of flux-loops in the ground state manifold that have been previously suggested to be a sharp diagnostic of the Coulomb phase [160].

Readers familiar with the existing literature on Coulomb phases will note that it is already known [155, 138] that classical $O(N)$ spins with a nearest neighbor antiferromagnetic interaction on the pyrochlore lattice

- (a) exhibit a Coulomb phase with one gauge field for $N = 1$ (Ising) spins which is the case relevant to spin ice and indeed observed in experiments,
- (b) exhibit order by disorder for $N = 2$ and
- (c) exhibit a Coulomb phase with N gauge fields for $N \geq 3$.

It is interesting to situate the current work in this context. To this end imagine starting with $O(3)$ symmetric Heisenberg spins that live on the sphere (Fig. 12.2c) whose ground state correlations are governed by three independently fluctuating gauge fields. Excitations above this manifold are gapless and involve arbitrarily small charges under the gauge fields. If we restrict their range by generating an easy axis (Fig. 12.2a) we return to the Ising case where the number of gauge fields is now down to one and the excitations are gapped and quantized. The import of this current chapter is that if we restrict the range to four symmetric points on the sphere (Fig. 12.2b) the number of gauge fields is unchanged although the excitations again become gapped and quantized. We believe that this reduction can be extended to higher dimensions by considering generalizations of kagome/pyrochlore [1] involving $d + 1$ -simplices in d dimensions and starting with $O(d)$ spins and restricting them to $d + 1$ state Potts configurations.

We would be remiss if we did not note that this chapter generalizes the early results of Kondev and Henley [189] from the two dimensional lattice known variously as the square lattice with crossings or planar pyrochlore, to three dimensions. Readers who peruse the early paper will spot the family resemblance immediately.

In the balance of the chapter, we will set up the Potts model and its mapping to vector spins (Section II), map these in turn to a coarse grained description in

terms of pseudo-magnetic flux/gauge fields and confirm the resulting predictions for the correlations (Section III), discuss the bionic excitations (Section IV), study the statistics of loops (Section V) and conclude with some brief remarks (Section VI).

12.2 The Model

The pyrochlore is a lattice of corner-sharing tetrahedra which can be constructed from the diamond lattice by placing a site at the midpoint of each bond (Fig. 12.1). The result is a quadripartite structure, which may alternatively be described as an fcc lattice with a four-site basis. From the former construction, it is evident that the centers of the tetrahedra lie on the sites of the diamond lattice: in other words, the dual lattice of the pyrochlore is the diamond lattice – a fact which we will make use of extensively below. We now turn to the Potts model which we will introduce from the perspective of the Heisenberg model as this will yield a vector spin representation of the Potts spins which will be central to this chapter.

The pyrochlore lattice is highly frustrated from the perspective of classical collinear antiferromagnetism: the nearest-neighbor classical Heisenberg antiferromagnet on this lattice has an extensive ground state degeneracy and remains a quantum paramagnet at all temperatures [216]. Since they will be relevant to us, we briefly summarize some details of the Coulomb phase for $O(3)$ (Heisenberg) spins on the pyrochlore. The canonical nearest-neighbor Heisenberg Hamiltonian

$$H = J \sum_{\langle i,j \rangle} \mathbf{S}_i \cdot \mathbf{S}_j \quad (12.1)$$

can be re-written, up to an overall constant, as

$$H = \frac{J}{2} \sum_{\boxtimes} \left(\sum_{i \in \boxtimes} \mathbf{S}_i \right)^2,$$

where the sum in parenthesis runs over the four spins at the corners of each tetrahedron, and the outer sum runs over all tetrahedra in the lattice. Thus, the ground states are defined by spins satisfying *local* constraints:

$$\sum_{i \in \boxtimes} S_i^\alpha = 0 \quad (12.2)$$

for each tetrahedron and each spin component α .

As a result of these local constraints, each ground state can be mapped to a configuration of divergence-free fluxes, one for each spin component, on the dual diamond lattice. Upon coarse-graining, the entropic cost of fluctuations within the ground state manifold leads to an emergent ‘electrodynamics’ – with the coarse-grained fluxes playing the role of divergence-free lattice electromagnetic fields. The process yields asymptotically dipolar forms for spin (and field) correlation functions, a hallmark of the celebrated “Coulomb Phase”.

We now consider applying a symmetry breaking potential that restricts the Heisenberg spins to four symmetrically situated points in spin space (Fig. 12.2b). The spin on each pyrochlore site must now belong to the following set of four spins pointing towards the corners of a regular tetrahedron in spin-space:

$$\begin{aligned} \mathbf{S}_A &= (-1, 1, 1); & \mathbf{S}_B &= (1, -1, 1); \\ \mathbf{S}_C &= (-1, -1, -1); & \mathbf{S}_D &= (1, 1, -1). \end{aligned} \quad (12.3)$$

Observe that any two (different) spins in (12.3) make an angle of $\cos^{-1}(-\frac{1}{3})$ with one another, so that the dot-product of any two spins in the set is $\mathbf{S}_\alpha \cdot \mathbf{S}_\beta = 4\delta_{\alpha\beta} - 1$ where $\alpha, \beta = A, B, C$, or D . Thus the nearest neighbor interaction energy has the character of an antiferromagnetic Potts interaction between four states: it prefers neighbors to be different but is indifferent to how that is achieved. Formally, the Hamiltonian

(12.1) with the spins restricted to the set (12.3) is equivalent to the Hamiltonian

$$H_P = J \sum_{\langle i,j \rangle} \delta_{\sigma_i, \sigma_j}. \quad (12.4)$$

where the Potts spins σ_i can be in one of four states: A, B, C or D . In essence we have mapped from Potts variables to a set of vector spins. The ground state constraint (12.2) restricted to the set (12.3) is equivalent to the condition that each tetrahedron to contain all four Potts states.

The Potts model has a discrete macroscopic ground state degeneracy—a remnant of the continuous macroscopic degeneracy of the $O(3)$ model [216]. To show this, a strict lower bound on the entropy can be obtained by using the degeneracy of the three-state Potts model on the kagome [150, 31] and by viewing the pyrochlore as alternating layers of kagome and triangular planes. The result is the bound [236] $\Omega > 4(1.20872)^{N/2}$, corresponding to an entropy $S/k_B N > (1/2)\log(1.20872)$. A more direct estimate is the Pauling entropy [237] for this system. For a given tetrahedron, 4! of the possible 4^4 states are ground states. Treating the tetrahedral constraints as independent gives a ground state degeneracy

$$\Omega = 4^N \left(\frac{4!}{4^4} \right)^{N_{tet}} = \left(\frac{3}{2} \right)^{N/2},$$

where N is the number of spins and $N_{tet} = N/2$ is the number of tetrahedra. This corresponds to an entropy per spin $S/k_B N = (1/2)\log(3/2)$ which is, interestingly, the same as the Pauling estimate for the entropy of spin ice [56]. As advertised in the introduction, the reduction from Heisenberg spins to Potts spins suggests that the latter system will still exhibit a Coulomb phase. We now turn to a precise formulation of this conjecture.

12.3 Flux Fields and Correlations

12.3.1 Flux Fields

Our development of flux fields closely parallels the construction in the case of the $O(N)$ antiferromagnet [155, 138]. The essential idea is to map the spin variables to a flux field defined on the sites of the dual diamond lattice. The local ground state constraint (12.2) – which still applies to the Potts spins as defined in (12.3) – is then mapped into a requirement that the flux configuration be divergence-free.

We begin by defining bond vectors \mathbf{u}_κ pointing from the even to the odd sublattices of the bipartite diamond lattice (i.e., from the centers of ‘up’ to ‘down’ tetrahedra on the pyrochlore), which take the form

$$\begin{aligned} \mathbf{u}_1 &= \left(-\frac{1}{4}, \frac{1}{4}, \frac{1}{4} \right); & \mathbf{u}_2 &= \left(\frac{1}{4}, -\frac{1}{4}, \frac{1}{4} \right); \\ \mathbf{u}_3 &= \left(-\frac{1}{4}, -\frac{1}{4}, -\frac{1}{4} \right); & \mathbf{u}_4 &= \left(\frac{1}{4}, \frac{1}{4}, -\frac{1}{4} \right) \end{aligned} \quad (12.5)$$

where the fcc lattice constant has been chosen as $a = 1$. The spins live on the midpoints of the bonds; Fig. 12.1 illustrates the geometry of the lattice and the bond vectors.

Next, we define three vector flux fields on each bond, one for each spin component of the Potts spins represented in (12.3):

$$\mathbf{B}_\kappa^\alpha = S_\kappa^\alpha \mathbf{u}_\kappa, \quad (12.6)$$

where \mathbf{S}_κ denotes the spin on bond \mathbf{u}_κ , and $\alpha = 1, 2, 3$ labels the spin components. The flux field on a site of the diamond lattice is defined as the sum of the fields on

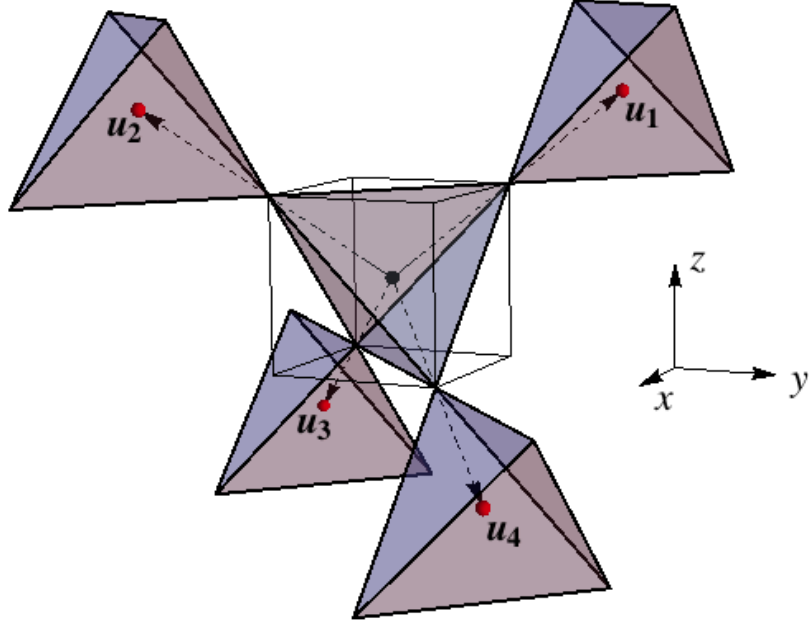


Figure 12.1: Geometry of the pyrochlore lattice. The centers of the up and down tetrahedra define the two sublattices of the diamond lattice, denoted by black and red dots. The pyrochlore lattice sites lie at the vertices of the tetrahedra. The vectors \mathbf{u}_κ define the bond vectors of diamond.

the four tetrahedral bonds emerging from that site,

$$\mathbf{B}^\alpha(\mathbf{R}) = \sum_{\kappa=1}^4 S_\kappa^\alpha(\mathbf{R}) \mathbf{u}_\kappa, \quad (12.7)$$

where \mathbf{R} is a diamond lattice vector, and κ sums over the four tetrahedral sites (on pyrochlore) surrounding the diamond site (tetrahedron center). The mapping from spin to flux variables is invertible (see Appendix).

From our definition of the Potts spins, (12.3), we see that in any ground state, for each spin component S^α , we have two “incoming” (+1) and two “outgoing” (−1) spins on each tetrahedron, i.e. each tetrahedron obeys a two-in, two-out ‘ice rule’ for each spin component. It follows from this, and our definition of the flux fields, that the local Potts constraint maps to a zero-divergence condition for each of the \mathbf{B}^α fields, $\nabla \cdot \mathbf{B}^\alpha = 0$. In an electrodynamic representation it is appropriate to refer to these flux fields as ‘magnetic’ fields and then their sources will be monopoles—this is

the nomenclature that is natural in the context of spin ice and is the one we will use here¹.

Naively, the problem just looks like three copies of spin ice, one for each spin component. Of course, the three components are not independent and therefore we might expect some correlation between the three magnetic fields. However, we will see shortly that our naive expectation is justified: at long distances, these cross-correlations vanish and the physics is described by three independent divergence-free ‘Maxwell’ fields.

12.3.2 Coarse-grained Free Energy and Correlations

Thus far, we have given a characterization of the ground state manifold in terms of divergence-free configurations of three magnetic fields. However, in order to compute correlations in the limit $T \rightarrow 0$, we need a more workable description of the ground state manifold which we will now obtain by coarse graining.

Let us consider one of the three magnetic fields, say \mathbf{B}^1 . If we were to flip the direction of flux on one of the “in” bonds at a diamond site (say by switching spins S_A and S_B), the zero divergence condition would require us to also flip the direction of an “out” bond at the site. We can continue flipping spins in such fashion until we get either a closed loop of S_A, S_B spins, or a string of S_A, S_B spins that extends across the entire system (for finite systems, the latter eventually closes through periodic boundary conditions). Flipping spins that lie on closed loops leaves the net magnetic flux through the system unchanged, while flipping spins on spanning strings changes the net flux threading the system. Since the average flux contributed by a closed loop is zero, systems with large numbers of closed “flippable” loops will have a small net \mathbf{B}^1 . On the other hand, a large and saturated net \mathbf{B}^1 requires the field on almost

¹Alternatively we could just as well refer to them as electric fields, sources as electric charges and the constraint as Gauss’s law. This is more natural in thinking of quantum models where there is a natural identification with lattice gauge theories.

every site of the dual lattice to point in the same direction and therefore the number of flippable loops is small – an intuitive picture is that the only flippable loops in a saturated field configuration are those that span the system.

Thus far, we have only talked of lattice magnetic fields that live on the bonds of the pyrochlore. To derive long-wavelength properties, we need to define smoothly varying continuum fields. We do this by coarse-graining - the field $\tilde{\mathbf{B}}^\alpha(\mathbf{r})$ is defined as the average of the lattice fields \mathbf{B}^α in some neighborhood of \mathbf{r} that is much larger than the lattice spacing but much smaller than the system size. The discrete constraint naturally translates into a divergence-free constraint for the coarse-grained fields.

Microscopically, there are many more configurations consistent with a small net coarse-grained $\tilde{\mathbf{B}}^1$ rather than a large saturated $\tilde{\mathbf{B}}^1$; the same arguments obviously apply to all three magnetic fields. Therefore configurations with small average fields are entropically favored. To lowest order, the (entirely entropic) free energy as a function of the coarse-grained fields and consistent with symmetries can be written as

$$\begin{aligned} F_{tot}(\tilde{\mathbf{B}}^\alpha(\mathbf{r})) &= -TS \\ &= \frac{1}{2} \frac{\kappa T}{a} \int d^3r \left(|\tilde{\mathbf{B}}^1(\mathbf{r})|^2 + |\tilde{\mathbf{B}}^2(\mathbf{r})|^2 + |\tilde{\mathbf{B}}^3(\mathbf{r})|^2 \right) \end{aligned} \quad (12.8)$$

where we've inserted a factor of the lattice-spacing a to make the stiffness, κ , dimensionless. Since we are restricting our attention for the moment to ground state configurations, the coarse-grained fields still satisfy the zero-divergence constraint, $\nabla \cdot \tilde{\mathbf{B}}^\alpha = 0$. The free energy (12.8) coupled with the divergence-free constraint yields three copies of Maxwell electrodynamics in a standard fashion. Introducing three vector potentials \mathbf{A}^α to implement the constraints, we can rewrite the free energy as

$$F = \frac{1}{2} \frac{\kappa T}{a} \int d^3r \sum_{\alpha=1}^3 |\nabla \times \mathbf{A}^\alpha(\mathbf{r})|^2$$

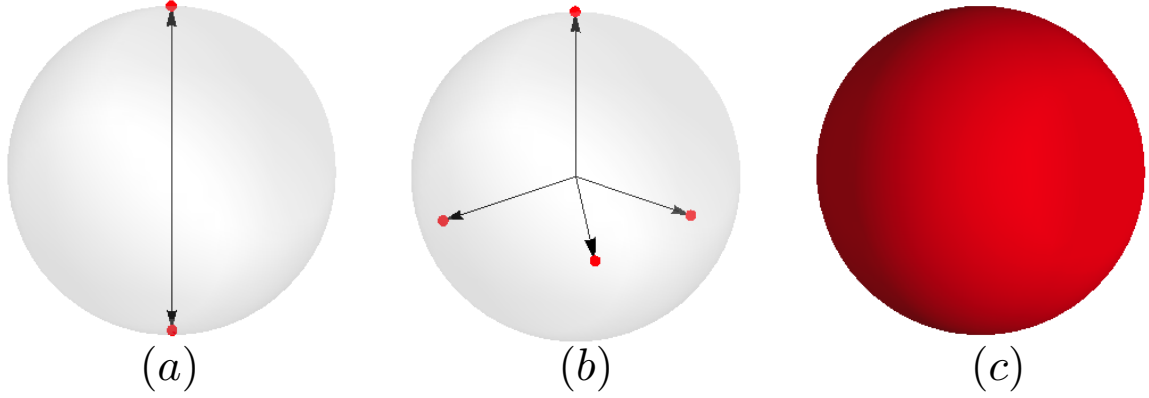


Figure 12.2: Spin space representation of Ising, Potts and Heisenberg spins (left to right). The red areas represent the accessible portions of spin space - Ising spins are confined to lie on only two points, 4-state Potts spins occupy only four points, and Heisenberg spins can lie anywhere on the sphere. While Ising spins only require a single gauge field for their description, Heisenberg spins require three such fields. Somewhat surprisingly Potts spins – which *a priori* would appear to have a much reduced symmetry compared to the Heisenberg case – also require three gauge fields.

We calculate the long distance correlators of the magnetic fields, and the result is the dipolar form typical for Coulomb phases

$$\begin{aligned}
 G_{ij}^{\alpha\beta}(\mathbf{r}) &\equiv \langle \tilde{B}_i^\alpha(\mathbf{r}) \tilde{B}_j^\beta(\mathbf{0}) \rangle \\
 &= \frac{a}{4\pi\kappa} \delta_{\alpha\beta} \frac{3r_i r_j - r^2 \delta_{ij}}{r^5}
 \end{aligned}
 \tag{12.9}$$

where i, j refer to the x, y, z components of each magnetic-field.

Finally, we reiterate that Ising spins, which occupy only two collinear points on a sphere in spin-space, require a single magnetic field \mathbf{B} to describe their Coulomb phase. Classical $O(3)$ spins can lie anywhere on a sphere, and they require three fields \mathbf{B}^1 , \mathbf{B}^2 and \mathbf{B}^3 for their description – one for each spin component. It is interesting that even though Potts spins are locked to just 4 points in spin space, they still require three magnetic fields for their complete description: the theory thus renormalizes at low temperatures to an effective $O(3)$ symmetry. Fig. 12.2 illustrates this idea.

12.3.3 Monte Carlo Simulations

In order to test our conjectured form (12.9) for the real-space correlation functions for the magnetic field, we turn now to a Monte Carlo study of the ground state manifold. We perform simulations on systems with $L \times L \times L$ unit cells with $L = 8, 16, 32$ and periodic boundary conditions; since there are 4 sites per pyrochlore unit cell, this corresponds to $4L^3$ spins. The simulations were performed using a standard “worm-update” algorithm. In each update step we first identify a closed “worm” of alternating spin flavors (for instance $AB \dots AB$), and then flip all the spins along the worm (i.e. interchange the spins $A \leftrightarrow B$). This move respects the Potts constraint since each bond in the worm is only part of a single tetrahedron, and exchanging spin-flavors on a bond still leaves a tetrahedron with all four Potts flavors. There are $\binom{4}{2} = 6$ types of worms, and the starting site for a worm and its type were chosen randomly for each update. It is instructive to think of this in the language of fluxes: interchanging A and B sites corresponds, via Eq. (12.3), to identifying a closed loop of type 1,2 and 3 fluxes and then reversing the first two of these. Reversing closed loops of fluxes clearly leaves the solenoidal constraints intact.

We simulate M independent Markov chains, each with N configurations along the chain (M and N were typically 100 and 10,000 respectively). To generate these, we begin with M independent “seed” ground state configurations and use the worm update described above to generate the states along the chain. To ensure that successive states along the chain were roughly independent, we perform several (~ 30) such worm updates before recording a new configuration which is then added to the chain.

In analyzing the data, we first obtain the average value of the correlation functions for each Markov chain, and then average these across all M chains. The error is estimated as the standard error of the single-chain averaged correlation function across the M independent chains.

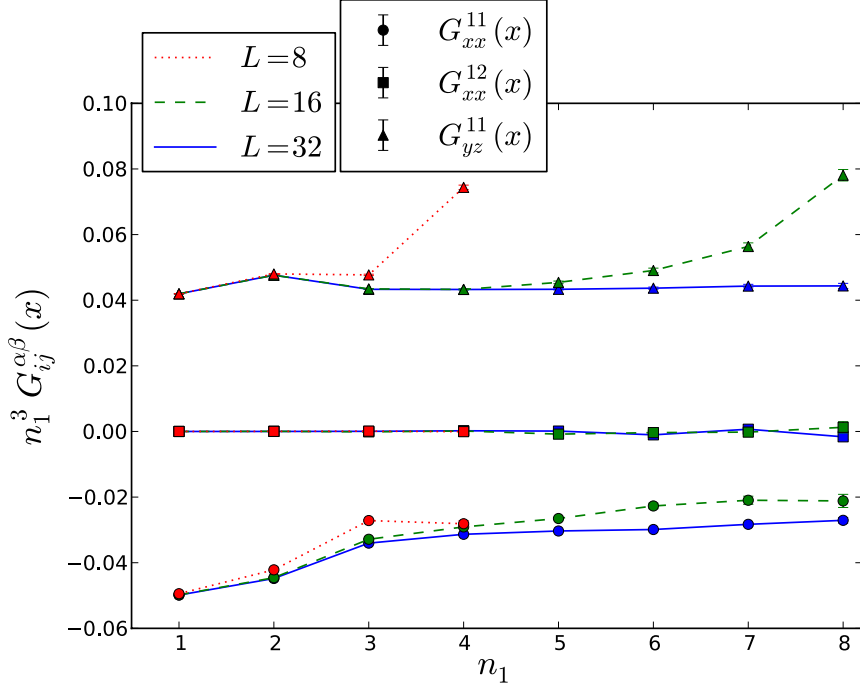


Figure 12.3: Monte Carlo data for three representative correlation functions $G_{xx}^{11}(\mathbf{r}_1)$, $G_{xx}^{12}(\mathbf{r}_1)$ and $G_{yz}^{11}(\mathbf{r}_1)$ in the direction $\mathbf{r}_1 = n_1(0, \frac{1}{2}, \frac{1}{2})$ for lattice sizes $L = 8, 16, 32$. The correlators are multiplied by the cube of the distance n_1^3 , and the horizontal trends are consistent with the expected dipolar form (12.9). All cross-correlators $G_{ij}^{\alpha\beta}$ for $\alpha \neq \beta$ vanish (only G_{xx}^{12} displayed) confirming the diagonal form for the free energy (12.8).

We compute the average correlation function $G_{ij}^{\alpha\beta}(\mathbf{r}) = \langle B_i^\alpha(\mathbf{x} + \mathbf{r}) B_j^\beta(\mathbf{x}) \rangle$ in two independent directions \mathbf{r} for all 36 combinations of α, β, i, j . The vectors \mathbf{r} were chosen as $\mathbf{r}_1 = n_1(0, \frac{1}{2}, \frac{1}{2})$ and $\mathbf{r}_2 = n_2(0, 0, 1)$ with $n_1, n_2 \in \mathbb{Z}$. These correspond to the fcc lattice vectors $\mathbf{r}_1 = n_1 \mathbf{a}_1$ and $\mathbf{r}_2 = n_2(\mathbf{a}_1 + \mathbf{a}_2 - \mathbf{a}_3)$ where the \mathbf{a}_i are fcc basis vectors with lattice constant $a = 1$.

The correlations fall off as $1/r^3$ consistent with the dipolar form (12.9). Figs. 12.3 and 12.4 show the representative correlators $G_{xx}^{11}(\mathbf{r})$, $G_{xy}^{11}(\mathbf{r})$, and $G_{xx}^{12}(\mathbf{r})$ multiplied by n_i^3 , in the two directions \mathbf{r}_1 and \mathbf{r}_2 . The agreement with the dipolar form is best in the regime $a \ll r \ll L$. The cross-correlators $G_{ij}^{\alpha\beta}(\mathbf{r})$ for $\alpha \neq \beta$ vanish in all directions for all i, j , confirming the diagonal form for the effective free energy (12.8).

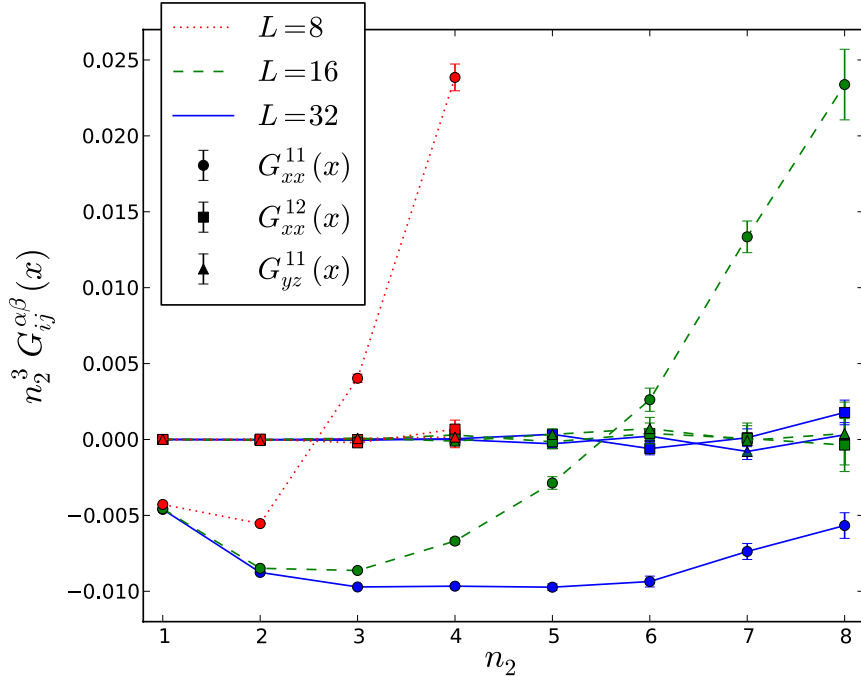


Figure 12.4: Monte Carlo data for three representative correlation functions $G_{xx}^{11}(\mathbf{r}_2)$, $G_{xx}^{12}(\mathbf{r}_2)$ and $G_{yz}^{11}(\mathbf{r}_2)$ in the direction $\mathbf{r}_2 = n_2(0,0,1)$ for lattice sizes $L = 8, 16, 32$. Once again, the correlators are multiplied by the cube of the distance n_2^3 , and the trends are consistent with the expected dipolar form (12.9). Note that the correlations are weaker in the direction \mathbf{r}_2 as compared to \mathbf{r}_1 because same values of n for the two cases correspond to larger physical distances r_2 .

We also checked that the ratios of correlations for different i, j asymptote to the values predicted by (12.9). For example, $G_{xx}^{11}/G_{zz}^{11} \rightarrow -2$ in the direction \mathbf{r}_1 .

Finally, we use correlation data to numerically estimate a value for the stiffness, κ/a through (12.9). Correlations in the direction \mathbf{r}_1 yielded an average stiffness $\kappa_1 = 7.38 \pm 0.46$, while correlations in the direction \mathbf{r}_2 gave $\kappa_2 = 8.13 \pm 0.93$; the values in the two directions are equal within the margins of error. The lattice constant a is set to unity.

12.4 Charges, defects and Dirac Strings

While the effective free energies for the Heisenberg and Potts models are the same, the two differ in the nature of their excitations. Excitations above the ground state

Potts manifold are gapped and quantized, with “bionic” defects that are charged under two of the three gauge fields.

In the ground states, each site of the dual diamond lattice has two incoming and two outgoing fluxes for each of the three magnetic fields. We can create defects by violating the zero-divergence constraint at a dilute set of points in the lattice. Such defects are “charged” under the different fields, with positive (negative) charges equal to the net outgoing (incoming) fluxes of each type at the defect. This is the usual charge in the sense of Gauss’s law: each such charge represents a source of magnetic flux, and a violation of the divergence-free constraint for at least one of the fields.

It is convenient to first catalog defects in the Potts language: a defect arises when the four spins surrounding a dual lattice site violate the Potts rule. The simplest defects are those in which one spin flavor is repeated on a tetrahedron; for instance, we can have a defect tetrahedron with spins S_B, S_B, S_C and S_D . There are twelve such defect tetrahedrons: we have four choices for the spin flavor that gets repeated (S_B in our example), and three choices for the flavor that the repeated spin replaces (S_A in the example).

Each of these defects have different charges under the three gauge fields. Looking at the spins in (12.3), we see that an “up” tetrahedron with S_B, S_B, S_C, S_D has spin components $S^x = (1, 1, -1, 1)$, $S^y = (-1, -1, -1, 1)$ and $S^z = (1, 1, -1, -1)$. Thus, its charges under the three magnetic fields \mathbf{B}^1 , \mathbf{B}^2 and \mathbf{B}^3 are $Q_1 = +2$, $Q_2 = -2$ and $Q_3 = 0$ respectively. All twelve defects have a similar structure, in that they are doubly charged under two of the three magnetic fields – hence the name bions. Table 12.1 catalogues the charges of the different bions. (These charges are reversed for corresponding defects on “down” tetrahedra, since the sense of “in” and “out” flux is reversed). Figure 12.5 depicts the 12 possible bions in Q_1, Q_2, Q_3 space.

Charge conservation demands that the defects are always created in oppositely charged pairs. One way to do this is to imagine creating a pair of bions by exchanging

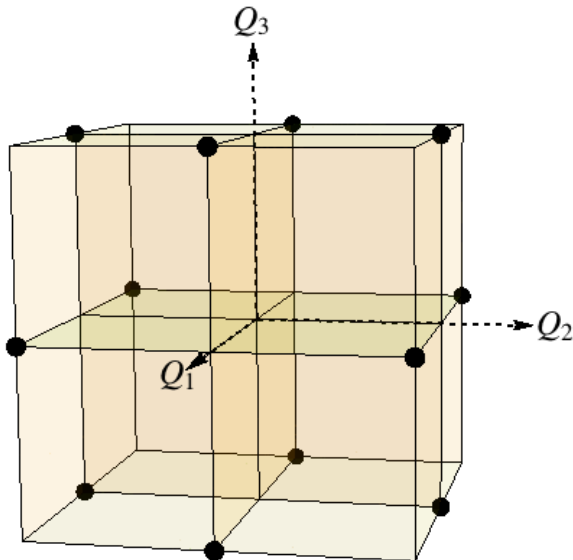


Figure 12.5: Charges of the twelve types of bions (black dots) shown in Q_1, Q_2, Q_3 space, where Q_i represents the charge under the field B^i . Each bion is charged under two gauge fields. The twelve charges naturally map to six oriented edges of a tetrahedron.

spins along a “Dirac string” containing two flavors of spin. For instance, we create a BBCD defect by replacing an A spin with a B spin on an “up” tetrahedron. This creates a second, oppositely charged defect on the adjoining “down” tetrahedron. The second defect can be moved away from the first by continually flipping a string of A, B type spins. The second defect is of type AACD when it lies on another “up” tetrahedron; we may verify that the tetrahedron AACD carries opposite charge $Q_1 = -2, Q_2 = +2$ and $Q_3 = 0$. We can think of the Dirac string as a flux tube carrying two flavors of flux (\mathbf{B}^1 and \mathbf{B}^2 in our example) that connects bions that are oppositely charged under two magnetic fields. Figure 12.6 shows a Dirac string connecting two bions.

Additionally, we can also imagine creating composite defects by adding two or more of the twelve fundamental bions. The composite charges form an fcc lattice which is a natural extension of Figure 12.5. There is an intuitive geometric picture for understanding the charge structure of the bions. The four spins point to the four corners of a tetrahedron in spin-space (and all spin-components sum to zero);

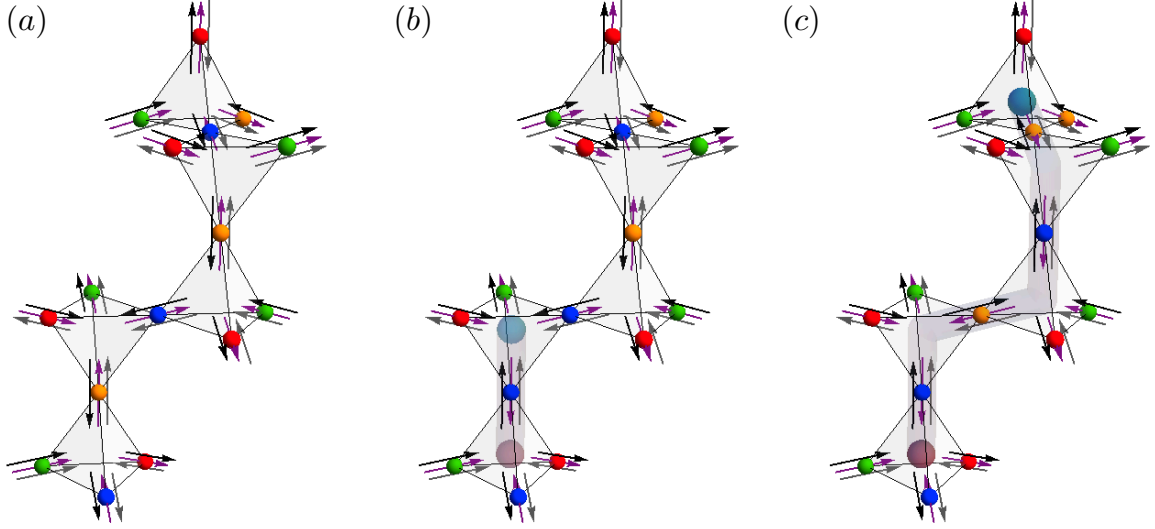


Figure 12.6: Dirac string connecting two bions. The colors orange , blue, green and red represent the spin flavors S_A, S_B, S_C and S_D respectively. The three arrows on each site represent the three magnetic fields B^1 (black), B^2 (purple), and B^3 (gray). (a) Ground state configuration of the 4-state Potts model with no defects. Each tetrahedron has all four spin flavors, and all three magnetic fields obey two-in-two-out rules at each tetrahedron. (b) Switching S_A (orange) to S_B (blue) on the bottom tetrahedron creates (BBCD) type bions on two adjoining tetrahedra (red and blue spheres). The magnetic fields are no longer divergence-free, and the bion on the up tetrahedron has charges $Q_1 = +2, Q_2 = -2, Q_3 = 0$ (opposite charges for the bion on the down tetrahedron). (c) The bions move apart by flipping a trail of S_A, S_B spins. The Dirac string acts as a flux tube carrying B^1 and B^2 type magnetic fluxes between the two bions.

replacing S_A with S_B to create a defect gives a vector of charges $\mathbf{Q} = -\mathbf{S}_A + \mathbf{S}_B$ under the different gauge fields. The charge \mathbf{Q} thus corresponds to an edge of the spin-space tetrahedron. In this way, all twelve fundamental bions can be mapped to six *oriented* edges of a tetrahedron in spin-space.

The bions act as sources of magnetic flux and experience a Coulomb force under each of the three magnetic fields. The origin of this force is purely entropic in nature. We imagine a finite number N_b of bions scattered throughout the lattice at positions $\mathbf{r}_1, \mathbf{r}_2, \dots, \mathbf{r}_{N_b}$. We can compute the partition function Z by integrating over all configurations of magnetic fields consistent with the distribution of bions. This gives the free energy of the sources in accordance with $Z/Z_0 = e^{-F_{int}/T}$, where Z_0 is

the partition-function in the absence of bions. Explicitly this yields:

$$\begin{aligned}
F_{int} &= \sum_{\substack{i=1 \\ j < i}}^{N_b} \frac{aT}{4\pi\kappa} \frac{(Q_1^i Q_1^j + Q_2^i Q_2^j + Q_3^i Q_3^j)}{|\mathbf{r}_i - \mathbf{r}_j|} \\
&+ \sum_{i=1}^{N_b} \alpha \frac{aT}{4\pi\kappa} \frac{(Q^i)^2}{a}
\end{aligned} \tag{12.10}$$

where i, j sum over all pairs of bions and Q_α^i represents the charge of the i th bion under the field \mathbf{B}^α . The first term in (12.10) represents the Coulomb interaction energy of pairs of bions separated by distance $|\mathbf{r}_i - \mathbf{r}_j|$, while the second term is the free energy of individual, isolated bions arising from self-interaction in the field theory. The self-interaction term has an ultraviolet ambiguity, represented by the unknown constant α , which (naturally) cannot be fixed by the coarse-grained free energy alone.

Also note that (12.10) predicts that the interaction energy between a pair of bions is sensitive to their type. For example, bions of type $AABC$ and $DDBC$ (equally and oppositely charged under \mathbf{B}_1 and \mathbf{B}_3) interact more strongly than say $AABC$ and $AABD$ which are charged under different gauge fields.

This is a good place to briefly comment on the finite-temperature properties of the Potts spins - in particular the form of the correlation function Eq. (12.9). We know that the dipolar form of the correlation function is derived from the divergence-free constraint on the magnetic fields. This constraint is exactly satisfied at $T = 0$ and gradually weakened as the temperature T is increased. Heuristically, we might expect the correlation to be dipolar up to some (temperature dependent) correlation length $\xi(T)$, and decay exponentially on length scales longer than ξ . It is easily seen [156] that for Ising spins, the creation energy of gapped ice-rule violating defects (monopoles) yields $\xi \sim e^{2J/3T}$. On the other hand, for Heisenberg spins the gapless excitations yield much softer violations of the divergence-free rule and, correspondingly, a much shorter finite-temperature correlation length given by [125] $\xi \sim 1/\sqrt{T}$.

For gapped Potts spins, the creation energy of a Bionic defect is $4J$ which gives $\xi(T) \sim e^{4J/3T}$; the gap to excitations helps preserve the dipolar form of the correlations to higher temperatures. As is typical, the gap also manifests itself in the exponential low-temperature decay of various thermodynamic quantities but these are not the focus of this chapter.

12.5 Worm length distributions

Coulomb phases come with a natural incipient loop structure—absent defects one can define closed lines of flux thanks to the underlying conservation laws. This makes the statistics of the loops worthy of interest. Indeed Jaubert, Haque and Moessner (JHM) [160] have studied loop statistics for the ground state manifold of spin ice and found a characteristic scaling of their probability distribution which they have related to the properties of random walks in three dimensions. This suggests that this scaling might be more generally associated with Coulomb phases and we will investigate and verify that possibility here.

Specifically, JHM have studied the distribution of worm lengths for spin ice which is easily done by keeping track of the worms used to update configurations in the Monte Carlo. As in our problem, worms in spin ice are closed strings of alternating spin flavors but now with the feature that while there is only one species of worm, at each step there is a binary choice that must be made randomly². For these JHM found a characteristic scaling for probability distribution of worm lengths $p(\ell)$,

$$p(\ell) = \frac{1}{L^3} f\left(\frac{\ell}{L^2}\right) \quad (12.11)$$

²Ref. [160] also studied closed loops of up and down spins alone but they have no analog in the 4-state Potts problem.

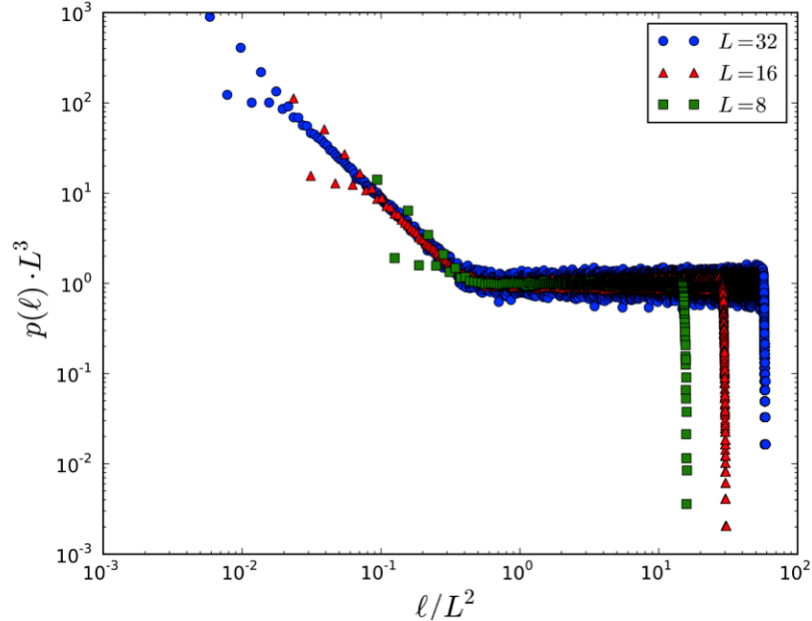


Figure 12.7: Probability distribution of worm-lengths ℓ for system-sizes $L = 8, 16, 32$. We clearly see two regimes – an $\ell^{-3/2}$ scaling for short loops, and an ℓ independent scaling for winding loops.

where ℓ refers to the worm length and L is the linear dimension of the system size. This scaling form unifies two populations of worms: short worms whose probability scales as $p(\ell) \sim \ell^{-3/2}$, and long winding worms (that close after spanning the system through periodic boundary conditions) for which $p(\ell) \sim L^{-3}$.

We have investigated analogous worm-length distributions in the Potts model. It should be noted that the Potts model has six species of worms (each worm has only two Potts spin flavors and $\binom{4}{2} = 6$). However, by symmetry, all six worm types have identical distributions in the Coulomb phase. Fig. 12.7 shows the worm-length distributions obtained for system sizes $L = 8, 16$, and 32 plotted in scaled variables. Leaving aside the deviations at very small and very large loops sizes we see that that the loop distribution indeed obeys the scaling form (12.11) which is then independent evidence that the Potts model is in a Coulomb phase. We direct the reader to Ref. [160] for a rationalization of this scaling in terms of the properties of random walks.

12.6 Concluding Remarks

To summarize, we have shown that the classical antiferromagnetic four-state Potts model on the pyrochlore lattice is in a Coulomb phase described by three emergent gauge fields as $T \rightarrow 0$. It is instructive to view the Potts model as arising from a symmetry breaking potential that restricts $O(3)$ spins to just four points in spin space. Nevertheless, we have shown that the long-wavelength effective free energies of the $O(3)$ and Potts models are identical.

An important point of difference between the Heisenberg and Potts models lies in the nature of excitations above the ground state manifold. While the Heisenberg model involves gapless excitations, the Potts model has gapped excitations with a novel charge structure. We find twelve types of “bionic” defects, each charged under two of the three gauge fields. The charges are deconfined and can be connected by “worm-like” flux tubes of alternating spin flavor. We computed probability distributions for lengths of closed worms, and found scaling laws in accordance with previous diagnostics of the Coulomb phase.

The evident next step in this program is to incorporate quantum dynamics in a quantum Potts model exhibiting a Rokhsar-Kivelson point.

12.A Spin-Spin Correlation Functions

It is useful to have a reference for converting the flux-field correlation functions (12.9) to spin-spin correlation functions for the Potts spins living on the four sublattices of pyrochlore. We have three flux fields $\mathbf{B}^1, \mathbf{B}^2, \mathbf{B}^3$ each with three components, for a total of nine flux components; these are labeled B_i^α for $\alpha = 1, 2, 3$ and $i = x, y, z$ in (12.9). On the other hand we have four Potts spins on every diamond site, each with three components, for a total of twelve spin components; we label these S_κ^α for $\alpha = 1, 2, 3$ and $\kappa = 1, 2, 3, 4$. However, the constraint equations on the Potts

spins (12.2) ensure that there are only nine *independent* spin components, thereby permitting an invertible mapping from flux-fields to spins.

As an example, we use the definitions of the flux fields on the diamond sites (12.7) and the definitions of the bond vectors \mathbf{u}_κ (12.5), to explicitly write the x, y, z components of

$$\mathbf{B}^1(\mathbf{r}) = S_1^x(\mathbf{r})\mathbf{u}_1 + S_2^x(\mathbf{r})\mathbf{u}_2 + S_3^x(\mathbf{r})\mathbf{u}_3 + S_4^x(\mathbf{r})\mathbf{u}_4$$

as

$$\begin{aligned} B_x^1 &= \frac{1}{4}(-S_1^x + S_2^x - S_3^x + S_4^x) \\ B_y^1 &= \frac{1}{4}(S_1^x - S_2^x - S_3^x + S_4^x) \\ B_z^1 &= \frac{1}{4}(S_1^x + S_2^x - S_3^x - S_4^x) \end{aligned}$$

where we have dropped the explicit dependence on \mathbf{r} to simplify our notation. Finally we impose the spin constraint equations (12.2) to eliminate S_4^α and we get

$$\begin{aligned} B_x^1 &= \frac{1}{2}(-S_1^x - S_3^x) \\ B_y^1 &= \frac{1}{2}(-S_2^x - S_3^x) \\ B_z^1 &= \frac{1}{2}(S_1^x + S_2^x). \end{aligned}$$

A similar exercise can be carried out for the \mathbf{B}^2 and \mathbf{B}^3 spins to give the following matrix of transformations:

$$\begin{pmatrix} B_x^1 \\ B_y^1 \\ B_z^1 \\ B_x^2 \\ B_y^2 \\ B_z^2 \\ B_x^3 \\ B_y^3 \\ B_z^3 \end{pmatrix} = \begin{pmatrix} -\frac{1}{2} & 0 & 0 & 0 & 0 & 0 & -\frac{1}{2} & 0 & 0 \\ 0 & 0 & 0 & -\frac{1}{2} & 0 & 0 & -\frac{1}{2} & 0 & 0 \\ \frac{1}{2} & 0 & 0 & \frac{1}{2} & 0 & 0 & 0 & 0 & 0 \\ 0 & -\frac{1}{2} & 0 & 0 & 0 & 0 & 0 & -\frac{1}{2} & 0 \\ 0 & 0 & 0 & 0 & -\frac{1}{2} & 0 & 0 & -\frac{1}{2} & 0 \\ 0 & \frac{1}{2} & 0 & 0 & \frac{1}{2} & 0 & 0 & 0 & 0 \\ 0 & 0 & -\frac{1}{2} & 0 & 0 & 0 & 0 & 0 & -\frac{1}{2} \\ 0 & 0 & 0 & 0 & 0 & -\frac{1}{2} & 0 & 0 & -\frac{1}{2} \\ 0 & 0 & \frac{1}{2} & 0 & 0 & \frac{1}{2} & 0 & 0 & 0 \end{pmatrix} \begin{pmatrix} S_1^x \\ S_1^y \\ S_1^z \\ S_2^x \\ S_2^y \\ S_2^z \\ S_3^x \\ S_3^y \\ S_3^z \end{pmatrix}$$

We can invert the relation above to obtain the spins in terms of the flux fields as follows:

$$\begin{pmatrix} S_1^x \\ S_1^y \\ S_1^z \\ S_2^x \\ S_2^y \\ S_2^z \\ S_3^x \\ S_3^y \\ S_3^z \end{pmatrix} = \begin{pmatrix} -1 & 1 & 1 & 0 & 0 & 0 & 0 & 0 & 0 \\ 0 & 0 & 0 & -1 & 1 & 1 & 0 & 0 & 0 \\ 0 & 0 & 0 & 0 & 0 & 0 & -1 & 1 & 1 \\ 1 & -1 & 1 & 0 & 0 & 0 & 0 & 0 & 0 \\ 0 & 0 & 0 & 1 & -1 & 1 & 0 & 0 & 0 \\ 0 & 0 & 0 & 0 & 0 & 0 & 1 & -1 & 1 \\ -1 & -1 & -1 & 0 & 0 & 0 & 0 & 0 & 0 \\ 0 & 0 & 0 & -1 & -1 & -1 & 0 & 0 & 0 \\ 0 & 0 & 0 & 0 & 0 & 0 & -1 & -1 & -1 \end{pmatrix} \begin{pmatrix} B_x^1 \\ B_y^1 \\ B_z^1 \\ B_x^2 \\ B_y^2 \\ B_z^2 \\ B_x^3 \\ B_y^3 \\ B_z^3 \end{pmatrix}$$

These relations allow us to express spin-spin correlation functions as simple linear combinations of the B_i^α correlations.

12.B Symmetries and Stability of the Free Energy

We have claimed in the bulk of the chapter that the long-wavelength coarse-grained free energy is insensitive to breaking Heisenberg ($O(3)$) symmetry down to a Potts symmetry. In this section, we formalize this claim using a renormalization-group argument. We will show that the lowest order terms that can be added to the free energy (and are allowed by symmetry considerations) are irrelevant in an RG sense.

Consider a given ground state configuration of Potts spins on the pyrochlore lattice. Permuting the spins (say by exchanging spins of type S_A and S_B on every tetrahedron) gives another ground state configuration. Each such “internal” symmetry of the microscopic spin degrees of freedom should translate into a symmetry of the coarse-grained $\tilde{\mathbf{B}}$ fields³ in accordance with Appendix A. In fact, six permutation group elements are required to generate all $4! = 24$ permutations of the Potts spins; these map to the following symmetries of the free energy:

$$\begin{aligned}
 f(\tilde{\mathbf{B}}_1, \tilde{\mathbf{B}}_2, \tilde{\mathbf{B}}_3) &= f(\tilde{\mathbf{B}}_2, \tilde{\mathbf{B}}_1, \tilde{\mathbf{B}}_3) \\
 &= f(\tilde{\mathbf{B}}_3, \tilde{\mathbf{B}}_2, \tilde{\mathbf{B}}_1) \\
 &= f(\tilde{\mathbf{B}}_1, \tilde{\mathbf{B}}_3, \tilde{\mathbf{B}}_2) \\
 &= f(-\tilde{\mathbf{B}}_1, -\tilde{\mathbf{B}}_2, \tilde{\mathbf{B}}_3) \\
 &= f(-\tilde{\mathbf{B}}_1, \tilde{\mathbf{B}}_2, -\tilde{\mathbf{B}}_3) \\
 &= f(\tilde{\mathbf{B}}_1, -\tilde{\mathbf{B}}_2, -\tilde{\mathbf{B}}_3)
 \end{aligned} \tag{12.12}$$

An example best illustrates how one arrives at the symmetries in Eq. (12.12). A given tetrahedron has magnetic fields defined by

$$\begin{aligned}
 \mathbf{B}_1 &= S_A^x \mathbf{u}_a + S_B^x \mathbf{u}_b + S_C^x \mathbf{u}_c + S_D^x \mathbf{u}_d \\
 &= -\mathbf{u}_a + \mathbf{u}_b - \mathbf{u}_c + \mathbf{u}_d
 \end{aligned}$$

³We choose a coarse-graining procedure that respects the microscopic symmetries.

$$\begin{aligned}
\mathbf{B}_2 &= S_A^y \mathbf{u}_a + S_B^y \mathbf{u}_b + S_C^y \mathbf{u}_c + S_D^y \mathbf{u}_d \\
&= +\mathbf{u}_a - \mathbf{u}_b - \mathbf{u}_c + \mathbf{u}_d
\end{aligned}$$

$$\begin{aligned}
\mathbf{B}_3 &= S_A^z \mathbf{u}_a + S_B^z \mathbf{u}_b + S_C^z \mathbf{u}_c + S_D^z \mathbf{u}_d \\
&= +\mathbf{u}_a + \mathbf{u}_b - \mathbf{u}_c - \mathbf{u}_d
\end{aligned}$$

where $\{a, b, c, d\} \in \text{Permutation}\{1, 2, 3, 4\}$ label the \mathbf{u} sublattice vectors on which the spins $\{S_A, S_B, S_C, S_D\}$ live. Then, exchanging spins S_A and S_B leads to the modified fields

$$\begin{aligned}
\mathbf{B}'_1 &= S_B^x \mathbf{u}_a + S_A^x \mathbf{u}_b + S_C^x \mathbf{u}_c + S_D^x \mathbf{u}_d \\
&= +\mathbf{u}_a - \mathbf{u}_b - \mathbf{u}_c + \mathbf{u}_d \\
&= \mathbf{B}_2
\end{aligned}$$

$$\begin{aligned}
\mathbf{B}'_2 &= S_B^y \mathbf{u}_a + S_A^y \mathbf{u}_b + S_C^y \mathbf{u}_c + S_D^y \mathbf{u}_d \\
&= -\mathbf{u}_a + \mathbf{u}_b - \mathbf{u}_c + \mathbf{u}_d \\
&= \mathbf{B}_1
\end{aligned}$$

$$\begin{aligned}
\mathbf{B}'_3 &= S_B^z \mathbf{u}_a + S_A^z \mathbf{u}_b + S_C^z \mathbf{u}_c + S_D^z \mathbf{u}_d \\
&= +\mathbf{u}_a + \mathbf{u}_b - \mathbf{u}_c - \mathbf{u}_d \\
&= \mathbf{B}_3
\end{aligned}$$

with \mathbf{B}_1 and \mathbf{B}_2 exchanged. The same analysis carries through for all tetrahedra, and exchanging S_A and S_B everywhere on the lattice is equivalent to exchanging

the coarse grained fields $\tilde{\mathbf{B}}_1$ and $\tilde{\mathbf{B}}_2$. This gives the first of the symmetries listed in Eq. (12.12); the others can be derived in an analogous manner.

Let us pause to consider the implications of Eq. (12.12). The first three equations require a symmetry under exchanging any of the \mathbf{B}_α fields; this justifies having the same coefficient in front of all three quadratic, diagonal terms in the free energy Eq. (12.8). The last three equations forbid quadratic terms that are off-diagonal in the fields. For example, a term like $\tilde{\mathbf{B}}_1\tilde{\mathbf{B}}_2$ is not a symmetry under $\{\tilde{\mathbf{B}}_1, \tilde{\mathbf{B}}_2, \tilde{\mathbf{B}}_3\} \rightarrow \{-\tilde{\mathbf{B}}_1, \tilde{\mathbf{B}}_2, -\tilde{\mathbf{B}}_3\}$. At this point quadratic terms like $\tilde{B}_1^x\tilde{B}_1^y$ can still be added, though we will soon show that these are forbidden by spatial symmetries.

Having considered transformations of the “internal” spin degrees of freedom, we now turn to lattice transformations. The space group $Fd\bar{3}m$ of the pyrochlore lattice consists of the 24 element tetrahedral point group $\bar{4}3m$ and a further 24 nonsymmorphic elements, involving a combination of rotations or reflections with translation by half a lattice vector. For the pyrochlore dressed with Potts spins, the space group elements transform one ground state configuration into another.

The \mathbf{B}_α , are lattice vector fields whose transformation under the space group elements (like rotations R) derives from the transformation of the lattice bond vectors \mathbf{u} . For example, the field \mathbf{B}_1 transforms as:

$$\begin{aligned} \mathbf{B}_1^i(\mathbf{r}) &= \sum_{\kappa=1}^4 S_\kappa^x(\mathbf{r})\mathbf{u}_\kappa^i \\ &\rightarrow \sum_{\kappa=1}^4 S_\kappa^x(R\mathbf{r})R^{ij}\mathbf{u}_\kappa^j \\ &\equiv R^{ij}\mathbf{B}_1^j(R\mathbf{r}). \end{aligned}$$

Since the free energy involves an integral over all space, the change in the spatial location of the fields ($\mathbf{r} \rightarrow R\mathbf{r}$) can be undone by a simple change of integration variables; what matters is the transformation of the vector indices of the fields. Microscopically, the transformation of the vector indices derives entirely from a permutation of sub-

lattice indices i.e. a spin belonging to sublattice 1 of a tetrahedron at location \mathbf{r} gets rotated to, say, sublattice 3 of the tetrahedron at location $R\mathbf{r}$. In this way, all we're concerned about is the action of the space group elements in permuting sublattice indices. The $4!$ permutations of the sublattice indices lead to the additional symmetries:

$$\begin{aligned}
f(B_\alpha^x, B_\alpha^y, B_\alpha^z) &= f(B_\alpha^y, B_\alpha^x, B_\alpha^z) \\
&= f(B_\alpha^z, B_\alpha^y, B_\alpha^x) \\
&= f(B_\alpha^x, B_\alpha^z, B_\alpha^y) \\
&= f(-B_\alpha^x, -B_\alpha^y, B_\alpha^z) \\
&= f(-B_\alpha^x, B_\alpha^y, -B_\alpha^z) \\
&= f(B_\alpha^x, -B_\alpha^y, -B_\alpha^z)
\end{aligned} \tag{12.13}$$

where $\alpha = 1, 2, 3$ labels the type of magnetic field and we have used a compressed notation to label the nine arguments of the free energy function.

We should emphasize that permuting sublattices is very different from permuting spins. In the latter case, we exchange spins of types S_A and S_B regardless of the sublattices on which they lie; in the former, we exchange the spins living on sublattice 1 and 2 regardless of their type. As shown by Eqs. (12.12), (12.13), exchanging spins leads to symmetries under exchanging different *types* of \mathbf{B} fields, while exchanging sublattices leads to symmetries under exchanging different spatial *components* of a given type of field.

As before, let us consider an example to understand the symmetries listed in Eq. (12.13). Fix the center of one tetrahedron as the origin and rotate the lattice by π about the axis $(0, 0, z)$. (This is the C_z element of the tetrahedral point group). This axis bisects the edges $\mathbf{u}_{12} \equiv (\mathbf{u}_1 - \mathbf{u}_2)$ and \mathbf{u}_{34} of the tetrahedron at the origin. The rotation by π does a dual exchange of sublattice indices $1 \rightleftharpoons 2$ and $3 \rightleftharpoons 4$ on each

tetrahedron (in addition to rotating the tetrahedron's center). A given tetrahedron has \mathbf{B}_1 fields defined by

$$\begin{aligned} B_1^x &= S_1^x u_1^x + S_2^x u_2^x + S_3^x u_3^x + S_4^x u_4^x \\ &= 0.25(-S_1^x + S_2^x - S_3^x + S_4^x) \end{aligned}$$

$$\begin{aligned} B_1^y &= S_1^x u_1^y + S_2^x u_2^y + S_3^x u_3^y + S_4^x u_4^y \\ &= 0.25(S_1^x - S_2^x - S_3^x + S_4^x) \end{aligned}$$

$$\begin{aligned} B_1^z &= S_1^x u_1^z + S_2^x u_2^z + S_3^x u_3^z + S_4^x u_4^z \\ &= 0.25(S_1^x + S_2^x - S_3^x - S_4^x) \end{aligned}$$

where $\{S_1, S_2, S_3, S_4\}$ are the spins living on sublattices $\{\mathbf{u}_1, \mathbf{u}_2, \mathbf{u}_3, \mathbf{u}_4\}$ respectively as in Appendix A. Now, exchange $\mathbf{u}_1 \rightleftharpoons \mathbf{u}_2$ and $\mathbf{u}_3 \rightleftharpoons \mathbf{u}_4$. The transformed field equations are:

$$\begin{aligned} (B_1^x)' &= S_1^x u_2^x + S_2^x u_1^x + S_3^x u_4^x + S_4^x u_3^x \\ &= 0.25(+S_1^x - S_2^x + S_3^x - S_4^x) \\ &= -B_1^x \end{aligned}$$

$$\begin{aligned} (B_1^y)' &= S_1^x u_2^y + S_2^x u_1^y + S_3^x u_4^y + S_4^x u_3^y \\ &= 0.25(-S_1^x + S_2^x + S_3^x - S_4^x) \\ &= -B_1^y \end{aligned}$$

$$\begin{aligned}
(B_1^z)' &= S_1^x u_2^z + S_2^x u_1^z + S_3^x u_4^z + S_4^x u_3^z \\
&= 0.25(S_1^x + S_2^x - S_3^x - S_4^x) \\
&= B_1^z.
\end{aligned}$$

The transformation has flipped the sign of the first two components of \mathbf{B}_1 corresponding to the fourth symmetry in Eq. (12.13). Of course, exactly the same transformations carry through for \mathbf{B}_2 and \mathbf{B}_3 . Also note that in 3D, the matrix for rotating by π about the z axis looks like

$$R_\pi^z = \begin{pmatrix} -1 & 0 & 0 \\ 0 & -1 & 0 \\ 0 & 0 & 1 \end{pmatrix}$$

whose action is also to flip the first two vector indices of the fields it acts on.

Finally, armed with the symmetries in Eqs. (12.12), (12.13) it is easy to see that the simplest terms we can add to the quadratic free energy defined in Eq. (12.8) are *cubic* in the fields, and symmetric with respect to exchanging the types of fields and the x, y, z components of each field:

$$F = F_{quad} + \int d^3r (B_x^1 B_y^2 B_z^3 + B_y^1 B_x^2 B_z^3 + \text{permutations}). \quad (12.14)$$

The added terms are cubic in the gradient of the vector potential and thus irrelevant under a renormalization-group analysis for determining the long-wavelength correlations of the fields. This confirms the stability of the quadratic, diagonal free energy used in the bulk of our analysis. In future work, it would be interesting to explicitly derive the perturbative corrections to the correlations stemming from Eq. (12.14).

| Type of Defect | Charges and Flux Lines | |
|----------------|---------------------------------------|---|
| A A B C | $Q_1 = -2$ $Q_2 = 0$ $Q_3 = +2$ | } Connected by a Dirac string of type A D |
| D D B C | $Q_1 = +2$ $Q_2 = 0$ $Q_3 = -2$ | |
| A A B D | $Q_1 = 0$ $Q_2 = +2$ $Q_3 = +2$ | } Connected by a Dirac string of type A C |
| C C B D | $Q_1 = 0$ $Q_2 = -2$ $Q_3 = -2$ | |
| A A C D | $Q_1 = -2$ $Q_2 = +2$ $Q_3 = 0$ | } Connected by a Dirac string of type A B |
| B B C D | $Q_1 = +2$ $Q_2 = -2$ $Q_3 = 0$ | |
| B B A C | $Q_1 = 0$ $Q_2 = -2$ $Q_3 = +2$ | } Connected by a Dirac string of type B D |
| D D A C | $Q_1 = 0$ $Q_2 = +2$ $Q_3 = -2$ | |
| B B A D | $Q_1 = +2$ $Q_2 = 0$ $Q_3 = +2$ | } Connected by a Dirac string of type B C |
| C C A D | $Q_1 = -2$ $Q_2 = 0$ $Q_3 = -2$ | |
| C C A B | $Q_1 = -2$ $Q_2 = -2$ $Q_3 = 0$ | } Connected by a Dirac string of type C D |
| D D A B | $Q_1 = +2$ $Q_2 = +2$ $Q_3 = 0$ | |

Table 12.1: Catalog of defects and charges. Each defect is charged under two gauge fields - hence they are called bions.

Bibliography

- [1] High-dimensional generalizations of the kagomé and diamond crystals and the decorrelation principle for periodic sphere packings. *J. Stat. Mech.: Theory and Expt.*, 2011(10):P10017, 2011.
- [2] D. Abanin, W. De Roeck, and F. Huveneers. A theory of many-body localization in periodically driven systems. *arXiv preprint arXiv:1412.4752*, 2014.
- [3] D. A. Abanin, W. De Roeck, and W. W. Ho. Effective Hamiltonians, prethermalization and slow energy absorption in periodically driven many-body systems. *ArXiv e-prints*, Oct. 2015, e-print arXiv:1510.03405.
- [4] R. Abou-Chacra, D. J. Thouless, and P. W. Anderson. A selfconsistent theory of localization. *Journal of Physics C: Solid State Physics*, 6(10):1734, 1973.
- [5] E. Abrahams, P. W. Anderson, D. C. Licciardello, and T. V. Ramakrishnan. Scaling theory of localization: Absence of quantum diffusion in two dimensions. *Phys. Rev. Lett.*, 42:673–676, Mar 1979.
- [6] I. Affleck, T. Kennedy, E. H. Lieb, and H. Tasaki. Rigorous results on valence-bond ground states in antiferromagnets. *Physical Review Letters*, 59(7):799–802, Aug. 1987.
- [7] I. Affleck, T. Kennedy, E. H. Lieb, and H. Tasaki. Valence bond ground-states in isotropic quantum antiferromagnets. *Communications in Mathematical Physics*, 115:477–528, 1988.
- [8] K. Agarwal, S. Gopalakrishnan, M. Knap, M. Müller, and E. Demler. Anomalous diffusion and griffiths effects near the many-body localization transition. *Physical review letters*, 114(16):160401, 2015.
- [9] V. Alba, M. Haque, and A. M. Läuchli. Entanglement spectrum of the heisenberg xxz chain near the ferromagnetic point. *Journal of Statistical Mechanics: Theory and Experiment*, 2012(08):P08011, 2012.
- [10] V. Alba, M. Haque, and A. M. Läuchli. Entanglement spectrum of the two-dimensional bose-hubbard model. *Phys. Rev. Lett.*, 110:260403, Jun 2013.

- [11] A. Altland and M. R. Zirnbauer. Nonstandard symmetry classes in mesoscopic normal-superconducting hybrid structures. *Physical Review B*, 55(2):1142, 1997.
- [12] B. Altshuler, H. Krovi, and J. Roland. Anderson localization makes adiabatic quantum optimization fail. *Proceedings of the National Academy of Sciences*, 107(28):12446–12450, 2010.
- [13] B. L. Altshuler, Y. Gefen, A. Kamenev, and L. S. Levitov. Quasiparticle lifetime in a finite system: A nonperturbative approach. *Phys. Rev. Lett.*, 78:2803–2806, Apr 1997.
- [14] L. Amico, R. Fazio, A. Osterloh, and V. Vedral. Entanglement in many-body systems. *Rev. Mod. Phys.*, 80:517–576, May 2008.
- [15] P. W. Anderson. Absence of diffusion in certain random lattices. *Phys. Rev.*, 109:1492–1505, Mar 1958.
- [16] P. W. Anderson. Infrared catastrophe in fermi gases with local scattering potentials. *Phys. Rev. Lett.*, 18:1049–1051, Jun 1967.
- [17] I. Arad, Z. Landau, and U. Vazirani. Improved one-dimensional area law for frustration-free systems. *Phys. Rev. B*, 85:195145, May 2012.
- [18] E. Ardonne, P. Fendley, and E. Fradkin. Topological order and conformal quantum critical points. *Annals of Physics*, 310(2):493 – 551, 2004.
- [19] D. P. Arovas, A. Auerbach, and F. D. M. Haldane. Extended Heisenberg models of antiferromagnetism: Analogies to the fractional quantum Hall effect. *Physical Review Letters*, 60(6):531–534, Feb. 1988.
- [20] A. Aspect, M. Inguscio, C. Müller, and D. Delande. Anderson localization. *Physics today*, 62:30–35, 2009.
- [21] Y. Y. Atas, E. Bogomolny, O. Giraud, and G. Roux. Distribution of the ratio of consecutive level spacings in random matrix ensembles. *Phys. Rev. Lett.*, 110:084101, Feb 2013.
- [22] S. Aubry and G. André. Analyticity breaking and anderson localization in incommensurate lattices. *Ann. Israel Phys. Soc*, 3(133):18, 1980.
- [23] M. Y. Azbel. Eigenstates and properties of random systems in one dimension at zero temperature. *Physical Review B*, 28(8):4106, 1983.
- [24] Y. Bahri, R. Vosk, E. Altman, and A. Vishwanath. Localization and topology protected quantum coherence at the edge of hot matter. *Nat Commun*, 6, July 2015.

- [25] J. H. Bardarson, F. Pollmann, and J. E. Moore. Unbounded growth of entanglement in models of many-body localization. *Phys. Rev. Lett.*, 109:017202, Jul 2012.
- [26] D. Basko. Weak chaos in the disordered nonlinear schrödinger chain: destruction of anderson localization by arnold diffusion. *Annals of Physics*, 326(7):1577–1655, 2011.
- [27] D. Basko, I. Aleiner, and B. Altshuler. Metalinsulator transition in a weakly interacting many-electron system with localized single-particle states. *Annals of Physics*, 321(5):1126 – 1205, 2006.
- [28] V. M. Bastidas, C. Emary, G. Schaller, and T. Brandes. Nonequilibrium quantum phase transitions in the ising model. *Phys. Rev. A*, 86:063627, Dec 2012.
- [29] B. Bauer and C. Nayak. Area laws in a many-body localized state and its implications for topological order. *Journal of Statistical Mechanics: Theory and Experiment*, 2013(09):P09005, 2013.
- [30] B. Bauer and C. Nayak. Analyzing many-body localization with a quantum computer. *Phys. Rev. X*, 4:041021, 2014.
- [31] R. J. Baxter. Colorings of a hexagonal lattice. *J. Math. Phys.*, 11(3):784–789, 1970.
- [32] C. Beenakker. Search for majorana fermions in superconductors. *Annual Review of Condensed Matter Physics*, 4(1):113–136, 2013.
- [33] E. Berg, E. G. Dalla Torre, T. Giamarchi, and E. Altman. Rise and fall of hidden string order of lattice bosons. *Physical Review B*, 77(24):245119, 2008.
- [34] W. Beugeling, R. Moessner, and M. Haque. Finite-size scaling of eigenstate thermalization. *Phys. Rev. E*, 89:042112, Apr 2014.
- [35] J. Billy, V. Josse, Z. Zuo, A. Bernard, B. Hambrecht, P. Lugan, D. Clément, L. Sanchez-Palencia, P. Bouyer, and A. Aspect. Direct observation of anderson localization of matter waves in a controlled disorder. *Nature*, 453(7197):891–894, 2008.
- [36] G. Biroli, L. F. Cugliandolo, and A. Sicilia. Kibble-zurek mechanism and infinitely slow annealing through critical points. *Phys. Rev. E*, 81:050101, May 2010.
- [37] S. Blanes, F. Casas, J. Oteo, and J. Ros. The magnus expansion and some of its applications. *Physics Reports*, 470(5):151–238, 2009.
- [38] K. Y. Bliokh, Y. P. Bliokh, V. Freilikher, A. Z. Genack, and P. Sebbah. Coupling and level repulsion in the localized regime: From isolated to quasiextended modes. *Phys. Rev. Lett.*, 101:133901, Sep 2008.

- [39] O. Bohigas, M. J. Giannoni, and C. Schmit. Characterization of chaotic quantum spectra and universality of level fluctuation laws. *Phys. Rev. Lett.*, 52:1–4, Jan 1984.
- [40] P. Bonderson. PhD thesis, Caltech, 2007.
- [41] P. Bonderson, M. Freedman, and C. Nayak. Measurement-only topological quantum computation. *Physical review letters*, 101(1):010501, 2008.
- [42] P. Bordia, H. P. Lüschen, S. S. Hodgman, M. Schreiber, I. Bloch, and U. Schneider. Coupling identical one-dimensional many-body localized systems. *Phys. Rev. Lett.*, 116:140401, Apr 2016.
- [43] A. Bray. Theory of phase-ordering kinetics. *Advances in Physics*, 43(3):357–459, 1994.
- [44] N. Bray-Ali, L. Ding, and S. Haas. Topological order in paired states of fermions in two dimensions with breaking of parity and time-reversal symmetries. *Phys. Rev. B*, 80:180504, Nov 2009.
- [45] M. Bukov, L. D’Alessio, and A. Polkovnikov. Universal high-frequency behavior of periodically driven systems: from dynamical stabilization to floquet engineering. *Advances in Physics*, 64(2):139–226, 2015.
- [46] M. Bukov, S. Gopalakrishnan, M. Knap, and E. Demler. Prethermal floquet steady states and instabilities in the periodically driven, weakly interacting bose-hubbard model. *Phys. Rev. Lett.*, 115:205301, Nov 2015.
- [47] M. Bukov, M. Heyl, D. A. Huse, and A. Polkovnikov. Heating and many-body resonances in a periodically driven two-band system. *Phys. Rev. B*, 93:155132, Apr 2016.
- [48] F. J. Burnell and S. Simon. Space-time geometry of topological phases. *Annals of physics*, 325(11):2550–2593, Nov. 2010.
- [49] F. J. Burnell, S. H. Simon, and J. K. Slingerland. Condensation of achiral simple currents in topological lattice models: Hamiltonian study of topological symmetry breaking. *Phys. Rev. B*, 84:125434, Sep 2011.
- [50] F. J. Burnell, S. H. Simon, and J. K. Slingerland. Phase transitions in topological lattice models via topological symmetry breaking. *New Journal of Physics*, 14(1):015004, 2012.
- [51] P. Calabrese and A. Lefevre. Entanglement spectrum in one-dimensional systems. *Phys. Rev. A*, 78(3):032329, Sep 2008.
- [52] J. Cano, M. Cheng, M. Mulligan, C. Nayak, E. Plamadeala, and J. Yard. Bulk-edge correspondence in $(2 + 1)$ -dimensional abelian topological phases. *Phys. Rev. B*, 89:115116, Mar 2014.

- [53] E. Canovi, M. Kollar, and M. Eckstein. Stroboscopic prethermalization in weakly interacting periodically driven systems. *Phys. Rev. E*, 93:012130, Jan 2016.
- [54] A. C. Cassidy, C. W. Clark, and M. Rigol. Generalized thermalization in an integrable lattice system. *Phys. Rev. Lett.*, 106:140405, Apr 2011.
- [55] C. Castelnovo, C. Chamon, C. Mudry, and P. Pujol. From quantum mechanics to classical statistical physics: Generalized rokhsar–kivelson hamiltonians and the “stochastic matrix form” decomposition. *Annals of Physics*, 318(2):316 – 344, 2005.
- [56] C. Castelnovo, R. Moessner, and S. Sondhi. Spin ice, fractionalization, and topological order. *Annual Review of Condensed Matter Physics*, 3(1):35–55, 2012.
- [57] C. Castelnovo, R. Moessner, and S. L. Sondhi. Thermal quenches in spin ice. *Phys. Rev. Lett.*, 104:107201, Mar 2010.
- [58] J.-S. Caux and F. H. L. Essler. Time evolution of local observables after quenching to an integrable model. *Phys. Rev. Lett.*, 110:257203, Jun 2013.
- [59] C. d. C. Chamon and X. G. Wen. Sharp and smooth boundaries of quantum hall liquids. *Phys. Rev. B*, 49:8227–8241, Mar 1994.
- [60] A. Chandran, F. J. Burnell, V. Khemani, and S. L. Sondhi. Kibblezurek scaling and string-net coarsening in topologically ordered systems. *Journal of Physics: Condensed Matter*, 25(40):404214, 2013.
- [61] A. Chandran, J. Carrasquilla, I. H. Kim, D. A. Abanin, and G. Vidal. Spectral tensor networks for many-body localization. *Phys. Rev. B*, 92:024201, Jul 2015.
- [62] A. Chandran, A. Erez, S. S. Gubser, and S. L. Sondhi. Kibble-zurek problem: Universality and the scaling limit. *Phys. Rev. B*, 86:064304, Aug 2012.
- [63] A. Chandran, M. Hermanns, N. Regnault, and B. A. Bernevig. Bulk-edge correspondence in entanglement spectra. *Phys. Rev. B*, 84:205136, Nov 2011.
- [64] A. Chandran, V. Khemani, C. R. Laumann, and S. L. Sondhi. Many-body localization and symmetry-protected topological order. *Phys. Rev. B*, 89:144201, Apr 2014.
- [65] A. Chandran, V. Khemani, and S. L. Sondhi. How universal is the entanglement spectrum? *Phys. Rev. Lett.*, 113:060501, Aug 2014.
- [66] A. Chandran, I. H. Kim, G. Vidal, and D. A. Abanin. Constructing local integrals of motion in the many-body localized phase. *Phys. Rev. B*, 91:085425, Feb 2015.

- [67] A. Chandran and C. Laumann. Semiclassical limit for the many-body localization transition. *Physical Review B*, 92(2):024301, 2015.
- [68] A. Chandran, C. R. Laumann, and V. Oganesyan. Finite size scaling bounds on many-body localized phase transitions. *ArXiv e-prints*, Sept. 2015, e-print arXiv:1509.04285.
- [69] A. Chandran, A. Pal, C. R. Laumann, and A. Scardicchio. Many-body localization beyond eigenstates in all dimensions. *ArXiv e-prints*, May 2016, e-print arXiv:1605.00655.
- [70] A. Chandran and S. L. Sondhi. Interaction stabilized steady states in the driven $O(N)$ model. *ArXiv e-prints*, June 2015, e-print arXiv:1506.08836.
- [71] X. Chen, Z.-C. Gu, Z.-X. Liu, and X.-G. Wen. Symmetry protected topological orders and the group cohomology of their symmetry group. *Phys. Rev. B*, 87:155114, Apr 2013.
- [72] X. Chen, Z.-C. Gu, and X.-G. Wen. Local unitary transformation, long-range quantum entanglement, wave function renormalization, and topological order. *Phys. Rev. B*, 82:155138, Oct 2010.
- [73] X. Chen, Z.-C. Gu, and X.-G. Wen. Classification of gapped symmetric phases in one-dimensional spin systems. *Phys. Rev. B*, 83:035107, Jan 2011.
- [74] X. Chen, Z.-X. Liu, and X.-G. Wen. Two-dimensional symmetry-protected topological orders and their protected gapless edge excitations. *Phys. Rev. B*, 84:235141, Dec 2011.
- [75] J.-y. Choi, S. Hild, J. Zeiher, P. Schauß, A. Rubio-Abadal, T. Yefsah, V. Khemani, D. A. Huse, I. Bloch, and C. Gross. Exploring the many-body localization transition in two dimensions. *ArXiv e-prints*, Apr. 2016, e-print arXiv:1604.04178.
- [76] L. Cincio and G. Vidal. Characterizing topological order by studying the ground states on an infinite cylinder. *Phys. Rev. Lett.*, 110:067208, Feb 2013.
- [77] J. I. Cirac, D. Poilblanc, N. Schuch, and F. Verstraete. Entanglement spectrum and boundary theories with projected entangled-pair states. *Phys. Rev. B*, 83:245134, Jun 2011.
- [78] L. D'Alessio and M. Rigol. Long-time behavior of isolated periodically driven interacting lattice systems. *Phys. Rev. X*, 4:041048, Dec 2014.
- [79] B. Damski. The simplest quantum model supporting the kibble-zurek mechanism of topological defect production: Landau-zener transitions from a new perspective. *Phys. Rev. Lett.*, 95:035701, Jul 2005.

- [80] B. Damski and W. H. Zurek. Soliton creation during a bose-einstein condensation. *Phys. Rev. Lett.*, 104:160404, Apr 2010.
- [81] J. Davies, P. Lee, and T. Rice. Properties of the electron glass. *Physical Review B*, 29(8):4260, 1984.
- [82] G. De Chiara, L. Lepori, M. Lewenstein, and A. Sanpera. Entanglement spectrum, critical exponents, and order parameters in quantum spin chains. *Phys. Rev. Lett.*, 109:237208, Dec 2012.
- [83] C. De Grandi, V. Gritsev, and A. Polkovnikov. Quench dynamics near a quantum critical point. *Phys. Rev. B*, 81:012303, Jan 2010.
- [84] A. De Luca, B. Altshuler, V. Kravtsov, and A. Scardicchio. Anderson localization on the bethe lattice: nonergodicity of extended states. *Physical review letters*, 113(4):046806, 2014.
- [85] W. DeGottardi, D. Sen, and S. Vishveshwara. Topological phases, majorana modes and quench dynamics in a spin ladder system. *New Journal of Physics*, 13(6):065028, 2011.
- [86] A. Dembo and O. Zeitouni. *Large deviations techniques and applications*, volume 38. Springer Science & Business Media, 2009.
- [87] M. den Nijs and K. Rommelse. Preroughening transitions in crystal surfaces and valence-bond phases in quantum spin chains. *Physical Review B*, 40(7):4709–4734, Sept. 1989.
- [88] S. Deng, G. Ortiz, and L. Viola. Dynamical non-ergodic scaling in continuous finite-order quantum phase transitions. *EPL (Europhysics Letters)*, 84(6):67008, 2008.
- [89] J. M. Deutsch. Quantum statistical mechanics in a closed system. *Phys. Rev. A*, 43:2046–2049, Feb 1991.
- [90] T. Devakul and R. R. P. Singh. Early breakdown of area-law entanglement at the many-body delocalization transition. *Phys. Rev. Lett.*, 115:187201, Oct 2015.
- [91] M. W. Doherty, N. B. Manson, P. Delaney, F. Jelezko, J. Wrachtrup, and L. C. Hollenberg. The nitrogen-vacancy colour centre in diamond. *Physics Reports*, 528(1):1–45, 2013.
- [92] J. Dubail and N. Read. Entanglement spectra of complex paired superfluids. *Phys. Rev. Lett.*, 107:157001, Oct 2011.
- [93] S. Ducci, P. L. Ramazza, W. González-Viñas, and F. T. Arecchi. Order parameter fragmentation after a symmetry-breaking transition. *Phys. Rev. Lett.*, 83:5210–5213, Dec 1999.

- [94] S. Dusuel, M. Kamfor, R. Orús, K. P. Schmidt, and J. Vidal. Robustness of a perturbed topological phase. *Phys. Rev. Lett.*, 106:107203, Mar 2011.
- [95] J. Dziarmaga. Dynamics of a quantum phase transition: Exact solution of the quantum ising model. *Phys. Rev. Lett.*, 95:245701, Dec 2005.
- [96] L. DAlessio and A. Polkovnikov. Many-body energy localization transition in periodically driven systems. *Annals of Physics*, 333:19 – 33, 2013.
- [97] J. T. Edwards and D. J. Thouless. Numerical studies of localization in disordered systems. *Journal of Physics C: Solid State Physics*, 5(8):807, 1972.
- [98] J. Eisert, M. Cramer, and M. B. Plenio. Colloquium: Area laws for the entanglement entropy. *Rev. Mod. Phys.*, 82(1):277–306, Feb. 2010.
- [99] D. V. Else, B. Bauer, and C. Nayak. Floquet Time Crystals. *ArXiv e-prints*, Mar. 2016, e-print arXiv:1603.08001.
- [100] D. V. Else and C. Nayak. On the classification of topological phases in periodically driven interacting systems. *ArXiv e-prints*, Feb. 2016, e-print arXiv:1602.04804.
- [101] M. Endres, T. Fukuhara, D. Pekker, M. Cheneau, P. Schauß, C. Gross, E. Demler, S. Kuhr, and I. Bloch. The/higgs/'amplitude mode at the two-dimensional superfluid/mott insulator transition. *Nature*, 487(7408):454–458, 2012.
- [102] F. Evers and A. D. Mirlin. Anderson transitions. *Rev. Mod. Phys.*, 80:1355–1417, Oct 2008.
- [103] G. Feher. Electron spin resonance experiments on donors in silicon. i. electronic structure of donors by the electron nuclear double resonance technique. *Phys. Rev.*, 114:1219–1244, Jun 1959.
- [104] G. Feher, R. C. Fletcher, and E. A. Gere. Exchange effects in spin resonance of impurity atoms in silicon. *Phys. Rev.*, 100:1784–1786, Dec 1955.
- [105] G. Feher and E. A. Gere. Electron spin resonance experiments on donors in silicon. ii. electron spin relaxation effects. *Phys. Rev.*, 114:1245–1256, Jun 1959.
- [106] C. Fernández-González, N. Schuch, M. M. Wolf, J. I. Cirac, and D. Pérez-García. Gapless hamiltonians for the toric code using the projected entangled pair state formalism. *Phys. Rev. Lett.*, 109:260401, Dec 2012.
- [107] A. M. Ferrenberg and D. P. Landau. Critical behavior of the three-dimensional ising model: A high-resolution monte carlo study. *Phys. Rev. B*, 44:5081–5091, Sep 1991.
- [108] L. Fidkowski. Entanglement spectrum of topological insulators and superconductors. *Phys. Rev. Lett.*, 104:130502, Apr 2010.

- [109] L. Fidkowski and A. Kitaev. Topological phases of fermions in one dimension. *Phys. Rev. B*, 83:075103, Feb 2011.
- [110] D. S. Fisher. Critical behavior of random transverse-field ising spin chains. *Phys. Rev. B*, 51:6411–6461, Mar 1995.
- [111] L. Fleishman and P. W. Anderson. Interactions and the anderson transition. *Phys. Rev. B*, 21:2366–2377, Mar 1980.
- [112] E. Fradkin and S. H. Shenker. Phase diagrams of lattice gauge theories with higgs fields. *Phys. Rev. D*, 19(12):3682–3697, Jun 1979.
- [113] K. Fredenhagen and M. Marcu. Confinement criterion for qcd with dynamical quarks. *Phys. Rev. Lett.*, 56:223–224, Jan 1986.
- [114] K. Fredenhagen and M. Marcu. Dual interpretation of order parameters for lattice gauge theories with matter fields. *Nuclear Physics B - Proceedings Supplements*, 4(0):352 – 357, 1988.
- [115] M. Friesdorf, A. H. Werner, W. Brown, V. B. Scholz, and J. Eisert. Many-body localization implies that eigenvectors are matrix-product states. *Phys. Rev. Lett.*, 114:170505, May 2015.
- [116] D. Gaiotto, A. Kapustin, N. Seiberg, and B. Willett. Generalized global symmetries. *Journal of High Energy Physics*, 2015(2):1–62, 2015.
- [117] J. R. Garrison and T. Grover. Does a single eigenstate encode the full Hamiltonian? *ArXiv e-prints*, Mar. 2015, e-print arXiv:1503.00729.
- [118] Y. Gefen, R. Berkovits, I. V. Lerner, and B. L. Altshuler. Anderson orthogonality catastrophe in disordered systems. *Phys. Rev. B*, 65:081106, Feb 2002.
- [119] S. M. Giampaolo, S. Montangero, F. Dell’Anno, S. De Siena, and F. Illuminati. Universal aspects in the behavior of the entanglement spectrum in one dimension: Scaling transition at the factorization point and ordered entangled structures. *Phys. Rev. B*, 88:125142, Sep 2013.
- [120] C. Gils, S. Trebst, A. Kitaev, A. W. W. Ludwig, M. Troyer, and Z. Wang. Topology-driven quantum phase transitions in time-reversal-invariant anyonic quantum liquids. *Nature Physics*, 5:834, 2009.
- [121] S. Gopalakrishnan, M. Müller, V. Khemani, M. Knap, E. Demler, and D. A. Huse. Low-frequency conductivity in many-body localized systems. *Phys. Rev. B*, 92:104202, Sep 2015.
- [122] S. Gopalakrishnan and R. Nandkishore. Mean-field theory of nearly many-body localized metals. *Physical Review B*, 90(22):224203, 2014.

- [123] I. V. Gornyi, A. D. Mirlin, and D. G. Polyakov. Interacting electrons in disordered wires: Anderson localization and low- t transport. *Phys. Rev. Lett.*, 95:206603, Nov 2005.
- [124] D. Gottesman and M. B. Hastings. Entanglement versus gap for one-dimensional spin systems. *New J. Phys.*, 12(2):025002, 2010.
- [125] K. Gregor. *Aspects of frustrated magnetism and topological order*. PhD thesis, Princeton University, 2006.
- [126] K. Gregor, D. A. Huse, R. Moessner, and S. L. Sondhi. Diagnosing deconfinement and topological order. *New Journal of Physics*, 13(2):025009, 2011.
- [127] T. Grover. Certain General Constraints on the Many-Body Localization Transition. *ArXiv e-prints*, May 2014, e-print arXiv:1405.1471.
- [128] T. Grover and M. P. Fisher. Quantum disentangled liquids. *Journal of Statistical Mechanics: Theory and Experiment*, 2014(10):P10010, 2014.
- [129] Z.-C. Gu and X.-G. Wen. Tensor-entanglement-filtering renormalization approach and symmetry-protected topological order. *Phys. Rev. B*, 80:155131, Oct 2009.
- [130] F. D. M. Haldane. Continuum dynamics of the 1-D Heisenberg antiferromagnet: Identification with the O(3) nonlinear sigma model. *Physics Letters A*, 93(9):464–468, 1983.
- [131] F. D. M. Haldane. Nonlinear Field Theory of Large-Spin Heisenberg Antiferromagnets: Semiclassically Quantized Solitons of the One-Dimensional Easy-Axis Néel State. *Physical Review Letters*, 50(15):1153–1156, Apr. 1983.
- [132] T. H. Hansson, V. Oganesyan, and S. L. Sondhi. Superconductors are topologically ordered. *Annals of Physics*, 313(2):497 – 538, 2004.
- [133] M. Z. Hasan and C. L. Kane. *Colloquium* : Topological insulators. *Rev. Mod. Phys.*, 82:3045–3067, Nov 2010.
- [134] F. Hassler, A. Akhmerov, C. Hou, and C. Beenakker. Anyonic interferometry without anyons: how a flux qubit can read out a topological qubit. *New Journal of Physics*, 12(12):125002, 2010.
- [135] M. B. Hastings. An area law for one-dimensional quantum systems. *J. Stat. Mech.*, 2007(08):P08024, 2007.
- [136] M. B. Hastings and X.-G. Wen. Quasiadiabatic continuation of quantum states: The stability of topological ground-state degeneracy and emergent gauge invariance. *Phys. Rev. B*, 72:045141, Jul 2005.
- [137] C. L. Henley. From classical to quantum dynamics at rokhsar–kivelson points. *Journal of Physics: Condensed Matter*, 16(11):S891, 2004.

- [138] C. L. Henley. Power-law spin correlations in pyrochlore antiferromagnets. *Phys. Rev. B*, 71:014424, Jan 2005.
- [139] C. L. Henley. The “coulomb phase” in frustrated systems. *Annu. Rev. Cond. Mat. Phys.*, 1(1):179–210, 2010.
- [140] M. Hermanns, A. Chandran, N. Regnault, and B. A. Bernevig. Haldane statistics in the finite-size entanglement spectra of $1/m$ fractional quantum hall states. *Phys. Rev. B*, 84:121309, Sep 2011.
- [141] M. Hermele, M. P. A. Fisher, and L. Balents. Pyrochlore photons: The $U(1)$ spin liquid in a $S = \frac{1}{2}$ three-dimensional frustrated magnet. *Phys. Rev. B*, 69(6):064404, Feb 2004.
- [142] M. Hindmarsh and A. Rajantie. Defect formation and local gauge invariance. *Phys. Rev. Lett.*, 85:4660–4663, Nov 2000.
- [143] P. C. Hohenberg and B. I. Halperin. Theory of dynamic critical phenomena. *Rev. Mod. Phys.*, 49:435–479, Jul 1977.
- [144] Y. Hu, S. D. Stirling, and Y.-S. Wu. Ground-state degeneracy in the levin-wen model for topological phases. *Phys. Rev. B*, 85:075107, Feb 2012.
- [145] T. L. Hughes, E. Prodan, and B. A. Bernevig. Inversion-symmetric topological insulators. *Phys. Rev. B*, 83:245132, Jun 2011.
- [146] S. Humeniuk and T. Roscilde. Quantum monte carlo calculation of entanglement rényi entropies for generic quantum systems. *Phys. Rev. B*, 86:235116, Dec 2012.
- [147] D. A. Huse, M. P. A. Fisher, and D. S. Fisher. Are superconductors really superconducting? *Nature*, 358(6387):553–559, 08 1992.
- [148] D. A. Huse, R. Nandkishore, and V. Oganesyan. Phenomenology of fully many-body-localized systems. *Phys. Rev. B*, 90:174202, Nov 2014.
- [149] D. A. Huse, R. Nandkishore, V. Oganesyan, A. Pal, and S. L. Sondhi. Localization-protected quantum order. *Phys. Rev. B*, 88:014206, Jul 2013.
- [150] D. A. Huse and A. D. Rutenberg. Classical antiferromagnets on the kagomé lattice. *Phys. Rev. B*, 45:7536–7539, Apr 1992.
- [151] R. Hyman and K. Yang. Impurity Driven Phase Transition in the Antiferromagnetic Spin-1 Chain. *Physical Review Letters*, 78(9):1783–1786, Mar. 1997.
- [152] M. Žnidarič, T. c. v. Prosen, and P. Prelovšek. Many-body localization in the heisenberg xxz magnet in a random field. *Phys. Rev. B*, 77:064426, Feb 2008.
- [153] J. Z. Imbrie. On many-body localization for quantum spin chains. *Journal of Statistical Physics*, 163(5):998–1048, 2016.

- [154] Y. Imry, Y. Gefen, and D. J. Bergman. Dielectric anomalies near the anderson metal-insulator transition. *Physical Review B*, 26(6):3436, 1982.
- [155] S. V. Isakov, K. Gregor, R. Moessner, and S. L. Sondhi. Dipolar spin correlations in classical pyrochlore magnets. *Phys. Rev. Lett.*, 93:167204, Oct 2004.
- [156] S. V. Isakov, R. Moessner, and S. L. Sondhi. Why spin ice obeys the ice rules. *Phys. Rev. Lett.*, 95:217201, Nov 2005.
- [157] S. Iyer, V. Oganesyan, G. Refael, and D. A. Huse. Many-body localization in a quasiperiodic system. *Physical Review B*, 87(13):134202, 2013.
- [158] J. K. Jain. *Composite Fermions*. Cambridge University Press, 2007.
- [159] A. J. A. James and R. M. Konik. Understanding the entanglement entropy and spectra of 2d quantum systems through arrays of coupled 1d chains. *Phys. Rev. B*, 87:241103, Jun 2013.
- [160] L. D. C. Jaubert, M. Haque, and R. Moessner. Analysis of a fully packed loop model arising in a magnetic coulomb phase. *Phys. Rev. Lett.*, 107:177202, Oct 2011.
- [161] L. Jiang, T. Kitagawa, J. Alicea, A. R. Akhmerov, D. Pekker, G. Refael, J. I. Cirac, E. Demler, M. D. Lukin, and P. Zoller. Majorana Fermions in Equilibrium and in Driven Cold-Atom Quantum Wires. *Phys. Rev. Lett.*, 106(22):220402, June 2011.
- [162] S. Johri, R. Nandkishore, and R. N. Bhatt. Many-body localization in imperfectly isolated quantum systems. *Phys. Rev. Lett.*, 114:117401, Mar 2015.
- [163] A. Kapustin and N. Seiberg. Coupling a qft to a tqft and duality. *Journal of High Energy Physics*, 2014(4):1–45, 2014.
- [164] M. Kargarian and G. A. Fiete. Topological phases and phase transitions on the square-octagon lattice. *Phys. Rev. B*, 82:085106, Aug 2010.
- [165] A. Karlhede, S. A. Kivelson, K. Lejnell, and S. L. Sondhi. Textured edges in quantum hall systems. *Phys. Rev. Lett.*, 77:2061–2064, Sep 1996.
- [166] T. Kennedy and H. Tasaki. Hidden $Z_2 \times Z_2$ symmetry breaking in Haldane-gap antiferromagnets. *Physical Review B*, 45(1):304–307, 1992.
- [167] V. Khemani, A. Chandran, H. Kim, and S. L. Sondhi. Eigenstate thermalization and representative states on subsystems. *Phys. Rev. E*, 90:052133, Nov 2014.
- [168] V. Khemani and D. Huse. unpublished.
- [169] V. Khemani, A. Lazarides, R. Moessner, and S. L. Sondhi. Phase structure of driven quantum systems. *Phys. Rev. Lett.*, 116:250401, Jun 2016.

- [170] V. Khemani, S.-P. Lim, D. Sheng, and D. Huse. unpublished.
- [171] V. Khemani, R. Moessner, S. A. Parameswaran, and S. L. Sondhi. Bionic coulomb phase on the pyrochlore lattice. *Phys. Rev. B*, 86:054411, Aug 2012.
- [172] V. Khemani, R. Nandkishore, and S. Sondhi. Nonlocal adiabatic response of a localized system to local manipulations. *Nature Physics*, 11(7):560–565, 2015.
- [173] V. Khemani, F. Pollmann, and S. L. Sondhi. Obtaining highly excited eigenstates of many-body localized hamiltonians by the density matrix renormalization group approach. *Phys. Rev. Lett.*, 116:247204, Jun 2016.
- [174] T. W. B. Kibble. Topology of cosmic domains and strings. *Journal of Physics A: Mathematical and General*, 9(8):1387, 1976.
- [175] H. Kim and D. A. Huse. Ballistic spreading of entanglement in a diffusive nonintegrable system. *Phys. Rev. Lett.*, 111:127205, Sep 2013.
- [176] A. Kitaev and C. R. Laumann. *Topological Phases And Quantum Computation, Lecture Notes Of The Les Houches Summer School*, volume 89 of *Lecture Notes of the Les Houches Summer School*. OUP Oxford, 2008.
- [177] A. Kitaev and J. Preskill. Topological entanglement entropy. *Phys. Rev. Lett.*, 96:110404, Mar 2006.
- [178] A. Y. Kitaev. Fault-tolerant quantum computation by anyons. *Annals of Physics*, 303:2–30, 2003.
- [179] A. Y. Kitaev. Anyons in an exactly solved model and beyond. *Annals of Physics*, 321:2–111, 2006.
- [180] T. Kitagawa, E. Berg, M. Rudner, and E. Demler. Topological characterization of periodically driven quantum systems. *Phys. Rev. B*, 82(23):235114, Dec. 2010.
- [181] T. Kitagawa, T. Oka, A. Brataas, L. Fu, and E. Demler. Transport properties of nonequilibrium systems under the application of light: Photoinduced quantum Hall insulators without Landau levels. *Physical Review B*, 84(23):235108, Dec. 2011.
- [182] J. A. Kjäll, J. H. Bardarson, and F. Pollmann. Many-body localization in a disordered quantum ising chain. *Phys. Rev. Lett.*, 113:107204, Sep 2014.
- [183] J. A. Kjäll, M. P. Zaletel, R. S. K. Mong, J. H. Bardarson, and F. Pollmann. Phase diagram of the anisotropic spin-2 xxz model: Infinite-system density matrix renormalization group study. *Phys. Rev. B*, 87:235106, Jun 2013.
- [184] M. Knap, A. Shashi, Y. Nishida, A. Imambekov, D. A. Abanin, and E. Demler. Time-dependent impurity in ultracold fermions: Orthogonality catastrophe and beyond. *Physical Review X*, 2(4):041020, 2012.

- [185] J. Kockelkoren and H. Chaté. Comment on “deterministic equations of motion and phase ordering dynamics”. *Phys. Rev. E*, 65:058101, May 2002.
- [186] J. Kockelkoren and H. Chaté. Late stages of coarsening in model c. *Physica D: Nonlinear Phenomena*, 168 -169(0):80 – 92, 2002.
- [187] J. B. Kogut. An introduction to lattice gauge theory and spin systems. *Reviews Of Modern Physics*, 51(4):659–713, Oct. 1979.
- [188] F. Kolley, S. Depenbrock, I. P. McCulloch, U. Schollwöck, and V. Alba. Entanglement spectroscopy of su(2)-broken phases in two dimensions. *Phys. Rev. B*, 88:144426, Oct 2013.
- [189] J. Kondev and C. L. Henley. Four-coloring model on the square lattice: A critical ground state. *Phys. Rev. B*, 52:6628–6639, Sep 1995.
- [190] S. Kondov, W. McGehee, J. Zirbel, and B. DeMarco. Three-dimensional anderson localization of ultracold matter. *Science*, 334(6052):66–68, 2011.
- [191] S. S. Kondov, W. R. McGehee, W. Xu, and B. DeMarco. Disorder-induced localization in a strongly correlated atomic hubbard gas. *Phys. Rev. Lett.*, 114:083002, Feb 2015.
- [192] S. S. Kondov, W. R. McGehee, W. Xu, and B. DeMarco. Disorder-induced localization in a strongly correlated atomic hubbard gas. *Phys. Rev. Lett.*, 114:083002, Feb 2015.
- [193] T. Kuwahara, T. Mori, and K. Saito. Floquet–magnus theory and generic transient dynamics in periodically driven many-body quantum systems. *Annals of Physics*, 367:96–124, 2016.
- [194] L. Labonté, C. Vanneste, and P. Sebbah. Localized mode hybridization by fine tuning of two-dimensional random media. *Opt. Lett.*, 37(11):1946–1948, Jun 2012.
- [195] L. Lamata, J. León, D. Pérez-García, D. Salgado, and E. Solano. Sequential implementation of global quantum operations. *Phys. Rev. Lett.*, 101:180506, Oct 2008.
- [196] A. M. Läuchli, E. J. Bergholtz, J. Suorsa, and M. Haque. Disentangling entanglement spectra of fractional quantum hall states on torus geometries. *Phys. Rev. Lett.*, 104:156404, Apr 2010.
- [197] C. R. Laumann. Unpublished, 2013.
- [198] A. Lazarides, A. Das, and R. Moessner. Equilibrium states of generic quantum systems subject to periodic driving. *Physical Review E*, 90(1), jul 2014.
- [199] A. Lazarides, A. Das, and R. Moessner. Fate of many-body localization under periodic driving. *Phys. Rev. Lett.*, 115:030402, Jul 2015.

- [200] L. Lepori, G. De Chiara, and A. Sanpera. Scaling of the entanglement spectrum near quantum phase transitions. *Phys. Rev. B*, 87:235107, Jun 2013.
- [201] Y. B. Lev, G. Cohen, and D. R. Reichman. Absence of diffusion in an interacting system of spinless fermions on a one-dimensional disordered lattice. *Physical review letters*, 114(10):100601, 2015.
- [202] M. Levin and Z.-C. Gu. Braiding statistics approach to symmetry-protected topological phases. *Phys. Rev. B*, 86:115109, Sep 2012.
- [203] M. Levin and X.-G. Wen. Detecting topological order in a ground state wave function. *Phys. Rev. Lett.*, 96(11):110405, 2006.
- [204] M. A. Levin and X.-G. Wen. String-net condensation: A physical mechanism for topological phases. *Phys. Rev. B*, 71:045110, 2005.
- [205] H. Li and F. D. M. Haldane. Entanglement spectrum as a generalization of entanglement entropy: Identification of topological order in non-abelian fractional quantum hall effect states. *Phys. Rev. Lett.*, 101(1):010504, Jul 2008.
- [206] I. Lifshitz and V. Kirpichenkov. Tunnel transparency of disordered systems. *Zh. Eksp. Teor. Fiz.*, 77(3):989–1016, 1979.
- [207] N. H. Lindner, G. Refael, and V. Galitski. Floquet topological insulator in semiconductor quantum wells. *Nature Physics*, 7(6):490–495, June 2011.
- [208] D. J. Luitz, N. Laflorencie, and F. Alet. Many-body localization edge in the random-field heisenberg chain. *Phys. Rev. B*, 91:081103, Feb 2015.
- [209] P. Mag. Conduction in non-crystalline systems: 1. localized electronic states in disordered systems. *Philos. Mag*, 17:1259, 1968.
- [210] W. Magnus. On the exponential solution of differential equations for a linear operator. *Communications on pure and applied mathematics*, 7(4):649–673, 1954.
- [211] G. D. Mahan. *Many-Particle Physics*. Plenum, New York, N.Y., 2nd edition, 1993.
- [212] A. Maniv, E. Polturak, and G. Koren. Observation of magnetic flux generated spontaneously during a rapid quench of superconducting films. *Phys. Rev. Lett.*, 91:197001, Nov 2003.
- [213] M. A. Metlitski, C. A. Fuertes, and S. Sachdev. Entanglement entropy in the $o(n)$ model. *Phys. Rev. B*, 80:115122, Sep 2009.
- [214] M. A. Metlitski and T. Grover. Entanglement Entropy of Systems with Spontaneously Broken Continuous Symmetry. *arXiv*, Dec. 2011, e-print arXiv:1112.5166.

- [215] M. S. Miguel, J. D. Gunton, G. Dee, and P. S. Sahni. Theory of spinodal decomposition in relaxational tricritical models. *Phys. Rev. B*, 23:2334–2345, Mar 1981.
- [216] R. Moessner and J. T. Chalker. Properties of a classical spin liquid: The heisenberg pyrochlore antiferromagnet. *Phys. Rev. Lett.*, 80:2929–2932, Mar 1998.
- [217] R. Moessner and K. S. Raman. Quantum dimer models. In C. Lacroix, P. Mendels, and F. Mila, editors, *Introduction to Frustrated Magnetism*, volume 164 of *Springer Series in Solid-State Sciences*, pages 437–479. Springer Berlin Heidelberg, 2011.
- [218] R. Moessner and S. L. Sondhi. Three-dimensional resonating-valence-bond liquids and their excitations. *Phys. Rev. B*, 68:184512, Nov 2003.
- [219] R. Monaco, J. Mygind, M. Aaroe, R. J. Rivers, and V. P. Koshelets. Zurek-kibble mechanism for the spontaneous vortex formation in Nb-Al/al_{ox}/Nb josephson tunnel junctions: New theory and experiment. *Phys. Rev. Lett.*, 96:180604, May 2006.
- [220] N. Mott. Conduction in glasses containing transition metal ions. *Journal of Non-Crystalline Solids*, 1(1):1 – 17, 1968.
- [221] N. F. Mott. Electrons in disordered structures. *Advances in Physics*, 16:49–144, Jan. 1967.
- [222] R. Nandkishore, S. Gopalakrishnan, and D. A. Huse. Spectral features of a many-body-localized system weakly coupled to a bath. *Phys. Rev. B*, 90:064203, Aug 2014.
- [223] R. Nandkishore and D. A. Huse. Many-body localization and thermalization in quantum statistical mechanics. *Annual Review of Condensed Matter Physics*, 6(1):15–38, 2015.
- [224] R. Nandkishore and A. C. Potter. Marginal anderson localization and many-body delocalization. *Phys. Rev. B*, 90:195115, Nov 2014.
- [225] F. Nathan and M. S. Rudner. Topological singularities and the general classification of floquet-bloch systems. *New Journal of Physics*, 17(12):125014, 2015.
- [226] C. Nayak, S. H. Simon, A. Stern, M. Freedman, and S. D. Sarma. Non-abelian anyons and topological quantum computation. *Reviews of Modern Physics*, 80(3):1083, 2008.
- [227] V. Oganesyan and D. A. Huse. Localization of interacting fermions at high temperature. *Phys. Rev. B*, 75:155111, Apr 2007.

- [228] V. Oganesyan, A. Pal, and D. A. Huse. Energy transport in disordered classical spin chains. *Physical Review B*, 80(11):115104, 2009.
- [229] T. Oka and H. Aoki. Photovoltaic Hall effect in graphene. *Physical Review B*, 79(8):081406, Feb. 2009.
- [230] M. Ovadia, D. Kalok, I. Tamir, S. Mitra, B. Sacépé, and D. Shahar. Evidence for a finite-temperature insulator. *Scientific reports*, 5, 2015.
- [231] M. Ovadia, D. Kalok, I. Tamir, S. Mitra, B. Sacépé, and D. Shahar. Evidence for a finite-temperature insulator. *Scientific reports*, 5, 2015.
- [232] Z. Ovadyahu. Suppression of inelastic electron-electron scattering in anderson insulators. *Phys. Rev. Lett.*, 108:156602, Apr 2012.
- [233] D. N. Page. Average entropy of a subsystem. *Phys. Rev. Lett.*, 71:1291–1294, Aug 1993.
- [234] A. Pal and D. A. Huse. Many-body localization phase transition. *Phys. Rev. B*, 82:174411, Nov 2010.
- [235] Z. Papić, B. A. Bernevig, and N. Regnault. Topological entanglement in abelian and non-abelian excitation eigenstates. *Phys. Rev. Lett.*, 106:056801, Feb 2011.
- [236] S. A. Parameswaran, S. L. Sondhi, and D. P. Arovas. Order and disorder in aklt antiferromagnets in three dimensions. *Phys. Rev. B*, 79:024408, Jan 2009.
- [237] L. Pauling. The structure and entropy of ice and of other crystals with some randomness of atomic arrangement. *J. Am. Chem. Soc.*, 57(12):2680–2684, 1935.
- [238] D. Pekker and B. K. Clark. Encoding the structure of many-body localization with matrix product operators. *ArXiv e-prints*, Oct. 2014, e-print arXiv:1410.2224.
- [239] D. Pekker, G. Refael, E. Altman, E. Demler, and V. Oganesyan. Hilbert-glass transition: New universality of temperature-tuned many-body dynamical quantum criticality. *Phys. Rev. X*, 4:011052, Mar 2014.
- [240] J. Pendry. Quasi-extended electron states in strongly disordered systems. *Journal of Physics C: Solid State Physics*, 20(5):733, 1987.
- [241] I. Peschel. Calculation of reduced density matrices from correlation functions. *Journal of Physics A: Mathematical and General*, 36(14):L205, 2003.
- [242] I. Pizorn, F. Verstraete, and R. M. Konik. Tree tensor networks and entanglement spectra. *Phys. Rev. B*, 88:195102, Nov 2013.
- [243] D. Poilblanc. Entanglement spectra of quantum heisenberg ladders. *Phys. Rev. Lett.*, 105:077202, Aug 2010.

- [244] D. Poilblanc, N. Schuch, D. Pérez-García, and J. I. Cirac. Topological and entanglement properties of resonating valence bond wave functions. *Phys. Rev. B*, 86:014404, Jul 2012.
- [245] A. Polkovnikov. Universal adiabatic dynamics in the vicinity of a quantum critical point. *Phys. Rev. B*, 72:161201, Oct 2005.
- [246] A. Polkovnikov. Microscopic diagonal entropy and its connection to basic thermodynamic relations. *Annals of Physics*, 326(2):486 – 499, 2011.
- [247] A. Polkovnikov, K. Sengupta, A. Silva, and M. Vengalattore. *Colloquium* : Nonequilibrium dynamics of closed interacting quantum systems. *Rev. Mod. Phys.*, 83:863–883, Aug 2011.
- [248] F. Pollmann, E. Berg, A. M. Turner, and M. Oshikawa. Symmetry protection of topological phases in one-dimensional quantum spin systems. *Phys. Rev. B*, 85:075125, Feb 2012.
- [249] F. Pollmann, V. Khemani, J. I. Cirac, and S. L. Sondhi. Efficient variational diagonalization of fully many-body localized Hamiltonians. *ArXiv e-prints*, June 2015, e-print arXiv:1506.07179.
- [250] F. Pollmann, A. M. Turner, E. Berg, and M. Oshikawa. Entanglement spectrum of a topological phase in one dimension. *Phys. Rev. B*, 81(6):064439, Feb. 2010.
- [251] P. Ponte, A. Chandran, Z. Papi, and D. A. Abanin. Periodically driven ergodic and many-body localized quantum systems. *Annals of Physics*, 353:196 – 204, 2015.
- [252] P. Ponte, Z. Papić, F. Huveneers, and D. A. Abanin. Many-body localization in periodically driven systems. *Phys. Rev. Lett.*, 114:140401, Apr 2015.
- [253] A. C. Potter, T. Morimoto, and A. Vishwanath. Topological classification of interacting 1D Floquet phases. *ArXiv e-prints*, Feb. 2016, e-print arXiv:1602.05194.
- [254] A. C. Potter, R. Vasseur, and S. A. Parameswaran. Universal properties of many-body delocalization transitions. *Phys. Rev. X*, 5:031033, Sep 2015.
- [255] A. C. Potter and A. Vishwanath. Protection of topological order by symmetry and many-body localization. *arXiv preprint arXiv:1506.00592*, 2015.
- [256] E. Prodan, T. L. Hughes, and B. A. Bernevig. Entanglement spectrum of a disordered topological chern insulator. *Phys. Rev. Lett.*, 105(11):115501, Sep 2010.
- [257] A. M. Pruisken. On localization in the theory of the quantized hall effect: A two-dimensional realization of the θ -vacuum. *Nuclear Physics B*, 235(2):277–298, 1984.

- [258] K. Pyka, J. Keller, H. L. Partner, R. Nigmatullin, T. Burgermeister, D.-M. Meier, K. Kuhlmann, A. Retzker, M. B. Plenio, W. H. Zurek, A. del Campo, and T. E. Mehlstübler. Topological defect formation and spontaneous symmetry breaking in ion coulomb crystals. *Nature Communications*, 4(2291), 2013.
- [259] X.-L. Qi, H. Katsura, and A. W. W. Ludwig. General relationship between the entanglement spectrum and the edge state spectrum of topological quantum states. *Phys. Rev. Lett.*, 108:196402, May 2012.
- [260] L. Rademaker and M. Ortuño. Explicit local integrals of motion for the many-body localized state. *Phys. Rev. Lett.*, 116:010404, Jan 2016.
- [261] A. Rahmani and C. Chamon. Exact results on the quench dynamics of the entanglement entropy in the toric code. *Phys. Rev. B*, 82:134303, Oct 2010.
- [262] D. Rainis and D. Loss. Majorana qubit decoherence by quasiparticle poisoning. *Physical Review B*, 85(17):174533, 2012.
- [263] A. Rajantie. Formation of topological defects in gauge field theories. *International Journal of Modern Physics A*, 17(01):1–43, 2002.
- [264] N. Regnault and B. A. Bernevig. Fractional chern insulator. *Phys. Rev. X*, 1:021014, Dec 2011.
- [265] J. Rehn, A. Lazarides, F. Pollmann, and R. Moessner. How periodic driving heats a disordered quantum spin chain. *ArXiv e-prints*, Mar. 2016, e-print arXiv:1603.03054.
- [266] A. Richardella, P. Roushan, S. Mack, B. Zhou, D. A. Huse, D. D. Awschalom, and A. Yazdani. Visualizing critical correlations near the metal-insulator transition in $\text{Ga}_1\text{XmMnxAs}$. *Science*, 327(5966):665–669, 2010.
- [267] M. Rigol, V. Dunjko, and M. Olshanii. Thermalization and its mechanism for generic isolated quantum systems. *Nature*, 452(7189):854–858, Apr. 2008.
- [268] M. Rigol, V. Dunjko, V. Yurovsky, and M. Olshanii. Relaxation in a completely integrable many-body quantum system: An *Ab Initio* study of the dynamics of the highly excited states of 1d lattice hard-core bosons. *Phys. Rev. Lett.*, 98:050405, Feb 2007.
- [269] G. Roati, C. DErrico, L. Fallani, M. Fattori, C. Fort, M. Zaccanti, G. Modugno, M. Modugno, and M. Inguscio. Anderson localization of a non-interacting bose–einstein condensate. *Nature*, 453(7197):895–898, 2008.
- [270] D. S. Rokhsar and S. A. Kivelson. Superconductivity and the quantum hard-core dimer gas. *Phys. Rev. Lett.*, 61:2376–2379, Nov 1988.
- [271] V. Ros, M. Müller, and A. Scardicchio. Integrals of motion in the many-body localized phase. *Nuclear Physics B*, 891:420–465, Feb. 2015.

- [272] R. Roy and F. Harper. Abelian Floquet SPT Phases in 1D. *ArXiv e-prints*, Feb. 2016, e-print arXiv:1602.08089.
- [273] M. S. Rudner, N. H. Lindner, E. Berg, and M. Levin. Anomalous edge states and the bulk-edge correspondence for periodically driven two-dimensional systems. *Physical Review X*, 3(3):031005, 2013.
- [274] P. D. Sacramento, N. Paunković, and V. R. Vieira. Fidelity spectrum and phase transitions of quantum systems. *Phys. Rev. A*, 84:062318, Dec 2011.
- [275] F. Sagués, J. M. Sancho, and J. García-Ojalvo. Spatiotemporal order out of noise. *Rev. Mod. Phys.*, 79:829–882, Jul 2007.
- [276] H. Sambe. Steady States and Quasienergies of a Quantum-Mechanical System in an Oscillating Field. *Phys. Rev. A*, 7(6):2203–2213, June 1973.
- [277] U. Schollwöck. The density-matrix renormalization group in the age of matrix product states. *Annals of Physics*, 326(1):96–192, 1 2011.
- [278] C. Schön, E. Solano, F. Verstraete, J. I. Cirac, and M. M. Wolf. Sequential generation of entangled multiqubit states. *Phys. Rev. Lett.*, 95:110503, Sep 2005.
- [279] M. Schreiber, S. S. Hodgman, P. Bordia, H. P. Lüschen, M. H. Fischer, R. Vosk, E. Altman, U. Schneider, and I. Bloch. Observation of many-body localization of interacting fermions in a quasirandom optical lattice. *Science*, 349(6250):842–845, 2015.
- [280] N. Schuch, D. Pérez-García, and I. Cirac. Classifying quantum phases using matrix product states and projected entangled pair states. *Phys. Rev. B*, 84:165139, Oct 2011.
- [281] N. Schuch, M. M. Wolf, F. Verstraete, and J. I. Cirac. Entropy scaling and simulability by matrix product states. *Phys. Rev. Lett.*, 100(3):030504, 2008.
- [282] M. Serbyn, M. Knap, S. Gopalakrishnan, Z. Papić, N. Y. Yao, C. R. Laumann, D. A. Abanin, M. D. Lukin, and E. A. Demler. Interferometric probes of many-body localization. *Phys. Rev. Lett.*, 113:147204, Oct 2014.
- [283] M. Serbyn, Z. Papić, and D. A. Abanin. Local conservation laws and the structure of the many-body localized states. *Phys. Rev. Lett.*, 111:127201, Sep 2013.
- [284] M. Serbyn, Z. Papić, and D. A. Abanin. Universal slow growth of entanglement in interacting strongly disordered systems. *Phys. Rev. Lett.*, 110:260601, Jun 2013.
- [285] J. H. Shirley. Solution of the Schrödinger equation with a Hamiltonian periodic in time. *Physical Review*, 138(4B):B979–B987, 1965.

- [286] B. Shklovskii and A. Efros. Zero-phonon ac hopping conductivity of disordered systems. *Zh. Eksp. Teor. Fi*, 81:406–415, 1981.
- [287] R. R. P. Singh, R. G. Melko, and J. Oitmaa. Thermodynamic singularities in the entanglement entropy at a two-dimensional quantum critical point. *Phys. Rev. B*, 86:075106, Aug 2012.
- [288] U. Sivan and Y. Imry. Energy-level correlation function and ac conductivity of a finite disordered system. *Physical Review B*, 35(12):6074, 1987.
- [289] J. Smith, A. Lee, P. Richerme, B. Neyenhuis, P. W. Hess, P. Hauke, M. Heyl, D. A. Huse, and C. Monroe. Many-body localization in a quantum simulator with programmable random disorder. *arXiv preprint arXiv:1508.07026*, 2015.
- [290] M. Srednicki. Entropy and area. *Phys. Rev. Lett.*, 71:666–669, Aug 1993.
- [291] M. Srednicki. Chaos and quantum thermalization. *Phys. Rev. E*, 50:888–901, Aug 1994.
- [292] M. Srednicki. Thermal fluctuations in quantized chaotic systems. *Journal of Physics A: Mathematical and General*, 29(4):L75, 1996.
- [293] J.-M. Stéphan, G. Misguich, and V. Pasquier. Rényi entropy of a line in two-dimensional ising models. *Phys. Rev. B*, 82:125455, Sep 2010.
- [294] B. Swingle. *arXiv:1307.0507*.
- [295] B. Swingle and T. Senthil. Geometric proof of the equality between entanglement and edge spectra. *Phys. Rev. B*, 86:045117, Jul 2012.
- [296] M. Thakurathi, A. A. Patel, D. Sen, and A. Dutta. Floquet generation of majorana end modes and topological invariants. *Phys. Rev. B*, 88:155133, Oct 2013.
- [297] R. Thomale, A. Sterdyniak, N. Regnault, and B. A. Bernevig. Entanglement gap and a new principle of adiabatic continuity. *Phys. Rev. Lett.*, 104:180502, May 2010.
- [298] D. J. Thouless. Quantization of particle transport. *Physical Review B*, 27(10):6083–6087, 1983.
- [299] P. Titum, E. Berg, M. S. Rudner, G. Refael, and N. H. Lindner. The anomalous floquet-anderson insulator as a non-adiabatic quantized charge pump. *arXiv preprint arXiv:1506.00650*, 2015.
- [300] P. Titum, N. H. Lindner, M. C. Rechtsman, and G. Refael. Disorder-induced floquet topological insulators. *Phys. Rev. Lett.*, 114:056801, Feb 2015.

- [301] S. Trebst, P. Werner, M. Troyer, K. Shtengel, and C. Nayak. Breakdown of a topological phase: Quantum phase transition in a loop gas model with tension. *Phys. Rev. Lett.*, 98(7):070602, Feb 2007.
- [302] D. I. Tsomokos, A. Hama, W. Zhang, S. Haas, and R. Fazio. Topological order following a quantum quench. *Phys. Rev. A*, 80:060302, Dec 2009.
- [303] I. S. Tupitsyn, A. Kitaev, N. V. Prokof'ev, and P. C. E. Stamp. Topological multicritical point in the phase diagram of the toric code model and three-dimensional lattice gauge higgs model. *Phys. Rev. B*, 82:085114, Aug 2010.
- [304] A. M. Turner, F. Pollmann, and E. Berg. Topological phases of one-dimensional fermions: An entanglement point of view. *Physical review b*, 83(7):075102, 2011.
- [305] A. M. Turner, Y. Zhang, and A. Vishwanath. Entanglement and inversion symmetry in topological insulators. *Phys. Rev. B*, 82:241102, Dec 2010.
- [306] R. Vasseur, S. A. Parameswaran, and J. E. Moore. Quantum revivals and many-body localization. *Phys. Rev. B*, 91:140202, Apr 2015.
- [307] R. Vasseur, A. C. Potter, and S. A. Parameswaran. Quantum criticality of hot random spin chains. *Phys. Rev. Lett.*, 114:217201, May 2015.
- [308] F. Verstraete and J. I. Cirac. Matrix product states represent ground states faithfully. *Phys. Rev. B*, 73:094423, Mar 2006.
- [309] F. Verstraete, J. J. Garcia-Ripoll, and J. I. Cirac. *Phys. Rev. Lett.*, 93:207204, 2004.
- [310] F. Verstraete, V. Murg, and J. I. Cirac. Matrix product states, projected entangled pair states, and variational renormalization group methods for quantum spin systems. *Advances In Physics*, 57(2):143–224, Mar. 2008.
- [311] F. Verstraete, M. M. Wolf, D. Perez-Garcia, and J. I. Cirac. Criticality, the area law, and the computational power of projected entangled pair states. *Phys. Rev. Lett.*, 96:220601, Jun 2006.
- [312] G. Vidal. Efficient classical simulation of slightly entangled quantum computations. *Phys. Rev. Lett.*, 91:147902, Oct 2003.
- [313] J. Vidal, S. Dusuel, and K. P. Schmidt. Low-energy effective theory of the toric code model in a parallel magnetic field. *Phys. Rev. B*, 79(3):033109, Jan 2009.
- [314] D. Vollhardt and P. Wölfle. Diagrammatic, self-consistent treatment of the anderson localization problem in $d \leq 2$ dimensions. *Phys. Rev. B*, 22:4666–4679, Nov 1980.
- [315] C. W. von Keyserlingk, V. Khemani, and S. L. Sondhi. Absolute Stability and Spatiotemporal Long-Range Order in Floquet systems. *ArXiv e-prints*, May 2016, e-print arXiv:1605.00639.

- [316] C. W. von Keyserlingk and S. L. Sondhi. 1D Many-body localized Floquet systems II: Symmetry-Broken phases. *ArXiv e-prints*, Feb. 2016, e-print arXiv:1602.06949.
- [317] C. W. von Keyserlingk and S. L. Sondhi. Phase Structure of 1d Interacting Floquet Systems I: Abelian SPTs. *ArXiv e-prints*, Feb. 2016, e-print arXiv:1602.02157.
- [318] R. Vosk and E. Altman. Many-body localization in one dimension as a dynamical renormalization group fixed point. *Phys. Rev. Lett.*, 110:067204, Feb 2013.
- [319] R. Vosk and E. Altman. Dynamical quantum phase transitions in random spin chains. *Phys. Rev. Lett.*, 112:217204, May 2014.
- [320] R. Vosk, D. A. Huse, and E. Altman. Theory of the many-body localization transition in one-dimensional systems. *Phys. Rev. X*, 5:031032, Sep 2015.
- [321] H. Watanabe and M. Oshikawa. Absence of quantum time crystals. *Phys. Rev. Lett.*, 114:251603, Jun 2015.
- [322] F. Wegner. The mobility edge problem: continuous symmetry and a conjecture. *Zeitschrift für Physik B Condensed Matter*, 35(3):207–210, 1979.
- [323] F. J. Wegner. Duality in generalized ising models and phase transitions without local order parameters. *J. Math. Phys.*, 12(10):2259, 1971.
- [324] X.-G. Wen. Topological orders in rigid states. *International Journal of Modern Physics B*, 4(02):239–271, 1990.
- [325] X. G. Wen and Q. Niu. Ground-state degeneracy of the fractional quantum hall states in the presence of a random potential and on high-genus riemann surfaces. *Phys. Rev. B*, 41:9377–9396, May 1990.
- [326] E. Westerberg, A. Furusaki, M. Sigrist, and P. A. Lee. Random quantum spin chains: A real-space renormalization group study. *Phys. Rev. Lett.*, 75:4302–4305, Dec 1995.
- [327] S. R. White. Density matrix formulation for quantum renormalization groups. *Phys. Rev. Lett.*, 69:2863–2866, Nov 1992.
- [328] F. Wilczek. Quantum time crystals. *Phys. Rev. Lett.*, 109:160401, Oct 2012.
- [329] F. Wu, Y. Deng, and N. Prokof'ev. Phase diagram of the toric code model in a parallel magnetic field. *Phys. Rev. B*, 85:195104, May 2012.
- [330] B. Yan, S. A. Moses, B. Gadway, J. P. Covey, K. R. Hazzard, A. M. Rey, D. S. Jin, and J. Ye. Observation of dipolar spin-exchange interactions with lattice-confined polar molecules. *Nature*, 501(7468):521–525, 2013.

- [331] K. Yang. Field theoretical description of quantum hall edge reconstruction. *Phys. Rev. Lett.*, 91:036802, Jul 2003.
- [332] H. Yao and X.-L. Qi. Entanglement entropy and entanglement spectrum of the kitaev model. *Phys. Rev. Lett.*, 105:080501, Aug 2010.
- [333] N. Y. Yao, C. R. Laumann, S. Gopalakrishnan, M. Knap, M. Müller, E. A. Demler, and M. D. Lukin. Many-body localization in dipolar systems. *Phys. Rev. Lett.*, 113:243002, Dec 2014.
- [334] X. Yu, D. Pekker, and B. K. Clark. Finding matrix product state representations of highly-excited eigenstates of many-body localized Hamiltonians. *ArXiv e-prints*, Sept. 2015, e-print arXiv:1509.01244.
- [335] M. P. Zaletel. Detecting two-dimensional symmetry-protected topological order in a ground-state wave function. *Phys. Rev. B*, 90:235113, Dec 2014.
- [336] M. P. Zaletel, R. S. K. Mong, and F. Pollmann. Topological characterization of fractional quantum hall ground states from microscopic hamiltonians. *Phys. Rev. Lett.*, 110:236801, Jun 2013.
- [337] S. C. Zhang, T. H. Hansson, and S. Kivelson. Effective-field-theory model for the fractional quantum hall effect. *Phys. Rev. Lett.*, 62:82–85, Jan 1989.
- [338] Y. Zhang, T. Grover, A. Turner, M. Oshikawa, and A. Vishwanath. Quasi-particle statistics and braiding from ground-state entanglement. *Phys. Rev. B*, 85:235151, Jun 2012.
- [339] B. Zheng. Deterministic equations of motion and phase ordering dynamics. *Phys. Rev. E*, 61:153–156, Jan 2000.
- [340] W. Zurek. Cosmological experiments in superfluid helium? *Nature*, 317(6037):505–508, 1985.
- [341] W. Zurek. Cosmological experiments in condensed matter systems. *Physics Reports*, 276(4):177 – 221, 1996.
- [342] W. H. Zurek, U. Dorner, and P. Zoller. Dynamics of a quantum phase transition. *Phys. Rev. Lett.*, 95:105701, Sep 2005.
- [343] M. Zwolak and G. Vidal. Mixed-state dynamics in one-dimensional quantum lattice systems: A time-dependent superoperator renormalization algorithm. *Phys. Rev. Lett.*, 93:207205, Nov 2004.